UQAR

Université du Québec
à Rimouski

Effet des paramètres de fabrication additive et de post-traitement sur les performances de l'acier maraging

Étude de sensibilité, exploration, modélisation et optimisation de la technique de la fusion laser sélective et des post-traitements appliqués à l'acier maraging (C300)

Mémoire présenté

dans le cadre du programme de maîtrise en ingénierie

en vue de l'obtention du grade de maître ès sciences appliquées (M.Sc.A.)

PAR
© FAICAL HABASSI

[FÉVRIER 2022]

Composition du jury :

Abderrazak El Ouafi, président du jury, Université du Québec à Rimouski

Noureddine Barka, directeur de recherche, Université du Québec à Rimouski

Mohammad Jahazi, codirecteur de recherche, École de technologie supérieure

Soufiène Amira, examinateur externe, Centre Québécois de la Recherche et de Développement de l'Aluminium (CQRDA)

Dépôt initial le [25 novembre 2021]   Dépôt final le [23 février 2022]

UNIVERSITÉ DU QUÉBEC À RIMOUSKI

Service de la bibliothèque

Avertissement

Dédicaces

Je dédie cette thèse :

À mon modèle, mon maître du sacrifice, de patience et de persévérance… Mon père. À ma source de bonnes valeurs de la vie, de joie, de motivation, de soutien, de bonté et de bénédiction… Ma mère. En témoignage et en gratitude de leur dévouement, de leur soutien permanent durant tout mes années d'études, de leurs sacrifices illimités, de leur réconfort moral, de leurs incessants encouragements, supports et prières, eux qui ont consenti tant d'effort pour mon éducation, mon instruction et pour me voir atteindre ce but, pour tout cela et pour ce qui ne peut être dit, mes affectations sans limites. Depuis mon jeune âge, vous m'avez inculqué les bonnes valeurs, principes, et caractères de la vie, vous m'avez éduqué pour que le comportement humble soit la priorité. Merci pour tous vos sacrifices, vos soucis et vos peurs pour moi. Je ne pourrais certes vous rendre la pareille, mais j'implore ALLAH pour me permettre au moins d'être une source de bonheur pour vous. Qu'ALLAH vous garde joyeux et heureux pour toute votre vie.

À ceux qui sont la source de mon inspiration et de mon courage, à qui je dois de l'amour et de la reconnaissance :

À la mémoire de mon premier professeur… À mon oncle Salih;

À tout ce qui m'a fait apprendre quelque chose un jour;

Mes sœurs et mon frère;

À toute personne qui m'est chère et qui m'a soutenue;

À la mémoire de mes grands-pères, ma grand-mère, mes oncles.

REMERCIEMENTS

En premier lieu, je tiens à remercier DIEU, notre créateur, de m'avoir permis d'accomplir ce travail dans les meilleures conditions d'avoir éclairé mon chemin et m'avoir doté de la connaissance.

*En deuxième lieu, je tiens à remercier du plus profond de mon cœur le professeur **Noureddine Barka** (directeur de recherche), professeur à l'Université de Québec à Rimouski, qui m'a donné la chance de mener ces travaux de recherche qui constituent aussi une passion pour moi et qui a fait preuve d'une grande disponibilité à mon égard. J'exprime ma pleine gratitude pour la confiance qu'il m'a accordée dès mon arrivée, pour son esprit scientifique qui restera une grande source d'inspiration, son soutien, ses précieux conseils ainsi que les moments d'échanges sans lesquels l'achèvement de mes études ne serait pas possible. Je tiens aussi à remercier du plus profond de mon cœur le professeur **Mohammed Jahazi** (co-directeur de recherche), professeur à l'École de Technologie supérieure, pour son soutien, ses précieux conseils et son intérêt à apporter son expertise et sa supervision sur les travaux réalisés. Une reconnaissance particulière pour sa passion de la recherche et sa quête insatiable de l'innovation qui nous a amenés à pousser les limites au-delà de nos objectifs.*

*En troisième lieu, je tiens à remercier l'ensemble des membres du jury de mémoire pour leurs remarques pertinentes et les échanges scientifiques le jour de ma soutenance. Je tiens à remercier M. **Abderrazak El Ouafi** de m'avoir fait l'honneur de présider le jury de mon mémoire. J'exprime ma plus grande reconnaissance envers M. **Soufiène Amira** d'avoir rapporté et évalué mon travail de mémoire et pour sa qualité de relecture.*

Mes sincères remerciements aux collègues de laboratoires de recherche de l'Université de Québec à Rimouski, spécialement M. Herinandrianina Ramiarison et M. Sasan Sattarpanah pour leur aide expérimentale et leur discussion fructueuse. Mes sincères remerciements aussi à M. Mohammad Saadati, post-doctorant et Mme Manel Houria, doctorante à l'École de Technologie supérieure (ÉTS), pour son aide dans la caractérisation de l'EBSD.

Rien n'aurait été possible sans la présence et le soutien indéfectible de ma famille. Que mes parents, mes sœurs, mon frère trouvent en cet aboutissement le fruit de la confiance qu'ils m'ont toujours accordée, et des sacrifices qu'ils ont faits pour moi durant ces années.

Enfin, j'adresse mes sincères remerciements à toutes celles et tous ceux qui m'ont aidé à différents stades de ce travail.

RÉSUMÉ

La fusion sélective laser (SLM) est un procédé prometteur qui est en voie de développement grâce aux innovations techniques et aux travaux de recherches actives qui ont vu le jour dans les récentes années. L'acier maraging (C300), qui appartient à la gamme des métaux qui peuvent être mis en œuvre par la fabrication additive grâce à sa bonne imprimabilité, a été utilisé dans différents domaines, tels que l'outillage, le moulage, l'aérospatial, et l'industrie automobile, en raison de ses hautes caractéristiques mécaniques. Cependant, certaines limitations sont toujours là, y compris le coût de production, la nécessité de post-traitement des pièces telles que construites et les effets non encore maîtrisés des différents paramètres du processus et des caractéristiques de post-traitement thermique. C'est pourquoi la fusion sélective laser des aciers maraging fait toujours un sujet intéressant de recherche et développement.

Néanmoins, beaucoup reste encore à faire pour perfectionner l'utilisation de la technique SLM pour la production des pièces complexes à haute résistance afin d'avoir un procédé rentable et efficace. Dans cette mémoire, l'influence de plusieurs traitements thermiques sur les différentes propriétés mécaniques des SLM-acier maraging (C300) ainsi que la sensibilité des ces propriétés mécaniques aux paramètres du procédé, spécialement la puissance laser, la vitesse de balayage, l'espace d'hachurage et la densité d'énergie laser, ont été examinées expérimentalement. À cet effet, plusieurs séries d'expériences ont été faites dans le cadre de la recherche en faisant varier les paramètres de SLM et de traitements thermiques pour disposer de données satisfaisantes pour pousser l'analyse en profondeur. Les paramètres de processus SLM et de traitement thermique ont été mesurés pour leur effet sur la formation de défauts, la microstructure et les propriétés mécaniques. Des outils statistiques tels que l'ANOVA sont utilisés pour cela, précédés d'une planification d'expérience faisant appel à la méthode Taguchi et un design factoriel complet. L'optimisation est faite à l'aide d'outils numériques qui sont des méthodes itératives et algorithmiques aidant à trouver les valeurs optimales. Les résultats de l'étude ont montré l'efficacité de cette approche en mettant en avant la sensibilité et l'apport des traitements thermiques en termes des performances mécaniques.

Mots clés : fusion laser sélective, paramètres de procédé, acier maraging, traitement thermique, propriétés mécaniques, optimisation, Taguchi, ANOVA.

ABSTRACT

Selective laser fusion (SLM) is a promising process, which is under development thanks to the technical innovations and the active research works which have emerged in recent years. Maraging steel (C300), which belongs to the range of metals affected by additive manufacturing thanks to its good printability, has been used in different fields, such as tooling, casting, aerospace, and automotive, due to its high mechanical characteristics. However, some limitations are still there, including the cost of production, the necessity of post-treatment of as-built parts, and the unchecked effects of various process parameters and heat post-treatment characteristics. Therefore, the selective laser melting of maraging steels is still a curious subject of research and development.

However, much remains to be done to perfect the use of the SLM technique to produce complex high-strength parts, in order to have a cost-effective and efficient process. In this paper, the influence of several thermal routes on the different mechanical properties of SLM-steel maraging (C300) as well as the sensitivity of these mechanical properties to process parameters, especially laser power, scanning speed, space hatching, and laser energy density, have been investigated experimentally. To this end, several series of experiments have been carried out within the framework of the research by varying the parameters of SLM and heat treatments to obtain satisfactory data for further analysis in depth. SLM process and heat treatment parameters were measured for their effect on defect formation, microstructure, and mechanical properties. Statistical tools such as ANOVA are used for this preceded by an experiment planning using the Taguchi method and a full-factorial design. The optimization is done using numerical tools which are iterative and algorithmic methods helping to find the optimal values. The results of the study showed the effectiveness of this approach by highlighting the sensitivity and contribution of heat treatments in terms of mechanical performance.

Keywords : selective laser melting, process parameters, maraging steel, heat treatment, mechanical properties, optimization, Taguchi, ANOVA.

TABLE DES MATIÈRES

LISTE DES TABLEAUX

LISTE DES FIGURES

LISTE DES ABRÉVIATIONS, DES SIGLES ET DES ACRONYMES

AM   Fabrication additive

SLM   Fusion laser sélective

PBF   Fusion sur lit de poudre

L-PBF   Fusion sur lit de poudre laser

DMLS   Frittage laser direct des métaux

EBM   Fusion par faisceau d'électrons

Ra   Rugosité

STL   Stéréolithographie CAO

SLS   Frittage laser sélectif

LOM   Fabrication d'objets laminés

LENS   Mise en forme du filet conçue au laser

BBC   Cubique centrée sur le corps

ANOVA   Analyse de la variance

RSM   Méthodologie de surface de réponse

ASTM   American Society for Testing and Materials

DMIG   Département mathématiques, informatique et génie

CLSM   Microscopie confocale à balayage laser

SEM	Microscopie électronique à balayage
EDS	Spectroscopie à rayons X à dispersion d'énergie
EBSD	Diffraction de rétrodiffusion d'électrons
SS	Somme des carrés
Adj MS	Carré moyen ajusté
Adj SS	Somme des carrés ajustés
UQAR	Université du Québec à Rimouski
E	Module de Young
Ys	Limite d'élasticité
Ys0.2%	Limite d'élasticité à la traction à 0.2% de déformation
UTS	Résistance à la traction ultime
Nf	Nombre de cycles jusqu'à défaillance
Po	Porosité
FEM	Méthode d'éléments finis
HT	Traitement d'homogénéisation en solution
AT	Traitement de vieillissement
HAT	Traitement d'homogénéisation en solution et vieillissement (HT+AT)
Ta	Température de vieillissement ($\circ$ C)
S	Concentration de la solution de refroidissement (%)
timea	Temps de vieillissement (min)

LISTE DES SYMBOLES

P	Puissance laser
V	Vitesse de scan
H	Distance/espace d'hachurage
t	épaisseur de couche
ED	Densité d'énergie
°C	Degré Celsius
HRC	Dureté en HRC
HV	Dureté en Vickers
Hz	Hertz
J	Joule
K	Kelvin
kg	kilogramme
kgf	kilogramme force
kW	kilowatt
min	Minute
MPa	Mégapascal
GPa	Gigapascal
J/mm3	Joule par millimètre au cube
K/s	kelvin par second

mm/s	Millimètre par second
mm	Millimètre
Kip	kilo-pound
Kpa	kilopascal
KN	kilo newton
Ni	Nickel
Co	Cobalt
Mo	Molybdène
Ti	Titanium
Al	Aluminium
Mn	Manganèse
cm	Centimètre
DDL	Degré de liberté
f	Fréquence
R2(adjus)	Coefficient de détermination ajustée
R2 (prev)	Coefficient de détermination prédictive
R2	Coefficient de détermination prédictive
s	Seconde
Sum of squares	Somme des carrés séquentielle
W	Watt

wt %   Pourcentage de masse

µm   Micromètre

INTRODUCTION GÉNÉRALE

1. GENERALITES

Les aciers maraging, qui sont des typiques alliages fer-nickel martensitiques avec une faible teneur de carbone et un taux important d'éléments d'addition, possèdent une haute propriété mécanique, telle qu'une ténacité élevée à des niveaux de résistance élevés, une excellente fabricabilité, une excellente soudabilité, une précision dimensionnelle, et une simplicité du traitement [1]. Pour ces raisons, les aciers maraging sont largement utilisés dans des industries requérant de hautes précisions, tels que le moulage [2], l'outillage [3], l'industrie automobile [4-5] et l'aérospatiale [6-7]. Ces aciers sont caractérisés par une structure martensitique typique durcissable par des traitements thermiques de vieillissement [8]. La tendance industrielle vers des aciers plus résistants est encore là, car elle permet une certaine optimisation de masse en gardant de bonnes résistances pour une application donnée.

La fusion sélective laser (SLM), à côté des autres techniques de fabrication additive (AM), est une technique de production en développement chaque jour [9]. Elle est capable de produire des pièces à géométries complexes en petits lots de production et pendant le prototypage, à partir d'un modèle CAO. À raison de ces différents avantages par rapport aux méthodes traditionnelles en termes de propriétés physiques et mécaniques, y compris la liberté, la simplicité et la flexibilité en termes de conception, le gain en termes de matière première qui peut aller jusqu'à 40 %, ainsi que la création de composants complexes à haute résistance, la technique SLM a trouvé diverses utilisations dans plusieurs secteurs, notamment les milieux médicaux, l'industrie automobile et aérospatiale [10]. Cependant le processus SLM met en jeu une variété des phénomènes physiques complexes, tels que le transfert de chaleur, le transfert de masse, le phénomène d'absorption et le mouvement fluide au sein de bain de fusion [11]. Par conséquent, de nombreuses études liées au traitement

d'une large gamme des matériaux attachés à l'AM en général et au SLM en particulier, y compris les alliages d'aluminium [12], les alliages de nickel [13], les alliages de titane [14], les aciers inoxydables [15] et les aciers outils [16-17]. En raison de la complexité physique et de l'hétérogénéité microstructurale générée, l'optimisation des paramètres de processus et de traitement thermique, qui est généralement indispensable, devient un problème critique fréquent. Un volume considérable de recherches a été publié sur différents matériaux qui peuvent être fabriqués de manière additive. Thijs et al. [14] (2010) ont étudié l'évolution microstructurale lors de la fusion laser sélective de Ti-6Al-4V. Liverani et al. [15] (2017) ont investigué l'effet des paramètres du procédé de fusion sélective au laser (SLM) sur la microstructure et les propriétés mécaniques de l'acier inoxydable austénitique 316 L. Tao et al. [13] (2019) ont expliqué le mécanisme de la croissance cristalline, l'espacement intercellulaire et la microségrégation du superalliage Inconel 718 fondu au laser sélectif. Read et al. [12] (2015) ont optimisé les paramètres de processus pour l'alliage d'aluminium fondu au laser sélectif et étudié la microstructure et les propriétés mécaniques. Liu et al. [18] (2020) ont étudié l'influence du pressage isostatique à chaud (HIP) sur les propriétés mécaniques de l'alliage de magnésium produit par fusion laser sélective (SLM).

Concernant les aciers à outils, qui ont généralement une tendance à devenir cassants sous des vitesses de refroidissement rapides, ce qui est l'une de difficultés de processus SLM. Cependant, les aciers maraging, en particulier le 18Ni (300), qui obtiennent leur dureté et leur résistance à partir d'un processus de traitement thermique après la construction sont souvent utilisés, car ils restent ductiles pendant la fabrication, empêchant la formation de fissures. Les aciers maraging sont donc des candidats évidents pour l'AM en générale, et la SLM en particulier, surtout que leurs performances mécaniques sont déjà élevées via les techniques traditionnelles. Ils sont bien impliqués dans des applications automobiles [4-5], aéronautiques [6-7], ainsi que les outils de production [3]. Ils acquièrent le caractère maraging (résistant) de sa microstructure martensitique renforcée par des nano-inclusions suite à des traitements thermiques de vieillissement [8].

La formation de martensite suite à des traitements en solution peut être atteinte à des températures d'austénitisation et des vitesses de refroidissement plus faibles, en raison du taux élevé de nickel qui permet une plus grande flexibilité sur les conditions de traitement sans compromettre la résistance du matériau [19]. Les nano-inclusions permettent une ténacité, une résistance, et une dureté plus élevée sans compromettre la ductilité [20]. En raison de leurs performances mécaniques supérieures, la fabrication de certains composés d'outillages, d'automobiles ou d'aérospatiaux à partir d'acier maraging (C300) via AM est un sujet de recherche difficile, qui tire encore l'attention des chercheurs. Parmi les techniques AM existantes, la fusion sélective laser (SLM) est la méthode la plus utilisée pour la production d'aciers maraging. Un nombre considérable de recherches sur l'acier maraging fabriqué par fabrication additive ont été menées ces dernières années. Le contenu de la recherche couvrait l'optimisation des procédés, la microstructure, la dureté, les performances de traction, les performances d'impact et le traitement thermique.

Wu et al. [16] (2020), Becker et al. [17] (2016), et Kempen et al. [21] (2011) ont étudié les effets des paramètres de procédé et du traitement thermique sur l'acier maraging fondu au laser sélectif. Ils ont découvert que la densité relative maximale de la pièce fondue au laser sélectif pouvait atteindre plus de 99 % et que la résistance à la traction ultime dépassait 1200 MPa à l'état tel que construit et 2000 MPa après un traitement de mise en solution et de vieillissement. Les traitements utilisés peuvent être considérés comme longs (le temps total de traitement varie entre 5 et 50 heures). Ullah et al. [22] (2020) et Mooney et al. [23] (2019) ont rapporté l'anisotropie plastique de pièces 18Ni (300) avec trois directions de fabrication (0◦, 45◦ et 90◦) fabriquées à l'aide d'une machine de fabrication additive laser. Cependant, un traitement thermique peut diminuer significativement cette anisotropie. Ils ont observé que l'orientation horizontale (0°) génère une dureté plus élevée que l'orientation verticale (90°) et l'orientation inclinée (45°). De Oliveira et al. [24] (2021) ont constaté que les échantillons avec une direction verticale à 90° offrent un meilleur comportement à la compression et une meilleure capacité d'absorption d'énergie que les pièces horizontales à 0°.

D'autre part, ils ont signalé que les échantillons traités thermiquement peuvent atteindre une résistance à la compression ultime plus élevée que les pièces telle que construite, avec une contrainte totale et une capacité d'absorption d'énergie très inférieure. Un pic de contrainte de compression similaire (~ 200 MPa) a été rapporté par Contuzzi et al. [25] (2013), à l'état tel que construit. Meneghetti et al. [26] (2017) ont rapporté que les échantillons d'acier maraging orientés 0° fabriqués de manière additive présentaient une résistance à la fatigue inférieure à celle des échantillons orienter 90°. Yao et al. [27] (2020) ont illustré que compte tenu de l'hétérogénéité du gradient de température, de la distribution de l'apport de chaleur et du taux de croissance, la microstructure de l'acier maraging SLM (C300) présente deux morphologies différentes, qui sont une sous-structure équiaxe et colonnaire. Ils ont observé que les échantillons tels que construits ont une orientation de grain aléatoire avec des textures faibles, ce qui est attribué au motif de balayage du faisceau (rotation de 67°). Condé et al. [19] (2019) ont étudié l'influence du traitement thermique sur la microstructure et les propriétés mécaniques. Les résultats ont montré que le traitement de vieillissement direct sans traitement en solution pouvait conduire à la dureté et à la résistance à la flexion les plus élevées avec une composition non homogénéisée conservée. De plus, la température plus élevée était nécessaire (980 ℃) pour obtenir la dissolution efficace de la microstructure telle que construite.

***

2.   PROBLÉMATIQUES

La complexité physique aura lieu au cours du processus SLM, les effets de paramètres de processus incontrôlables, ainsi que les longs traitements thermiques indispensables restent toujours les majeures difficultés face à l'industrialisation en masse du processus SLM pour les aciers, y compris les aciers maraging. Diverses recherches ont atteint les propriétés mécaniques les plus élevées après le traitement de vieillissement en optimisant la température et le temps de vieillissement, comme Wu et al. [16] (2020) (vieillissement à 550 ℃ pour 50 heures), Condé et al. [15] (2019) (traitement en solution à 820-980 ℃ pour 1 heure +

vieillissement à 420-480 ℃ pour 3-6 heures), Becker et al. [17] (2016) (traitement en solution à 830 ℃ pour 1 heures + vieillissement à 490 ℃ pour 6 heures), et Kempen et al. [21] (2011) (vieillissement à 480 ℃ pour 5 heures). Néanmoins, il reste encore de quoi à faire, y compris la sensibilité des performances mécaniques des aciers maraging aux paramètres de processus de fusion sélective laser SLM, l'optimisation des paramètres de processus et l'affinement de leur effet sur les performances mécaniques, l'optimisation des paramètres de traitement thermique sans compromettre les niveaux élevés des performances mécaniques, l'usinabilité de l'acier maraging fabrique par SLM et l'effet des paramètres de processus d'usinage, ainsi que la modélisation et la simulation de la fusion sélective laser des aciers maraging.

<p style="text-align:center">***</p>

3.   OBJECTIF DE L'ETUDE

L'objectif de cette étude est de comprendre les effets du traitement en solution et du traitement de vieillissement sur les propriétés mécaniques des échantillons d'acier maraging (C300) fabriqués par fusion laser sélective et d'établir des corrélations entre la dureté et les propriétés de processus de traitement thermique, d'une part, ainsi que d'investiguer la sensibilité des performances mécaniques de l'acier maraging (C300) aux paramètres de processus SLM, d'autre part. Pour réaliser le premier objectif spécifique qui est principalement axé sur l'exploration de l'effet des paramètres des traitements thermiques en solution et de vieillissement, des travaux expérimentaux pour mettre en évidence l'effet de la solution de refroidissement, la température et le temps de vieillissement seront menés. Une interrelation de corrélation entre la dureté et ses différents paramètres de processus thermique sera mise en place. Ces recherches ont pour but de recommander un traitement thermique optimal de courte durée, par rapport aux durées les plus fréquentes de la littérature, qui sont en général 1 heures pour le traitement en solution et 5-6 heures pour le vieillissement.

Le second objectif spécifique vise à maximiser le plus possible l'efficacité de la fusion sélective laser des aciers maraging, plusieurs travaux d'analyses sont nécessaires avant d'atteindre le but ultime. Un de ces objectifs est de savoir l'effet des paramètres de processus sur la qualité et les performances mécaniques des pièces finales qui en découlent et dégager une tendance à partir cette analyse pour pouvoir améliorer le processus. Ces recherches ont pour but d'investiguer profondément la sensibilité des performances mécaniques de l'acier maraging (C300) aux paramètres de processus de fusion sélective laser (SLM). Des travaux d'optimisation vont permettre de trouver les paramètres optimaux pour avoir la meilleure soudure selon les critères d'évaluation qui ont été admis dans cette étude, c'est-à-dire la microstructure et les propriétés mécaniques.

<center>***</center>

4.   MÉTHODOLGIE

La première phase du travail consiste à déterminer l'effet de paramètres de traitement thermiques en solution et de vieillissement de courte et moyenne durée, spécialement la solution de refroidissement, la température de vieillissement et le temps de vieillissement, ainsi que d'optimiser ce processus thermique pour obtenir les meilleures performances mécaniques. Pour cela, plusieurs séries de traitements thermiques, élaborées suivant un plan d'expérience Taguchi des trois facteurs à trois niveaux, seront conduites. Le plan d'expérience Taguchi tient compte des combinaisons indépendantes les plus significatives entre les divers niveaux de paramètres. Les travaux de fabrication par fusion sélective laser, d'une série des coupons de traction, seront exécutés en suivant ce plan en collaboration avec le centre d'Investissement Québec « CRIQ ». Les coupons fabriqués seront soumis à une caractérisation de microstructure, à des tests de dureté, et à des essais mécaniques de traction conformément au standard ASTM E8. Ces caractérisations mécaniques et métallurgiques seront faites dans les laboratoires de génie de mécanique de l'UQAR et de L'ÉTS. Considérant la dureté des coupons tels que construits et traités thermiquement, une fois les résultats expérimentaux obtenus, des outils d'analyses statistiques comme l'ANOVA seront

appliqués pour déterminer l'effet des paramètres de processus thermique sur la qualité et les performances mécaniques de l'acier maraging (C300) fabriqué par SLM. Un modèle de prédiction sera développé à partir des analyses pour déterminer à l'avance la dureté des pièces en acier maraging (C300) fabriquées par SLM à partir des paramètres de traitement thermique considérés. Le modèle servira également à l'optimisation des paramètres de traitement thermique par l'usage d'une surface de réponse qui permettra de déterminer les valeurs optimales.

La seconde phase est l'exploration ayant pour but de voir la sensibilité des performances mécaniques des aciers maraging aux paramètres de processus SLM. Les paramètres de processus considérés sont la puissance laser, la vitesse laser, et l'espace d'hachurage. L'optimisation commence par l'exploitation des résultats de l'exploration en définissant des plages de paramètres qui seront utilisés pour la construction du plan d'expérience. Pour cela, un plan d'expérience Taguchi des trois facteurs à trois niveaux sera élaboré. Les travaux de fabrication par fusion sélective laser, d'une série des coupons de traction, seront exécutés en suivant ce plan en collaboration avec le centre d'Investissement Québec « CRIQ ». Les coupons fabriqués seront soumis à une caractérisation de microstructure, à des tests de dureté et à des essais mécaniques de traction conformément au standard ASTM E8. Ces caractérisations mécaniques et métallurgiques seront faites dans les laboratoires de génie de mécanique de l'UQAR et de L'ÉTS. Une fois les résultats expérimentaux obtenus, des outils statistiques comme l'analyse de la variance ANOVA seront menés pour connaître l'importance et l'effet des paramètres de processus SLM considérés sur les propriétés de l'acier maraging (C300). L'analyse statistique permettra de proposer des modèles de prédiction permettant une estimation de la densification et des propriétés mécaniques à partir des paramètres. Le modèle servira également à l'optimisation des paramètres de processus par l'usage d'une surface de réponse qui permettra de déterminer les valeurs optimales.

***

5. **STRUCTURE DU MEMOIRE**

Ce manuscrit s'articule en quatre parties principales. Le premier chapitre est une synthèse bibliographique et une mise en situation générale. Il dresse un état de l'art des procédés de fabrication additive métallique, en donnant une attention spécifique au processus SLM. Le principe d'AM, les techniques, les domaines d'applications, les matériaux attachés, les paramètres les plus influents et les défauts typiques sont présentés.

Le chapitre 2 est dédié à la description spécifique de statuts présents de progression de la fusion sélective laser de l'acier maraging. La microstructure typique, les propriétés finales de l'acier maraging, l'état courant, les problématiques et les perspectives sont présentés et comparés à ceux de l'acier maraging (C300) obtenu par voie conventionnelle. Les chapitres suivants sont consacrés à la présentation des résultats expérimentaux et d'optimisation, qui répondent aux premiers et deuxièmes objectifs.

Le chapitre 3 traite de l'influence des paramètres de post-traitements thermiques considérés sur la microstructure et les propriétés mécaniques de l'acier maraging. Les évolutions microstructurales et mécaniques, suite aux traitements thermiques, obtenus sur l'acier maraging, sont analysées et étudiées. Une optimisation statistique suivant une approche ANOVA est conduite, pour délivrer un modèle de prédiction de dureté à partir des paramètres de post-traitements thermiques considérés. La validation des paramètres optimaux de post-traitements thermiques est effectuée à travers les tests de traction.

Le chapitre 4 traite de l'influence des principaux paramètres du procédé (puissance laser, vitesse de balayage, espace d'hachurage) sur la microstructure et les propriétés mécaniques de l'acier maraging (C300) élaboré par SLM. Cette partie vise à déterminer la sensibilité de propriétés mécaniques en termes de paramètres de processus et à mieux comprendre les interactions entre les paramètres SLM et les propriétés finales de l'acier maraging (C300).

***

[1] : Würzinger, P., Rabitsch, R., & Meyer, W. (2004). Production of maraging steel grades and the influence of specified and nonspecified elements for special applications. Journal of materials science, 39(24), 7295-7302.

[2] : Bai, Y., Yang, Y., Xiao, Z., & Wang, D. (2018). Selective laser melting of maraging steel: mechanical properties development and its application in mold. Rapid Prototyping Journal.

[3] : Mazur, M., Leary, M., McMillan, M., Elambasseril, J., & Brandt, M. (2016). SLM additive manufacture of H13 tool steel with conformal cooling and structural lattices. Rapid Prototyping Journal.

[4] : Fieger, T. V., Sattler, M. F., & Witt, G. (2018). Developing laser beam welding parameters for the assembly of steel SLM parts for the automotive industry. Rapid Prototyping Journal.

[5] : Leal, R., Barreiros, F. M., Alves, L., Romeiro, F., Vasco, J. C., Santos, M., & Marto, C. (2017). Additive manufacturing tooling for the automotive industry. The International Journal of Advanced Manufacturing Technology, 92(5), 1671-1676.

[6] : Iliopoulos, A., Jones, R., Michopoulos, J., Phan, N., & Singh Raman, R. K. (2018). Crack growth in a range of additively manufactured aerospace structural materials. Aerospace, 5(4), 118.

[7] : Ahn, J., & Kim, T. (2020). A Study of the Affected Layer and Stress Corrosion Crack of Ultra-high-strength Steel (300M) for Aircraft Parts. Journal of the Korean Society of Manufacturing Process Engineers, 19(4), 1-8.

[8] : Bodziak, S., Al-Rubaie, K. S., Dalla Valentina, L., Lafratta, F. H., Santos, E. C., Zanatta, A. M., & Chen, Y. (2019). Precipitation in 300 grade maraging steel built by selective laser melting: Aging at 510 C for 2 h. Materials Characterization, 151, 73-83.

[9] : Abdulhameed, O., Al-Ahmari, A., Ameen, W., & Mian, S. H. (2019). Additive manufacturing: Challenges, trends, and applications. Advances in Mechanical Engineering, 11(2), 1687814018822880.

[10] : Yap, C. Y., Chua, C. K., Dong, Z. L., Liu, Z. H., Zhang, D. Q., Loh, L. E., & Sing, S. L. (2015). Review of selective laser melting: Materials and applications. Applied physics reviews, 2(4), 041101.

[11] : Yuan, P., & Gu, D. (2015). Molten pool behaviour and its physical mechanism during selective laser melting of TiC/AlSi10Mg nanocomposites : simulation and experiments. Journal of Physics D: Applied Physics, 48(3), 035303.

[12] : Read, N., Wang, W., Essa, K., & Attallah, M. M. (2015). Selective laser melting of AlSi10Mg alloy: Process optimisation and mechanical properties development. Materials & Design (1980-2015), 65, 417-424.

[13] : Tao, P., Li, H., Huang, B., Hu, Q., Gong, S., & Xu, Q. (2019). The crystal growth, intercellular spacing and microsegregation of selective laser melted Inconel 718 superalloy. Vacuum, 159, 382-390.

[14] : Thijs, L., Verhaeghe, F., Craeghs, T., Van Humbeeck, J., & Kruth, J. P. (2010). A study of the microstructural evolution during selective laser melting of Ti –6Al – 4V. Acta materialia, 58(9), 3303-3312.

[15] : Liverani, E., Toschi, S., Ceschini, L., & Fortunato, A. (2017). Effect of selective laser melting (SLM) process parameters on microstructure and mechanical properties of 316L austenitic stainless steel. Journal of Materials Processing Technology, 249, 255-263.

[16] : Wu, W., Wang, X., Wang, Q., Liu, J., Zhang, Y., Hua, T., & Jiang, P. (2020). Microstructure and mechanical properties of maraging 18Ni-300 steel obtained by powder bed based selective laser melting process. Rapid Prototyping Journal.

[17] : Becker, T. H., & Dimitrov, D. (2016). The achievable mechanical properties of SLM produced Maraging Steel 300 components. Rapid Prototyping Journal.

[18] : Liu, S., & Guo, H. (2020). Influence of hot isostatic pressing (HIP) on mechanical properties of magnesium alloy produced by selective laser melting (SLM). Materials Letters, 265, 127463.

[19] : Conde, F. F., Escobar, J. D., Oliveira, J. P., Béreš, M., Jardini, A. L., Bose, W. W., & Avila, J. A. (2019). Effect of thermal cycling and aging stages on the microstructure and bending strength of a selective laser melted 300-grade maraging steel. Materials Science and Engineering: A, 758, 192-201.

[20] : Göbl, M., Eder, H., Prestl, A., Siller, I., & Schnitzer, R. (2020). Diffusion Bonding of High-Alloyed Tool Steels with Maraging and Precipitation Hardening Steels. Metals, 10(12), 1622.

[21] : Kempen, K., Yasa, E., Thijs, L., Kruth, J. P., & Van Humbeeck, J. (2011). Microstructure and mechanical properties of Selective Laser Melted 18Ni-300 steel. Physics Procedia, 12, 255-263.

[22] : Ullah, R., Akmal, J. S., Laakso, S., & Niemi, E. (2020). Anisotropy of additively manufactured 18Ni-300 maraging steel: Threads and surface characteristics. Procedia CIRP, 93, 68-78.

[23] : Mooney, B., Kourousis, K. I., & Raghavendra, R. (2019). Plastic anisotropy of additively manufactured maraging steel: Influence of the build orientation and heat treatments. Additive Manufacturing, 25, 19-31.

[24] : de Oliveira, A. R., de Andrade Mendes Filho, A., Masoumi, M., & Del Conte, E. G. (2021). Compression and energy absorption of maraging steel primitive scaffolds produced by powder bed fusion. The International Journal of Advanced Manufacturing Technology, 116(3), 1271-1283.

[25] : Contuzzi, N., Campanelli, S. L., Casavola, C., & Lamberti, L. (2013). Manufacturing and characterization of 18Ni marage 300 lattice components by selective laser melting. Materials, 6(8), 3451-3468.

[26] : Meneghetti, G., Rigon, D., Cozzi, D., Waldhauser, W., & Dabalà, M. (2017). Influence of build orientation on static and axial fatigue properties of maraging steel specimens produced by additive manufacturing. Procedia Structural Integrity, 7, 149-157.

[27] : Yao, Y., Wang, K., Wang, X., Li, L., Cai, W., Kelly, S., ... & Yan, F. (2020). Microstructural heterogeneity and mechanical anisotropy of 18Ni-330 maraging steel fabricated by selective laser melting: The effect of build orientation and height. Journal of Materials Research, 35(15), 2065-2076.

[28] : Conde, F. F., Escobar, J. D., Oliveira, J. P., Béreš, M., Jardini, A. L., Bose, W. W., & Avila, J. A. (2019). Effect of thermal cycling and aging stages on the microstructure and bending strength of a selective laser melted 300-grade maraging steel. Materials Science and Engineering: A, 758, 192-201.

CHAPITRE 1

FABRICATION ADDITIVE MÉTALLIQUE : TECHNIQUES, CONCEPTION DU PROCESSUS, PRINCIPAUX DÉFAUTS, ÉTAT DE L'ART ET ÉTAT ACTUEL

(Article à soumettre)

Faical. HABASSI[1, *], Noureddine. BARKA[1], Mohammed. JAHAZI[2],

[1] Mathematics, Computer Science and Engineering Department, Université du Québec à Rimouski (UQAR), 300 Allée des Ursulines, Rimouski, QC G5L 3A1, Québec, Canada

[2] Mechanical Engineering Department, École de Technologie supérieure (ÉTS), 1100 Rue Notre-Dame Ouest, Montréal, QC H3C 1K3, Québec, Canada

*Corresponding author. E-mail : Faical.Habassi@uqar.ca

1.1 RESUME EN FRANÇAIS DU PREMIER ARTICLE

L'attention industrielle et académique à la fabrication additive métallique (MAM) s'est accrue ces dernières années, en particulier en ce qui concerne diverses techniques d'adaptation de FA, l'optimisation des processus, la microstructure et la caractérisation mécanique. Cela est dû à sa capacité à supprimer toutes les difficultés et complexités géométriques. En théorie, aucune forme n'est inaccessible avec l'impression 3D, ouvre la voie à des créations qui seraient impossibles à réaliser avec les techniques de production traditionnelles. Plusieurs travaux de recherche ont été menés couvrant différentes pistes, dans le but d'étudier les procédés de fabrication métallique additive laser appliqué à de multiples matériaux. Cependant, de nombreuses lacunes subsistent encore dans le domaine, et doivent être explicitement étudiées afin de permettre aux chercheurs d'explorer d'autres directions. C'est pourquoi un examen périodique est nécessaire afin de mieux comprendre l'évolution

des processus AM puisque la technologie AM se développe rapidement et se poursuit sans relâche.

À cette fin, le présent manuscrit vise à mener une étude approfondie des principes du MAM, des matériaux compatibles, des avantages et des limites, ainsi que de ses différentes technologies ou systèmes. Une grande attention sera accordée aux systèmes à lit de poudre (en particulier la fusion laser sélective (SLM)). De plus, ses paramètres de processus les plus importants, leurs effets, ainsi que les principaux défauts rencontrés dans les techniques AM et/ou SLM, tels que la porosité, l'imprécision, la contrainte résiduelle et d'autres problèmes courants identifiés dans la littérature, seront présentés. Dans l'ensemble, cet article fournit un aperçu complet de l'état de l'art des techniques de FA, de leurs méthodes de contrôle, des défis et des orientations de recherche futures possibles.

Ce premier article, intitulé « *Metallic Additive Manufacturing : techniques, process design, main defects, state of art and present statement* » fut essentiellement rédigé par son premier auteur Faical Habassi qui a également conduit une recherche bibliographique approfondie de la littérature récente afin d'explorer un rapport présent de l'état actuel et l'avancement de la technologie de fabrication additive. L'article donne un intérêt spécial à la technique de fusion sélective laser (SLM). Noureddine Barka est le second auteur de cet article. Il est à l'origine de ce projet de recherche en proposant l'approche et la méthodologie pour aborder la problématique. Il a également contribué à l'amélioration de la rédaction pour la version finale. Le troisième auteur de l'article est Mohammed Jahazi qui a apporté son expertise du domaine de matériaux et procédé de fabrication.

1.2   TITRE DU PREMIER ARTICLE

Metallic Additive Manufacturing: techniques, process design, main defects, state of art and present statement

1.3 ABSTRACT

Industrial and academic attention to metallic additive manufacturing (MAM) have grown in recent years, particularly with respect to various AM adaptation techniques, process optimization, microstructure, and mechanical characterization. This is due to its ability to suppress all geometric difficulties and complexities. In theory, no shape is unattainable with 3D printing, which paves the way for creations that would be impossible to achieve with traditional production techniques. Several research works have been carried out covering different tracks, in a bid to investigate laser additive metallic manufacturing processes applied to multiple materials. However, many gaps still remain in the field, and must be explicitly studied in order to allow researchers to explore other directions. That is why a periodical review is required in order to better understand the evolution of AM processes since AM technology is developing rapidly and continues unabated.

To this end, the present manuscript aims to conduct an in-depth study of MAM principles, compatible materials, benefits and limitations, as well as its different technologies or systems. Great focus will be given to powder bed systems (especially selective laser melting (SLM)). Additionally, its most important process parameters, their effects, as well as the main defects encountered in AM and/or SLM techniques, such as porosity, inaccuracy, residual stress, and other common problems identified from the literature, will be presented. Overall, this paper provides a comprehensive outlook on the state of the art of AM techniques, their control methods, challenges, and possible future research directions.

1.4 INTRODUCTION

Unlike most conventional manufacturing techniques, such as machining, casting, and forging, which are based on material shrinkage, additive manufacturing, also known as 3D printing, rapid prototyping, or free-form manufacturing, is a process for producing parts by adding materials in successive layers, without tools, from numerical data in a 3D model [1-2]. The primary advantage of AM is that no shape is impossible using it. Indeed, 3D printing

paves the way for creations that would be impossible to achieve with conventional production techniques.

The very first AM technique used was stereolithography. A patent registered under the title *Device for Producing a Model of an Industrial Part* was published on July 16, 1984, by Jean-Claude André et al. [3] on behalf of the Cilas-Alcatel corporation. About a month later (August 8, 1984), Charles W. Hull [4] filed a patent for the same technology. In 1986, the first company (3D Systems) founded by Charles W. Hull [4] commercialized the stereolithography process.

However, the manufacture and sale of stereolithography machines did not begin until 1997 by the French company Optoform, founded by André-Luc Allanic and Philippe Schaeffer. The company was acquired in 2001 by 3D Systems. Additive manufacturing is therefore not a very recent technique and has in fact been used for more than 2 decades in the industrial market. Nevertheless, over this period, its industrial use has mainly been dedicated to prototyping, not to producing service components [5-6].

The additive manufacturing process [ASTM 52915 [7]] follows several general steps: design, slicing, programming, manufacturing, and support structure removal to obtain the final product (Figure 1.1). A file designed in CAD is usually generated in STL format. Next, a fixed-thickness digital slicing in horizontal layers are applied to the part. The thickness of the layers is one of the most important process parameters and is defined as a function of the manufacturing technology and the material used. The orientation of the part in space must also be considered since it has a significant influence on the actual fabrication and on the result. The next step, which is the production of the part, could take long to accomplish, depending on the process parameters. Once the 3D printed product is complete, post-processing is usually applied for dimensioning purposes in order to remove or reduce any residual stresses. Other finishing operations (polishing, machining, etc.) can then be applied to obtain the final part.

MAM is based on the principle of using high-power energy sources to incrementally fuse metal powder and ensure controlled re-solidification, layer by layer. The technology can produce complex geometries in pure metals or alloys to meet the needs of various industrial sectors and can be applied through several processes or technologies. Of all the MAM processes, the literature treats powder bed melting (PBF) as the most promising additive metal building process capable of achieving the most complex geometric patterns. The process is highly applicable in a wide range of industrial sectors, including biomedicine, automotive and aerospace. Selective laser melting (SLM), direct metal laser sintering (DMLS) and electron beam melting (EBM) are the primary metallic additive manufacturing (MAM) applications belonging to the 3D powder bed fusion printing family [8-13].

Although considered the most promising process for creating high quality parts in terms of mechanical performance, powder bed fusion faces certain challenges and limitations. These are related to securing a good surface finish, a homogeneous and porous microstructure, high static mechanical properties, and a high fatigue life. These limitations are attributable to the complex interactions between the different physical (thermal heat and mass transfer), mechanical (fluid flow) and metallurgical (phase change and microstructural evolution) behaviors seen during laser metal AM. The simultaneous existence of these different phenomena gives rise to instability among thermal gradients and other process variability [14-15], and thus, of fusion. It is therefore clear that the process parameters and the raw material characteristics significantly affect the resulting mechanical and microstructural performance, and these effects are of critical interest for MAM. This multiphysics problem must therefore be thoroughly understood in order to develop and optimize the MAM process.

To overcome the above challenges, several experimental investigations have been conducted [16-18]. As an aside, it should be noted that such work can be quite time

consuming and costly. Some such research [16-18] has focused on numerical process simulation, which can represent a promising tool for understanding this multiphysics problem. These works attempt to develop numerical prediction models to control the thermal behaviour, allowing it to understand the heat and mass transfers that will take place during MAM. The models and simulations in this process fall short in terms of providing a quantitative representation of prediction accuracy, and this hinders their application in process control and optimization. This explains the difficulty of finding models that are ready to be adapted for this problem, and why the degree of accuracy and uncertainty of the models must be studied repeatedly.

The objective of this work is to review MAM in general (section 2), which will help us to later align our study with the resources and objectives of research carried out under the auspices of the University of Quebec at Rimouski's additive manufacturing research unit. The rest of the article is broken down as follows: Section 3 presents the basics of the laser powder bed fusion (L-PBF) process, especially the SLM method, as well as a summary of previously published journal articles. Concluding remarks are then presented at the end of the article.

1.5 NOMENCLATURE

AM: Additive manufacturing

MAM: Metallic additive manufacturing

3D: Three-dimensional

PBF: Powder bed fusion

SLM: Selective laser melting

DMLS: Direct metal laser sintering

HIP: Hot isotactic pressing

1.6   METALLIC ADDITIVE MANUFACTURING

1.6.1   definition

MAM, as a manufacturing process, is based on the superposition of layers of metal created one by one to build a 3D object. When creating a layer, a high-power energy source (laser, arc or electron beam) is used to melt the raw material, usually a metal powder. The molten material then undergoes a controlled re-solidification to create a layer of defined thickness.

Various types of MAM equipment are commercially available. Metal FA is present in several systems within the industrial market, with MAM processes varying from one piece of equipment to another. These systems can be classified into families or categories. Table 1.1 presents the seven best known metallic and non-metallic additive manufacturing categories. These generally fall under wire feed, powder feed and powder bed systems. Each type has certain advantages, depending on its intended applications.

Table 1. 1. 7 Types of Additive Manufacturing [7].

AM Type	Definition
VAT Photopolymerization	*A liquid photopolymer immersed in a vat is selectively cured by light-activated polymerization.*
Sheet Lamination	*Selectively cut sheets of material are bonded to form an object.*
Material Jetting	*Droplets of material are deposited from a nozzle that moves horizontally over the construction platform, where solidification is produced using ultraviolet (UV) light.*
Binder Jetting (3D Printing)	*A liquid bonding agent is selectively deposited to bond powdery materials.*
Material Extrusion	*the material is selectively distributed through a nozzle or through an orifice. Example: FDM Fused Deposition Modeling.*
Powder Bed Fusion	*Thermal energy selectively melts some areas of a powder bed.*
Directed Energy Deposition	*Focused thermal energy is used to melt materials during deposition.*

1.6.2   Terminology

The vocabulary defined in this section summarizes some of the concepts and conventions encountered when studying additive manufacturing (see Figure 1.1):

o   Substrate: Support on which the part is manufactured.

o   Deposition: Contribution of material obtained with a heat source and a metal wire.

o   Layer: All passes deposited at a given height relative to the substrate. A layer may consist of one or more passes.

o   Deposition direction: Direction of movement of the impact of the heat source on the substrate or the lower layer. It also corresponds to the direction in which the pass is made.

o   Fabrication direction: The direction in which the part is fabricated. It is normal to the layer.
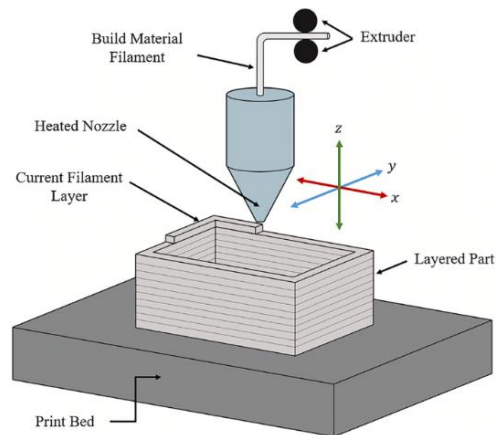
Figure 1. 1. Same terms used in metallic additive manufacturing (AM) [21].

o   Deposition speed: The speed at which the point of impact of the heat source moves relative to the substrate or lower layer.

o   Deposition rates: Amount of metal deposited per unit time in a continuous deposit. It is generally expressed in kg/h or cm3/h.

o   Wire speed: Speed at which the wire is unwound into the molten bath.

o Manufacturing speed: Speed at which the part is manufactured. It takes time into account.

1.6.3 Materials

Depending on the process, numerous materials can be used in MAM: titanium alloys (e.g., Ti-6Al-4V), aluminum alloys (e.g., AlSi10Mg), nickel alloys (e.g., Inconel718), as well as steels such as C-Mn steels, stainless steels, and tools/maraging steels. The range of materials used is given in Table 1.2.

Table 1. 2. List of the main metals used in metallic AM [19-23].

Metallic alloys	Example of alloys
Tool steels	Maraging 200/250/300
	H13
	AISI 420
Titanium	Ti-6Al-4V
	Titanium Grade 2
	Ti-Al6-Nb7
Stainless steel	SS 316L
	15-5 PH
	SS 440
Aluminum	Al-Mg-Sc/Scalmalloy
Nickel / Inconel	Inconel 718
	Inconel 625
	Inconel 738
Cobalt-chrome	CoCrWC
	ASTM F75
Hastelloy	Hastelloy X

Copper	CC 480 K

1.6.4   Development Interests and Limitations

AM was not invented to replace all the other traditional manufacturing techniques (machining, molding, welding, forming, casting, shaping, sintering, forging, injection, etc.). Rather, it is a complementary technique dedicated to the realization of creations that would be impossible with traditional techniques, as well as to the production of small series, notably the mass manufacture of customized parts.

1.6.4.1   Benefits of the AM Process

Metallic AM technologies provide many essential benefits [20-29], including:

- o Freedom of Design: No shape is impossible. 3D printing goes beyond traditional production techniques and paves the way for more varied creations (Figure 1.2).

Figure 1. 2. SpaceX AM built Super Draco rocket engines [24].

- o Parts relief/lighter parts: AM provides a good level of topological optimization (Figure 1.3).
- o Raw material economy: Raw material consumption is up to 25 times lower than

28

with machining.

o Part customization and repair (Figure 1.4): A key advantage of AM is that it allows the mass production of customized parts. It is also very suitable for the repair of metal parts.

o Removal of assemblies and welds: Manufacture of permanently articulated parts in one step [30].

Figure 1. 3. Examples of topological optimization in AM [28].

o Manufacture without specific tools: AM is a stand-alone technology that does not require the use of specific tools.

Figure 1. 4. The repair of damaged Titanium blisk using lasers metal deposition process [29].

1.6.4.2   Technology Limitations to the Development of AM in Industry

Like all other manufacturing processes, AM has certain limitations. There is general agreement that while the market in this area is growing very rapidly, it is not yet mature. Among the main limitations to the development of this process are the printing time and the machine cost. The following factors also represent obstacles for manufacturers:

- o Room size/area: In the case of powder bed technology, the size of the room is limited to the size of the powder bed (in SLM 800 machines: $500 \times 280 \times 850$) [30].
- o Surface finish of the final object: AM is unable to achieve the same quality obtained through conventional machining, and 90% of parts are returned for machining. On average, roughness (Ra) and precision are respectively 5 to 20 µm and 0.1 to 0.5 mm. Post-processing requires more time than machining.
- o Customized approaches for selected metals: Hard-to-weld alloys require specific approaches.
- o Lack of reliability: AM processes are not yet sufficiently repeatable.
- o Small series only: AM is generally only suitable for single or small series.
- o Multiple skills: The technology requires a high level of skill and process control.

1.6.5   Metallic AM systems

In this section, only applications of laser MAM are classified into different categories, although several other technologies do exist as well. The classification criteria used are related to the nature of the energy source, the type of feedstocks/raw material supplies, the maximum construction volume, etc. Three main families are considered: (i) wire feeding systems (ii) powder feeding systems, and (iii) powder bed systems that interest us most.

The section also provides a detailed review of the three process categories. Technological solutions for additive manufacturing are presented and discussed.

(i) *Wire-powered/wire feed systems*

Metal AM processes using a wire feedstock may be adapted to units that include a laser, electron beam or plasma arc energy source [31]. In addition to the diversity of the energy source, wire feed systems differ from the others in terms of deposit accuracy, adaptability to high deposit rate treatment, large construction volumes and installation costs. However, further machining operations should be applied to final products.

A laser wire AM unit is composed mainly of a laser source, a numerically controlled/CNC robot, a welding head and a wire feed load. This is in addition to other accessories such as tray preheating devices and gas protection devices.
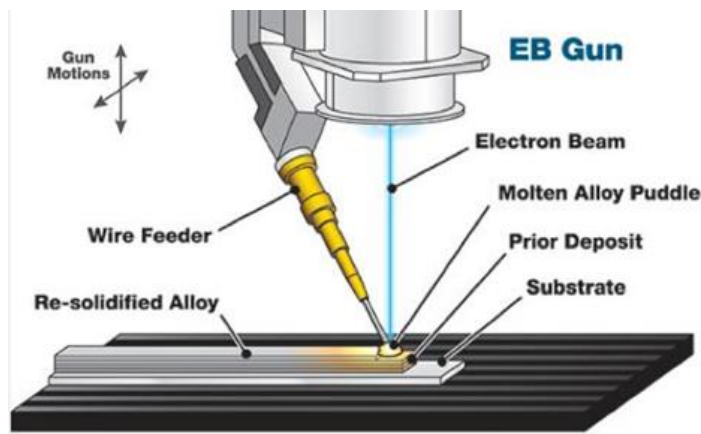
Figure 1. 5. Laser-wire process principle [31].

The principle of this process, described in Figure 1.5, is that a set of photons are used to create a melting bath on the substrate or on the previous layer and to merge the input metal to obtain a deposition. The focal spot and thread must be precisely adjusted and positioned. These settings vary depending on the behaviour of the alloy used during the deposition, as well as on its laser beam absorption characteristics.

The laser wire process is applicable on a wide range of materials such as aluminum-based alloys, titanium or nickel alloys, stainless steels and C-Mn steels. It is mainly applied with titanium alloys "Ti-6Al-4V" in the aerospace sector [32].

The laser wire process is characterized by several parameters related either to the energy source, such as laser power, laser wavelength, power distribution in the focal spot, focal distance, or to the wire, in terms of speed, diameter, direction of supply, point of impact of the wire, as well as the angle between the wire and the head or between the wire and the substrate and the rate of deposition. Some of these are intrinsic parameters specific to the laser wire unit (wavelength, laser beam size and shape, focal distance, etc.). However, other parameters, such as laser power, wire supply/feed and speed and deposition rate, may be adjusted as needed during the manufacturing process [33].

(ii) *Powder feed systems*

The process of MAM with powder feeding systems is more adaptable to volume increase than other processes [34]. The two most common configurations on the market are the fixed repository/deposition head and moving part configuration and the fixed part and the moving repository/deposition head configuration.
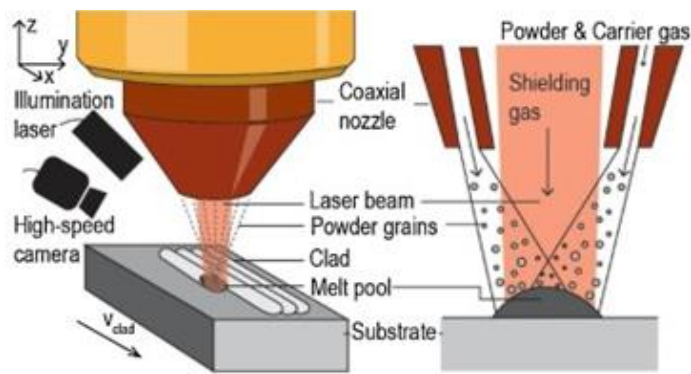
Figure 1. 6. Powder spray manufacturing principle [34].

The operating principle of these systems is that a quantity of powder is transported on the substrate using a nozzle [34]. This is done before a laser scans and fuses one or more layers into the desired shape. Among the advantages of this type of system are its larger construction volume and its ability to repair worn or damaged components [34]. A generic illustration of AM powder feed systems is shown in Figure 1.6.

32

(iii) Powder bed systems

Among the different MAM systems and processes, the literature identifies powder bed systems as constituting the most promising technology for the manufacture of parts with complex geometry [14, 18, 35-36]. Powder bed fusion (PBF) is the best-known technology in this family of systems [14, 18]. The two main PBF processes are selective laser melting (SLM) and electron beam melting (EBM) [14, 18]. These systems are based on the use of a programmed source of energy to scan and melt or sinter the powder of a layer applied on the construction tray, according to the desired geometry [14, 18]. Once a layer is completed, the construction platform is lowered by the pre-melted layer thickness and an additional powder layer are spread on the work platform. The process is repeated until the desired component construction is completed. When a powder bed is used in the SLM process, it is specifically referred to as the laser powder bed fusion (L-PBF) process [14, 18].

A generic illustration of an AM powder bed system is shown in Figure 1.7. A powder bed is formed by raking the powder onto the work tray. Powder bed systems in general, and the L-PBF process in particular, have many advantages. They are applicable to a wide range of materials such as ceramics, polymers, and metals [34] and can realize complex geometries while reducing manufacturing time and walls without the need for a support structure. Moreover, they are also capable of minimizing waste in terms of raw materials, and produce high-resolution characteristics, adjust properties during parts processing, create internal passages, produce almost dense components, and maintain dimensional control throughout manufacturing processes [9, 14, 18, 35-36]. The main limitation of these AM systems is their small construction volume.

Most powder bed systems are manufactured by European companies. EOS, a German company, is one of the leading manufacturers of AM units by SLM.
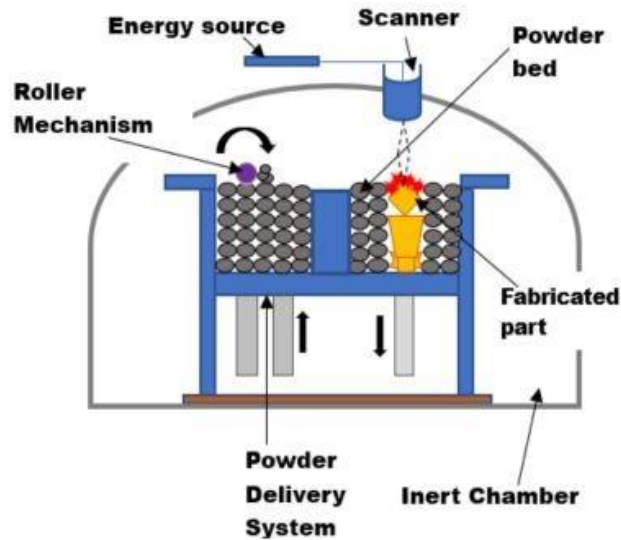
Figure 1. 7. AM powder bed process principle [18].

1.6.6 Areas of Application

Additive manufacturing represents a true technological breakthrough, as it forces a rethink of the engineering underlying systems design and production. Accordingly, the industry is investing heavily in what is a promising manufacturing sector. Currently, AM is present in several areas of applications in various business sectors [37], including aeronautics, automotive, medical, jewelry, sport and design and fashion.

In the medical sector, for one, the most used metal for metallic 3D printing of certain products (dental, prosthesis, etc.) is titanium. On the other hand, MAM is widely used in the aeronautics and aerospace sectors to produce high quality, small-series functional parts. The preferred metals in these sectors are stainless steel, chromium-cobalt alloys, tool steels/maraging steels, aluminum, titanium, etc.

In the industrial market, AM is mainly used for prototyping in the sectors involved in the production of large series. For small-series production, however, AM is used to

manufacture functional parts [38]. Prototyping can save a lot of time and money, as it allows to quickly transform design ideas into reality before launching actual mass production [39].

1.7 POWDER BED MELTING-SLM METHOD

Selective laser melting is one of the most promising additive powder-bed melting processes. This process results in final products having more complex geometry and much better spatial resolution than other additive manufacturing technologies [40-43]. Moreover, it generates fine microstructures due to the very high cooling speeds involved. It allows the production of complex functional prototypes and tools from a metallic powder, with minimum pre-intervention and post-treatments [44]. Below, we review the principle of the SLM process, the stages of the development of a piece by SLM, the different characteristics of the process, the shortcomings of this technology, and studies that have looked at laser-material interaction in SLM.

1.7.1 Definition and Principle

Selective laser melting, as other AM technologies, is in a way driven by micro-welding [45]. During an SLM process, a focused laser beam scans the substrate or powder bed surface, layer by layer, while being engulfed by an inert gas, to create a powder melting bath on the surface provided by the base STL file. The powder grains trapped by the bath of the melted material solidify, after which the platform can spread a new layer of powder. This must be repeated for each layer to create additional overlapping sections (Figure 1.8) [9]. Construction support is required for most parts. Once the process is complete, we recover the manufacturing tray and the part(s) manufactured, removing the construction support, which will be destroyed, as well as a quantity of untreated powder (Figure 1.9) [50].
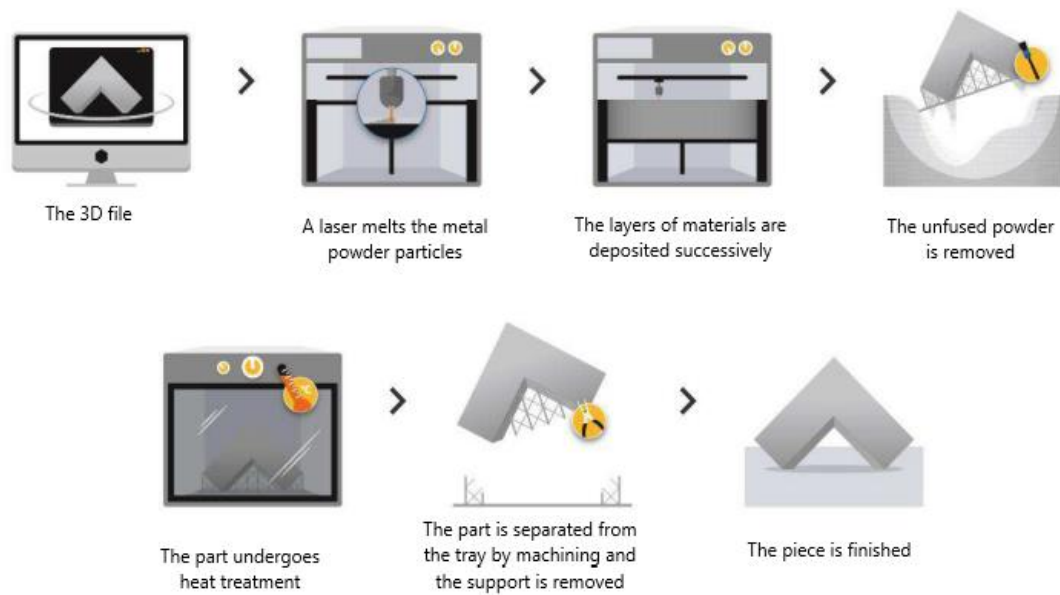
Figure 1. 8. Process steps of SLM [9].

This chapter was designed to provide a brief description of SLM technology and the critical challenges of the process of industrialization [46]. The influence of process parameters and post-processing heat treatment [47-50] on the quality of the final product and its mechanical and microstructural properties will be discussed to understand the process [51-55]. The literature isolates and highlights certain points or characteristics as deserving of further study. Several researchers have shown that some limitations underlie certain difficulties seen in the application of additive manufacturing processes, and the latter must therefore be studied before proceeding [52-53]. The property-performance interaction relationship must be fully understood and controlled, after which the properties of the final product can be predicted when selecting process parameters. Challenges here include ensuring instant control of surface quality and dimensional accuracy and overcoming microstructural heterogeneity. Moreover, removal and buckling problems can surface during the recovery of final parts. Furthermore, other problems can be encountered when printing specific thin-walled, large-scale parts. These—and more—are among the challenges that users of SLM technology have recently faced.

36
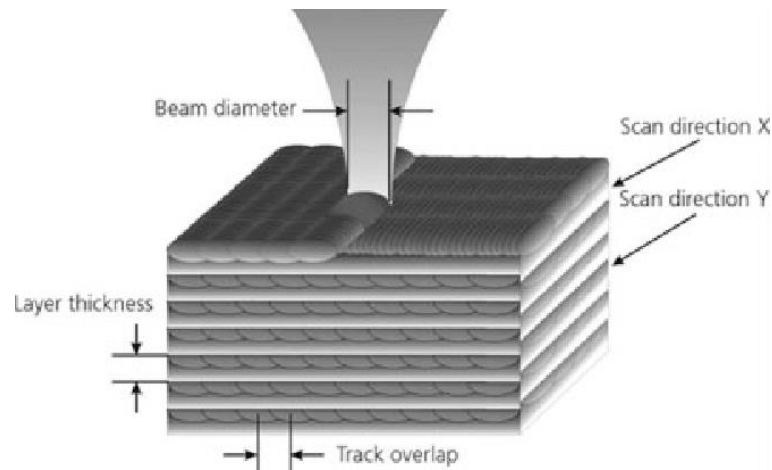
Figure 1. 9. The basic principle of the SLM process [50].

1.7.2   Process Selection

In order to carry out a multi-criterion selection according to feasibility, a list of criteria to be used must first be defined. In general, the criteria considered in the selection method developed are the same criteria for the parts to be manufactured and for the machines used.

The framework of this chapter does not allow us to delve deep into a detailed discussion of selection guidelines. However, once the technology is selected, some selection criteria can be used, such as the cost of the prototype, the variety of materials, the surface quality, the precision, the post-finishing, the impact resistance, and the bending resistance. Some other criteria must be considered, and some of them are presented below:

- o   Type of the treated powder
- o   Pre-processing
- o   Printing time
- o   Accuracy
- o   Surface Quality
- o   Post-treatment
- o   Mechanical performance

For each criterion, the performance of each option (process technology and machine) must be evaluated against it (the criterion). The relative importance of each of these criteria varies from one specific production case to another, depending on the user's needs regarding the part to be manufactured in that specific situation.

1.7.3   SLM Process Characteristics

Typically, using a solid CAD model and a metal powder, the SLM technology can create high quality, almost entirely dense physical objects and acceptable mechanical properties in a short period of time [46]. Unlike with the Selective Laser Sintering (SLS) process, completely dense objects can be obtained without the need to use post-processing SLM [47]. Supports are usually added to the virtually sliced 3D model. A powder layer is introduced on the substrate, in the form defined by the CAD. In general, the layers have a thickness of between 20 µm - 75 µm [48]. A laser with optical fibers sweeps and fuses the powder layer to create a pool of melted material. Then, a controlled re-solidification stage is conducted by the AM unit. Once a layer is finished, the work tray is lowered by an amount equal to the layer thickness and an additional layer of powder is spread. This process is repeated until the completion of the part (Figure 1.9). During the SLM process, an internal atmosphere, using an internal gas (generally argon [49]) must be ensured. At the end of the manufacturing, a supports removal stage must be completed. These are often difficult to remove, which is why they must be properly designed.

According to the literature, SLM can deal with a wide range of materials, such as cobalt alloys [50], nickel [51-52], titanium [53-56], as well as stainless steel [57-58] and C-Mn steel [59-60]. Over the past few years, SLM has been introduced as the most promising and recent AM process. This is due to its ability to meet manufacturing needs in terms of print time and price-performance ratio. It also overcomes certain geometric restrictions related to the routines of conventional manufacturing techniques, especially in the case of metal powders, such as casting and powder metallurgy. Thus, a melting bath control process is required to

38

ensure a complete melting of the metal powder [61]. According to Reheme et al. [62], this control process is initially aimed at maximizing the density of manufactured parts. The SLM AM process gives rise to several physical phenomena such as the transfer and diffusion of energy, mass transfer, phase change, and flow into the melting bath [63]. During the printing (heating) and cooling processes, the melting bath can be controlled through the temperature gradient and the required amount of energy [63-65].

However, these temperature gradients are very high, and their accumulation causes the generation of high residual stresses [66-67]. The estimation of the quality of the manufactured object, the dimensional accuracy, the internal stresses, and the metallurgical, mechanical, and microstructural performances are very importance. Nevertheless, process parameters greatly influence the different characteristics and performances delivered by the SLM process. Among the most critical process parameters for high quality production are laser power, laser speed, hatching space and orientation, and layer thickness. Pre-processing and post-processing are critical steps in the SLM (AM) process.

1.7.4   Most Influential Parameters

Although it is the most promising process, the L-PBF process faces some challenges in creating high quality parts in terms of surface roughness, mechanical performance, and fatigue life. These challenges can be attributed to the complexity of L-PBF processes and to the risk of incomplete fusion. This complexity stems from the fact that the L-PBF process depends on several parameters and produces a complex multiphysics problem. The quality and performance of the product manufactured by L-PBF can be affected by more than 130 parameters [68]. Depending on the case, potential uncertainties regarding the input parameters of the L-PBF process reduce the experimental accuracy of the process or the predictive accuracy of such a model. Most contributing parameters influence the surface quality, the internal morphology and the mechanical, metallurgical and microstructural performance. However, some parameters have a much greater influence than do others.

Certain parameters (Figure 1.10) play a greater role and influence the mechanical performance (tensile strength, fatigue strength), metallurgical performance (density, porosity, internal morphology of the part), as well as the surface quality (roughness, surface morphology) of printed parts, including laser characteristics such as laser power, print speed, orientation, hatching spaces and overlap amount. The performance of manufactured parts can also be affected by the characteristics of the powder used, such as the size and morphology of the powder.

This section aims to examine some of the controllable parameters that most affect the final quality of manufactured parts, including laser power, scanning speed, layer thickness, hatching distance, printing strategy and orientation, and post-processing.
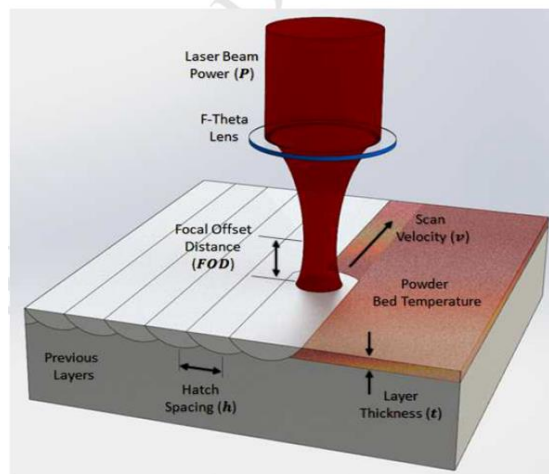
Figure 1. 10. Some operating parameters studied for SLM processing [66].

1.7.4.1 Laser Power

Laser power is one of the most critical parameters of the L-PBF process, which determines the surface quality and performance of the manufactured object. It can be defined by the amount of energy emitted by the laser to fuse a layer of powder. Possible laser power uncertainties result in a disturbance of melting/fusion because of an underestimation or overestimation of penetration depth. According to the literature, the source of such

uncertainties may be related to optical systems. When the power is too small, it may result in an incomplete melting/fusion of the powder, whereas when it is too high, it can lead to a vaporization of the merged/fused material. In the latter case, solidification will trap gas bubbles within its final geometry. This leads to high porosity rates [69]. James et al. [70] used a metal powder of a maraging 300 steel with a customized L-PBF system, using 100W-400W power range. They found that as the laser power increased, the relative density increased gradually, and a maximum value of 99.8% was found at 300 W. However, after 300 W, the part began to lose the dense character, and the density decreased to 99.2% for a power of 400 W. The power value of 300 W is part of a combination that gives a roughness value Ra = 35 µm.

Yadroitsev et al. [71] evaluated the impact of parameters related to energy density on the geometrical performance of a stainless-steel alloy treated with L-PBF. They observed that the laser power is the parameter having the most influence on the geometrical characteristics of single tracks. They classified the parameters of the process, from the most to the least influential. This classification starts with the laser power, and then layer thickness, the digitization speed, and finally, the least important, the grain size. Lameck et al. [72] performed an inter-correspondence analysis between the parameters used and the performance delivered by the L-PBF process. They used a powder of maraging steel. Their work led them to conclude that the increase in laser power causes temperature gradients that can lead to an increase in residual stress amplitudes and corresponding distortions. Qui et al. [73] used titanium alloy powder with a customized SLM system. They found that an increase in power from 150 W to 200 W led to a decrease in porosity. In a similar work using stainless steel, Gu et al. [74] varied the power, decreasing it from 195 W to 70 W, while keeping the energy density constant. They found that the porosity increased, and that the density decreased as the power decreased. Bai et al. [75] first studied the influence of the parameters of a customized L-PBF process on the relative density of a maraging steel. The study was then extended to tensile strength, shock resistance, microstructure, and microhardness. They found that the porosity first decreased and then increased with an increase in laser power (of course, the same goes for laser speed). This was because a low laser power at a high-scanning

speed generated a low energy density, which was not enough for fusion. Otherwise, a sufficiently high energy density takes place, resulting in high vaporization and subsequent accumulations of voids and inclusions. In their study, Abele et al. [76] varied the power from 165 W to 180 W for stainless steel parts. They found that the porosity decreased, and the tensile strength increased as the power increased. They also observed that the laser power had the least impact on the tensile strength.

Yao et al. [77] studied a maraging steel powder treated with the AM L-PBF process. They showed that beyond a critical density of 180 J/mm 2, the manufactured part is practically dense. Similarly, they observed that the laser power was the most influential parameter influencing the traction properties.

1.7.4.2   Laser scanning speed.

The laser speed or scanning speed is the speed at which the laser beam travels through the powder layer as it melts. This is one of the critical parameters of the SLM process, and directly influences the fusion and re-solidification of powder [78]. This parameter affects not only the final product quality, but also the printing time. Slight variations in laser velocity cause a disturbance of the fusion process, through its effect on peak temperature and fusion bath geometry [79]. A scanning speed that is too high may not give the laser beam enough time to fuse the powder. Increasing the scanning speed requires a higher laser power and a lower hatching distance to ensure a fusion process at the proper energy density. Lameck et al. [72] also concluded that an increase in scanning speed itself leads to an increase in residual stress amplitudes and corresponding distortions, through the temperature gradients generated. Song et al. [80] evaluated the effect of an increase in scanning speed on the hardness of a nickel alloy (NiCR) [80]. They found that when the scanning speed increased from 100 mm/s to 300 mm/s, the hardness of the final part increased as well. In their study, Kempen et al. [81] used steel powder (18Ni300) with a powder bed system to evaluate the influence of laser speed variations on the relative density and hardness of fabricated parts.

42

They found that an increase in speed from 120 mm/s to 600 mm/s led to a significant decrease in hardness and density. De Souza et al. [82] evaluated the microstructure and mechanical performance of a maraging 300 steel part fabricated by the SLM process, at a constant laser power of 400 W, and at a scanning speed of 600-1500 mm/s. They observed that the scanning speed has a slight influence on the manufacturing time. In fact, this time decreased as the scanning speed increased. Very high speeds result in much higher shear stresses in the melting bath. A high surface tension generated within a liquid medium increases the probability of balls formation, consequently increasing both the porosity and the surface roughness. Similarly, they showed that at the top surface of the manufactured parts, the scanning speed is the most influential parameter on the roughness. The resulting high surface roughness is due to the increase in speed gradually shrinking the scanned track until it becomes discontinuous and broken into balls. Sun et al. [83] conducted an AM study with an SLM system on a titanium powder (Ti-6Al-4V). They found that the density of this alloy decreased as the scanning speed increased. Qiu et al. [73] also treated titanium powder (Ti-6Al-4V) with an L-PBF system. They observed that an increase in speed from 800 mm/s to 1500 mm/s leads to a decrease in porosity and subsequently improves the relative density. Vandenbroucke et al. [84] used a similar AM system to produce parts made of titanium alloys (Ti-6Al-4V). Their work aimed to minimize porosity while maintaining certain requirements in terms of mechanical performance, such as stiffness, strength, hardness, and of parts. They observed that by increasing the speed (at low levels) from 90 mm/s to 190 mm/s, at a constant power and layer thickness, the powder layers risk being incompletely melted. This results in large pores, and subsequently, in a reduced relative density. Delgado et al. [85] compared the impact of a change in scanning speed between two different AM systems using stainless steel powders. They found that at an increased scanning speed, a change in AM systems does not lead to significant changes in either hardness or ultimate tensile strength. In their study, Abele et al. [76] varied the scanning speed from 1150 mm/s to 1350 mm/s for stainless steel parts. They found that the porosity increased, and that the tensile strength decreased as the speed increased. A similar study on stainless steel parts, in which a reduction of speed from 1200 mm/s to 600 mm/s led to an increase in density, and subsequently, to a decrease in porosity

level, was carried out by Gu et al. [74]. In their comparative study, Liu et al. [86] used the powder of a stainless-steel alloy with two types of powder, with different grain sizes. They observed a remarkable decrease in density. Similarly, they managed to push the ultimate tensile strength to the maximum. This indicates that they were within the optimal scanning speeds range.

1.7.4.3   Layer thickness.

The thickness of a layer is one of the basic parameters of the AM by L-PBF process. It is defined by the predefined thickness of powder bed at each scan [87]. SLM is capable of processing layers with thicknesses ranging from 20 µm - 75 µm [48]. The quality of the parts and their different performances are directly influenced by the layer thickness [88-92]. The accuracy of the layer thickness can be controlled both through the density of the powder bed and the movement and position of the substrate and cover arm [93].

During the L-PBF process, the layer thickness can be changed after each re-solidification phase. This has a proportional and direct influence on the overall manufacturing time. However, the layer thickness is limited by a step interval [48]. A layer that is too thick may not be sufficiently fused. Increasing the layer thickness requires a higher laser power and a slower laser speed. Some research works have studied the effects of a layer thickness as a process parameter on one or more performances of an SLM manufactured part. Daffily [94] noted that any increase in layer thickness leads to a decrease in the relative density of the manufactured object, and subsequently, in an increase in porosity [94]. The decrease in the magnitude of the residual stress can be attributed to a reduced thermal energy input and cooling rate. Lameck et al. [72] also concluded that as the layer thickness increased, both the residual stresses and distortions decreased. However, a corresponding increase in porosity was equally observed. Sun et al. [83] evaluated the influence of layer thickness variation on the relative density of a Ti-6Al-4V alloy with a customized L-PBF system [83]. They showed that the layer thickness and the relative density of the final product are inversely

proportional. Kempen et al. [81] studied the sensitivity of the density and hardness of a steel alloy (18Ni300) part to changes in layer thickness [81]. They also showed that when the layer thickness increased from 0.03 mm to 0.06 mm, the relative density and hardness of the final product decreased. In addition, some AM systems can provide almost constant performances with variable layer thicknesses, especially in terms of hardness and relative density. De Souza et al. [82] also showed that the layer thickness had a greater influence on the manufacturing time than did the scanning speed. They observed that when the layer thickness increased by about ~1.6, the fabrication time was reduced by up to 60%, while maintaining a reasonable surface roughness. In their comparative study, Delgado et al. [85] used stainless steel alloy powder on two different AM systems to evaluate the effect of a change in layer thickness [85]. They found that as the layer thickness increased, one system produced parts with a lower hardness, while no significant change in hardness was noticed for the other.

1.7.4.4   Hatching Space

The hatching distance is also a critical parameter that can be controlled by the AM unit via SLM. The laser passes through a powder layer following sequential tracks. The distance between the centers of two successive tracks is presented by the hatching distance (Figure 1.11). If the hatch distance values are too small, and below a critical value related to the laser beam diameter, an overlap between the laser passes is created. This overlap could burn the edge of the extreme tracks. Overly large values, however, can cause empty gaps due to an insufficient overlap, and subsequently, an incomplete melting of the metal powder.
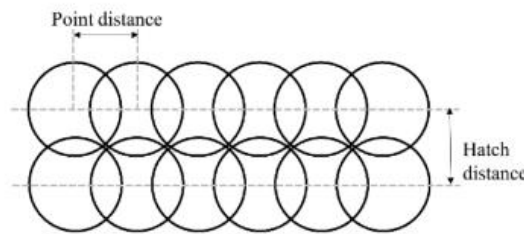
Figure 1. 11. Graphical representation of hatching space [98].

In their investigation, Abele et al. [76] quantified the impact of energy density parameters on the porosity and mechanical characteristics of a stainless-steel part. They observed that the hatching distance had the greatest impact on the ultimate tensile strength. They found that as the hatching distance increased from 0.12 mm to 0.19 mm, the tensile strength decreased, and the porosity increased. Bai et al. [75] also found that any increase in the scan space beyond a critical value generates incomplete fusion, and consequently, a low relative density.

Sun et al. [83] used a titanium powder (Ti-6Al-4V) to conduct an AM study with a customized L-PBF system while modifying the hatching distance. They also found that the density of this alloy increased as the hatching distance decreased. Vandenbroucke and Kruth [84] used a similar AM system to produce parts in titanium alloys (Ti-6Al-4V). They conducted a work aimed at minimizing porosity while maintaining certain requirements in terms of mechanical performance, such as rigidity, strength, hardness, and ductility of the parts. They observed that by increasing the hatching distance from 0.12 mm to 0.14 mm, at a constant power and layer thickness, the laser tracks risk being incompletely melted. This induces large pores and thus a decrease in the measured relative density.

1.7.4.5   Printing Strategy and Direction

The printing strategy is one of the most contributing parameters that determines the roughness and morphology of the surface of a manufactured part. This is due to its direct impact on powder fusion, heat transfer, re-solidification, as well as local and global distribution of defects. As shown in Figure 1.12 [95], there are different scanning strategies that can be used by the L-PBF process, such as "unidirectional", "cross-hatching", "spiral" and "zigzag". On the edges of the tracks to be scanned, a greater accumulation of defects occurs due to instability in the power level and a gradual reduction in the scanning speed, which produces a higher laser energy. This problem is much more present in "unidirectional" and "Zigzag" scanning strategies [96-97], whereas the "cross-layer" printing strategy can

balance the laser energy absorbed by the layers, to prevent further accumulation of defects. Multi-directional or zigzag scan refusion is suggested, especially for the last layer, to improve the surface roughness [98-99].
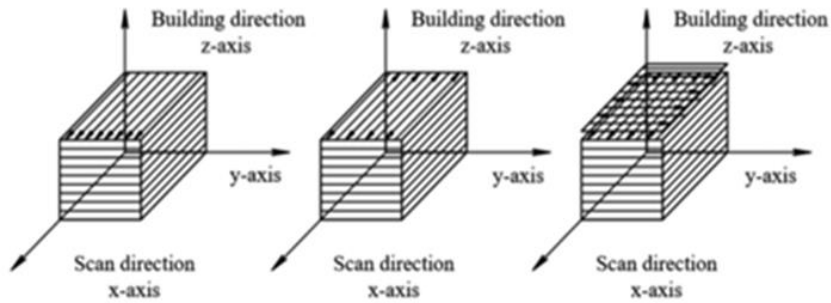
Figure 1. 12. Most Known printing strategy [61].

In their investigation, Huang et al. [100] and Yang et al. [101] worked on a study to reduce the formation of defects in the overlap area between tracks. To this end, they adapted an interlayer scaling and an orthogonal scanning strategy. Each time a layer is solidified, the laser beam re-scans the overlap areas between the tracks, as shown in Figure 1.13, to ensure a complete fusion of powders during the deposition of the next layer. Dai et al. [102] used an SLM AM process to study the influence of the scanning pattern and melting bath characteristics on the mechanical and microstructural performances of AISI12 steel powder parts. They found that refusion can be an effective method for pore removal.
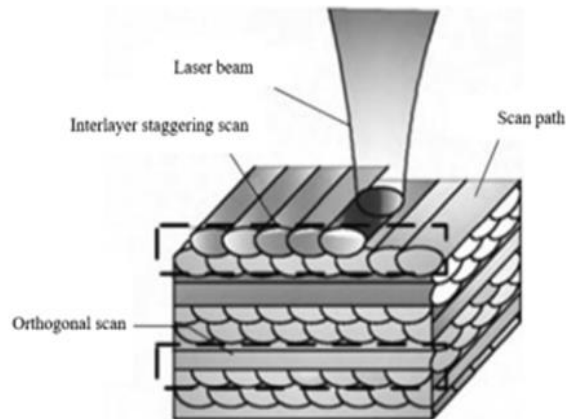
Figure 1. 13. Orthogonal scan strategy [61].

47

The printing direction is another parameter that determines the roughness and morphology of the surface, as well as the mechanical performance of a manufactured part. This is due to the change in solidification time and porosity rate generated by the process. De Souza et al. [82] concluded that parts with a 0°, 45° and 90° printing direction have a strong anisotropy. Therefore, the most significant factor affecting the mechanical performance of the part is porosity. A minimum porosity of 0.08% to 0.06% respectively on the surface and core was obtained for 900 mm/s speed combinations. In their comparative work, Bahardwaj et al. [103] used a powder of a maraging 300 steel, with a customized AM process, adapting two scanning directions, 0° and 90°, respectively. They found that the traction limits for the 90° direction are higher. This was due to the nucleation and coalescence of the micro-voids. Maneghetti et al. [104] analyzed the effects of the scanning orientation (respectively at 0° and 90° relative to the longitudinal axis of the specimen) on the axial and static fatigue properties of the maraging steel parts produced by an L-PBF process. They found that the construction direction did not have a significant influence on the mechanical properties, even for aged parts. They also concluded that the axial fatigue strength for a 0° orientation is the lowest.

1.7.4.6   Morphology and Powder Size

Powder size and morphology, as the most important contributing characteristics of powder, are crucial for the regularity and fluidity of the powder bed and the quality and surface roughness of the manufactured object. In addition, powder specifications can affect the other performances of the part, such as porosity. A smaller powder leads to a reduction in porosity. For instance, a powder that is too small and has a very irregular morphology impedes the smooth deposition of layers. Several methods of metal powder production affect the formation of defects [105-107], including the rotary plasma electrode, the electrolytic method, gas atomization, and water atomization. Bourell et al. [108] used a stainless 316L steel powder with a customized SLM system. They found that using a powder that is too

large (usually more than 100 µm) requires a much higher energy density for fusion. This results in a higher porosity rate for a specific energy density. In their work, Wang et al. [109] investigated the effects of powder size changes on the quality of 316L parts produced by SLM technology. They proved that the density of this alloy tends to increase as the size of the powders decreases. An average powder size of about 26 µm leads to almost dense parts with a relative density of 99.75%, while a powder twice the size (~50 µm) leads to a drop in relative density to 97.50%. In their comparison work, Jankus et al. [110] used a 316L stainless steel powder with particles ranging between 20 and 120 µ in size, as well as a powder of a GP1 maraging steel with particles ranging between 10 and 80 µ in size. They found that the GP1 powder grains melted more fully than those of the 316L and that the surfaces of both 316L and GP1 parts, have a worse adhesion between particles. The surface roughness was evaluated respectively at 11.4 µg m for GP1 and 13.7 µg m for the 316L.

1.7.4.7 heat treatment/post treatment

Post treatment is a controllable parameter, which is usually needed to relax the stresses generated by the process. It is a critical parameter of L-PBF processes, and crucial for the density and microstructural morphology of the manufactured object. This can be attributed to its ability to decompose martensite, relax stresses and reduce pores. Post-treatment by annealing and hot isostatic shrinkage and pressing martensite decomposition is the method that has attracted the most attention in the literature [111-115]. Several studies show that heat treatment by annealing generates a microstructure comparable to that obtained by HIP treatment. The relationship between maximum temperature, cooling rate and holding time is the key tool to accurately determine the final microstructural composition [115]. Krakhmaley et al. [116] applied HIP heat treatment under pressure to an advanced stainless maraging steel manufactured by L-PBF. They concluded that the pressure could affect the process, diminishing the hardness. Therefore, to ensure a certain level of hardness and high mechanical performance, during post-pressure heat treatment (like HIP), new thermal treatment regimens must be adapted. Guo et al. [117] evaluated the influence of post-

treatment on the microstructure and performance of an 18Ni300 steel fabricated by an L-PBF process. A comparison was made between parts manufactured by aged AM with parts consisting of conventional casting materials, both treated in solution (tempered/quenched) and aged. They found that the two different parts, in terms of manufacturing method, had a comparable hardness and resistance. For aged AM parts, the rate of inverted austenite formed increased as the aging time or temperature increased, whereas the precipitation hardening due to aging decreased. This is most pronounced for aging temperatures above 540 ℃. Conde et al. [118] applied different heat treatments to maraging steel parts manufactured by an SLM process, to homogenize and refine the microstructure and ensure a martensite-austenite reversion. They found that the as-built part had a non-homogeneous microstructure with a retained austenite density of 4% and no remarkable precipitation. The hardness of the as-built parts was higher than that of the homogenized parts. They also observed that direct aging of a part can give it the most toughness, smallest strain to failure, and highest flexural strength compared to the preferential secondary precipitates generated. Rather high homogenization temperatures (980 ℃) were recommended to guarantee a more efficient microstructural dissolution. The introduction of an inter-critical tempering process can provide both flexural strength and a reasonable ductility.

1.7.5   possible defects

The SLM process still faces certain limitations. In fact, due to the complexity of the L-PBF process and the wide range of contributing parameters, some defects may be inevitably introduced because of a wrong choice of one or more parameters, which can create dynamic instability in the melt bath. They may also be due to several other reasons, such as thermal build-up in the printing chamber, environmental disturbances such as gas contamination, and any other disturbances that may be experienced by the machine. The type and nature of the defect vary from one material to another, with some materials being susceptible to certain specific defects. In all cases, these defects must be corrected, especially for critical

applications. The most common defects are incomplete melting, geometric and dimensional inaccuracies, residual stress, cracking/fissuring and porosity. This section provides an in-depth discussion of the main possible defects.

1.7.5.1   Incomplete Melting Holes

Incomplete melting, or lack of melting, occurs mainly because of an insufficient estimation of the energy required to melt all the particles of the powder in a layer, during an L-PBF process. This type of defect appears in a layer because some of the metal powders in that layer have not yet melted, and therefore, the overlay is insufficient to deposit the next layer [119-122]. The shape of a localized melting defect between layers is very similar to that of cracking [123-124].

1.7.5.2   Geometric and Dimensional Inaccuracy

Different types of geometrical and dimensional inaccuracies can be observed in an AM fabricated part, including curved surfaces, shapes of dimensional deviations, such as geometrical inaccuracies, as well as indentations/shrinkage (longitudinal, transverse) and distortions (angular, rotational, bending) [125]. Geometrical defects are caused and influenced by machine error in the process parameters and by the staircase effect due to the stepped overlapping of the layers. Indeed, the slicing thickness of a part's STL file is directly responsible for the creation of the staircase effect. The influence of the deviating staircase effect becomes more and more pronounced as the deviating layer becomes thicker [126-127]. The layer thickness, or the height errors, may somewhat thus be considered as the main sources of curved surfaces and volumetric errors: the presence of a staircase effect generally leads to volumetric errors as well. These volumetric defects introduce geometric and dimensional tolerance errors on the part manufactured by AM, which affects its adhesion. As for shape errors due to dimensional deviations, they occur because of laser positioning errors and/or platform movement errors [128-129].

Dimensional inaccuracy can be caused by several parameters, each to a certain degree. However, some of them contribute to a greater extent and are more important for the dimensional accuracy. The most important parameters on dimensional inaccuracy cited by the literature are shrinkage, construction direction, effective laser diameter, tap/grip density, gas flow rate and microstructural undulation [130-131]. Regarding shrinkage, cyclic phase change can cause thermal volume shrinkage following an SLM process. During an L-PBF process, rapid cyclic melting followed by re-solidification and cooling of the manufactured part gives rise to very high temperature gradients. This type of shrinkage becomes ever more significant as the laser power increase and/or the hatch spacing and scanning speed decrease. It can also be affected by layer thickness, plateau temperature and the time interval between the superposition of two consecutive layers. Indeed, any increase in layer thickness, time interval and plateau temperature lead to a decrease in shrinkage [132-133]. The accumulation of these temperature gradients with volume shrinkage together generates a warping which gives rise to a degree of dimensional imprecision, and subsequently, a poor final quality [134-136]. The supports are generally essential to reduce excess heat from the manufactured part, and consequently, reduce the risk of warping [137]. Accordingly, optimized, and well-designed brackets can improve the accuracy of the L-PBF produced part. Distortions also occur because of thermal expansion and volume shrinkage. This is especially problematic for thin-walled parts [138]. To reduce this type of dimensional error, the manufacturing strategy must be optimized by conducting a compensation technique and parameter control.

1.7.5.3   Residual Stress

Some defects are very common and even inherent, including residual stress for an AM manufacturing process. Practically no manufactured part is free of residual stress. At the microscopic scale, it is impossible to deal with the generation of this type of stress. This is because very high thermal gradients are generated during AM processes. The impact of such a stress can cause poor mechanical properties, including fracture toughness, fatigue

performance, geometrical distortions, and changes in grain microstructure such as delamination of layers during deposition [139]. Residual stresses can also lead to some geometrical inaccuracies, which introduce deformations on the part, including geometrical and tolerance errors.

A residual stress is a static multiaxial stress remaining in the part after the removal of an external load (force, moment, etc.) [140]. Permanent damage caused by this stress is apparent if it exceeds the local yield strength of the metal and/or the local tensile strength. Such a situation can cause buckling/warping due to plastic deformation or can produce cracks or dislocations [141]. The thermal phenomenon occurring during the AM manufacturing process can introduce macroscopic residual stresses due to differential heating and cooling of the solid during and after solidification.

To reduce the damage caused by residual stresses, certain post-treatments are recommended in the literature. Optimization and residual stress control studies have always been an important research topic.

1.7.5.4   Cracks and Delamination

Cracking and fissuring are among the dramatic effects of residual stress on the behaviour of an AM manufactured part. This applies to practically all AM processes, except EBM. The large temperature gradients caused by the high and localized energy input in terms of application area are sources of high residual stresses. They cause crack initiation and propagation in affected objects [142-143].

The presence of these gradients introduces strong deformations within the molten bath and generates tensile stresses throughout the manufacturing process. These deformations disrupt the normal flow of the solidified grains. For several materials, the residual tensile stresses generated by the manufacturing process are responsible for hot tearing and cracking. This type of cracking is classified as solidification cracking. Another category of cracks, often propagating along grain boundaries, is classified as boundary cracking. Such cracking

is caused by the difference in morphology at the boundaries and possible precipitates within the grain boundaries [144-145]. Incomplete fusion can result in the separation of adjacent layers, known as delamination. Delamination between layers is considered to be cracking or fissuring. Cracks and delamination affect not only the thermal signature, but also the mechanical performance generated by the manufacturing process, in an AM manufactured part. Often, this type of defect is quite visible and irreparable. Indeed, no post-treatment can repair the damage of such defects. However, the defect can be avoided, which is why a preheating treatment of the construction plate is recommended.

1.7.5.5   Porosity

Porosity is the most common and controllable defect in an AM manufactured in part, through the manipulation of process parameters. This defect is unavoidable but choosing the right process parameters can limit its effects. Pores are volumetric defects appearing microscopically as cavities of roughly spherical shape and small size, generally no more than a few tens of microns [146]. The formation of pores can be related to process parameters, powder morphology, shielding gas and any other parameters involved in melting and re-solidification [147-151]. Porosities can be classified into two categories: spherical pores resulting from gas inclusions and non-spherical pores, with a variety of sizes induced by the technique and process parameters. At the very high temperatures and cooling rates that characterize the AM process, spherical gas bubbles are likely to be trapped between particles of molten powder. This spherical porosity is unavoidable, randomly distributed in the object manufactured by AM, and is practically difficult to eliminate completely.

1.8   SUMMARY AND FUTURE OUTLOOK

The main aim of this paper was to present an analysis of recent works examining various significant aspects of metallic additive manufacturing (MAM) development,

especially the principle underlying the technology, its advantages and limitations, application areas, related materials, MAM techniques and systems, process design, most critical process parameters, main defects, and control methods, such as post-processing heat treatment. Special interest has been given to the SLM technique, in order to directly align it with our research. The main conclusions and future research directions for this work are as follows:

• The MAM process and its equipment are under continuous development. It comprises a variety of application techniques, making it easily adaptable for any material. Some examples of popular AM systems are VAT Photopolymerization (polymers), Sheet Lamination (plastic, woven fibre composites or metal), Material Jetting (Polymers), Wire-powered/wire feed, Powder feed and Powder bed systems (metals).

• The final quality of the parts delivered by the various MAM techniques encourages mass production. However, some major hurdles continue to face MAM integration into industrial mass production.

• Future in-depth systematic research is recommended in order to satisfy the real objectives and needs of the industry regarding the industrialization of MAM in mass production. The main challenges are the reduction of manufacturing costs, in order to provide optimal protocols for materials attached to AF and why not further expand the range of materials.

• Notwithstanding the many advantages presented by MAM, such as rapid prototyping, freedom, and flexibility in terms of design, optimization of raw materials, using different types of new materials, and the good mechanical performances delivered, MAM faces a few challenges, including metal support structures, the time and cost required to remove supports after construction, the effect of the complex physical environment involved on the metallurgical and mechanical quality of parts, the imperfect surface finish of metal parts, the geometric precision, the effect of process parameters, the optimization of long and essential post-processing, and part size limitations (especially for SLM), which slow down the adoption of MAM somewhat.

• In particular, SLM is a promising technology and researchers are exploring it for various materials such as nickel alloys, titanium alloys, aluminum alloys, and steels. At the same time, the possibility of its application to other advanced materials such as metal matrix composites should be explored.

• Recent research, efforts and advances of MAM, including SLM, around the development of new materials, have made it possible to improve the industrialization of additive techniques by helping to overcome some of the challenges mentioned above. Nevertheless, there is still room for improvement and further investigation. For example, more systematic work needs to be done in terms of studying the relationship of geometric precision, microstructure, and mechanical properties with parametric processes, on the one hand, and the characteristics of heat treatments, on the other hand.

• During SLM, for example, strong thermal stresses with a different history from one layer to another will occur, which makes it difficult to control and/or predict the evolution of the microstructure, which is critical for the final mechanical properties. Therefore, more systematic work in terms of the study of metallurgical behaviour within parts is needed.

• Problems faced in SLM—AM in general—include defects, cracks, dislocations, residual stresses, and microstructural anisotropy. This paper presented the main defects and analyzed the mechanism of formation of typical defects with optimized methods. This could help in a design process that is appropriate to required outputs.

• Current developments in the different AM processes, including SLM, such as the printing of maraging steels, stainless steels, titanium alloys, and multi-materials, open new opportunities, which will allow to present AM as the key to Industry 4.0. Significant developments and valuable additions are available in the literature. Nevertheless, there are still opportunities for improvement and further investigation.

Information gaps are the major reason why AM techniques, including SLM, have not yet been explored to the maximum. The present work can serve as a catalyst for future work to overcome the different challenges mentioned above. To this end, it is strongly

recommended to complete in-depth systematic works seeking complete process control, optimization of the different parameters, and the prediction of final properties.

1.9 REFERENCES

[1] : Righettini, P., & Strada, R. (2021). Driving Technologies for the Design of Additive Manufacturing Systems. HighTech and Innovation Journal, 2(1), 20-28.

[2] : Wittekind, C., & Harris, G. (2021). Searching for the inscrutable: A search for clarity in digital manufacturing definitions, terminologies, and technologies. In IIE Annual Conference. Proceedings (pp. 686-691). Institute of Industrial and Systems Engineers (IISE).

[3] : André J.-C., L e M ehaut ´ e A. et D e W itte O., « Dispositif pour réaliser un modèle de pièce industrielle », Brevet FR 2 567 668 – A1, Date de dépôt : 16-07-1984, date de publication : 17-01-1986.

[4] : Hull C.W., "Method and apparatus for production of three-dimensional objects by stereolythography", Brevet EP 0 171 069 – A2, Date de dépôt : 08-08-1984, date de publication : 12-02-1986.

[5] : Dubois P., A oussat A. et D uchamp R., « Prototypage rapide – Généralités », Dossier Techniques de l'Ingénieur, l'expertise technique et scientifique de référence, BM7017, 10/04/2000.

[6] : Bernard A. et Taillandier G., « Le prototypage rapide », Ed. Hermès, 1998.

[7] : AFNOR, « NF ISO/ASTM 52915 Spécification normalisée pour le format de fichier pour la fabrication additive (AMF) », 2016.

[8] : Ashima, R., Haleem, A., Bahl, S., Javaid, M., Mahla, S. K., & Singh, S. (2021). Automation and manufacturing of smart materials in Additive Manufacturing technologies using Internet of Things towards the adoption of Industry 4.0. Materials Today: Proceedings, 45, 5081-5088.

[9] : https://www.a3dm-magazine.fr/news/fabrication-additive-metallique/procede-de-fabrication-additive-slm

[10] : Saremian, R., Badrossamay, M., Foroozmehr, E., Kadkhodaei, M., & Forooghi, F. (2021). Experimental and numerical investigation on lattice structures fabricated by selective laser melting process under quasi-static and dynamic loadings. The International Journal of Advanced Manufacturing Technology, 112(9), 2815-2836.

[11] : Eyers, D. R., & Potter, A. T. (2017). Industrial Additive Manufacturing: A manufacturing systems perspective. Computers in Industry, 92, 208-218.

[12] : Gisario, A., Kazarian, M., Martina, F., & Mehrpouya, M. (2019). Metal additive manufacturing in the commercial aviation industry: A review. Journal of Manufacturing Systems, 53, 124-149.

[13] : Barbier, L. (2020). Industry 4.0 Adoption for US Aerospace and Defense Industry.

[14] : Rivera, F. J. M., & Arciniegas, A. J. R. (2020). Additive manufacturing methods: techniques, materials, and closed-loop control applications. The International Journal of Advanced Manufacturing Technology, 109(1), 17-31.

[15] : Taheri, H., Shoaib, M. R. B. M., Koester, L. W., Bigelow, T. A., Collins, P. C., & Bond, L. J. (2017). Powder-based additive manufacturing-a review of types of defects, generation mechanisms, detection, property evaluation and metrology. International Journal of Additive and Subtractive Materials Manufacturing, 1(2), 172-209.

[16] : Barroqueiro, B., Andrade-Campos, A., Valente, R. A. F., & Neto, V. (2019). Metal additive manufacturing cycle in aerospace industry: A comprehensive review. Journal of Manufacturing and Materials Processing, 3(3), 52.

[17] : Mirkoohi, E., Ning, J., Bocchini, P., Fergani, O., Chiang, K. N., & Liang, S. Y. (2018). Thermal modeling of temperature distribution in metal additive manufacturing considering effects of build layers, latent heat, and temperature-sensitivity of material properties. Journal of Manufacturing and Materials Processing, 2(3), 63.

[18] : Aversa, A., Marchese, G., Saboori, A., Bassini, E., Manfredi, D., Biamino, S., ... & Lombardi, M. (2019). New aluminum alloys specifically designed for laser powder bed fusion: a review. Materials, 12(7), 1007.

[19] : Ngo, T. D., Kashani, A., Imbalzano, G., Nguyen, K. T., & Hui, D. (2018). Additive manufacturing (3D printing): A review of materials, methods, applications and challenges. Composites Part B: Engineering, 143, 172-196.

[20] : Revilla-León, M., Meyer, M. J., & Özcan, M. (2019). Metal additive manufacturing technologies: literature review of current status and prosthodontic applications. Int. J. Comput. Dent, 22, 55-67.

[21] : Shah, J., Snider, B., Clarke, T., Kozutsky, S., Lacki, M., & Hosseini, A. (2019). Large-scale 3D printers for additive manufacturing: design considerations and challenges. The International Journal of Advanced Manufacturing Technology, 104(9), 3679-3693.

[22] : Das, A., Chatham, C. A., Fallon, J. J., Zawaski, C. E., Gilmer, E. L., Williams, C. B., & Bortner, M. J. (2020). Current understanding and challenges in high temperature additive manufacturing of engineering thermoplastic polymers. Additive Manufacturing, 34, 101218.

[23] : Gibson, I., Rosen, D., Stucker, B., & Khorasani, M. (2021). Materials for Additive Manufacturing. In Additive Manufacturing Technologies (pp. 379-428). Springer, Cham.

[24] : SpaceX, SuperDracos, 2014. https://www.flickr.com /photos/spacex/16789102495/in/photolist-rzAxfp-AVPiao/ (accessed Mar. 16, 2021).

[25] : Oter, Z. C., & Coskun, M. (2021). Effect of building platform position on the surface quality, dimensional accuracy, and geometrical precision of direct metal laser sintering (DMLS) parts. Dimensional Accuracy, and Geometrical Precision of Direct Metal Laser Sintering (DMLS) Parts (February 15, 2021).

[26] : Valencia, E. A., Berrazueta, M., Leines, D., Lema, H., Rodriguez, D. A., & Hidalgo, V. (2020). Aerodynamic design and testing of a Ram Air Turbine for Small Fixed-Wing UAVs. In AIAA Propulsion and Energy 2020 Forum (p. 3957).

[27] : Attarzadeh, F., Fotovvati, B., Fitzmire, M., & Asadi, E. (2020). Surface roughness and densification correlation for direct metal laser sintering. The International Journal of Advanced Manufacturing Technology, 107(5), 2833-2842.

[28] : Nirish, M., & Rajendra, R. (2020). Suitability of metal additive manufacturing processes for part topology optimization–A comparative study. Materials Today: Proceedings, 27, 1601-1607.

[29] : Mahamood, R. M. (2018). Areas of application of laser metal deposition process–part repair and remanufacturing. In Laser Metal Deposition Process of Metals, Alloys, and Composite Materials (pp. 143-164). Springer, Cham.

[30] : Mehrpouya, M., Vosooghnia, A., Dehghanghadikolaei, A., & Fotovvati, B. (2021). The benefits of additive manufacturing for sustainable design and production. In Sustainable Manufacturing (pp. 29-59). Elsevier..

[31] : Zhang, L. C., Liu, Y., Li, S., & Hao, Y. (2018). Additive manufacturing of titanium alloys by electron beam melting: a review. Advanced Engineering Materials, 20(5), 1700842.

[32] : Kolamroudi, M. K., Asmael, M., Ilkan, M., & Kordani, N. (2021). Developments on Electron Beam Melting (EBM) of Ti –6Al –4V: A Review. Transactions of the Indian Institute of Metals, 1-8.

[33] : Akbari, M., & Kovacevic, R. (2019). Closed loop control of melt pool width in robotized laser powder–directed energy deposition process. The International Journal of Advanced Manufacturing Technology, 104(5), 2887-2898.

[34] : Prasad, H. S., Brueckner, F., & Kaplan, A. F. (2020). Powder incorporation and spatter formation in high deposition rate blown powder directed energy deposition. Additive Manufacturing, 35, 101413.

[35] : Herderick, E., 2011, "Additive Manufacturing of Metals: A Review," Materials Science and Technology Conference and Exhibition 2011, MS and T ' 11, Vol. 2, pp. 1413 – 1425.

[36] : Gokuldoss, P. K., Kolla, S., and Eckert, J., 2017, "Additive Manufacturing Processes: Selective Laser Melting, Electron Beam Melting and Binder Jetting-Selection Guidelines," Materials (Basel), 10(6), 672.

[37] : M anoharan V., C hou S.M., F orrester S., Chai et G.B.b, K ong P.W., "Application of additive manufacturing techniques in sports footwear", Virtual and Physical Prototyping, 8, 4, 2013, 249-252.

[38] : Durakovic, B. (2018). Design for additive manufacturing: Benefits, trends and challenges. Periodicals of Engineering and Natural Sciences (PEN), 6(2), 179-191.

[39] : Chen, J., Ghannam, R., Imran, M., & Heidari, H. (2018, October). Wireless power transfer for 3d printed unmanned aerial vehicle (uav) systems. In 2018 IEEE Asia Pacific Conference on Postgraduate Research in Microelectronics and Electronics (PrimeAsia) (pp. 72-76). IEEE.

[40] : Yin, Y., Stecke, K. E., & Li, D. (2018). The evolution of production systems from Industry 2.0 through Industry 4.0. International Journal of Production Research, 56(1-2), 848-861.

[41] : Zhu, Y., Zou, J., & Yang, H. Y. (2018). Wear performance of metal parts fabricated by selective laser melting: a literature review. Journal of Zhejiang University-Science A, 19(2), 95-110.

[42] : Ravichander, B. B., Amerinatanzi, A., & Shayesteh Moghaddam, N. (2020). Study on the Effect of Powder-Bed Fusion Process Parameters on the Quality of as-Built IN718 Parts Using Response Surface Methodology. Metals, 10(9), 1180.

[43] : Wang, Y., Chen, X., Jayalakshmi, S., Singh, R. A., Sergey, K., & Gupta, M. (2020). Process Parameters, Product Quality Monitoring, and Control of Powder Bed Fusion. Transactions on Intelligent Welding Manufacturing, 89-108.

[44] : Kuo, C. C., Nguyen, T. D., Zhu, Y. J., & Lin, S. X. (2021). Rapid Development of an Injection Mold with High Cooling Performance Using Molding Simulation and Rapid Tooling Technology. Micromachines, 12(3), 311.

[45] : Taufek, T., Manurung, Y. H., Lüder, S., Graf, M., & Salleh, F. M. (2020, April). Distortion analysis of SLM product of SS316L using inherent strain method. In IOP Conference Series: Materials Science and Engineering (Vol. 834, No. 1, p. 012011). IOP Publishing.

[46] : Ahmed, N. (2019). Direct metal fabrication in rapid prototyping: A review. Journal of Manufacturing Processes, 42, 167-191.

[47] : Lesyk, D. A., Martinez, S., Mordyuk, B. N., Dzhemelinskyi, V. V., Lamikiz, A., & Prokopenko, G. I. (2020). Post-processing of the Inconel 718 alloy parts fabricated by selective laser melting: Effects of mechanical surface treatments on surface topography, porosity, hardness and residual stress. Surface and Coatings Technology, 381, 125136.

[48] : de Souza, A. F., Al-Rubaie, K. S., Marques, S., Zluhan, B., & Santos, E. C. (2019). Effect of laser speed, layer thickness, and part position on the mechanical properties of maraging 300 parts manufactured by selective laser melting. Materials Science and Engineering: A, 767, 138425.

[49] : Carluccio, D., Demir, A. G., Bermingham, M. J., & Dargusch, M. S. (2020). Challenges and opportunities in the selective laser melting of biodegradable metals for load-bearing bone scaffold applications. Metallurgical and Materials Transactions A, 51(7), 3311-3334.

[50] : Mergulhão, M. V., & Neves, M. D. M. D. (2018). Characteristics of biometallic alloy to additive manufacturing using selective laser melting technology. Journal of Biomaterials and Nanobiotechnology, 9(01), 89.

[51] : Yi, J., Kang, J., Wang, T., Wang, X., Feng, T., Feng, Y., & Wu, P. (2021). Microstructure and mechanical behavior of bright crescent areas in Inconel 718 sample fabricated by selective laser melting. Materials & Design, 197, 109259.

[52] : Wang, H., Hu, Y., Ning, F., & Cong, W. (2020). Ultrasonic vibration-assisted laser engineered net shaping of Inconel 718 parts: Effects of ultrasonic frequency on microstructural and mechanical properties. Journal of Materials Processing Technology, 276, 116395.

[53] : Kaschel, F. R., Celikin, M., & Dowling, D. P. (2020). Effects of laser power on geometry, microstructure and mechanical properties of printed Ti-6Al-4V parts. Journal of Materials Processing Technology, 278, 116539.

[54] : Bambach, M., Sizova, I., Sydow, B., Hemes, S., & Meiners, F. (2020). Hybrid manufacturing of components from Ti-6Al-4V by metal forming and wire-arc additive manufacturing. Journal of Materials Processing Technology, 282, 116689.

[55] : Bambach, M., Sizova, I., Szyndler, J., Bennett, J., Hyatt, G., Cao, J., ... & Merklein, M. (2021). On the hot deformation behavior of Ti-6Al-4V made by additive manufacturing. Journal of Materials Processing Technology, 288, 116840.

[56] : Wei, K., Zeng, X., Li, F., Liu, M., & Deng, J. (2020). Microstructure and mechanical property of Ti-5Al-2.5 Sn/Ti-6Al-4V dissimilar titanium alloys integrally fabricated by selective laser melting. Jom, 72(3), 1031-1038.

[57] : Saboori, A., Aversa, A., Marchese, G., Biamino, S., Lombardi, M., & Fino, P. (2020). Microstructure and mechanical properties of AISI 316L produced by directed energy deposition-based additive manufacturing: A review. Applied Sciences, 10(9), 3310.

[58] : Yang, Y., Gong, Y., Li, C., Wen, X., & Sun, J. (2021). Mechanical performance of 316 L stainless steel by hybrid directed energy deposition and thermal milling process. Journal of Materials Processing Technology, 291, 117023.

[59] : Bai, Y., Zhao, C., Yang, J., Hong, R., Weng, C., & Wang, H. (2021). Microstructure and machinability of selective laser melted high-strength maraging steel with heat treatment. Journal of Materials Processing Technology, 288, 116906.

[60] : He, Y., Zhong, M., Beuth, J., & Webler, B. (2020). A study of microstructure and cracking behavior of H13 tool steel produced by laser powder bed fusion using single-tracks, multi-track pads, and 3D cubes. Journal of Materials Processing Technology, 286, 116802.

[61] : Zhang, B., Li, Y., & Bai, Q. (2017). Defect formation mechanisms in selective laser melting: a review. Chinese Journal of Mechanical Engineering, 30(3), 515-527.

[62] : Rehme O, Emmelmann C. Reproducibility for properties of selective laser melting products. In Lasers in Manufacturing 2005, LIM, International WLT-Conference on Lasers in Manufacturing, 3; 227-232.

[63] : Meier, C., Penny, R. W., Zou, Y., Gibbs, J. S., & Hart, A. J. (2017). Thermophysical phenomena in metal additive manufacturing by selective laser melting: fundamentals, modeling, simulation, and experimentation. Annual Review of Heat Transfer, 20.

[64] : Gibson, B. T., Bandari, Y. K., Richardson, B. S., Henry, W. C., Vetland, E. J., Sundermann, T. W., & Love, L. J. (2020). Melt pool size control through multiple closed-loop modalities in laser-wire directed energy deposition of Ti-6Al-4V. Additive Manufacturing, 32, 100993.

[65] : Xiong, Z. H., Liu, S. L., Li, S. F., Shi, Y., Yang, Y. F., & Misra, R. D. K. (2019). Role of melt pool boundary condition in determining the mechanical properties of selective laser melting AlSi10Mg alloy. Materials Science and Engineering: A, 740, 148-156.

[66] : Singla, A. K., Banerjee, M., Sharma, A., Singh, J., Bansal, A., Gupta, M. K., ... & Goyal, D. K. (2021). Selective laser melting of Ti6Al4V alloy: Process parameters, defects and post-treatments. Journal of Manufacturing Processes, 64, 161-187.

[67] : Fang, Z. C., Wu, Z. L., Huang, C. G., & Wu, C. W. (2020). Review on residual stress in selective laser melting additive manufacturing of alloy parts. Optics & Laser Technology, 129, 106283.

[68] : Yadroitsev, I., 2009, Selective Laser Melting : Direct Manufacturing of 3D-Objects by Selective Laser Melting of Metal Powders, LAP LAMBERT Academic Publishing, AG & Co KG: Saarbrücken, Germany.

[69] : Wang, X., Liu, Y., Li, L., Yenusah, C. O., Xiao, Y., & Chen, L. (2021). Multi-scale phase-field modeling of layer-by-layer powder compact densification during solid-state direct metal laser sintering. Materials & Design, 203, 109615.

[70] : Mutua, J., Nakata, S., Onda, T., & Chen, Z. C. (2018). Optimization of selective laser melting parameters and influence of post heat treatment on microstructure and mechanical properties of maraging steel. Materials & Design, 139, 486-497.

[71] : Yadroitsev I, Yadroitsava I, Bertrand P, Smurov I (2012) Factor analysis of selective laser melting process parameters and geometrical characteristics of synthesized single tracks. Rapid Prototyping Journal 18:201–208. doi:10.1108/13552541211218117.

[72] : Mugwagwa, L., Yadroitsev, I., & Matope, S. (2019). Effect of Process Parameters on Residual Stresses, Distortions, and Porosity in Selective Laser Melting of Maraging Steel 300. Metals, 9(10), 1042.

[73] : Qiu C, Adkins NJE, Attallah MM (2013) Microstructure and tensile properties of selectively laser-melted and of HIPed laser-melted Ti –6Al –4V. Materials Science and Engineering A578:230–239. doi:10.1016/j.msea.2013.04.099.

[74] : Gu H, Gong H, Pal D, Rafi K, Starr T, and Stucker B (2013) Influences of energy density on porosity and microstructure of selective laser melted 17-4PH stainless steel. Proceedings of Solid Freeform Fabrication Symposium, 474–489.

[75] : Bai, Y., Yang, Y., Wang, D., & Zhang, M. (2017). Influence mechanism of parameters process and mechanical properties evolution mechanism of maraging steel 300 by selective laser melting. Materials Science and Engineering: A, 703, 116-123.

[76] : Abele E, Stoffregen HA, Kniepkamp M, Lang S, and Hampe M (2015) Selective laser melting for manufacturing of thin-walled porous elements. Journal of Materials Processing Technology 215:114–22. doi:10.1016/j.jmatprotec.2014.07.017.

[77] : Yao, Y., Huang, Y., Chen, B., Tan, C., Su, Y., & Feng, J. (2018). Influence of processing parameters and heat treatment on the mechanical properties of 18Ni300 manufactured by laser based directed energy deposition. Optics & Laser Technology, 105, 171-179.

[78] : Kusuma, C., 2016, The Effect of Laser Power and Scan Speed on Melt Pool Characteristics of Pure Titanium and Ti-6Al-4V Alloy for Selective Lase Melting, Wright State University, Dayton, OH.

[79] : Criales, L. E., Arısoy, Y. M., and Özel, T., 2016, "Sensitivity Analysis of Material and Process Parameters in Finite Element Modeling of Selective Laser Melting of Inconel 625," Int. J. Adv. Manuf. Technol., 86(9 – 12), pp. 2653 – 2666.

[80] : Song B, Dong S, Coddet P, Liao H, Coddet C (2014) Fabrication of NiCr alloy parts by selective laser melting: columnar microstructure and anisotropic mechanical behavior. Materials & Design 53:1–7. doi:10.1016/j.matdes.2013.07.010.

[81] : Kempen K, Yasa E, Thijs L, Kruth JP, Humbeeck JV (2011) Microstructure and mechanical properties of selective laser melted 18Ni-300 steel. Physics Procedia, 12:255–263. doi:10.1016/j.phpro.2011.03.033.

[82] : de Souza, A. F., Al-Rubaie, K. S., Marques, S., Zluhan, B., & Santos, E. C. (2019). Effect of laser speed, layer thickness, and part position on the mechanical properties of maraging 300 parts manufactured by selective laser melting. Materials Science and Engineering: A, 767, 138425.

[83] : Sun J, Yang Y, and Wang D (2013) Parametric optimization of selective laser melting for forming Ti6Al4V samples by Taguchi method. Optics & Laser Technology 49:118–124. doi:10.1016/j.optlastec.2012.12.002.

[84] : Vandenbroucke B, Kruth JP (2007) Selective laser melting of biocompatible metals for rapid manufacturing of medical parts. Rapid Prototyping Journal 13:196–203. doi:10.1108/13552540710776142.

[85] : Delgado J, Ciurana J, and Rodríguez CA (2012) Influence of process parameters on part quality and mechanical properties for DMLS and SLM with iron-based materials. The International Journal of Advanced Manufacturing Technology 60:601–610. doi:10.1007/s00170-011-3643-5.

[86] : Liu B, Wildman R, Tuck C, Ashcroft I, Hague R, (2011) Investigation the effect of particle size distribution on processing parameters optimisation in selective laser melting process. Proceedings of Solid Freeform Fabrication Symposium, 227–238.

[87] : Mahesh, M., Lane, B., Donmez, A., Feng, S., Moylan, S., and Fesperman, R., 2015, "Measurement Science Needs for Real-Time Control of Additive Manufacturing Powder Bed Fusion Processes," Natl. Inst. Stand. Technol. pp. 1 – 50.

[88] : Ma, M., Wang, Z., Gao, M., and Zeng, X., 2015, "Layer Thickness Dependence of Performance in High-Power Selective Laser Melting of 1Cr18Ni9Ti Stainless Steel," J. Mater. Process. Technol., 215(1), pp. 142 – 150.

[89] : Zhang, B., Dembinski, L., and Coddet, C., 2013, "The Study of the Laser Parameters and Environment Variables Effect on Mechanical Properties of High Compact Parts Elaborated by Selective Laser Melting 316L Powder," Mater. Sci. Eng. A, 584, pp. 21 – 31.

[90] : Su fi iarov, V. S., Popovich, A. A., Borisov, E. V., Polozov, I. A., Masaylo, D. V., and Orlov, A. V., 2017, "The Effect of Layer Thickness at Selective Laser Melting," Procedia Eng., 174, pp. 126 – 134.

[91] : Savalani, M. M., and Pizarro, J. M., 2016, "Effect of Preheat and Layer Thickness on Selective Laser Melting (SLM) of Magnesium," Rapid Prototyp. J., 22(1), pp. 115 – 122.

[92] : Sheshadri, R., Nagaraj, M., Lakshmikanthan, A., Chandrashekarappa, M. P. G., Pimenov, D. Y., Giasin, K., ... & Wojciechowski, S. (2021). Experimental investigation of selective laser melting parameters for higher surface quality and microhardness properties: taguchi and super ranking concept approaches. journal of materials research and technology, 14, 2586-2600.

[93] : McGlau fl in, M., and Moylan, S., 2016, "Powder Bed Layer Geometry," ASPE/euspen Summer Topical Meeting. Advancing Precision in Additive Manufacturing, Raleigh, NC, June 27 – 30, pp. 108 – 113.

[94] : Singh, S. N., Chowdhury, S., Nirsanametla, Y., Deepati, A. K., Prakash, C., Singh, S., ... & Pruncu, C. (2021). A comparative analysis of laser additive manufacturing of high layer thickness pure Ti and Inconel 718 alloy materials using finite element method. Materials, 14(4), 876.

[95] : Zhao, X., Dong, S., Yan, S., Liu, X., Liu, Y., Xia, D., ... & Han, H. (2020). The effect of different scanning strategies on microstructural evolution to 24CrNiMo alloy steel during direct laser deposition. Materials Science and Engineering: A, 771, 138557.

[96] : Wang, D., Wu, S., Yang, Y., Dou, W., Deng, S., Wang, Z., & Li, S. (2018). The effect of a scanning strategy on the residual stress of 316L steel parts fabricated by selective laser melting (SLM). Materials, 11(10), 1821.

[97] : Jia, H., Sun, H., Wang, H., Wu, Y., & Wang, H. (2021). Scanning strategy in selective laser melting (SLM): a review. The International Journal of Advanced Manufacturing Technology, 1-23.

[98] : Wu, Z., Bao, H., Xing, Y., & Liu, L. (2021). Tribological characteristics and advanced processing methods of textured surfaces: a review. The International Journal of Advanced Manufacturing Technology, 1-37.

[99] : Calignano F, Manfredi D, Ambrosio E, Iuliano L, Fino P (2013) Influence of process parameters on surface roughness of aluminum parts produced by DMLS. Int J Adv Manuf Technol 67: 2743 – 2751

[100] : Huang, W. D. Y. Y. Q., & Wei-hui, Y. L. W. (2010). Density improvement of metal parts directly fabricated via selective laser melting. Journal of South China University of Technology (Natural Science Edition), 06.

[101] : YANG, Y., SONG, C., & WANG, D. (2014). Selective laser melting and its application on personalized medical parts. Journal of Mechanical Engineering, 21, 140-151.

[102] : D. Dai, D. Gu, H. Zhang, J. Xiong, C. Ma, C. Hong, and R. Poprawe, Influence of scan strategy and molten pool configuration on microstructures and tensile properties of selective laser melting additive manufactured aluminum based parts, Opt. Laser Technol., 99, 91-100 (2018).

[103] : Bhardwaj, T., & Shukla, M. (2019). Effect of Scan Direction on Tensile properties and Fractography of Laser Additive Manufactured Maraging Steel. Materials Today: Proceedings, 18, 3842-3848.

[104] : Meneghetti, G., Rigon, D., Cozzi, D., Waldhauser, W., & Dabalà, M. (2017). Influence of build orientation on static and axial fatigue properties of maraging steel specimens produced by additive manufacturing. Procedia Structural Integrity, 7, 149-157.

[105] : WANG D, YANG Y Q, SU X B, et al. Study on energy input and its influences on single-track, multi-track, and multi-layer in SLM. The International Journal of Advanced Manufacturing Technology, 2012, 58(9-12): 1189-1199.

[106] : KURZYNOWSKI T, CHLEBUS E, KUZNICKA B, et al. Parameters in selective laser melting for processing metallic powders. Society of Photo-Optical Instrumentation Engineers (SPIE) Conference Series, 2012:823914-823914-6.

[107] : KEMPEN K, THIJS L, YASA E, et al. Process optimization and microstructural analysis for selective laser melting of AlSi10 Mg.Proceedings Solid Freeform Fabrication Symposium, Texas, USA. 2011

[108] : Bourell, D., Stucker, B., Spierings, A. B., Herres, N., & Levy, G. (2011). Influence of the particle size distribution on surface quality and mechanical properties in AM steel parts. Rapid Prototyping Journal.

[109] : WANG L, WEI Q S, HE W T, et al. Influence of powder characteristic and process parameters on SLM formability. Journal of HuaZhong University of Science and Technology (Natural Science Edition), 2012, 40(6): 20-23.

[110] : Jankus, S. M., & Bendikiene, R. (2019). Effect of Powder Type and Particles Size on Microstructure of Selective Laser Sintered Parts. In Key Engineering Materials (Vol. 799, pp. 252-256). Trans Tech Publications Ltd.

[111] : Qiu C, Adkins N J E and Attallah M M 2013 Microstructure and tensile properties of selectively laser-melted and of HIPed laser-melted Ti-6Al-4V Mater. Sci. Eng. A 578 230–9

[112] : Waddell, M., Walker, K., Bandyopadhyay, R., Kapoor, K., Mallory, A., Xiao, X., ... & Sangid, M. D. (2020). Small fatigue crack growth behavior of Ti-6Al-4V produced via selective laser melting: In situ characterization of a 3D crack tip interactions with defects. International Journal of Fatigue, 137, 105638.

[113] : Li, H., Jia, D., Yang, Z., Liao, X., Jin, H., Cai, D., & Zhou, Y. (2021). Effect of heat treatment on microstructure evolution and mechanical properties of selective laser melted Ti –6Al –4V and TiB/Ti –6Al –4V composite: A comparative study. Materials Science and Engineering: A, 801, 140415.

[114] : Zhao X, Li S, Zhang M, Liu Y, Sercombe T B, Wang S, Hao Y, Yang R and Murr L E 2016 Comparison of the microstructures and mechanical properties of Ti –6Al–4V fabricated by selective laser melting and electron beam melting Jmade 95 21–31

[115] : Liverani, E., Lutey, A. H., Ascari, A., & Fortunato, A. (2020). The effects of hot isostatic pressing (HIP) and solubilization heat treatment on the density, mechanical properties, and microstructure of austenitic stainless steel parts produced by selective laser melting (SLM). The International Journal of Advanced Manufacturing Technology, 107(1), 109-122.

[116] : Krakhmalev, P., Fredriksson, G., Thuvander, M., Åsberg, M., Vilardell, A. M., Oikonomou, C., ... & Kazantseva, N. (2020). Influence of heat treatment under hot isostatic pressing (HIP) on microstructure of intermetallic-reinforced tool steel manufactured by laser powder bed fusion. Materials Science and Engineering: A, 772, 138699.

[117] : Guo, W. F., Guo, C., & Zhu, Q. (2018). Heat treatment behavior of the 18Ni300 maraging steel additively manufactured by selective laser melting. In Materials Science Forum (Vol. 941, pp. 2160-2166). Trans Tech Publications Ltd.

[118] : Conde, F. F., Escobar, J. D., Oliveira, J. P., Béreš, M., Jardini, A. L., Bose, W. W., & Avila, J. A. (2019). Effect of thermal cycling and aging stages on the microstructure and bending strength of a selective laser melted 300-grade maraging steel. Materials Science and Engineering: A, 758, 192-201.

[119] : Kempen, K., Vrancken, B., Buls, S., Thijs, L., Van Humbeeck, J., & Kruth, J. P. (2014). Selective laser melting of crack-free high density M2 high speed steel parts by baseplate preheating. Journal of Manufacturing Science and Engineering, 136(6).

[120] : Sander, J., Hufenbach, J., Giebeler, L., Wendrock, H., Kühn, U., & Eckert, J. (2016). Microstructure and properties of FeCrMoVC tool steel produced by selective laser melting. Materials & Design, 89, 335-341.

[121] : Krell, J., Röttger, A., Geenen, K., & Theisen, W. (2018). General investigations on processing tool steel X40CrMoV5-1 with selective laser melting. Journal of Materials Processing Technology, 255, 679-688.

[122] : Boes, J., Röttger, A., Mutke, C., Escher, C., & Theisen, W. (2018). Microstructure and mechanical properties of X65MoCrWV3-2 cold-work tool steel produced by selective laser melting. Additive Manufacturing, 23, 170-180.

[123] : Choo, H., Sham, K. L., Bohling, J., Ngo, A., Xiao, X., Ren, Y., ... & Garlea, E. (2019). Effect of laser power on defect, texture, and microstructure of a laser powder bed fusion processed 316L stainless steel. Materials & Design, 164, 107534.

[124] : Bartlett, J. L., & Li, X. (2019). An overview of residual stresses in metal powder bed fusion. Additive Manufacturing, 27, 131-149.

[125] : Masubuchi K. Analysis of welded structures: residual stresses, distortion, and their consequences. Elsevier; 2013.

[126] : Yuan, J., Chen, C., Yao, D., & Chen, G. (2020). 3D printing of oil paintings based on material jetting and its reduction of staircase effect. Polymers, 12(11), 2536.

[127] : Malekipour, E., & El-Mounayri, H. (2018). Common defects and contributing parameters in powder bed fusion AM process and their classification for online monitoring and control: a review. The International Journal of Advanced Manufacturing Technology, 95(1), 527-550.

[128] : Umaras, E., & Tsuzuki, M. S. (2017). Additive manufacturing-considerations on geometric accuracy and factors of influence. IFAC-PapersOnLine, 50(1), 14940-14945.

[129] : Rupal, B. S., Ahmad, R., & Qureshi, A. J. (2018). Feature-based methodology for design of geometric benchmark test artifacts for additive manufacturing processes. Procedia Cirp, 70, 84-89.

[130] : Maamoun, A. H., Xue, Y. F., Elbestawi, M. A., & Veldhuis, S. C. (2018). Effect of selective laser melting process parameters on the quality of al alloy parts: Powder characterization, density, surface roughness, and dimensional accuracy. Materials, 11(12), 2343.

[131] : Kozak, J., & Zakrzewski, T. (2018, October). Accuracy problems of additive manufacturing using SLS/SLM processes. In AIP Conference Proceedings (Vol. 2017, No. 1, p. 020010). AIP Publishing LLC.

[132] : Benedetti, L., Brulé, B., Decreamer, N., Evans, K. E., & Ghita, O. (2019). Shrinkage behaviour of semi-crystalline polymers in laser sintering: PEKK and PA12. Materials & Design, 181, 107906.

[133] : Calignano, F., Lorusso, M., Pakkanen, J., Trevisan, F., Ambrosio, E. P., Manfredi, D., & Fino, P. (2017). Investigation of accuracy and dimensional limits of part produced in aluminum alloy by selective laser melting. The International Journal of Advanced Manufacturing Technology, 88(1-4), 451-458.

[134] : Zhang, H., Wang, X., Xu, Y., Lu, Z., & Li, D. (2018). The thermal-mechanical behavior of WTaMoNb high-entropy alloy via selective laser melting (SLM): experiment and simulation. The International Journal of Advanced Manufacturing Technology, 96(1-4), 461-474.

[135] : Liu, W., Li, N., Zhou, B., Zhang, G., Liang, J., Zheng, T., & Xiong, H. (2019). Progress in additive manufacturing on complex structures and high-performance materials. Journal of Mechanical Engineering, 55(20), 128-151.

[136] : Manfredi D, Calignano F, Krishnan M, Canali R, Ambrosio EP, Atzeni E (2013) From powders to dense metal parts: characterization of a commercial AlSiMg alloy processed through direct metal laser sintering. Materials 6:856–869.

[137] : Calignano F (2014) Design optimization of supports for overhanging structures in aluminum and titanium alloys by selective laser melting. Mater Des 64:2013–2213.

[138] : Colegrove PA, Coules HE, Fairman J, Martina F, Kashoob T, Mamash H, et al. Microstructure and residual stress improvement in wire and arc additively manufactured parts through high-pressure rolling. J Mater Process Technol 2013; 213:1782–91.

[139] : Mukherjee T, Zhang W, DebRoy T. An improved prediction of residual stresses and distortion in additive manufacturing. Comput Mater Sci 2017; 126:360–72.

[140] : Vayssette, B., Saintier, N., Brugger, C., Elmay, M., & Pessard, E. (2018). Surface roughness of Ti-6Al-4V parts obtained by SLM and EBM: Effect on the High Cycle Fatigue life. Procedia engineering, 213, 89-97.

[141] : Sames WJ, List F, Pannala S, Dehoff RR, Babu SS. The metallurgy and processing science of metal additive manufacturing. Int Mater Rev 2016; 61:315–60.

[142] : ZHANG S, GUI R Z, WEI Q S, et al. Cracking behavior and formation mechanism of TC4 alloy formed by selective laser melting. Journal of Mechanical Engineering, 2013, 49(23): 21-27. (in Chinese)

[143] : Zhang, Y., Feng, E., Mo, W., Lv, Y., Ma, R., Ye, S., ... & Yu, P. (2018). On the microstructures and fatigue behaviors of 316L stainless steel metal injection molded with gas-and water-atomized powders. Metals, 8(11), 893.

[144] : Ogura, T., Ichikawa, S., & Saida, K. (2018). Theoretical approach to influence of nitrogen on solidification cracking susceptibility of austenitic stainless steels: computer simulation of hot cracking by solidification/segregation models. Welding International, 32(6), 436-444.

[145] : Fatoba, O. S., Adesina, O. S., & Popoola, A. P. (2018). Evaluation of microstructure, microhardness, and electrochemical properties of laser-deposited Ti-Co coatings on Ti-6Al-4V Alloy. The International Journal of Advanced Manufacturing Technology, 97(5-8), 2341-2350.

[146] : Taniguchi, N., Fujibayashi, S., Takemoto, M., Sasaki, K., Otsuki, B., Nakamura, T., ... & Matsuda, S. (2016). Effect of pore size on bone ingrowth into porous titanium implants fabricated by additive manufacturing: an in vivo experiment. Materials Science and Engineering: C, 59, 690-701.

[147] : Slotwinski, J. A., Garboczi, E. J., & Hebenstreit, K. M. (2014). Porosity measurements and analysis for metal additive manufacturing process control. Journal of research of the National Institute of Standards and Technology, 119, 494.

[148] : Slotwinski, J. A., & Garboczi, E. J. (2014, February). Porosity of additive manufacturing parts for process monitoring. In AIP conference proceedings (Vol. 1581, No. 1, pp. 1197-1204). American Institute of Physics.

[149] : Choren, J. A., Heinrich, S. M., & Silver-Thorn, M. B. (2013). Young's modulus and volume porosity relationships for additive manufacturing applications. Journal of materials science, 48(15), 5103-5112.

[150] : Yuan, L., Ding, S., & Wen, C. (2019). Additive manufacturing technology for porous metal implant applications and triple minimal surface structures: A review. Bioactive Materials, 4, 56-70.

[151] : Mugwagwa, L., Yadroitsev, I., & Matope, S. (2019). Effect of Process Parameters on Residual Stresses, Distortions, and Porosity in Selective Laser Melting of Maraging Steel 300. Metals, 9(10), 1042.

CHAPITRE 2

UNE REVUE DE LA FUSION LASER SÉLECTIVE DE L'ACIER MARAGING : MICROSTRUCTURE, COMPORTEMENTS MÉCANIQUES, ÉTAT DE L'ART ET PERSPECTIVES

(Article à soumettre)

Faical. HABASSI[1, *], Noureddine. BARKA[1], Mohammed. JAHAZI[2],

[1] Mathematics, Computer Science and Engineering Department, Université du Québec à Rimouski (UQAR), 300 Allée des Ursulines, Rimouski, QC G5L 3A1, Québec, Canada

[2] Mechanical Engineering Department, École de Technologie supérieure (ÉTS), 1100 Rue Notre-Dame Ouest, Montréal, QC H3C 1K3, Québec, Canada

∗Corresponding author. E-mail : Faical.Habassi@uqar.ca

2.1 RESUME EN FRANÇAIS DU DEUXIEME ARTICLE

Ces dernières années, la fusion laser sélective (SLM) est probablement devenue l'une des techniques à la croissance la plus rapide dans le processus de fabrication additive utilisé pour fabriquer des pièces métalliques par fusion laser. Comme d'autres procédés de fabrication additive métallique, le SLM peut être appliqué à une variété de matériaux, tels que l'acier maraging, afin de produire des géométries complexes qui ne se prêtent pas aux méthodes de fabrication conventionnelles, et le potentiel qu'il présente pour réduire le poids final sans compromettre les comportements des matériaux est particulièrement attrayant pour les applications aérospatiales et automobiles. Compte tenu de ses nombreuses applications et de ses performances élevées dans des situations où la sélection des matériaux est basée sur l'équilibre résistance-ténacité, le SLM de l'acier maraging est un domaine mûr pour la recherche. Il convient toutefois de noter que l'obtention des propriétés mécaniques souhaitées dans le produit final nécessite la maîtrise du post-processus grâce à l'introduction des

paramètres de fabrication appropriés. Pour atteindre cet objectif en termes de performances mécaniques et obtenir une microstructure à grains fins, il faut choisir un post-traitement adéquat. Cet article présente une revue détaillée des explorations académiques les plus récentes et des réalisations liées à l'acier maraging formé par SLM. Il présente les facteurs de post-traitement et de traitement thermique affectant les propriétés de l'acier maraging fabriqué à l'aide de la méthode. De plus, il met en lumière la façon dont la qualité, la taille et la morphologie des poudres, les paramètres de traitement et le traitement thermique peuvent influencer les propriétés métallographiques (microstructure, densité et porosité) et mécaniques (dureté ; traction, fatigue et contraintes résiduelles), ainsi que défauts associés aux aciers maraging, avec un focus sur le C300.

Ce deuxième article, intitulé « *A review of Selective laser melting of maraging steel : Microstructure, mechanical behaviors, state of art and perspectives* » fut essentiellement rédigé par son premier auteur Faical Habassi qui a également conduit une recherche bibliographique approfondie de la littérature des cinq dernières années afin d'explorer un rapport présent de l'état actuel et l'avancement de l'exploration de microstructure et des propriétés mécaniques de l'acier maraging fabriqué d'une manière additive. L'article donne un intérêt spécial à la technique de fusion sélective laser (SLM). Noureddine Barka est le second auteur de cet article. Il est à l'origine de ce projet de recherche en proposant l'approche et la méthodologie pour aborder la problématique. Il a également contribué à l'amélioration de la rédaction pour la version finale. Le troisième auteur de l'article est Mohammed Jahazi qui a apporté son expertise du domaine de matériaux et procédé de fabrication.

2.2 TITRE DU DEUXIEME ARTICLE

A review of Selective laser melting of maraging steel: Microstructure, mechanical behaviors, present statement and perspectives

74

2.3 ABSTRACT

In recent years, selective laser melting (SLM) has become probably one of the fastest growing techniques in the additive manufacturing process used to fabricate metal parts through laser melting. Like other additive metallic manufacturing processes, SLM can be applied to a variety of materials, such as maraging steel, in order to produce complex geometries not amenable to conventional manufacturing methods, and the potential it presents to reduce the final weight without compromising material behaviors is particularly attractive for aerospace and automotive applications. Given its numerous applications and its high performance in situations in which material selection is based on strength-toughness balance, SLM of maraging steel is an area ripe for research. Of note, however, achieving the desired mechanical properties in the final product requires mastery of the post-process through the introduction of the appropriate manufacturing parameters. To achieve this target in terms of mechanical performance and to obtain a fine-grained microstructure, an adequate post-treatment must be selected. This paper presents a detailed review of the most recent academic explorations and achievements related to maraging steel formed by SLM. It introduces the post-processing and heat treatment factors affecting the properties of maraging steel manufactured using the method. As well, it sheds light on how powder quality, size and morphology, processing parameters and heat treatment can influence the metallographic (microstructure, density, and porosity) and mechanical (hardness; tensile, fatigue, and residual stresses) properties, as well as defects associated with maraging steels, with a focus on C300.

2.4 INTRODUCTION

The additive manufacturing (AM) technology paves the way for creations that would be impossible with traditional production techniques. It can create high-quality metallic parts for use in numerous applications in the tool [1-3], automotive [4-6], aerospace [7-10] and medical industries [11-13]. AM technology can be applied via many techniques [14-15], such as Laminated Object Manufacturing (LOM) [16], Laser Engineered Net

75

Shaping (LENS) [17], Electron Beam Melting (EBM) [18], Selective Laser Sintering (SLS) [19] and Selective Laser Melting (SLM) [20-21]. AM technology consists of the following four basic steps [22]: (1) Develop a 3D solid model CAD file, (2) Convert CAD files into an AM file format using an adequate program, (3) Use an AM machine to manipulate the AM file and control the progress of the Layer-by-layer building process, and (4) Clean and finish the manufactured part.

Compared to conventional manufacturing techniques such as casting and forging, AM presents many advantages [23-24], including (1) rapid prototyping from CAD documents, which can allow geometric, dimensional and functional testing far before the design cycle, (2) the ability to produce complex geometries, such as the core and cavities, (3) a reduction of the need for a skilled workforce, (4) time savings and reduced raw material use, (5) the possibility of creating a metallic composite of dissimilar metals through metallurgical means, and (6) the possibility of reducing the assembly operations needed to create final parts. These advantages have led to AM becoming probably one of the fastest growing manufacturing techniques. It has been used for numerous practical industrial applications, including in the automotive and aerospace domains [4-10], thanks to a large number of accessible materials, such as stainless steel, nickel-based alloys, aluminum alloys, titanium alloys, and maraging steel alloys [20, 25].

As an AM technique, Selective Laser Melting (SLM) is now one of the most promising powder bed processes for metals [26-28]. It is an AM Powder Bed Fusion (PBF) technology that involves complicated physics, such as heating, melting and solidification of a metallic powder by a moving heat source, in the form of a laser, in a layer-by-layer fashion [29-30], and according to the desired geometry. As shown in Figure 2.1, once a layer is completed, the building platform is lowered by the pre-melted layer thickness value, and an additional powder layer is spread on the work platform. The process is repeated until the desired component construction is completed. This is then followed by an operation to remove powder from the building chamber before the final product is separated from the structure

plate [31-32]. When a powder bed is used in the SLM process, the process is known as a Laser Powder Bed Fusion process (L-PBF). For a successful SLM operation, certain factors must be mastered, including (1) the effects of process parameters, such as laser power, scanning speed, scanning strategy, (2) the effects of powder quality, as a function of elements such as the powder material, powder size, and morphology, and (3) the effects of post-treatment. Processing parameters significantly influence the quality of the final parts manufactured by SLM, and must therefore be selected with caution, in addition to being continuously monitored and adjusted as needed. Proper controlling these parameters can make it easier to achieve the required densification, microstructure, and mechanical properties [33-34]. The rapid temperature distribution changes during the heat source movement in the SLM process result in a short interaction time, which in turn leads to a high thermal gradient and residual stress in the molten pool [35-36]. The physical complexity of the AM process means several phenomena, such as heat, mass, and laser energy transfer [37], rapid material melting and solidification [38], instantaneous microstructure evolution [39-40], flow in a molten bath [41] material evaporation [42], must coexist. These factors affect the process, resulting in certain defects, such as incomplete powder melting, impurities, porosity, cracks, and distortions [43-44]. These defects are very critical for the physical, metallurgical, and mechanical quality of the final products manufactured by SLM. This significantly hampers the large industrialization of SLM processes [26-28].

As a nickel-based tool steel [45-50], Maraging steel owed owes its name from its typical structure, and the strengthening mechanism, which transforms the alloy to martensite with subsequent age hardening. These steels, which are characterized by a low carbon content, are widely known for their good mechanical properties such as their mechanical strength, wear resistance, toughness, machinability, weldability, etc. Thanks to these properties, it can be used in many fields, including in the tool manufacturing industry [45] and in automotive [46] and aerospace [47] applications. These high mechanical qualities are attributable to the main addition elements, including Ni, Co, Mo, Ti, Al, and largely account for the hardening of maraging steels by thermal aging. Some of them, such as Ti, Ni, Al, and Mo, are directly responsible for the formation of precipitates, while others, such as Co,

indirectly influence the precipitation process. These hardening precipitates, as their name indicates, increase the strength and mechanical characteristics of maraging steels. One of the most observed precipitates in maraging steels is Ni3Ti [48-49]. Many researchers have carried out in-depth work to explore and master the thermal, metallurgical, and mechanical behaviors of maraging steel during an SLM process. This complexity makes maraging steels important research topic [50-51]. Thanks to their excellent performance and low cost, maraging steels are generally mainly used in the presence of high working temperatures and in thermal fatigue injection molding operations [52]. Heat treatments and surface treatments are examples of interventions on the microstructure commonly used to strengthen, and therefore improve material characteristics [53-55]. The microstructure most often observed after quenching is a mostly lathed martensitic matrix structure, along with a small amount of austenite retained [56-57]. Some parts of the structure are lamellar in shape. Aging operations are always required after quenching to ensure better results.

The properties of maraging steel obtained by SLM are comparable, and in some cases, superior to those of conventionally manufactured steel. As mentioned earlier, complex printing parameters, powder quality, and heat treatments are among the most influential factors on the mechanical properties of printed metal parts, including those made of maraging steels [58-60], which is why a summary and the state of the art regarding parameters, micromorphology, properties, and defects of the SLM maraging steel (C300) process must be presented.

Accordingly, this review aims to identify the state of the art in SLM processing of maraging steel alloys and outline trends for future research allowing to further extend the application range of maraging steel-based materials. The review highlights the progress that has been made in the last five years in the field. The focus is on the microstructure, particularly the effect of rapid solidification versus what is seen in conventional manufacturing, as well as the evolution of mechanical behaviors as a function of SLM process parameters and post-processing conditions. Some sections are deliberately kept

78

shorter than others, for two main reasons. First, a detailed review has already been published covering additive manufactured maraging steels, and second, no clear conclusion could be drawn from the existing literature. The discussion is split into following sections, namely (i) Conventional Maraging Steel, (ii) SLM process, (iii) Microstructure of SLM maraging steel, (iv) typical defects, and (v) mechanical behaviors.
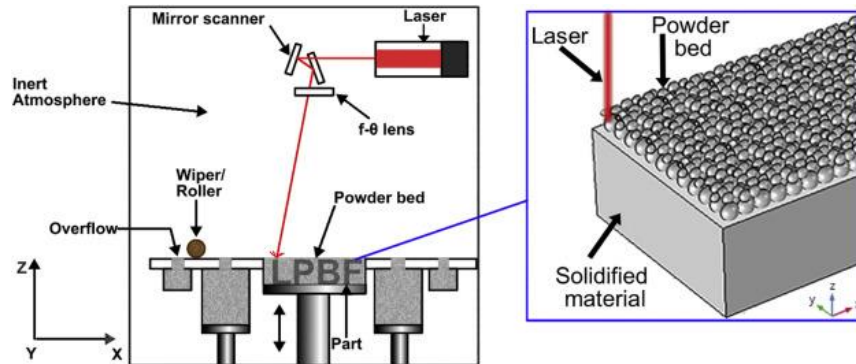
Figure 2. 1. A schematic diagram of the SLM process principal (adapted from [61]).

2.5 CONVENTIONAL MARAGING STEEL

2.5.1 Characteristics

Maraging steel is one of the tool steel categories. It is a solid martensitic alloy characterized by a relatively low carbon content and a high content of one of the other additive elements, such as Cobalt or Nickel, as shown in Table 2.1.

Maraging steel 18% Ni 300 (referred to for simplicity as maraging steel (C300) in this article) has already been recognized as a very important hardenable alloy in the mold and tooling industry. The combination of the advantages of the AM process with the good mechanical characteristics of maraging steel (C300) has made it very useful for the manufacture of high-quality mechanical components required in several fields, such as aerospace, parts, and tools [45-47].

Table 2. 1. Chemical composition (wt%) and strength of commercial grade maraging steels, Inco [62-63].

Alloy	Ni	Co	Mo	Ti	Al	Mn	Si
18NiCo (200)	18	8.5	3.3	0.2	0.10	≤ 0.10	≤ 0.10
18NiCo (250)	18	8	4.8	0.4	0.10	≤ 0.10	≤ 0.10
18NiCo (300)	18.5	9.0	4.8	0.7	0.10	≤ 0.10	≤ 0.10
18NiCo (350)	18	12	4.2	1.5	0.10	≤ 0.10	≤ 0.10
13NiCo (400)	13	15	10	0.2	–	≤ 0.10	≤ 0.10

The high levels of substitutional elements, such as Ni and Co, in maraging steel may be responsible for its malleable and robust microstructure. This is due to the ability of the substitutional elements (e.g., Ni, Co, Mo…) to provide reinforcement by precipitation after aging. Although cobalt is not part of the composition of reinforcing precipitates, its presence in maraging steel can increase the concentration instead of the rate of molybdenum (Mo) rich precipitates such as Ni3Mo by reducing its solubility limit. In their work, Conde et al. [64] found that the reinforcing precipitates most found in conventional maraging steels include Ni3Mo.

These reinforcement precipitates can block the propagation of defects and dislocations within the microstructural network and increase its mechanical performance. Table 2.2 represents some of the mechanical properties of conventional maraging steels [63].

Thanks to its solid and malleable character, maraging steel as an alloy presents many advantages in manufacturing processes. Its good characteristics, including high strength and toughness, allow it to be industrially recognized as a hardenable alloy that can be used in many sectors such as tooling, molding, aerospace, and defense. Maraging steel is composed mainly of a primary Fe-Ni phase system, containing substitutional elements such as nickel, cobalt, molybdenum, etc., which are finely dispersed, thus lending it its high strength and toughness.

Once a part is fabricated using a conventional manufacturing technique, and even if it was austenitized to reach the martensitic transformation, the resistances obtained always remain relatively low. High resistances can be obtained in these alloys because of the aging of the martensitic structure. Several processes and treatments, such as cold rolling, nitriding, carburizing, etc., can be applied to maraging steel, even before it is aged, without it cracking. Conventional techniques combine cold rolling with heat treatment, which can refine the grains, and subsequently, increase the hardness, uniformity, and durability of the treated part. The cyclic heating-cooling applied with the optional addition of aging or tempering operations during a conventional manufacturing process can make the steel stronger while maintaining sufficient flexibility during a remodeling or casting stage.

Currently, in addition to using conventional techniques, maraging steels can also be fabricated and handled by additive manufacturing. Since the appearance of this technology, maraging steels have rapidly been integrated into the range of metal powders suitable for AM processes [65]. The intersection of the good performance of maraging steels and the advantage of AM makes these alloys invaluable.

Table 2. 2. Properties of conventional Fe—Ni—Co maraging steels [62-63].

Alloy	Aging temperature (°C)	Yield strength (MPa)	Ultimate tensile strength (MPa)	Charpy (J)
18NiCo (200)	480	1316	1380	60
18NiCo (250)	480	1635	1690	35
18NiCo (300)	480	1835	1910	25
18NiCo (350)	480	2427	2468	16
13NiCo (400)	525	2530	2569	-

2.5.2 Heat Treatment

Using traditional manufacturing methods, maraging steel (C300) can only achieve high strength through a two-step heat treatment [66-67]. This combined heat treatment consists of an inherent solution homogenization [68] and isothermal aging [69]. With solution

homogenization treatment, the alloy is heated (usually at elevated temperatures, generally between 800-900 ℃ [68, 99-100,117, 147]) until it reaches its fully austenitic phase. The objective of this step is to disperse the distribution of hardening elements which have accumulated at the grain boundaries. Following the heating operation, a homogeneous solid solution is obtained [66-69]. Upon rapid cooling to room temperature, the austenitic structure transforms into an extremely ductile cubic-centered martensite (BCC) [70].

This homogenization route is only a preparation step that paves the way for the precipitation hardening response that follows. This thermal combination causes local precipitation of the second phase within the microstructure.

The maraging character is obtained at the end of the aging routes, which ensures the dispersion of the hardening particles. The precipitates generated following this dispersion can play the role of an obstacle that prevents the movement of dislocations. This in turn thus improves the strength and hardness of the alloy. Critical aging treatment parameters, such as temperature and aging time, have a decisive influence on the final metallurgical and mechanical quality [71-72].

2.6   SLM PROCESS

2.6.1   Powder sizes characteristics

The metal powder AM process core itself may be a primary area of research oriented towards the optimization of SLM system parameters. Good powder quality and morphology can eliminate or at least reduce microstructural defects including unmelted holes, porosity, and microcracks. The role played by the quality of the material powder (chemical composition, size, and morphology) in the quality and properties of the final manufactured part manufactured by SLM can be found in the literature [73-75].

The size and morphology of the powder are important contributing characteristics which are crucial for the consistency/evenness and fluidity of the powder bed [76-77], as well as for the quality and surface roughness of manufactured parts [78-79]. Additionally, powder specifications can affect other parts characteristics such as porosity. Irregular shapes and large particles can reduce the flowability of powders and affect the powder layer densities [76]. Using finer powder can reduce porosity. However, a powder that is too small and of regular morphology prevents the smooth deposition of layers. In addition, laser-powder interactions also have a significant influence on the SLM maraging steel process (C300). Large particles can weaken laser penetration, which tends to cause poor adhesion and low interlayer density [80].

The defined chemical composition of a given powder batch is critical for the workable properties of the finished part, and a high homogeneity is required. However, it is often difficult to achieve complete homogeneity in a batch of powder.

As with the chemistry of the powder, control of the morphology (size and shape) is essential. The latter can influence the final SLM part quality, the as-built surface roughness, and the relative density. Similarly, important properties of the final part, including porosity, can be affected by the shape and size distribution of the granules [77]. Currently, however, in-depth particle analysis has only very rarely been performed, especially with respect to the maraging steel (C300) manufactured by SLM [73-74, 76, 78]. In other related works [75, 83-84] using other types of steels, the results of virgin powder were compared to those of powder subjected to multiple AM manufacturing runs. Minor differences between virgin and recycled maraging steel powders were observed; the latter maintain the spherical morphology, but some reused particles show oxides on the surfaces [84]. A big difference was observed in the surface quality between parts with new and reused powder [84].

It should also be noted that there are several methods of producing metal powder that contribute to the formation of defects [85-88]; these include the rotating plasma electrode, the electrolytic method, gas atomization, and water atomization. The accumulation of these contributions will ultimately reduce the build quality of the AM part, mainly the surface

roughness and relative density [80, 85-86, 88]. Such powder packing defects can lead to irregularly shaped pores in the microstructure. This type of pore is differentiated from the spherical ones linked to the trapping of gases in the molten bath.

To date, few studies have been carried out examining the powder effect on maraging steel behaviors. Opatová et al. [87] reported that the recycling process may introduce a significant change in the chemical composition of virgin powder. A significant homogeneity particle distribution and generated defects were observed in their study. Because of the substantial differences in morphology observed between the virgin and recycled powders, some modifications of the SLM processing parameters were required in order to produce final parts with very similar relative densities. In a similar context, Salandre et al. [88] used several batches of powder with different particle size distributions of gas or water atomized powder. The water atomized powder was used in a bid to reduce both the environmental footprint and raw material costs. They found that both the gas and water atomization could produce outputs that were similar in terms of density (around 99%) and hardness (around 50 HRC). However, the gas atomized parts exhibited four times the ductility of that measured on heat-treated steel.

2.6.2   SLM Manufacturing processes

The complex physical phenomena that take place during the SLM process [29-30, 37, 39], such as heating, melting, and rapid solidification, lead to a specific morphology in terms of the microstructure, defects, and mechanical performance of manufactured parts [30, 36, 39, 42].

Several parameters used in SLM processes can affect the quality and performance of end products. The effect rate and significance vary from one parameter to another [37-38, 47]. Among the decisive factors in SLM are powder quality [80, 87-88], which is comprised of elements such as the type, morphology, and grain size; process parameters [34, 37], including, for example, laser power, laser speed, hatch space, layer thickness, spot

dimensions, and scanning strategy, and thermal post-processing characteristics [47], such as type, temperature, and processing time. The laser parameters (power, speed, hatch space, and layer thickness) can be adjusted and studied at the macro scale through the general parameters of energy density [89-91]. Some ranges of energy density have been evaluated in the literature [89-91]. As shown in Figure 2.2, a very low energy density (<20 j/mm 3) may be insufficient to achieve complete powder melting, which may result in final parts with major defects. On the other hand, a high enough energy density can cause strong agglomeration and a "pelletizing phenomenon" of powders, giving rise to trapped cavities, which can prevent the preparation of fully dense parts [89].
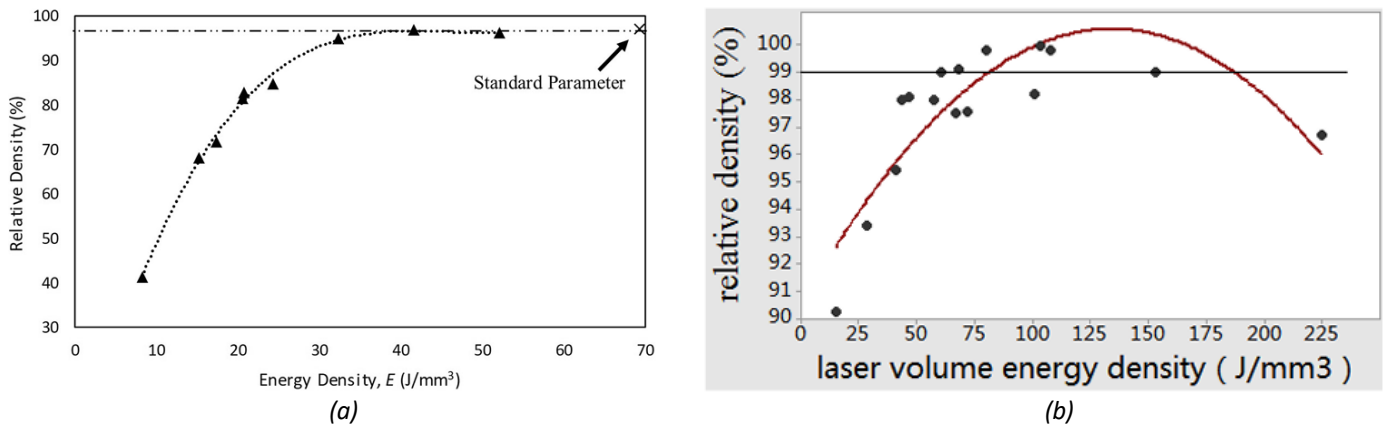
Figure 2. 2. Relationship between the laser volume energy density and relative density/porosity of formed parts [89-91].

Note that a part is classified as completely dense if it has a relative density of more than 99%. As reported in Table 2.3, Lee et al. [89] succeeded in manufacturing maraging steel alloys with an energy density of 8.3 j/mm 3 (laser power P = 150 W, scanning speed v = 1000 mm/s, hatching space h = 0.36 mm and layer thickness t = 0.05 mm), with a very low material density of 41%. The high rate of defects at this low energy density reduces the mechanical performance by up to 15% of those at the EOS standard state. Dhinakar et al. [90] also successfully manufactured full melting SLM maraging steel (C300) parts with different energy densities (ED = 8.6~21.7 j/mm 3). The produced parts have a high porosity (Po=49.5~21.5%). Huang et al. [91] investigated the density as well as other properties of SLM maraging steel under different energy densities. They produced high-density parts

between 75 J/mm3-185 J/mm 3 with no obvious macro defects. For the volume energy density of the laser outside the range [75 J/mm3 -185 J/mm 3], the relative density decreased significantly. This attests to the energy density being one of the critical process parameters needed to adjust the quality and performance of SLM maraging steels.

2.7 METALLURGICAL PROCESS AND MICROSTRUCTURE EVOLUTION OF SLM

2.7.1 Melting and solidification mode of powders

The SLM process consists primarily of 3 steps, namely, heating, melting, and solidification. During this very rapid process, a series of complex physical phenomena [29-30, 37, 39] such as heat transfer, mass transfer, absorption of energy, evaporation, phase change and melt flow take place inside the molten pool. The large temperature gradient in the molten pools is the major source of these phenomena [37]. As shown in Figure 2.3, the powder layers absorb the heat flux, produce a local molten pool, and the powder grain contributes to the solid and liquid phases [35, 39]. The entire region of powder treated by laser heat energy is melted to a greater depth than the layer thickness. Once a layer is completed, another powder layer is laid and melted until a complete part is built. The laser multi-pass causes a primary remelting, improving the quality of the part. The thermodynamic behaviour of the molten pool can be controlled by adjusting the processing parameters. This may allow the control of the form of the grains and the phase composition during the solidification step, allowing to achieve the desired microstructure and mechanical behaviour [29, 37]. This type of building process is very effective in creating well-bonded, high-density final parts [35, 37, 39].

The typical generated microstructure acquired at this very high-cooling rate is generally fine. The cooling rate and the solidification mode, so the microstructure, can be controlled by the process parameters especially the laser energy density, and the interaction time between the laser and the material [37]. The Gaussian distribution of the laser energy affects

the temperature gradient, the cooling, and the solidification mode, which vary at the different locations of the molten pool [29, 37]. That is why the morphological microstructure is not the same at different locations and varies from planar to cellular, dendritic, and equiaxed structure depending on the cooling and the solidification rate [29-30, 37, 39]. Inside the molten pool, the temperature gradients are very high, and the rate of solidification is very slow, which is why a planar grain substructure is most common. Far from the center of the molten pool, the temperature gradients decrease as the growth rate of the grains increase, which generates a progressive increase in the mass fraction of solute and of the constitutional supercooling zone. As a result, the substructures formed tend to be columnar grains (cellular and dendritic). Approaching to the center of the molten pool, equiaxial grains may possibly appear [29, 37, 93-94].

Luo et al. [93] reported that at a high cooling rate (usually up to 108 K/s), the microstructure of SLM maraging steel (C300) consists of four regions with different metallurgical characterizations. Typically, these four zones, namely, the inner fusion zone, the outer fusion zone, the heat-affected zone, and the base metal, differ significantly in terms of local substructure and grain morphology. The inner fusion zone is solidified with a column dendritic structure, whereas the outer fusion zone has a coarse equiaxial structure. Comparing the two fusion zones, grain refinement and the existence of texture would increase the hardness in the inner fusion zone than that of the outer fusion zone [93]. The outer fusion zone has a larger grain size and lack of texture, which can significantly affect the partial interfacial failure mode of spot welds because the crack initiates and propagates in the zone. As illustrated in Figure 2.3, the formation of the grains is propagated from the substrate to the center of the molten pool [29, 37]. This physical complexity, in which various phases take place, generates a large heterogeneity, especially in the solid-liquid interface, which may cause a growth of the columnar grain. In the same context, Yao et al. [94] illustrated that considering the heterogeneity of the temperature gradient, heat input distribution, and growth rate, the SLM maraging steel (C300) microstructure shows two different morphologies, namely, an equiaxed and a columnar substructure. They observed that as-built samples have

a random grain orientation with weak textures, which is attributable to the beam scanning patterns (67° rotation).

Not only the process parameters, such as energy density, construction orientation and angle rotation can largely affect the solidification behavior, thus the microstructure and the mechanical behavior, but also the different post-treatments have a great effect [89-94]. Yao et al. [94] reported that the build orientation can significantly change the configuration of the melt pool of the as-built maraging steel (C300) samples. They also observed that the build orientation has a noticeable effect on the microstructure.

Looking at the effects of the solidification mode and build direction on the mechanical behaviour of SLM maraging steel (C300), Yao et al. [94] observed that along the build height direction, the as-built sample has a higher hardness than that observed in the middle and top parts, possibly due to the finer cellular structure on the bottom, which is attributable to the high-cooling rate seen during the solidification process.
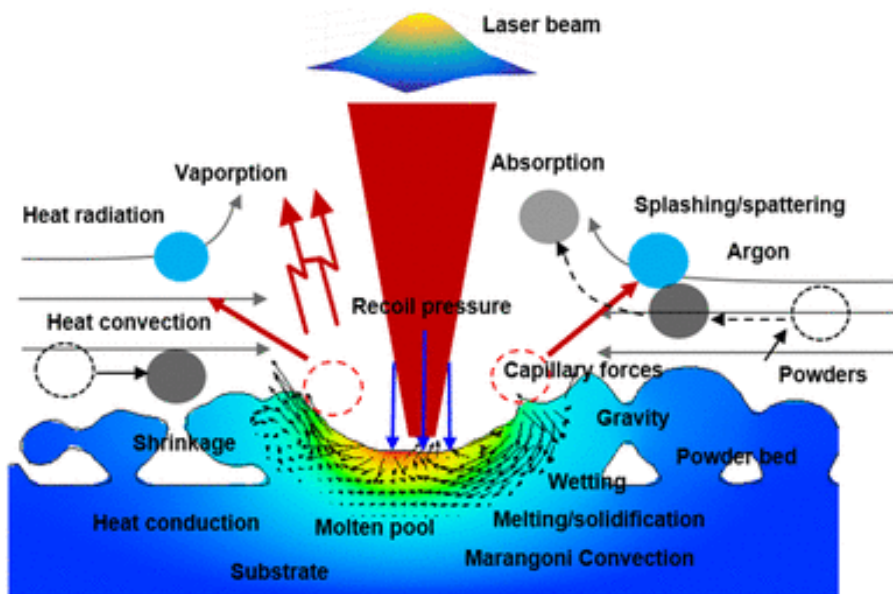
Figure 2. 3. Schematic diagram of the SLM molten pool - relationship between laser and powder bed [30].

2.7.2 Densification Behavior

Densification is one of the most decisive critical characteristics of SLM final products. It can greatly influence the material's microstructure, as well as its physical and mechanical properties. The typical definition of densification comprises melted and solidified powder, but avoids all defects, such as porosity, cracks, and balling effect [42-43]. A full melting process is necessary to avoid or limit incomplete fusion, gas impurities, and porosity defects. With various alloys, including maraging steel (C300), it is possible to generate completely melted and fully dense parts using SLM. The high densification produced by SLM may be attributed to two main reasons. On the one hand, the energy density is sufficient for the complete melting of the metal powder. On the other hand, a sufficient cooling and solidification time can limit the rate of pores and gaseous impurities, without using high energy densities, to avoid generating other types of defects such as oxidized and evaporated powders. Therefore, porosity is an inherent characteristic that can be minimized. Minimizing the porosity means higher density and higher material cohesion, which improve the mechanical properties of parts, such as hardness, and tensile strength. In this regard, each process parameter variation affects the densification, microstructure, and mechanical behaviour, which are examined in future works.

As shown in Table 2.3, which summarized the recent works covering the densification behaviour characterization of SLM maraging steel (C300), Huang et al. [91], Casalino et al. [95] and Kempen et al. [96] all observed excellent phase interactions at the solid-liquid interface, using a suitable laser power and hatching distance at low scanning speed. The gradient temperature and the manufacturing time, given the chance for the structural particles to fully diffuse and reorganized inside the molten pool. Their results showed that the density of the parts achieve a rate of 99.5%. In contrast, using a suitable laser power with a high-scanning speed, Lee et al. [89] reported a very low-density rate, which may be due to a large heterogeneity and anisotropy inside the molten pool. Their results showed a density rate of no more than 41%. In a similar condition, Dhinakara et al. [90] proved that the hatching space may greatly affect the densification behaviour of SLM maraging steel (C300). Increasing

only the hatch space from 300 to 750 μm, keep the other process parameters constant, may decrease the density of the parts by around 30%.

Table 2. 3. Effect of SLM process parameters on relative Density of Maraging steel (C300).

Author	Laser power (W)	Scan speed (mm/s)	Hatching space (μm)	Layer thickness (μm)	Energy density (J/mm 3)	(%)
Lee et al. [89] (2021)	150	1000	360	50	8.3	41
Dhinakara et al. [90] (2021)	285	960	750 300	40	8.6 21.7	50.5 78.5
Huang et al. [91] (2021)	180 260	1100 900	170 80	65 35	14.8 103.17	90.24 99.98
Casalino et al. [95] (2015)	100	180	140	30	132.3	99.9
Kempen et al. [96] (2011)	100	150	112	30	198.4	99.48

2.7.3 Microstructure

A. As-built state Microstructure

SLM maraging steel (C300) has a completely different microstructure from conventionally produced steels, which mostly consist of a fine cellular martensitic matrix [97]. The rapid cooling and solidification modes refine the microstructure of the as-built maraging steel (C300) [33-34, 93-94]. As shown in Figure 2.4, a columnar-cellular substructure is developed along the build direction [93-94, 102-103]. Three primary grain types may be developed in the maraging steel (C300) microstructure, for different temperature gradients and solidification rates, specifically columnar grain, fine cellular grain, and dendritic grain (Figure 2.4). In general, at the center of the molten pool, grains are relatively coarse (Figure 2.4) [93-94, 102-103] and take on the same orientation as the laser scanning direction [93-94].

Some previous works [93-94, 98-101] investigated the microstructure of as-built maraging steel (C300) and reported interesting results. Luo et al. [93] reported that the microstructure of SLM maraging steel (C300) consists of four regions with different metallurgical characterizations. The grain morphologies of the inner fusion zone and the outer fusion zone of the molten pool are solidified respectively with a column dendritic

structure and coarse equiaxial structure. In the same context, Yao et al. [94] illustrated that considering the heterogeneity of the temperature gradient, heat input distribution, and growth rate, the SLM maraging steel (C300) microstructure manifests two different morphologies, namely, an equiaxed and a columnar substructure. They observed that as-built samples have a random grain orientation with weak textures, which is attributed to the beam scanning patterns (67° rotation). Moreover, Casati et al. [98] carried out studies on as-built maraging steel parts fabricated by the L-PBF process. They found that these parts have a cellular solidification microstructure. The solidification cells are generally confined by residual austenite retained along the inter-boundaries [97]. Using a metal powder, Becker et al. [99] used a maraging C300 steel powder under a customized SLM process, and then performed an analysis of its mechanical performance and material microstructure. They found that the behaviour of the material is directly related to its microstructure. In the as-built condition, the material has an unfavorable fine microstructure characterized by high residual stresses. This microstructure can always be adapted by specific post-treatments. In the same context, Bai et al. [100] first investigated the influence of the parameters of the SLM process on the relative density of maraging steel. The investigation was then extended to the tensile strength, impact strength, microstructure, and microhardness. They found that the manufactured parts have a fine cell structure with coarse grains. Furthermore, Tan et al. [101] used a similar AM system to produce maraging C300 steel parts. In the as-fabricated state, they observed a fully dense dendritic cellular microstructure.
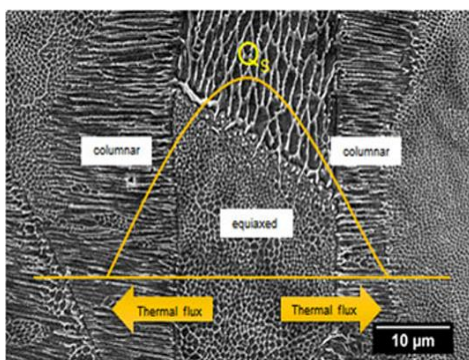
(a) P=380 W, V=960 mm/s, H=110 μm, t=40 μm [94]
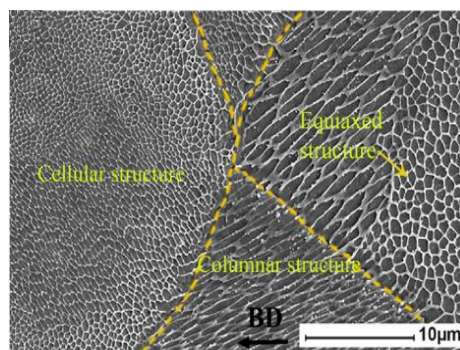
(b) P=285 W, V=960 mm/s, H=110 μm, t=40 μm [102]
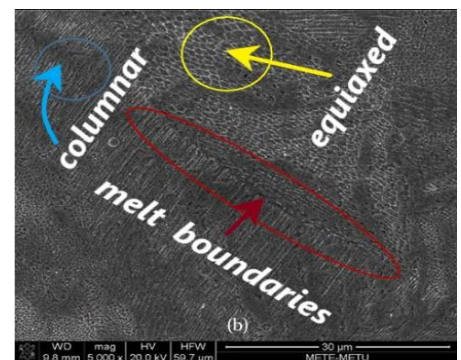
(c) [103]

Figure 2. 4. SEM images of the SLM-maraging steel (C300) samples. a P=380 W, V=960 mm/s, H=110 μm, t=40 μm [94]. b P=285 W, V=960 mm/s, H=110 μm, t=40 μm [102]. c [103].

As mentioned previously, the melting and solidification process involves a series of a few complex physical phenomena [29-30, 37, 39]. During the solidification process, a dendritic substructure formed around the center of the molten pool within a short time [94, 98-103]. Typically, with higher energy distribution, important temperature gradients, and rapid solidification mode, a cellular microstructure has been formed substitutional elements being concentrated in the grain boundary [104]. As the built height is increased, a somewhat automatic remelting process takes place (Figure 2.6 (a)), which leads to finer cell grains [37, 45, 46]. The process parameters, especially the built direction and the hatching strategy, are the key to controlling the cell (Figure 2.5) [104].

Columnar substructures begin to appear at low densities of volumetric laser energy [94, 98, 102-103]. At such densities, the hatch angle (rotation angle 67°) is the best tool to affect or limit the columnar structure (Figure 2.5) [105-107].
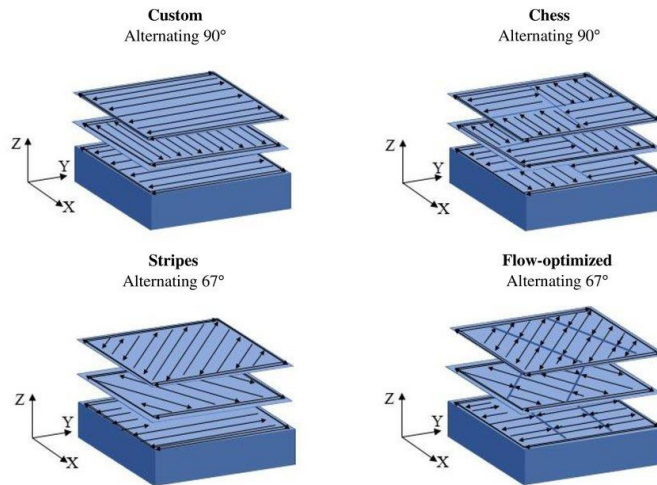
Figure 2. 5. Several scanning strategies. a "Cross-hatching" scanning strategy (the rotation of the scanning direction by 90°). b the rotation of the scanning direction by 67° [106].

An already solidified layer is reheated and re-solidified during the formation of the next layer. This reflows phenomenon generates coarser cellular particles from the first to the last

layer along the build direction (Figure 2.6 (a-b)). The growth rate of coarse grains is limited by controlling the density of laser energy (Equation 2.1).

$$E_D = \frac{P}{V*H*t} \qquad (2.1)$$

where E_D means the volumetric laser energy density (J/mm 3); P means the laser power (W); V means the scanning speed (mm/s); H means the hatching space (mm); and t means the layer thickness (mm).
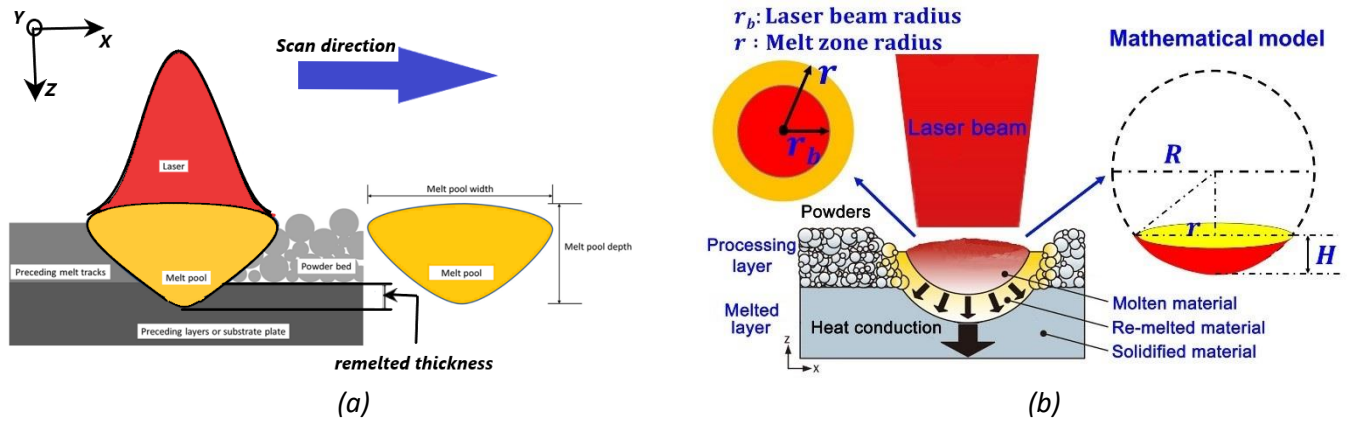
Figure 2. 6. Schematic diagram of remelted area [104].

B. Microstructure After Heat Treatment - Effect on Mechanical Behavior

Generally, a heat treatment consisting of 2 steps, namely, solution treatment (with a quenching step) and aging (Figure 2.7), is recommended for maraging steel (C300). Depending on the chemical composition of the steel, a temperature of around 800 °C may be sufficient to achieve a fully austenitic form before rapid cooling. Kim et al. [67] treated specimens that underwent solution treatment (ST) for 2 hours at two different temperatures (750 and 850 °C). In the literature, the most used temperature lies between 800 and 900 °C [108-110]. Simm et al. [108] explored 3 quenching treatments, respectively at 825 °C for 2 hours, 870 °C for 1 hour, and 960 ∘C for 1 hour. Wang et al. [109] and Murthy et al. [110] quenched their parts at 850 °C and 820 °C for 1 hour, respectively. In the as-built state, a cellular microstructure completely disappears, and a fully coarser martensitic matrix takes

place [93-94, 98-101], which can lead to a significant decrease in the mechanical behaviour of the as-built part [98-101]. After quenching, the cellular-dendritic microstructure disappears and is homogenized, and various types of hardening precipitates appear among the grains (Figure 2.7) [108-110]. In general, no, or very little, retained austenite was observed [111-112].

Aging heat treatment is essential to improving the mechanical resistance of a maraging steel part. The treatment also has a varying influence, depending on the aging temperature and the internal microstructure of such a part. The literature [49, 113] indicates that at low aging temperatures (<530 °C), the aged sample retains its cellular microstructure, while at higher temperatures (840 °C and above) [114-116], the quenching step leads to a total disappearance of the cellular microstructure and the appearance of a coarse martensitic microstructure. As a result, a reduction in some mechanical performances may be observed as compared to the as-built state [100].

Aging treatments give rise to strengthening precipitates, which lead to a hardening of the martensitic microstructure. This hardening can explain the tough character of maraging steels. The appearance of these precipitates is regularly accompanied by a reversion of the austenite retained between the cell boundaries. Campanelli et al. [117] analyzed maraging 300 steel powders treated by an SLM process. An age hardening treatment at 490 °C for 6 hours was applied. Following this treatment, an improvement in properties was noted, including a maximum hardness of 50 HRC and an ultimate tensile strength of 2097 MPa. In their investigation, Bai et al. [100] performed a hardening treatment, followed by an aging treatment. The solution treatment removed the cellular microstructure because of the reverse martensite-austenite transformation that took place. In parts that underwent the two successive treatments, the martensitic grain joints/boundaries became very blurred, and the appearance of a few precipitates was noted. A solution treatment was performed at 840 °C for 1 hour and an aging hardening treatment at 480 °C for 6 hours was applied as well. Following this treatment, an improvement in properties was observed, such as a maximum

hardness of 645 HV and ultimate tensile strength of 2164 MPa. Tan et al. [118] also used a similar AM system to produce maraging steel (C300) parts. They conducted an aging treatment at 490 ℃ for 6 hours. The precipitated phase generated by the heat treatment achieved a hardness of 55 HRC and an ultimate tensile strength of 2010 MPa.

(a)   *(b)*   *(c)*
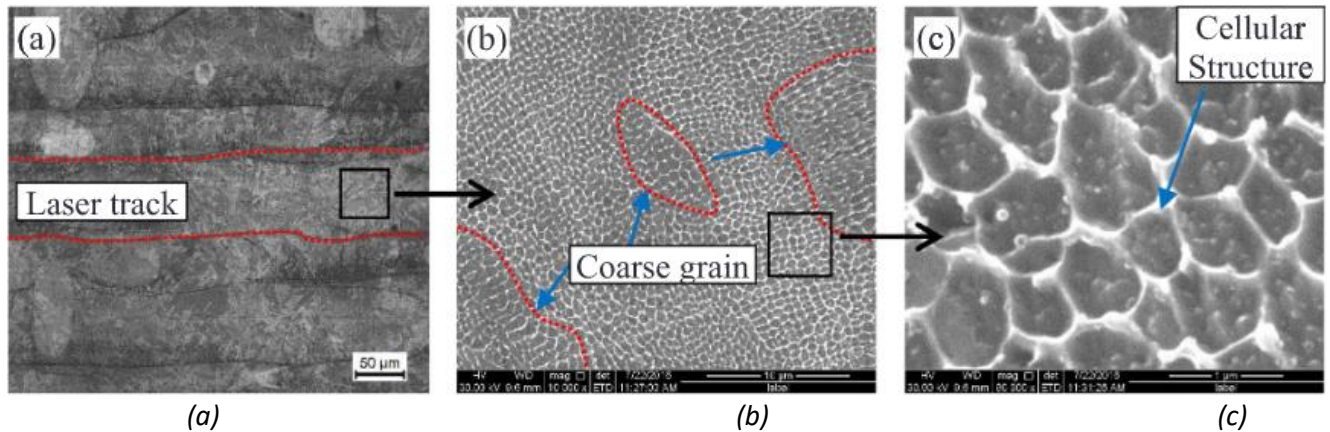
Figure 2. 7. SEM images showing the microstructure of SLM-formed maraging steel under different heat treatment: (a) as built; (b) ST (840℃, 1h); (c) ST (840℃, 1 hour) +AT (490℃, 6 hours). P=160 W, V=400 mm/s, H=70 µm, t=40 µm [100].

2.8   TYPICAL DEFECTS

2.8.1   Inhomogeneous grain size distribution

Looking at the thermal complexity, an inhomogeneous microstructure such as grain size differences is favored [57,71,80,81]. For example, from layer to layer along the build direction, cooling rates are lower, and reheating cycles are greater in the first layers compared to the upper layers. An already solidified layer is reheated and re-solidified during the formation of the next layer. This reflows phenomenon generates coarser cell particles from the first to the last layer along the build direction. This inhomogeneous microstructure affects the mechanical performance of protected parts [81–83].

2.8.2 Low Density / Porosity

In general, an SLM part is fully dense if its relative density is greater than 99% [89-91, 95-96]. In contrast, a low rate of porosity is required to achieve a high density, which can be controlled using adequate process parameters and a scanning strategy. The energy density is one of the most influential process parameters (combination of process parameters) which affect the densification behaviour. It is a global parameter which includes other principal laser parameters, such as laser power, scanning speed, hatching space, and layer thickness. The density of SLM maraging steel (C300) increases with increasing laser energy density until it reaches about 185 J/mm 3. The maximum density is around 99.8% at an energy density of about 105 J/mm 3 (P=260W, V=900mm/s, H=80 μm, t=35 μm), as reported by Huang et al. [91]. The experimental investigations reported by the authors showed that an increase in energy density from 14.8 J/mm 3 (P=180W, V=1100mm/s, H=170 μm, t=65) to 103 J/mm 3 (P=260W, V=900mm/s, H=80 μm, t=35 μm) can lead to an enhanced relative density ranging from 90.9% to 99.98%. Similar high-density results were reported by Casalino et al. [95] and Kempen et al. [96]. In a similar context, Lee et al. [89] reported that an increase in laser power from 8.3 J/mm 3 (P=150W, V=1000mm/s, H=360 μm, t=50 μm) to 69.4 J/mm 3 (P=200W, V=800mm/s, H=120 μm, t=30 μm) can lead to an enhanced relative density from ranging 41.3% to 97.2% and an improved mechanical behaviour (e.g., at the lowest relative density of 41%, the modulus and yield strength are only 15% and 13% of the value at the highest relative density of 97.2%, respectively) in as-built maraging 300 steel.

The parameters related to energy density, such as laser power, scanning speed, layer thickness, and hatch space, each has a significant effect on the porosity rate, which explains the densification behaviour. As shown in Figure 2.2, illustrated from previous works [89-91], there must be an optimal interval within which the appropriate energy density, laser power and scanning speed should be chosen to produce fully dense maraging steel (C300) parts. At low laser energy density, with a low laser power or high-scanning speed, an incomplete

melting and a balling defect was observed (Figure 2.8). Then, the porosity rate increased, and the product parts had a low density and a very low mechanical behaviour [89, 91]. At high density, with a high laser power or low scanning speed [95-96], Yao et al. [68] (Table 2.4)], a more spherical form of pores was observed, and their rate began to increase once the energy density was outside the optimal interval. The hatching space and the layer thickness also have a significant effect on the densification behaviour by affecting the overlapping amount. In fact, increasing the hatching space may not allow the laser to overlap enough and may result in insufficient melting of the powder. Dhinakara et al. [90] investigated the effect of the hatching space from 300 to 750 μm, with a constant process parameter, which may decrease the relative density of SLM maraging steel (C300) parts by around 30%. De Souza et al. [33] observed that the porosity of SLM maraging steel (C300) parts increased by ~0.23% as the manufacturing time was reduced by 30%, resulting in an increase of the layer thickness by a factor of up to ~1.6.

In addition, the porosity is typically affected by the scanning strategy and the powder morphology. On the one hand, there are different scanning strategies which can be used by the L-PBF process, such as the "unidirectional", "cross-hatching", "spiral" and "zigzag" strategies. On the edges of the tracks to be scanned, there is a greater accumulation of defects than at the center due to instability of the power level and a gradual reduction of the scanning speed, which causes a higher laser energy. This problem is much more pronounced for the "unidirectional" and "zigzag" scanning strategies [96-97]. To reduce the problem, a specific scanning strategy or SLM remelting process may improve the surface quality, densification, and mechanical behaviour by remelting the solidified layers [119-121]. Cheng et al. [119] compared two different scanning strategies, namely, Lateral Spatial (LS) and Spatial in Line (SiL), using SLM maraging steel. They reported no significant effect of scanning speed on the average surface roughness, Ra. For both scanning strategies, the resulted morphology of the molten pools was different. In the case of lateral spatial (LS) scanning strategy, obtained SLM maraging steel (C300) parts had higher density and hardness behaviour. Song et al. [120] investigated the effect of the remelting process on the surface quality and tensile behaviour of SLM maraging steel (C300) manufactured by Selective Laser Melting. They

observed that the remelting process contributed to a smoother top surface morphology. However, remelting had no obvious influence on the side surface morphology. The remelting process increased the side surface roughness by 49% and had no noticeable impact on the top surface roughness. It increased the Yield Strength (YS) by 5.5% and had no obvious impact on the Ultimate Tensile Strength (UTS). Similar results were reported by Demir et al. [121], who found that remelting strategies are effective in improving the part density and surface roughness, where the strategy based on a superficial melting, namely polishing, proved to be the best solution. The polishing strategy provided a smooth surface free of pits and protruded zones inherent to the initial volume melting pass.

However, a double scanning strategy can generate a very high level of the temperature gradient and thermal energy, which could introduce some additional pores. Therefore, a controlled process is required in this case. On the other hand, the powder size and morphology may significantly affect the porosity rate in SLM maraging steel (C300). Opatová et al. [87] reported that the recycling process may introduce a significant change in the chemical composition of the virgin powder. A large homogeneity particle distribution and generated defects were observed. Similar results were reported by Salandre et al. [88], who also observed that gas and water atomization can deliver final products that are similar in terms of density (around 99%) and hardness (around 50 HRC).

2.8.3   Cracks -Dislocations-Balling

One of the main defects that can be observed in SLM maraging steel (C300) consists of cracking and dislocations [122]. This type of defect results from a high-temperature gradient, a complex thermal history, and a rapid cooling and solidification mode [123]. A high rate of cracks and dislocations may have a dramatic effect on the surface quality, densification, and mechanical behaviour of as-built parts. The formation of cracks and dislocations may be controlled via process parameters [124-126] or corrected using post-processing [127]. Bai et al. [128] reported that inadequate process parameters will cause

discontinuities and distortion, resulting in poor surface quality and hole formation. They observed that a higher laser power has a positive effect on the surface quality; a low hatching space leads to material aggregation due to mass transfer between adjacent melt tracks, leading to a sharp reduction of surface quality; and a low scanning speed and layer thickness render the top surface much smoother.

The balling phenomenon, which is one of the most common defects during the SLM process [129-130], is an agglomeration of particles generally caused by insufficient melting and splashing during laser melting (Figure 2.8). This type of defect is very easily formed during the SLM process and is critical to the quality of the final SLM part, which may hinder further development of SLM technology [131-132]. The balling formation mode is typically affected by process parameters, as well as the laser energy density and material impurities and rather complicated characteristics [133–135]. The presence of balling phenomena, such as in the case of surface cracks, can significantly decrease the quality of SLM parts, including SLM managing steel (C300) parts, by affecting the thermodynamic and kinetic characteristics during SLM [135]. It can lead to various defects, which may reduce the surface roughness of the final parts and destroy the continuity of the forming process [132]. In some cases, a slower scanning speed is preferred to ensure adequate melting and obtain a stable molten pool, which limits overall efficiency somewhat [136].

As reported in previous works [137-139], the substrate preheating step can reduce the temperature gradient, which minimizes the cracks [140] caused by residual thermal stress [141-142]. Preheating at 200 ℃ usually helps to increase relative density and to eliminate crack formation [138-139, 142].
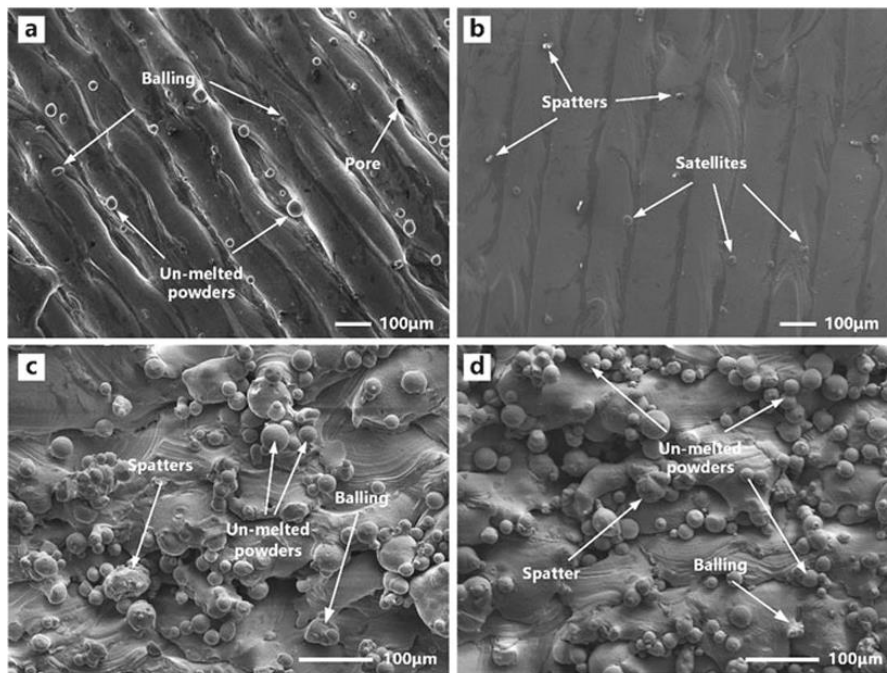
Figure 2. 8. SEM micrographs showing the surface morphology of the samples: a, b top surfaces for SLM and SLRM (remelted SLM), respectively; c, d side surfaces for SLM and SLRM, respectively (P=285W, V=900mm/s, H=110, t=40) [120].

2.9   MECHANICAL PROPERTIES OF SLM MARAGING STEELS

For specific industrial applications of SLM maraging steel (C300), the quality of the produced parts and their mechanical behaviors, such as hardness, tensile, compressive, and fatigue properties, are the major critical challenges [144-145]. Like the microstructure and the densification, the evolution of the mechanical behaviors of SLM maraging steel (C300) has been investigated by a few researchers [19, 33-34, 70-72, 96-101]. Furthermore, few SLM process parameters with some repetitive values, and the densification mechanisms have received the most attention (Table 2.4), which made the literature concerning the subject limited. Future works must explore new combinations of parameters, evaluate the sensitivity of mechanical performances on process parameters, modulate the sensitivity interrelation by statistical or FEM methods, optimize the module, and search for adequate post-processing than optimize it if possible.

100

This section presents a collection of the different types of investigations and significant results reported in the recent literature [33, 68, 71-72, 96, 98, 100-101, 147-149]. The main test parameters used, as well as the main results observed for the main mechanical behaviors (hardness, tensile, compression, fatigue, corrosion, and impact), in the as-built and heat-treated states, are presented in Tables 2.4-2.7. These tables were designed to correlate the material, the relative density of the samples and their observed mechanical performances, which can facilitate comparisons between the analyzed works. In addition, the tables summarize the main observations in the as-built state and follow the various treatments capable of directly influencing the mechanical performances. Finally, the most significant results are reported in the next sections, to show the main trends characterizing the behaviour of SLM maraging steel (C300) subjected to different mechanical tests. Therefore, the resulting mechanical behaviour reported in the literature is worth studying as it allows to present the state of the art on SLM maraging, identify existing gaps, and define future work avenues.

Table 2. 4. most used SLM process parameters and as-built maraging steel (C300) relative density and mechanical behavior.

Author	Particle size (μm)	Laser power (W)	Scan speed (mm/s)	Density (%)	Hardness	Tensile strength (MPa)	Ɛ-break (%)
Kempen et al. [96] (2011)	-	100	150	99.48	39.9 ± 0.1 HRC	1214 ± 99	13.3 ± 1.9
Casalino et al. [98] (2015)	~40	100	180	99.9	34 HRC	1170	8
Bai et al. [100] (2017)	15-40	160	400	99.19	381 HV	1177	7.9
Mutua et al. [147] (2017)	~20	300	700	99.8	330–403 HV	1125	10.38
Tan et al. [101] (2017)					35 HRC	1165	12.44
Yao et al. [68] (2018)	15-90	1600-2000	300-900	> 98.5	350.5 HV	959.21 ± 20.27	0.15
Guo et al. [148] (2018)	10-50	180	600	> 99	348.6 HV	1155	11.7
Yin et al. [71] (2018)	33-40	285	960	99.22 ± 0.32	350 HV	1180	12
De souza et al. [33] (2019)	5-35	400	600-1500	99.3 ± 0.6 %	380 ± 10 HV	1138 ± 10	16.5 ± 1.5
Wu et al. [142] (2020)	12-35	200	250	$98.2 \pm 0.52\%$	443.0 ± 66.2 HV	1173.1 ± 68	10.9 ± 0.45
Tascioglu et al. [149] (2021)	40	280	960	> 99	362 HV	-	-
Zhu et al. [72] (2021)	-	-	-	-	368 HV	1041.0 ± 1.4	14.0 ± 0.4

2.9.1 Microhardness

Generally, the hardness behaviour has a strong correlation with the densification rate, the process parameters, and the post-processing heat treatment [49, 72, 95-101, 112, 116, 122, 142-148]. Moreover, in the as-built state, they are positively related to the densification rate and to the tensile strength of SLM maraging steel (C300) [71-72, 96, 98, 100-101, 148]. Thus, a higher relative density means a higher hardness, and therefore, a higher strength of the material. The microhardness can provide a fast and critical means of evaluating the quality and mechanical performance of a part. This behaviour is directly related to the microstructure evolution and the phase formation inside the SLM maraging steel (C300) [96-101]. Tables 2.4 and 2.5 presents the most significant works that have examined these interrelations in recent years. They present the most used process parameters, the observed as-built mechanical behaviour (Table 2.4), and the effect of post-processing heat treatment on the mechanical behaviour (Table 2.5).

In the as-built state, Casalino et al. [98] investigated the effects of energy density on the microhardness behaviour of SLM maraging steel (C300) parts. They reported that the microhardness increased from 14 HRC to an average of 34 HRC as the energy density increased from 1.29 J/mm 2 (P=57 W, V=220 mm/s) to 2.78 J/mm 2 (P=100 W, V=180 mm/s), at a constant spot diameter of 200 µm. That result appears very normal, especially since the relative density (%) of as-built parts increases with an energy density of 2.78 J/mm 2 from 90.9 to 99.9%, obtaining nearly the full density. A similar hardness behaviour in the as-built state was reported by Mutua et al. [147] and Guo et al. [148]. Using a similar energy density, Casalino et al. [98], for 2.78 J/mm 2 (P=100 W, V=180 mm/s, d=200 μm), and Campanelli et al. [117] succeeded in producing samples capable of reaching a hardness of 37 HRC in the as-built state, which is in accordance with the EOS company data sheet.

The maximum average hardness (~440 HV and 40 HRC) of an SLM maraging steel (C300) as-built samples with the highest density (98.7% and 99%) were obtained

respectively by Wu et al. [142], at a laser power of 200 W, with a scanning speed of 250 mm/s, a layer thickness of 50 μm, and a spot diameter of 100 mm, and by Kempen et al. [96], at a laser power of 100 W, with a scanning speed of 150 mm/s and a hatching distance of 112 μm.

De Souza et al. [33] investigated the effects of laser speed and layer thickness on the mechanical behaviour of SLM maraging steel (C300), including the hardness. First, they reported that in general, the surface hardness was about 20% lower than that of the core. Also, at the same layer thickness, the hardness in the core tended to increase as the laser speed increased, which was attributable to the difference of remelting effect between layers. For example, at a layer thickness of 45, it was found that when the laser speed increases from 600 mm/s to 1500 mm/s, the hardness increased from 310 HV to 345 HV. In contrast, at the surface, which was the last deposited layer, the hardness tended to decrease by 20 HV, from 390 HV to 370 HV, as the laser speed increased from 600 mm/s to 1500 mm/s.

Becker et al. [99] investigated the effects of the scanning strategy on the hardness behaviour. They reported that the single exposure strategy results in a higher hardness (420 HV) in the as-built condition than does the double scanning strategy (340 HV). As shown in Table 2.5, the single exposure strategy used by Becker et al. [99] leads to a higher hardness in the as-annealed and in the as-aged states as well.

Mooney et al. [113] investigated the effect of build direction on the hardness behaviour of maraging steel (C300). They reported that a horizontal orientation (0°) leads to a higher hardness value than the vertical (90°) and inclined orientations (45°).

To improve the hardness behaviour many researchers have also studied the influence of heat treatment and second-phase particles on the hardness of SLM maraging steel (C300) parts. As reported above, the heat treatment generally consists of 2 main steps: annealing (also known as the quenching step) and aging. The quenching step leads to the total disappearance of the cellular microstructure and to the appearance of a coarse martensitic

microstructure. As a result, a reduction of some mechanical performances as compared to the as-built state may be observed [99-100, 116].

In the as-annealed (as-quenched) state, Becker et al. [99] analyzed the effects of the annealing temperature and hardness of SLM maraging 300 steel, using multi-process parameters. An annealing treatment at 830 °C was applied for 1 hour. They found that the annealed treatment could reduce the as-built hardness by an average of between 10 HV and 90 HV to a value of 330 HV. The same average reduction in hardness was reported by Casati et al. [116], from 371 HV in the as-built state to 279 HV after annealing treatment at 815 °C for 30 min. Bai et al. [100] also observed a lower hardness in the as-annealed state (840 °C, 1 hour) than in the as-built state. They found that the hardness is reduced from 381 HV to 341 HV, as shown in Table 2.5.

In the as-aged state (after the quenched step), Becker et al. [99] investigated the hardness behaviour of SLM maraging steel (C300) after aging at 490 °C for 6h. They reported that the hardness behaviour increases significantly to reach 600 HV. Similar results were reported by Casati et al. [116] (600 HV, 460 °C, 8h) and Guo et al. [148] (605 HV, 530 °C, 3h). Comparing the three works [99, 116, 148], it can clearly be seen that a certain hardness value can be achieved faster by increasing the aging temperature. For example, Guo et al. [148] observed similar hardness results as Becker et al. [99] twice as fast by increasing the aging temperature by ~8%. As shown in Table 2.5, after annealing and aging, the maximum average hardness (>700 HV~58 HRC) of the SLM maraging steel (C300) with the highest density (98.7%) was observed respectively by Zhao et al. [122] and Campanelli et al. [117].

A few researchers have preferred to ignore the quenching step and limited themselves to just an aging step (just-aged). Yin et al. [71] analyzed the relationship between the annealing temperature and hardness of SLM maraging 300 steel. An aging treatment for 3 hours at respectively 390 °C, 490 °C, and 590°C were applied. They found that the aging treatment could increase the as-built hardness until an aging temperature average, after which the hardness decreases again due to a high level of residual austenite. They also pointed out

that a high aging temperature (around or over 600°C) improves the hardness behaviour. In this work, the best hardness result was observed at 490 °C. A similar just-aged temperature was used by Tan et al. [101] (490 °C, 6 hours, 51~55 HRC), Mooney et al. [113] (490 °C, 6 hours, 608 HV), and Tascioglu et al. [149] (490 °C, 6 hours, 542 HV) leading to a high hardness behaviour, considering various process parameters. Using a just-aged treatment, the maximum average hardness (630 HV~55 HRC) of the SLM maraging steel (C300) sample with the highest density (>99%) was obtained respectively by Tan et al. [101], Casati et al. [98], Guo et al. [148], and Kempen et al. [96].

2.9.2   tensile properties

Besides compression, the tensile properties of SLM maraging steel (C300) parts are also an important mechanical behaviour. To date, one of the major challenging tasks in the SLM of maraging steel (C300) has been to produce final parts with a high tensile behaviour. Previous works proved that, in the optimal condition, SLM can produce final parts with mechanical performances comparable to those obtained using conventional manufacturing techniques [72, 96-100, 122, 147-148]. However, the large residual stress generated by SLM inside maraging steel (C300) parts can have significant effects on the mechanical behaviors, including the tensile properties. Due to cooling and solidification, as-built SLM maraging steel (C300) generally has a typical inhomogeneous microstructure and micro-texture, which improve the anisotropy of its mechanical behaviour. Its densification mechanisms and microstructure composition also have a significant effect on the mechanical behaviour. Therefore, the SLM process parameters may greatly influence the mechanical behaviour [72, 96-98, 100-101, 149]. Thermal post-processing is the simplest way to homogenize the microstructure of SLM maraging steel (C300) and significantly affect its mechanical behaviour. The main tensile properties of as-built and heat-treated SLM maraging steel (C300) reported in the literature are shown in Tables 2.4-2.5.

Many recent papers have investigated the performance of SLM maraging steel (C300) under tensile tests. Unlike compression, the tensile properties of SLM maraging steel (C300)

are more sensitive to different defects, such as porosity, microcracks, and residual stress, which can be attributed to low fracture strains and stresses under tension.

Recently, Zhu et al. [72] investigated the tensile behaviour of SLM maraging 300 steel parts. In the as-built state, they used a combination of parameters, which allowed them to generate an ultimate tensile strength of 1042 MPa, with an elongation of 14.5%. This was followed by an aging heat treatment at 500 °C for 3 hours. An improvement in properties was observed at a maximum ultimate tensile strength of 1686 MPa, with an elongation of 11.5%. Wu et al. [142] found that as-built SLM maraging steel (C300) shows an ultimate tensile strength of 1173 MPa with a tensile strain of 10.9%. They reported that the tensile behaviour may reach a very high level (2275 MPa, 4.5%) after a just-aging treatment at 550 °C for 50 hours. As illustrated in Table 2.5, similar results in both the as-built (1100-1300 MPa) and heat-treated (~>2000 MPa) states were reported by Casati et al. [98, 116], Bai et al. [100], Mutua et al. [147], Guo et al. [148], Zhao et al. [122], and Mooney et al. [113]. Kempen et al. [96] found a very good tensile behaviour in both the as-built (1290 MPa, 13%) and just-aged states at 480 °C for only 5 hours (2212 MPa, 2%). Campanelli et al. [117] used a combination of parameters which allowed generating a hardness of 34 HRC and an ultimate tensile strength of 1085 MPa. After heat treatment, an improvement in properties was noted and a maximum hardness of 50 HRC and ultimate tensile strength of 2097 MPa were obtained. In their investigation, Bai et al. [100] used as-manufactured parts with a hardness of 381 HV and ultimate tensile strength of 1177 MPa. This was followed by heat treatment, after which improved properties were observed at a maximum hardness of 645 HV and ultimate tensile strength of 2164 MPa. Additionally, Tan et al. [101] observed that as-fabricated parts have a hardness of 35 HRC and ultimate tensile strength of 1165 MPa. They applied a heat treatment which generated a hardness improvement to about 55 HRC and an ultimate tensile strength of 2014 MPa.

The maximum average tensile behaviour, in the as-built state (>1200 MPa, >13%), of the SLM maraging steel (C300) sample with the highest density (>99%) was obtained

respectively by Wu et al. [142], Becker et al. [99], and Kempen et al. [96]. In the heat-treated state, the maximum average tensile behaviour of the SLM maraging steel (C300) sample with the highest density (>99%) with an adequate strain rate (>2000 MPa, >5%) was obtained respectively by Mooney et al. [113] (2020 MPa, 8.3%), Guo et al. [148] (2090 MPa, 5.05%), and Mutua et al. [147] (2033 MPa, 5.27%).

Table 2. 5. Overview of published mechanical properties of maraging steel (C300). AB: as-built, SA: solution annealed, AH: aging heat treated.

Author	condition	E (GPa)	Sy (MPa)	Su (MPa)	E-break (%)	Hardness	Charpy impact (J)
[95], [99-101], [116]	Wrought AB Wrought AH	180 190	760-895 1865-2000	100-1170 1916-2050	6-15 6-8	30-37 HRC 530 HV/54HRC	
Kempen et al. [96] (2011)	SLM AB SLM AH (480°C,5h)	163 189	- 	1290 2212	13 2	40 HRC 58 HRC	42 5
Casalino et al. [95] (2015)	SLM AB	-	-	1085-1192	5-8	30-35 HRC	-
Becker et al. [99] (2016)	SLM AB SLM SA (830 °C, 1h) SLM SA+AH (490°C,6h)	181-194 158-164 217-220	900-1080 800-815 17201790	1010-1205 950-1000 1800-1850	8.3-12.1 11.8-13.5 4.4-5.1	340-420 HV 320-330 HV 590-600 HV	-
Casati et al. [116] (2016)	SLM AB SLM SA (815 °C, 0.5 h) SLM SA+AH (460 °C, 8h)	-	915 1957	1188 2017	6.1 1.5	371 HV 279 HV 600 HV	23 24 5
Bai et al. [100] (2017)	SLM AB SLM SA (840 °C, 1h) SLM SA+AH (480 °C, 6h)	-	-	1178 1080 2164	7.9 10.2 2.5	381 HV 341 HV 646 HV	24 26 5
Mutua et al. [147] (2017)	SLM AB SLM SA (820 °C, 1h) +AH (460 °C, 5h)	163 185		1125 2033	10.38 5.27	330–403 HV 618 HV	
Tan et al. [101] (2017)	SLM AB SLM AH (490°C,6h)			1165 2014	12.44 3.28	35~36 HRC 51~55 HRC	
Casati et al. [98] (2017)	SLM AB SLM AH	-	-	1200 2000	6 1.5	- 630 HV	
Yao et al. [68] (2018)	SLM AB SLM SA (830 °C, 1h) +AH (490 °C, 10h)			960 1562	0.15 0.12	350 HV 533 HV	
Guo et al. [148] (2018)	SLM AH (460°C,12h) SLM AH (530°C,3h)			2090 2032	5.05 5.12	629 HV 605 HV	
Yin et al. [71] (2018)	SLM AB SLM AH (390°C,3h) SLM AH (490°C,3h) SLM AH (590°C,3h)			1160 1680 1880 1390	12.5 6.8 4.7 6.8	360 HV 440 HV 560 HV 480 HV	
Mooney et al. [113] (2019)	SLM AB SLM AH (490°C,8h)	160 183		1100 2020	10 8.3	360 HV 608 HV	
Bodziak et al. [49] (2019)	SLM AB SLM AH (510,2h)	-	-	-	-	370 HV 573 HV	-
Campanelli et al. [117] (2019)	SLM AB SLM SA(900 °C, 1h)+AH(480 °C, 10h)	-	-	-	-	370 HV 700 HV	-

Author	Condition						
Wu et al. [142] (2020)	SLM AH (550°C,25h)			-	-	570 HV	
	SLM AH (550°C,50h)			2225 ± 51	4.2 ± 0.38	460 HV	
Tascioglu et al. [149] (2021)	SLM AH (490°C,6h)	-	-	-	-	542 HV	-
Zhu et al. [72] (2021)	SLM AH (500°C,3h)	-	-	1686	11.5	509 HV	-
Zhao et al. [122] (2021)	SLM AB	-	-	1159.7	14.8	428.3	-
	SLM SA (820°C,1H)			1028.1	16	366.5	
	SLM SA+AH(480°C,2h)			1943.3	8	683.2	
	SLM SA+AH (480 °C, 5h)			2009.5	7	711.5	

2.9.3   Compression properties

Only a few works [150, 152-154] have focused on compression properties to investigate the mechanical behaviour of SLM maraging steel (C300). The compression test is an important way to characterize the behaviors of parts. In this type of application, the dramatic effect of typical SLM defects, such as porosity, cracks, and residual strength, was limited or ignored. Table 2.6 studies and summarizes the primary explored compression behaviour reported by previous works [150, 152-154]. Table 2.6 shows the process design and the compression behaviors for maraging steel (C300). The main associated major works with different considerations and different results observed are reported in this section. The presented works compare the mechanical performance, including compression, to the densification mechanisms and the process parameters. The most recent significant works on SLM maraging steel (C300) are summarized in Table 2.6.

Cyr et al. [150] presented a preliminary study of experimental results of the tensile and compressive behaviour of maraging steel (C300) additively manufactured (P=285 W, V=960 mm/s, H=110μm, t=40μm). They reported that during the compression test with a compressive force of 200 Kip (kilo-pound), DMLS-maraging steel (C300) shows a moderately higher ultimate strength than in tension, where elongation increases dramatically. It was found that the compressive and ultimate strengths can reach 1450 MPa, with a very high elongation, which may exceed 40%. This strength differential had been reported earlier for conventionally manufactured maraging steel designed for marine industries [151]. Using the same process parameters (laser power P=285 W, scanning speed V=960 mm/s, hatching

108

space H=110μm, layer thickness t=40μm), with a rotation angle of 67° after each consecutive layer, Dehgahi et al. [152] reported that during the compression test, the compressive yield stress of as-built DMLS-maraging steel (C300) increased from 1232 MPa to 2004 MPa as the compression pressure increased from 100 Kpa (kilo-pascal) to 200 Kpa, and with strain rates of 13.76% and 33.46.

The SLM build direction may generate a non-isotropic geometry. The effect of build direction has been evaluated by a few works [153]. De Oliveira et al. [153] found that samples with a vertical direction at 90° offer a better compression behaviour and energy absorption capacity than horizontal parts at 0°. On the other hand, they reported that heat-treated samples can achieve higher ultimate compressive strengths than as-built parts, with a much lower total strain and energy absorption capacity. Similar compression peak stresses (~200 MPa) have been reported by Contuzzi et al. [154] in the as-built condition.

Table 2. 6. Overview of published Compression behaviors of maraging steel (C300).

Author	Process design	geometry	Test parameters	Output	Values (MPa?)
Cyr et al. [150] (2018)	-	Cubes of 25 × 25 × 25 mm	-	Yiled strength (MPa) An ultimate strength (MPa) Total Strain	1200 >1425 0.425
Dehgahi et al. [152] (2021)	As-built	Cylindric d=7mm L=8mm	Pressure 100 KPa, strain rate $1.5*10^3$ s^{-1}	Yiled strength (MPa) An ultimate strength (MPa) Total Strain (%) Toughness (MJ/m3)	1232 2005 13.76 245.3
			Pressure 200 KPa, strain rate $4*10^3$ s^{-1}	Yiled strength (MPa) An ultimate strength (MPa) Total Strain (%) Toughness (MJ/m3)	2004 2493 33.46 647.7
	Heat-treatment (490℃, 6 h)		Pressure 50 KPa, strain rate $1.5*10^2 s^{-1}$	Toughness (MJ/m3) Yiled strength (MPa) An ultimate strength (MPa) Total Strain (%)	3271 3397 0.09 24.0
			Pressure 90 KPa, strain rate $2*10^2$ s^{-1}	Toughness (MJ/m3) Yiled strength (MPa) An ultimate strength (MPa) Total Strain (%)	2864 3305 4.55 132.8

					Toughness (MJ/m3)
Contuzzi et al. [153] *(2013)*	*Cell sizes*	-	*250 KN load cell*	*Peak stress (MPa)*	*97-206*
De Oliveira et al. [154] *(2021)*	*As-built 0° (horizontal)*	-	*Maximum load of 250 kN*	*E (GPa)* *Yiled strength (MPa)* *An ultimate strength (MPa)* *Total Strain (%)* *Toughness (MJ/m3)*	*2.3* *114.3* *196* *21.9* *19.1*
	As-buit 90° (vertical)			 *E (GPa)* *Yiled strength (MPa)* *An ultimate strength (MPa)* *Total Strain (%)*	*2.1* *120.7* *212* *23.7* *20.6*
	Heat-treatment (480°C, 3 h) + 90° (vertical)			*Toughness (MJ/m3)* *E (GPa)* *Yiled strength (MPa)* *An ultimate strength (MPa)* *Total Strain (%)* *Toughness (MJ/m3)*	*2.2* *182.7* *246* *20.9* *17.3*

2.9.4   Fatigue properties

Fatigue failure is one of the most severe consequences of the propagation of dislocations and cracks. Of note, AM can produce maraging steel parts with fatigue rates comparable to those produced by conventional means. The most recent significant works on SLM maraging steel (C300) are summarized in Table 2.7.

Recently, Tyczyński et al. [155] investigated the fatigue behaviour of SLM maraging steel (C300) at a constant load pressure of 35 MPa. They found that at a low stress amplitude (<200 MPa), the tested part achieves several cycles to failure $Nf=3x10^5$ cycles. As the stress amplitude level goes up to 1200 MPa, the maximal number of cycles to failure decreases to $Nf=200$. In the as-built state, Bouzakis et al. [156] also observed that the fatigue behaviour of SLM maraging steel (C300) decreases as the load force and/or stress amplitude increases. They also reported that the presence of corrosion leads to a dramatic decrease in the maximum number of cycles to failure by up to 50%. For example, at a load force of 400 N and a stress amplitude of 500, Nf decreases from 12×10^5 to 6×10^5 cycles. It is important

to note that the wrought state (conventional maraging steel (C300)) always achieves a higher fatigue behaviour than SLM, even if there is corrosion.

Becker et al. [99] concluded that notwithstanding the influence of residual stresses and microstructure, the fatigue growth rates following specific heat treatments are practically similar to those of wrought material.

Antunes et al. [157] studied the growth of fatigue cracks in parts of powdered maraging C300 steel manufactured by an L-PBF process. They found that cyclic plastic deformation may be one of the best control mechanisms. They observed a low level of plastic deformation on the crack tip. This led to the conclusion that a reduced level of plasticity induces crack closure. Branco et al. [158] studied the low-cycle fatigue behaviour of AISI SLM maraging steel (C300). They reported that the cyclic stress response increased in a very short initial stage of about 2-3 cycles; it then decreased continuously at higher strain amplitudes and remained almost constant at lower strain amplitudes; in a third stage, for life ratios higher than 90%, there was a rapid drop in cycles.

Croccolo et al. [159] investigated the fatigue response of as-built DMLS maraging steel (C300) and the effects of aging, machining, and peening treatments. Comparing the fatigue S-N curves (Figure 2.9), they reported that the post-processing heat treatment without the micro-shot peening steps, can reduce the residual stress state induced by the DMLS process, which is not particularly high due to the properties of maraging steel (C300). The machining step can have a positive effect on the fatigue resistance, which can be useful for the removal of the surface layers treated by micro-shot peening before the heat treatment. They pointed out that the aging treatment makes DMLS maraging steel, which is the addition of a small outer surface machining steps, much more sensitive to nicks, which can make it very beneficial on refined surfaces. Otherwise, DMLS maraging steel without a machining step and with a moderately remarkable porosity, aging treatment can even be detrimental. They also found that a proper adjustment of post-treatment parameters can lead to a fatigue limit of the ultimate tensile strength of about 40%. In another investigation, Croccolo et al. [160] used a DMLS maraging steel (C300) to obtain information on the influence of the build

orientation on the fatigue resistance of the base material, in cases where all samples had undergone thermal and mechanical post-treatments. They reported that no significant difference in terms of fatigue properties was seen by changing the build orientation with respect to the built direction.
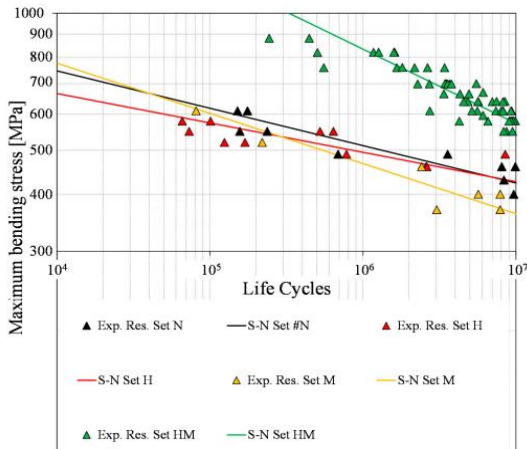
(a) Comparison between the S-N curves in the finite life domain for Sets N, M, and MP.
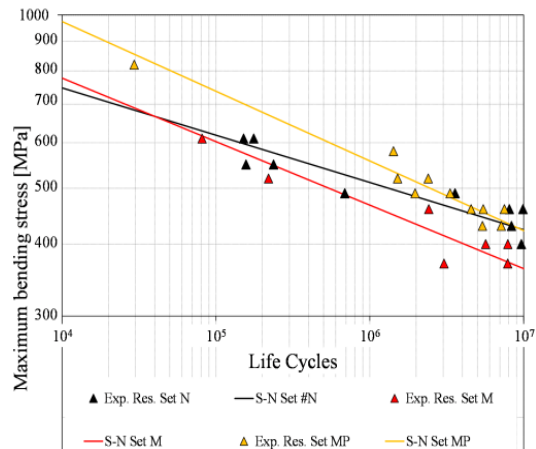
(b) Comparison between the S-N curves in the finite life domain for Sets N, M, H, and HM

	Machining		
Aging Heat Treatment	**No**	**Yes**	**Yes, with Subsequent Shot-Peening**
No	Set N	Set M	Set MP
Yes	Set H	Set HM	

(c) Design of the experimental campaign [160].

Figure 2. 9. The S-N curves in the finite life domain [160].

Furthermore, Santos et al [161] used a maraging 300 steel adapted to a DMLS process. They found that at a laser power of 100 W, the tensile and fatigue behaviors decreased as the scanning speed exceeded a certain value (especially at high levels of 400 or 600 mm/s). They found that at early cycles, the fatigue performance of parts fabricated by AM is similar to that of a conventionally sintered material. The fatigue strength became significantly lower as the lifetime at the point of comparison increased.

112

Table 2. 7. Overview of published Fatigue behaviors of maraging steel (C300).

Author	Test parameters					Fatigue behavior	
	Stress ratio	Frequency (Hz)	Subtract preheating temperature (°C)	Load Pressure (MPa)/ force (N)	Maximum stress σmax (MPa)	Process design	Nf (cycles)
Bouzakis et al. [156] (2021)	R=0	40	-	400N	500	wrought (SLM+GB: glass-blasting) (SLM as-built) SLM + Corrosion	1.05×10^6 $>2 \times 10^6$ 1.2×10^6 6×10^5
				700N	875	wrought (SLM+GB: glass-blasting) (SLM as-built) SLM + Corrosion	$>2 \times 10^6$ 20×10^3 55×10^3 20×10^3
Tyczyński et al. [155] (2021)		80		35 MPa	200 600 1200	SLM as-built	300 000 20 000 200
Uematsu et al. [162] (2021)	R=-1	2-10 Hz	-	100 kN (Max)	150 200 300 600	DMSL as-built	10^7 7×10^5 10^5 10^4-$2*10^4$
Branco et al. [158] (2021)	R=-1	-	-	-	512.9 602.7 990.8 1005.	A constant strain rate 8 $\times 10^{-3} s-1$, for all parts.	33 64 2399 5441

Finally, compared to conventional maraging steel parts, Uematsu et al. [162] reported that the specimens with a hybrid structure had lower fatigue strengths. They also pointed out that although post-aging treatments had an insignificant effect on residual stresses, the fatigue strengths of the as-built, aged, and semi-aged specimens were nearly the same. They found that post-aging could increase the fatigue strengths of conventional parts, while it had little effect on the fatigue lives of the DMLS-maraging steel (C300) in the finite life region. This can be attributed to the presence of the fatigue cracks and their propagation history.

2.9.5 Corrosion Properties

Corrosion is a natural phenomenon that happens after the repetitive exposure of metals to aggressive media, such as fluids in general and specifically acidic media - bases [163]. This can cause progressive damage to materials, which can degrade their properties, such as the appearance and strength. Tool steels, including maraging steels, are subject to stress

corrosion cracking like many steels [164-165]. It is thus essential to understand the behaviour of SLM maraging steel (C300) with respect to these corrosion properties. Very few studies have examined this phenomenon. The most significant recent such works are summarized in this section [122, 163].

Simson et al. [166] studied the corrosion resistance of SLM maraging steel (C300). They reported that the surface quality (as-built, turned, sandblasted, as milled, or ground) has no significant influence on the corrosion resistance, while the post-processing treatment may dramatically affect the corrosion behaviour of SLM maraging steel (C300). They found that the aging treatment reduces the corrosion resistance by around 50%, significantly more than solution-annealed treatments, which can lead to a lower corrosion resistance of age-hardened parts due to a galvanic effect. For solution-annealed parts, the range of current corrosion densities is icorr = 0.38 ~ 0.7 mA/cm², while for the aged-hardened parts, the current corrosion densities are approximately twice as high, located in the range of icorr = 1.2 ~ 1.55 mA/cm².

Zhao et al. [122] investigated the influence of the porosity rate on the mechanical property and corrosion behaviour of SLM maraging steel (C300). They found that internal grain distortion will take place because of aging treatment, which is able to force the pore voids to shrink or rupture, leading to a decrease in pore size. They also showed a negative relationship between the pore size and corrosion resistance of SLM (C300) maraging steel, making it a must to control the formation of macrospores, which are the main cause of local corrosion. On the other hand, solution treatment resulted in deeper corrosion pits compared to aging treatment. According to this study [122], after solution treatment, the depth of the pits increased by 45%, from 95,472 μm to 138,977 μm. After aging for 2 hours and 5 hours, the depth of the pits decreased by 10% and 15%, as compared to the samples treated in solution, respectively, at 124,756 μm and 117,945 μm. In their comparative work, Rajesh et al. [167] carried out a corrosion analysis on SLM maraging steel (C300) and SLM-316L. They reported that at 2% of NaCl solutions during corrosion testing, the SLM maraging steel

114

(C300) has a lower anodic coefficient and corrosion rate than stainless steel 316 L. Therefore, MS1 maraging steel is preferable to 316 L stainless steel in the automotive and aerospace industries due to its low wear rate, frictional force, and corrosion rate.

2.9.6 Charpy Impact Behavior

To assess the tensile strength and ductility of materials, a simple standard charpy impact test may represent the best and simplest solution. A high-temperature test medium can increase the capacity of materials [168], especially ductile materials [168-169], to absorb more energy than at lower test temperatures [169]. At low temperatures, steels, including maraging steel, lose their ductility, possibly due to low cleavage energy. Maraging steels are frequently subjected to such impact loads, especially for high-speed applications, such as defense and automotive. Therefore, it is essential to understand the impact behaviour of SLM maraging steel (C300). The most significant recent works [96, 100, 116, 16] are summarized in this section.

Masoumi et al. [170] studied the effect of microstructure and crystallographic texture on the charpy impact test for SLM maraging steel (C300). They reported that the energy of the charpy impact test increased with increasing {111}, {112} and {110}//ND texture fibers using a solution annealing at up to approximately 1000 ℃. They pointed out that the grain boundaries which are close to compact directions in the BCC lattice, such as {112}, {113} and {110}, showed more failure resistance than the boundaries related to the cleavage {001} planes. They also found that the charpy impact energy reached a maximum of 30.5 J using a solution annealing at 1000 ℃, without any significant loss in hardness. For high temperatures (>1000 ℃), rotated cubic components may be generated by the solution annealing, which can significantly decrease the impact toughness. At this solution annealing temperature (>1000 ℃), a higher rate of retained austenite may limit the negative effect of a high solution annealing temperature. As shown in Table 5, Bai et al. [100] investigated the charpy impact behaviour of SLM maraging steel (C300) for as-built, as-quenched (780-1020 ℃, 0.25-4 hours), as-aged (400-560 ℃, 1-12 hours) and just-aged (400-560 ℃, 1-12 hours) samples.

They observed that the charpy impact energy reached a value of 24 J in the as-built state. In the as-quenched state, the charpy impact energy increased as the temperature increased, until reaching 42 J, up to 960 ℃, and then it started to decrease. The charpy impact energy of the as-aged parts decreased dramatically, as the temperature increased, to reach the lowest level of 5 J at 480 ℃. At a high aging temperature (>480 ℃), a higher rate of retained austenite may limit the negative effect of aging, while the just-aged parts maintained a moderately high charpy impact energy as compared to the as-aged parts, whose charpy impact energy increased as the temperature increased. Very similar results have been reported by Casati et al. [116], in as-built, as-quenched (815 °C, 0.5 hours), and as-aged (460 ℃, 8 hours) samples. Also, Kempen et al. [96] found similar results in just-aged (480 ℃, 5 hours) parts (charpy impact energy of 5 J), but they successfully reached the maximum average of 40 J charpy impact energy in the as-built state.

2.10 SUMMARY AND OUTLOOK

The aim of this review was to present recent significant works on maraging steel manufactured by SLM. SLM has the capacity to produce complex geometries, with comparable or superior properties as conventional manufacturing methods, which will significantly promote the development of high-strength maraging steels. These advantages, coupled with a fast production time, the minimization of losses, design flexibility, and the possibility of controlling metallographic and mechanical behaviors through an oriented optimization of SLM process parameters, enable the development of a much more widespread SLM process applications in the future. The main conclusions from the state of the art of selective melting of maraging steels can be summarized as follows:

• The SLM process accommodates complex physical phenomena, such as heat transfer, mass transfer, phase change, and fluid mechanics in its molten pool. This gives rise to complex microstructural changes, including cellular refinement of grains, the development of local texture, the introduction of microstructural heterogeneity, variations in composition, the

116

formation of precipitates and dislocations, the introduction of residual stresses, and the formation of cracks. Despite, the current paper focusing on the microstructural aspect of SLM maraging steel, more in-depth work is needed to study the sensitivity of the microstructure, the formation of defects, and densification properties.

• Maraging steel is attractive to production by SLM, due to the different fields of application and its high printability.

• SLM maraging steels are known for their high strength and acceptable ductility, thanks to their ability to generate hardenable precipitates, in addition to their typical refined cellular microstructure. These microstructural characteristics also result in good mechanical behaviour, including hardness, tensile strength, and fatigue behaviour, comparable to conventional maraging steel.

• With high strengths, maraging steels, including maraging steels (C300), have moderately reduced ductility due to the presence of porosities generated by SLM.

• Defects, cracks, dislocations, residual stresses, and microstructural anisotropy are the current issues faced in the SLM of martensitic steels, such as maraging steel.

• The various defects (pores, cracks, dislocations, microstructural heterogeneity, and residual stress) generated by SLM can destroy not only the surface roughness and dimensional accuracy, but also the mechanical properties of final products. However, for current research, which shines the light on the mechanisms of defect formation and to methods of control by statistical models, analyses of variance, computer simulations, and experiments there is much more to be done.

• In general, the control of process parameters as well as the different heat treatment routes can reduce the formation of defects in the microstructure of maraging steel. However, finding ways to optimize these heat treatments is essential to achieve the required mechanical performance.

• In terms of process parameters, a lack of information about the sensitivity of the final mechanical behaviors of SLM maraging steel (C300) to various process parameters can be clearly observed. That is why more systematic works in terms of investigating the sensitivity relationship between the mechanical behaviors and the process parameters are required.

• In terms of post-processing heat treatment, it is recommended to investigate the effects of various treatments, including solution and aging treatment, to study the interrelation between each treatment temperature and time and related metallurgic and mechanical behaviors.

• The presence of austenite and the austenite-martensite transformation during SLM processes and after the various post-treatments are responsible for generating and controlling the resistance/ductility combinations acquired by SLM maraging steel parts.

• SLM can be considered as an intrinsic microthermal treatment thanks to the complex physical phenomena involved and the strong temperature gradients, which can generate stress concentrations, phase transformations, geometric occurrences, as well as nano-inclusions, which gives the option to ignore the thermal post-processing essential in the conventional case.

•In general, SLM maraging steel (C3000) exhibits a good tensile strength in the as-built state and a higher tensile strength in the heat-treated state. In contrast, the average total elongation always remains reduced, in general, 6% <<12% in the as-built state and dramatically smaller after the aging treatment (up to 1.5%). Future work is highly recommended in terms of investigating and clarifying the defect formation mechanisms and their influences on the mechanical performance of SLM maraging steel, under different SLM process conditions and different heat treatment routes.

• Compared to the conventional state, SLM maraging steel (C300) maintains comparable compressive strength. SLM maraging steels have greater compressive strengths than tensile strengths, with dramatically larger elongations.

• The fatigue and corrosion resistance of as-built SLM maraging steel (C300) remain low as compared to the conventional state, mainly due to the surface quality produced by SLM. In particular, the presence of macro-cracks negatively affects the fatigue and corrosion behaviors.

• Except for solution treatments (complete austenitization), high austenite content always leads to higher corrosion resistance.

Concentrated and in-depth systematic research can take both the SLM process and materials suitable for additive manufacturing, including maraging steel, to another level. It is even recommended to involve the SLM process in the manufacture and development of metal matrix composites.

2.11 REFERENCES

[1] : Strano, M., Rane, K., Farid, M. A., Mussi, V., Zaragoza, V., & Monno, M. (2021). Extrusion-based additive manufacturing of forming and molding tools. The International Journal of Advanced Manufacturing Technology, 1-13.

[2] : Masuo, C., Nycz, A., Noakes, M., Vaughan, D., & Niyanth, S. (2019). Feasibility Analysis of Utilizing Maraging Steel in a Wire Arc Additive Process for High-Strength Tooling Applications. Oak Ridge National Lab.(ORNL), Oak Ridge, TN (United States).

[3] : Law, W. K., Wong, K. C., Wang, H., Sun, Z., & Lim, C. S. (2021). Microstructure Evolution in Additively Manufactured Steel Molds: A Review. Journal of Materials Engineering and Performance, 1-17.

[4] : Zareanshahraki, F., Davenport, A., Cramer, N., Seubert, C., Lee, E., Cassoli, M., & Wang, X. (2021). Additive Manufacturing for Automotive Applications: Mechanical and Weathering Durability of Vat Photopolymerization Materials. 3D Printing and Additive Manufacturing.

[5] : Ding, H., Zhu, G., Xiang, C., Pei, F., Chen, J., Wang, Y., & Chen, Q. (2020). Excellent combination of plasticity and ultra-high strength in a low-alloy automotive steel treated by conventional continuous annealing. Materials Science and Engineering: A, 791, 139694.

[6] : Dhinakaran, V., & Ramgopal, R. (2021). Additive Manufacturing and Its Need, Role, Applications in the Automotive Industry. In Handbook of Research on Advancements in Manufacturing, Materials, and Mechanical Engineering (pp. 358-367). IGI Global.

[7] : Wuriti, G., Chattopadhyaya, S., & Thomas, T. (2021). Acoustic emission test method for investigation of M250 maraging steel pressure vessels for aerospace applications. Materials Today: Proceedings.

[8] : Tan, C., Weng, F., Sui, S., Chew, Y., & Bi, G. (2021). Progress and perspectives in laser additive manufacturing of key aeroengine materials. International Journal of Machine Tools and Manufacture, 103804.

[9] : Reddy, K. V. P., Mirzana, I. M., & Reddy, A. K. (2018). Application of Additive Manufacturing technology to an Aerospace component for better trade-off's. Materials Today: Proceedings, 5(2), 3895-3902.

[10] : Khorasani, M., Ghasemi, A., Rolfe, B., & Gibson, I. (2021). Additive manufacturing a powerful tool for the aerospace industry. Rapid Prototyping Journal.

[11] : Salmi, M. (2021). Additive manufacturing processes in medical applications. Materials, 14(1), 191.

[12] : Li, C., Pisignano, D., Zhao, Y., & Xue, J. (2020). Advances in medical applications of additive manufacturing. Engineering.

[13] : Kumar, R., Kumar, M., & Chohan, J. S. (2021). The role of additive manufacturing for biomedical applications: A critical review. Journal of Manufacturing Processes, 64, 828-850.

[14] : Gibson, I., Rosen, D., Stucker, B., & Khorasani, M. (2021). Development of additive manufacturing technology. In Additive manufacturing technologies (pp. 23-51). Springer, Cham.

[15] : Gibson, I., Rosen, D. W., Stucker, B., & Khorasani, M. (2021). Additive manufacturing technologies (Vol. 17). Cham, Switzerland: Springer.

[16] : Gupta, R., Dalakoti, M., & Narasimhulu, A. (2020). A Critical Review of Process Parameters in Laminated Object Manufacturing Process. Advances in Materials Engineering and Manufacturing Processes, 31-39.

[17] : Izadi, M., Farzaneh, A., Mohammed, M., Gibson, I., & Rolfe, B. (2020). A review of laser engineered net shaping (LENS) build and process parameters of metallic parts. Rapid Prototyping Journal.

[18] : Zhou, Q., Hayat, M. D., Chen, G., Cai, S., Qu, X., Tang, H., & Cao, P. (2019). Selective electron beam melting of NiTi: Microstructure, phase transformation and mechanical properties. Materials Science and Engineering: A, 744, 290-298.

[19] : Bhardwaj, T., Shukla, M., Rai, A. K., Biswal, R., Ranganathan, K., Ganesh, P., ... & Kaul, R. (2021). Experimental Investigation of Multiple Laser Shock Peening on Mechanical Properties of Laser Sintering Additively Manufactured Maraging Steel. Journal of Materials Engineering and Performance, 1-14.

[20] : Mooney, B., & Kourousis, K. I. (2020). A review of factors affecting the mechanical properties of maraging steel 300 fabricated via laser powder bed fusion. Metals, 10(9), 1273.

[21] : Zhang, X., Yocom, C. J., Mao, B., & Liao, Y. (2019). Microstructure evolution during selective laser melting of metallic materials: A review. Journal of Laser Applications, 31(3), 031201.

[22] : Yap, C. Y., Chua, C. K., Dong, Z. L., Liu, Z. H., Zhang, D. Q., Loh, L. E., & Sing, S. L. (2015). Review of selective laser melting: Materials and applications. Applied physics reviews, 2(4), 041101.

[23] : Horst, D. J., Duvoisin, C. A., & de Almeida Vieira, R. (2018). Additive manufacturing at Industry 4.0: a review. International journal of engineering and technical research, 8(8).

[24] : Pereira, T., Kennedy, J. V., & Potgieter, J. (2019). A comparison of traditional manufacturing vs additive manufacturing, the best method for the job. Procedia manufacturing, 30, 11-18.

[25] : LIU, Z., LIANG, J., SU, J., WANG, X., SUN, Y., WANG, C., & YANG, Z. (2020). Research and Application Progress in Ultra-HighStrength Stainless Steel. Acta Metall Sin, 56(4), 549-557.

[26] : Gunasekaran, J., Sevvel, P., & Solomon, I. J. (2021). Metallic materials fabrication by selective laser melting: a review. Materials Today: Proceedings, 37, 252-256.

[27] : Singla, A. K., Banerjee, M., Sharma, A., Singh, J., Bansal, A., Gupta, M. K., ... & Goyal, D. K. (2021). Selective laser melting of Ti6Al4V alloy: Process parameters, defects and post-treatments. Journal of Manufacturing Processes, 64, 161-187.

[28] : Carluccio, D., Demir, A. G., Bermingham, M. J., & Dargusch, M. S. (2020). Challenges and opportunities in the selective laser melting of biodegradable metals for load-bearing bone scaffold applications. Metallurgical and Materials Transactions A, 51(7), 3311-3334.

[29] : Gu, H., Wei, C., Li, L., Han, Q., Setchi, R., Ryan, M., & Li, Q. (2020). Multi-physics modelling of molten pool development and track formation in multi-track, multi-layer and multi-material selective laser melting. International Journal of Heat and Mass Transfer, 151, 119458.

[30] : Chen, Z., Xiang, Y., Wei, Z., Wei, P., Lu, B., Zhang, L., & Du, J. (2018). Thermal dynamic behavior during selective laser melting of K418 superalloy: numerical simulation and experimental verification. Applied Physics A, 124(4), 1-16.

[31] : Cao, Q., Zhang, J., Chang, S., Fuh, J. Y. H., & Wang, H. (2020). The effect of support structures on maraging steel MS1 parts fabricated by selective laser melting at different building angles. Rapid Prototyping Journal.

[32] : Cao, Q., Shi, Z., Bai, Y., Zhang, J., Zhao, C., Fuh, J. Y. H., & Wang, H. (2021). A novel method to improve the removability of cone support structures in selective laser melting of 316L stainless steel. Journal of Alloys and Compounds, 854, 157133.

[33] : de Souza, A. F., Al-Rubaie, K. S., Marques, S., Zluhan, B., & Santos, E. C. (2019). Effect of laser speed, layer thickness, and part position on the mechanical properties of maraging 300 parts manufactured by selective laser melting. Materials Science and Engineering: A, 767, 138425.

[34] : Wang, Y., Luo, L., Liu, T., Wang, B., Luo, L., Zhao, J., ... & Fu, H. (2021). Tuning process parameters to optimize microstructure and mechanical properties of novel maraging steel fabricated by selective laser melting. Materials Science and Engineering: A, 823, 141740.

[35] : He, Q., Xia, H., Liu, J., Ao, X., & Lin, S. (2020). Modeling and numerical studies of selective laser melting: Multiphase flow, solidification and heat transfer. Materials & Design, 196, 109115.

[36] : de Oliveira, A. R., & Del Conte, E. G. (2021). Concurrent improvement of surface roughness and residual stress of as-built and aged additively manufactured maraging steel post-processed by milling. The International Journal of Advanced Manufacturing Technology, 116(7), 2309-2323.

[37] : Siao, Y. H., & Wen, C. D. (2021). Influence of process parameters on heat transfer of molten pool for selective laser melting. Computational Materials Science, 193, 110388.

[38] : Pinomaa, T., Lindroos, M., Walbrühl, M., Provatas, N., & Laukkanen, A. (2020). The significance of spatial length scales and solute segregation in strengthening rapid solidification microstructures of 316L stainless steel. Acta Materialia, 184, 1-16.

[39] : Chae, H., Huang, E. W., Woo, W., Kang, S. H., Jain, J., An, K., & Lee, S. Y. (2021). Unravelling thermal history during additive manufacturing of martensitic stainless steel. Journal of Alloys and Compounds, 857, 157555.

[40] : Jarfors, A. E., Matsushita, T., Siafakas, D., & Stolt, R. (2021). On the nature of the anisotropy of Maraging steel (1.2709) in additive manufacturing through powder bed laser-based fusion processing. Materials & Design, 204, 109608.

[41] : Li, Y., Tian, S., Wu, C., & Tanaka, M. (2021). Experimental sensing of molten flow velocity, weld pool and keyhole geometries in ultrasonic-assisted plasma arc welding. Journal of Manufacturing Processes, 64, 1412-1419.

[42] : Platl, J., Leitner, H., Turk, C., Demir, A. G., Previtali, B., & Schnitzer, R. (2020). Defects in a laser powder bed fused tool steel. Advanced Engineering Materials, 2000833.

[43] : Bidare, P., Jiménez, A., Hassanin, H., & Essa, K. (2021). Porosity, cracks, and mechanical properties of additively manufactured tooling alloys: a review. Advances in Manufacturing, 1-30.

[44] : Bai, Y., Zhao, C., Wang, D., & Wang, H. (2022). Evolution mechanism of surface morphology and internal hole defect of 18Ni300 maraging steel fabricated by selective laser melting. Journal of Materials Processing Technology, 299, 117328.

[45] : Samei, J., Asgari, H., Pelligra, C., Sanjari, M., Salavati, S., Shahriari, A., ... & Mohammadi, M. (2021). A Hybrid Additively Manufactured Martensitic-Maraging Stainless Steel with Superior Strength and Corrosion Resistance for Plastic Injection Molding Dies. Additive Manufacturing, 102068.

[46] : Piekło, J., & Garbacz-Klempka, A. (2021). Use of Selective Laser Melting (SLM) as a Replacement for Pressure Die Casting Technology for the Production of Automotive Casting. Archives of Foundry Engineering, 21(2), 9.

[47] : Kasana, S. S., & Pandey, O. P. (2021). Effect of multipass cold plastic deformation and heat treatment on the mechanical properties of C250 marageing steel for aerospace applications. Proceedings of the Institution of Mechanical Engineers, Part L: Journal of Materials: Design and Applications, 1464420721989373.

[48] : Ren, K., Rong, Y., Wei, S., Xing, W., & Wang, G. (2020). Precipitation behaviour and its strengthening effect of maraging steel in laser cladding remanufacturing. In TMS 2020 149th Annual Meeting & Exhibition Supplemental Proceedings (pp. 457-468). Springer, Cham.

[49] : Bodziak, S., Al-Rubaie, K. S., Dalla Valentina, L., Lafratta, F. H., Santos, E. C., Zanatta, A. M., & Chen, Y. (2019). Precipitation in 300 grade maraging steel built by selective laser melting: Aging at 510 C for 2 h. Materials Characterization, 151, 73-83.

[50] : Branco, R., Berto, F., & Kotousov, A. (2021). Special Issue on Recent Trends in Advanced High-Strength Steels.

[51] : Gebisa, A. W., & Lemu, H. G. (2018, June). Additive manufacturing for the manufacture of gas turbine engine components: literature review and future perspectives. In Turbo Expo: Power for Land, Sea, and Air (Vol. 51128, p. V006T24A021). American Society of Mechanical Engineers.

[52] : Karr, U., Schuller, R., Fitzka, M., Schönbauer, B., Tran, D., Pennings, B., & Mayer, H. (2017). Influence of inclusion type on the very high cycle fatigue properties of 18Ni maraging steel. Journal of Materials Science, 52(10), 5954-5967.

[53] : Dehgahi, S., Alaghmandfard, R., Tallon, J., Odeshi, A., & Mohammadi, M. (2021). Microstructural evolution and high strain rate compressive behavior of as-built and heat-treated additively manufactured maraging steels. Materials Science and Engineering: A, 815, 141183.

[54] : Kim, D., Kim, T., Ha, K., Oak, J. J., Jeon, J. B., Park, Y., & Lee, W. (2020). Effect of heat treatment condition on microstructural and mechanical anisotropies of selective laser melted maraging 18Ni-300 steel. Metals, 10(3), 410.

[55] : Tezel, T., & Kovan, V. (2021). Heat treatment effect on fatigue behavior of 3D-printed maraging steels. Rapid Prototyping Journal.

[56] : Qian, F., & Rainforth, W. M. (2019). The formation mechanism of reverted austenite in Mn-based maraging steels. Journal of Materials Science, 54(8), 6624-6631.

[57] : Conde, F. F., Escobar, J. D., Oliveira, J. P., Jardini, A. L., Bose Filho, W. W., & Avila, J. A. (2019). Austenite reversion kinetics and stability during tempering of an additively manufactured maraging 300 steel. Additive Manufacturing, 29, 100804.

[58] : Sun, H., Chu, X., Liu, Z., Gisele, A., & Zou, Y. (2021). Selective laser melting of maraging steels using recycled powders: a comprehensive microstructural and mechanical investigation. Metallurgical and Materials Transactions A, 52(5), 1714-1722.

[59] : Mugwagwa, L., Yadroitsev, I., & Matope, S. (2019). Effect of process parameters on residual stresses, distortions, and porosity in selective laser melting of maraging steel 300. Metals, 9(10), 1042.

[60] : Dehgahi, S., Sanjari, M., Ghoncheh, M. H., Amirkhiz, B. S., & Mohammadi, M. (2021). Concurrent improvement of strength and ductility in heat-treated C300 maraging steels produced by laser powder bed fusion technique. Additive Manufacturing, 39, 101847.

[61] : Sidambe, A. T., Judson, D. S., Colosimo, S. J., & Fox, P. (2019). Laser powder bed fusion of a pure tungsten ultra-fine single pinhole collimator for use in gamma ray detector characterisation. International Journal of Refractory Metals and Hard Materials, 84, 104998.

[62] : Rohit, B., & Muktinutalapati, N. R. (2021). Fatigue Behavior of 18% Ni Maraging Steels: A Review. Journal of Materials Engineering and Performance, 1-14.

[63] : Li, S., Zhao, K., Wang, K., & Yang, M. (2017). Microstructural evolution and thermal stability after aging of a cobalt-containing martensitic bearing steel. Materials Characterization, 124, 154-164.

[64] : Conde, F. F., Escobar, J. D., Rodriguez, J., Afonso, C. R. M., Oliveira, M. F., & Avila, J. A. (2021). Effect of Combined Tempering and Aging in the Austenite Reversion, Precipitation, and Tensile Properties of an Additively Manufactured Maraging 300 Steel. Journal of Materials Engineering and Performance, 1-12.

[65] : Wohlers, T., & Gornet, T. (2014). History of additive manufacturing. Wohlers report, 24(2014), 118.

[66] : Li, J., Wang, X., Qi, W., Tian, J., & Gong, S. (2019). Laser nanocomposites-reinforcing/manufacturing of SLM 18Ni300 alloy under aging treatment. Materials Characterization, 153, 69-78.

[67] : Kim, D., Kim, T., Ha, K., Oak, J. J., Jeon, J. B., Park, Y., & Lee, W. (2020). Effect of heat treatment condition on microstructural and mechanical anisotropies of selective laser melted maraging 18Ni-300 steel. Metals, 10(3), 410.

[68] : Yao, Y., Huang, Y., Chen, B., Tan, C., Su, Y., & Feng, J. (2018). Influence of processing parameters and heat treatment on the mechanical properties of 18Ni300 manufactured by laser based directed energy deposition. Optics & Laser Technology, 105, 171-179.

[69] : Thorsteinsdóttir, E. G., Primdahl, D. S., Zhang, Y. B., Jensen, D. J., & Yu, T. (2019, August). Aging of 3D-printed maraging steel. In IOP Conference Series: Materials Science and Engineering (Vol. 580, No. 1, p. 012047). IOP Publishing.

[70] : Bai, Y., Wang, D., Yang, Y., & Wang, H. (2019). Effect of heat treatment on the microstructure and mechanical properties of maraging steel by selective laser melting. Materials Science and Engineering: A, 760, 105-117.

[71] : Yin, S., Chen, C., Yan, X., Feng, X., Jenkins, R., O'Reilly, P., ... & Lupoi, R. (2018). The influence of aging temperature and aging time on the mechanical and tribological properties of selective laser melted maraging 18Ni-300 steel. Additive Manufacturing, 22, 592-600.

[72] : Zhu, H. M., Zhang, J. W., Hu, J. P., Ouyang, M. N., & Qiu, C. J. (2021). Effects of aging time on the microstructure and mechanical properties of laser-cladded 18Ni300 maraging steel. Journal of Materials Science, 56(14), 8835-8847.

[73] : Sinico, M., Witvrouw, A., & Dewulf, W. (2019). Influence of the particle size distribution on surface quality of Maraging 300 parts produced by Laser Powder Bed Fusion. In Proceedings of the Special Interest Group meeting on Advancing Precision in Additive Manufacturing (pp. 31-34). euspen.

[74] : Horn, M., Langer, L., Schafnitzel, M., Dietrich, S., Schlick, G., Seidel, C., & Reinhart, G. (2020). Influence of metal powder cross-contaminations on part quality in Laser Powder Bed Fusion: copper alloy particles in maraging steel feedstock. Procedia CIRP, 94, 167-172.

[75] : Sukal, J., Palousek, D. A. V. I. D., & Koutny, D. A. N. I. E. L. (2018). The effect of recycling powder steel of porosity and surface roughness of SLM parts. MM Science Journal, 2643-2647.

[76] : Bayat, M., Nadimpalli, V. K., Biondani, F. G., Jafarzadeh, S., Thorborg, J., Tiedje, N. S., ... & Hattel, J. H. (2021). On the role of the powder stream on the heat and fluid flow conditions during Directed Energy Deposition of maraging steel—Multiphysics modeling and experimental validation. Additive Manufacturing, 43, 102021.

[77] : Ramadas, H., Sarkar, S., Chattopadhyay, A., & Nath, A. K. (2021). Effect of Morphology and Particle Size Distribution on the Reusability of 15-5 Precipitation Hardening Stainless Steel Powder in Laser Powder Bed Fusion Process. In Current Advances in Mechanical Engineering (pp. 817-824). Springer, Singapore.

[78] : Koutiri, I., Pessard, E., Peyre, P., Amlou, O., & De Terris, T. (2018). Influence of SLM process parameters on the surface finish, porosity rate and fatigue behavior of as-built Inconel 625 parts. Journal of Materials Processing Technology, 255, 536-546.

[79] : Linderhof, F., Mashlan, M., Doláková, H., Ingr, T., & Ivanova, T. (2021). Surface Micromorphology and Structure of Stainless and Maraging Steel Obtained via Selective Laser Melting: A Mössbauer Spectroscopy Study. Metals, 11(7), 1028.

[80] : Mukherjee, M., Kundu, J., Balla, V. K., Das, M., Babu, K. S., Krishna, G. M., & Shome, M. (2021). Microstructure and properties of parts manufactured by directed energy deposition of water-atomized low-alloy steel powders. Materials Science and Engineering: A, 814, 141232.

[81] : Narra, S. P., Wu, Z., Patel, R., Capone, J., Paliwal, M., Beuth, J., & Rollett, A. (2020). Use of non-spherical hydride-dehydride (HDH) powder in powder bed fusion additive manufacturing. Additive Manufacturing, 34, 101188.

[82] : Ghods, S., Schultz, E., Wisdom, C., Schur, R., Pahuja, R., Montelione, A., ... & Ramulu, M. (2020). Electron beam additive manufacturing of Ti6Al4V: Evolution of powder morphology and part microstructure with powder reuse. Materialia, 9, 100631.

[83] : Powell, D., Rennie, A. E., Geekie, L., & Burns, N. (2020). Understanding powder degradation in metal additive manufacturing to allow the upcycling of recycled powders. Journal of Cleaner Production, 268, 122077.

[84] : Zapico, P., Giganto, S., Barreiro, J., & Martinez-Pellitero, S. (2020). Characterisation of 17-4PH metallic powder recycling to optimise the performance of the selective laser melting process. Journal of Materials Research and Technology, 9(2), 1273-1285.

[85] : Leung, C. L. A., Marussi, S., Towrie, M., Atwood, R. C., Withers, P. J., & Lee, P. D. (2019). The effect of powder oxidation on defect formation in laser additive manufacturing. Acta Materialia, 166, 294-305.

[86] : Nie, Y., Tang, J., Teng, J., Ye, X., Yang, B., Huang, J., ... & Li, Y. (2020). Particle defects and related properties of metallic powders produced by plasma rotating electrode process. Advanced Powder Technology, 31(7), 2912-2920.

[87] : Opatová, K., Zetková, I., & Kučerová, L. (2020). Relationship between the size and inner structure of particles of virgin and re-used MS1 maraging steel powder for additive manufacturing. Materials, 13(4), 956.

[88] : Salandre, M., Garabedian, S., Gaillard, G., Williamson, T., & Joffre, T. (2021). Development of a New Tooling Steel (L40) for Laser Powder Bed Fusion: Influence of Particles Size Distribution and Powder Atomization on Mechanical Performances. Advanced Engineering Materials.

[89] : Lee, S. H. W., Choo, H. L., Mok, S. H., Cheng, X. Y., & Manurung, Y. H. P. (2021). Permeability and Mechanical Properties of Additively Manufactured Porous Maraging 300 Steel. Lasers in Manufacturing and Materials Processing, 8(1), 28-44.

[90] : Dhinakar, A., Li, B. E., Chang, Y. C., Chiu, K. C., & Chen, J. K. (2021). Air Permeability of Maraging Steel Cellular Parts Made by Selective Laser Melting. Materials, 14(11), 3118.

[91] : Huang, W., Zhang, W., & Chen, X. (2020, March). Effect of SLM Process Parameters on Relative Density of Maraging Steel (18Ni-300) Formed Parts. In IOP Conference Series: Materials Science and Engineering (Vol. 774, No. 1, p. 012027). IOP Publishing.

[92] : Sarafan, S., Wanjara, P., Gholipour, J., Bernier, F., Osman, M., Sikan, F., ... & Brochu, M. (2021). Evaluation of Maraging Steel Produced Using Hybrid Additive/Subtractive Manufacturing. Journal of Manufacturing and Materials Processing, 5(4), 107.

[93] : Luo, C., & Zhang, Y. (2019). Fusion zone characterization of resistance spot welded maraging steels via selective laser melting. Journal of Materials Processing Technology, 273, 116253.

[94] : Yao, Y., Wang, K., Wang, X., Li, L., Cai, W., Kelly, S., ... & Yan, F. (2020). Microstructural heterogeneity and mechanical anisotropy of 18Ni-330 maraging steel fabricated by selective laser melting: The effect of build orientation and height. Journal of Materials Research, 35(15), 2065-2076.

[95] : Casalino, G., Campanelli, S. L., Contuzzi, N., & Ludovico, A. D. (2015). Experimental investigation and statistical optimisation of the selective laser melting process of a maraging steel. Optics & Laser Technology, 65, 151-158.

[96] : Kempen, K., Yasa, E., Thijs, L., Kruth, J. P., & Van Humbeeck, J. (2011). Microstructure and mechanical properties of Selective Laser Melted 18Ni-300 steel. Physics Procedia, 12, 255-263.

[97] : Jägle, E. A., Sheng, Z., Kürnsteiner, P., Ocylok, S., Weisheit, A., & Raabe, D. (2017). Comparison of maraging steel micro-and nanostructure produced conventionally and by laser additive manufacturing. Materials, 10(1), 8.

[98] : Casati, R., Lemke, J. N., & Vedani, M. (2017). Microstructural and Mechanical Properties of As Built, Solution treated and Aged 18Ni (300 grade) Maraging Steel Produced by Selective Laser Melting.

[99] : Becker, T. H., & Dimitrov, D. (2016). The achievable mechanical properties of SLM produced Maraging Steel 300 components. Rapid Prototyping Journal.

[100] : Bai, Y., Yang, Y., Wang, D., & Zhang, M. (2017). Influence mechanism of parameters process and mechanical properties evolution mechanism of maraging steel 300 by selective laser melting. Materials Science and Engineering: A, 703, 116-123.

[101] : Tan, C., Zhou, K., Tong, X., Huang, Y., Li, J., Ma, W., ... & Kuang, T. (2016, July). Microstructure and mechanical properties of 18Ni-300 maraging steel fabricated by selective laser melting. In Proceedings of the 2016 6th International Conference on Advanced Design and Manufacturing Engineering (ICADME 2016) (pp. 404-410).

[102] : Dehgahi, S., Alaghmandfard, R., Tallon, J., Odeshi, A., & Mohammadi, M. (2021). Microstructural evolution and high strain rate compressive behavior of as-built and heat-treated additively manufactured maraging steels. Materials Science and Engineering: A, 815, 141183.

[103] : Aydın, İ. (2020). Investigating effects of heat treatment processes on microstructural and mechanical properties of additively manufactured 18ni300 maraging steel (Master's thesis, Middle East Technical University).

[104] : Tan, C., Zhou, K., Ma, W., Attard, B., Zhang, P., & Kuang, T. (2018). Selective laser melting of high-performance pure tungsten: parameter design, densification behavior and mechanical properties. Science and Technology of advanced MaTerialS, 19(1), 370-380.

[105] : Vicario, V., & Miceli, D. (2020). Optimization of LPB/SLM Process and Maraging Steel Powders for Plastic Injection Moulds. BHM Berg-und Hüttenmännische Monatshefte, 1-7.

[106] : Vishwakarma, J., Chattopadhyay, K., & Srinivas, N. S. (2020). Effect of build orientation on microstructure and tensile behaviour of selectively laser melted M300 maraging steel. Materials Science and Engineering: A, 798, 140130.

[107] : Jarfors, A. E., Shashidhar, A. C. G. H., Yepur, H. K., Steggo, J., Andersson, N. E., & Stolt, R. (2021). Build Strategy and Impact Strength of SLM Produced Maraging Steel (1.2709). Metals, 11(1), 51.

[108] : Simm, T. H., Sun, L., Galvin, D. R., Hill, P., Rawson, M., Birosca, S., ... & Perkins, K. (2017). The effect of a two-stage heat treatment on the microstructural and mechanical properties of a maraging steel. Materials, 10(12), 1346.

[109] : Wang, B., Duan, Q. Q., Zhang, P., Zhang, Z. J., Li, X. W., & Zhang, Z. F. (2020). Investigation on the cracking resistances of different ageing treated 18Ni maraging steels. Materials Science and Engineering: A, 771, 138553.

[110] : Murthy, C. V. S., Krishna, A. G., & Reddy, G. M. (2019). Microstructure and mechanical properties of similar and dissimilar metal gas tungsten constricted arc welds: Maraging steel to 13-8 Mo stainless steel. Defence Technology, 15(1), 111-121.

[111] : Conde, F. F., Avila, J. A., Oliveira, J. P., Schell, N., Oliveira, M. F., & Escobar, J. D. (2021). Effect of the as-built microstructure on the martensite to austenite transformation in a 18Ni maraging steel after laser-based powder bed fusion. Additive Manufacturing, 46, 102122.

[112] : Allam, T., Pradeep, K. G., Köhnen, P., Marshal, A., Schleifenbaum, J. H., & Haase, C. (2020). Tailoring the nanostructure of laser powder bed fusion additively manufactured maraging steel. Additive Manufacturing, 36, 101561.

[113] : Mooney, B., Kourousis, K. I., & Raghavendra, R. (2019). Plastic anisotropy of additively manufactured maraging steel: Influence of the build orientation and heat treatments. Additive Manufacturing, 25, 19-31.

[114] : Becker, T. H., & Dimitrov, D. (2016). The achievable mechanical properties of SLM produced Maraging Steel 300 components. Rapid Prototyping Journal.

[115] : Suryawanshi, J., Prashanth, K. G., & Ramamurty, U. (2017). Tensile, fracture, and fatigue crack growth properties of a 3D printed maraging steel through selective laser melting. Journal of alloys and compounds, 725, 355-364.

[116] : Casati, R., Lemke, J. N., Tuissi, A., & Vedani, M. (2016). Aging behaviour and mechanical performance of 18-Ni 300 steel processed by selective laser melting. Metals, 6(9), 218.

[117] : Campanelli, S. L., Contuzzi, N., Posa, P., & Angelastro, A. (2019). Study of the aging treatment on selective laser melted maraging 300 steel. Materials Research Express, 6(6), 066580.

[118] : Tan, C., Zhou, K., Tong, X., Huang, Y., Li, J., Ma, W., ... & Kuang, T. (2016, July). Microstructure and mechanical properties of 18Ni-300 maraging steel fabricated by selective laser melting. In Proceedings of the 2016 6th International Conference on Advanced Design and Manufacturing Engineering (ICADME 2016) (pp. 404-410).

[119] : Cheng, C. W., Jhang Jian, W. Y., & Makala, B. P. R. (2021). Selective Laser Melting of Maraging Steel Using Synchronized Three-Spot Scanning Strategies. Materials, 14(8), 1905.

[120] : Song, J., Tang, Q., Feng, Q., Ma, S., Han, Q., & Setchi, R. (2021). Effect of Re-melting Process on Surface Quality and Tensile Behaviour of a Maraging Steel Manufactured by Selective Laser Melting. In Sustainable Design and Manufacturing 2020 (pp. 251-260). Springer, Singapore.

130

[121] : Demir, A. G., & Previtali, B. (2017). Investigation of remelting and preheating in SLM of 18Ni300 maraging steel as corrective and preventive measures for porosity reduction. The International Journal of Advanced Manufacturing Technology, 93(5), 2697-2709.

[122] : Zhao, Z., Dong, C., Kong, D., Wang, L., Ni, X., Zhang, L., ... & Li, X. (2021). Influence of pore defects on the mechanical property and corrosion behavior of SLM 18Ni300 maraging steel. Materials Characterization, 111514.

[123] : Meier, C., Penny, R. W., Zou, Y., Gibbs, J. S., & Hart, A. J. (2017). Thermophysical phenomena in metal additive manufacturing by selective laser melting: fundamentals, modeling, simulation, and experimentation. Annual Review of Heat Transfer, 20.

[124] : Haghdadi, N., Laleh, M., Moyle, M., & Primig, S. (2021). Additive manufacturing of steels: a review of achievements and challenges. Journal of Materials Science, 56(1), 64-107.

[125] : Kahlert, M., Brenne, F., Vollmer, M., & Niendorf, T. (2021). Influence of microstructure and defects on mechanical properties of AISI H13 manufactured by electron beam powder bed fusion. Journal of Materials Engineering and Performance, 30(9), 6895-6904.

[126] : Ye, C., Zhang, C., Zhao, J., & Dong, Y. (2021). Effects of Post-processing on the Surface Finish, Porosity, Residual Stresses, and Fatigue Performance of Additive Manufactured Metals: A Review. Journal of Materials Engineering and Performance, 1-19.

[127] : Peng, X., Kong, L., Fuh, J. Y. H., & Wang, H. (2021). A Review of Post-Processing Technologies in Additive Manufacturing. Journal of Manufacturing and Materials Processing, 5(2), 38.

[128] : Bai, Y., Zhao, C., Wang, D., & Wang, H. (2022). Evolution mechanism of surface morphology and internal hole defect of 18Ni300 maraging steel fabricated by selective laser melting. Journal of Materials Processing Technology, 299, 117328.

[129] : Pellizzari, M., AlMangour, B., Benedetti, M., Furlani, S., Grzesiak, D., & Deirmina, F. (2020). Effects of building direction and defect sensitivity on the fatigue behavior of additively manufactured H13 tool steel. Theoretical and Applied Fracture Mechanics, 108, 102634.

[130] : Li, R., Liu, J., Shi, Y., Wang, L., & Jiang, W. (2012). Balling behavior of stainless steel and nickel powder during selective laser melting process. The International Journal of Advanced Manufacturing Technology, 59(9), 1025-1035.

[131] : Yasa, E. (2021). Selective laser melting: principles and surface quality. In Additive Manufacturing (pp. 77-120). Elsevier.

[132] : Simoni, F., Huxol, A., & Villmer, F. J. (2021). Improving surface quality in selective laser melting based tool making. Journal of Intelligent Manufacturing, 1-12.

[133] : He, Y., Zhong, M., Beuth, J., & Webler, B. (2020). A study of microstructure and cracking behavior of H13 tool steel produced by laser powder bed fusion using single-tracks, multi-track pads, and 3D cubes. Journal of Materials Processing Technology, 286, 116802.

[134] : Vilanova, M., Garciandia, F., Sainz, S., Jorge-Badiola, D., Guraya, T., & San Sebastian, M. (2021). The limit of hot isostatic pressing for healing cracks present in an additively manufactured nickel superalloy. Journal of Materials Processing Technology, 117398.

[135] : AlMangour, B., Grzesiak, D., Cheng, J., & Ertas, Y. (2018). Thermal behavior of the molten pool, microstructural evolution, and tribological performance during selective laser melting of TiC/316L stainless steel nanocomposites: Experimental and simulation methods. Journal of Materials Processing Technology, 257, 288-301.

[136] : Yao, Y., Zhu, H., Huang, C., Wang, J., Zhang, P., & Yao, P. (2019). Investigation on chip formation and surface integrity in micro end milling of maraging steel. The International Journal of Advanced Manufacturing Technology, 102(5), 1973-1984.

[137] : Kempen, K., Vrancken, B., Thijs, L., Buls, S., Van Humbeeck, J., & Kruth, J. P. (2013). Lowering thermal gradients in Selective Laser melting by pre-heating the baseplate. In Solid Freeform Fabrication Symposium Proceedings.

[138] : Narvan, M., Al-Rubaie, K. S., & Elbestawi, M. (2019). Process-structure-property relationships of AISI H13 tool steel processed with selective laser melting. Materials, 12(14), 2284.

[139] : Wang, Y., Luo, L., Liu, T., Wang, B., Luo, L., Zhao, J., ... & Fu, H. (2021). Tuning process parameters to optimize microstructure and mechanical properties of novel maraging steel fabricated by selective laser melting. Materials Science and Engineering: A, 823, 141740.

[140] : Wu, L., Das, S., Gridin, W., Leuders, S., Kahlert, M., Vollmer, M., & Niendorf, T. (2021). Hot Work Tool Steel Processed by Laser Powder Bed Fusion: A Review on Most Relevant Influencing Factors. Advanced Engineering Materials, 2100049.

[141] : Narvan, M., Ghasemi, A., Fereiduni, E., Kendrish, S., & Elbestawi, M. (2021). Part deflection and residual stresses in laser powder bed fusion of H13 tool steel. Materials & Design, 204, 109659.

[142] : Wu, W., Wang, X., Wang, Q., Liu, J., Zhang, Y., Hua, T., & Jiang, P. (2020). Microstructure and mechanical properties of maraging 18Ni-300 steel obtained by powder bed based selective laser melting process. Rapid Prototyping Journal.

[143] : Bouzakis, E., Arvanitidis, A., Kazelis, F., Maliaris, G., & Michailidis, N. (2020). Comparison of additively manufactured vs. conventional maraging steel in corrosion-fatigue performance after various surface treatments. Procedia CIRP, 87, 469-473.

[144] : Du, W., Bai, Q., & Zhang, B. (2018). Machining characteristics of 18Ni-300 steel in additive/subtractive hybrid manufacturing. The International Journal of Advanced Manufacturing Technology, 95(5), 2509-2519.

[145] : Tan, C., Weng, F., Sui, S., Chew, Y., & Bi, G. (2021). Progress and perspectives in laser additive manufacturing of key aeroengine materials. International Journal of Machine Tools and Manufacture, 103804.

[146] : Tan, C., Chew, Y., Duan, R., Weng, F., Sui, S., Ng, F. L., ... & Bi, G. (2021). Additive manufacturing of multi-scale heterostructured high-strength steels. Materials Research Letters, 9(7), 291-299.

[147] : Mutua, J., Nakata, S., Onda, T., & Chen, Z. C. (2018). Optimization of selective laser melting parameters and influence of post heat treatment on microstructure and mechanical properties of maraging steel. Materials & Design, 139, 486-497.

[148] : Guo, W. F., Guo, C., & Zhu, Q. (2018). Heat treatment behavior of the 18Ni300 maraging steel additively manufactured by selective laser melting. In Materials Science Forum (Vol. 941, pp. 2160-2166). Trans Tech Publications Ltd.

[149] : Tascioglu, E., Khan, H. M., Kaynak, Y., Coşkun, M., Tarakci, G., & Koç, E. (2021). Effect of aging and finish machining on the surface integrity of selective laser melted maraging steel. Rapid Prototyping Journal.

[150] : Cyr, E., Lloyd, A., & Mohammadi, M. (2018). Tension-compression asymmetry of additively manufactured Maraging steel. Journal of Manufacturing Processes, 35, 289-294.

[151] : Spitzig, W. A., Sober, R. J., & Richmond, O. (1976). The effect of hydrostatic pressure on the deformation behavior of maraging and HY-80 steels and its implications for plasticity theory. Metallurgical Transactions A, 7(11), 1703-1710.

[152] : Dehgahi, S., Alaghmandfard, R., Tallon, J., Odeshi, A., & Mohammadi, M. (2021). Microstructural evolution and high strain rate compressive behavior of as-built and heat-treated additively manufactured maraging steels. Materials Science and Engineering: A, 815, 141183.

[153] : Contuzzi, N., Campanelli, S. L., Casavola, C., & Lamberti, L. (2013). Manufacturing and characterization of 18Ni marage 300 lattice components by selective laser melting. Materials, 6(8), 3451-3468.

[154] : de Oliveira, A. R., de Andrade Mendes Filho, A., Masoumi, M., & Del Conte, E. G. (2021). Compression and energy absorption of maraging steel primitive scaffolds produced by powder bed fusion. The International Journal of Advanced Manufacturing Technology, 116(3), 1271-1283.

[155] : Tyczyński, P., Siemiątkowski, Z., Bąk, P., Warzocha, K., Rucki, M., & Szumiata, T. (2020). Performance of Maraging Steel Sleeves Produced by SLM with Subsequent Age Hardening. Materials, 13(15), 3408.

[156] : Bouzakis, E., Arvanitidis, A., Kazelis, F., Maliaris, G., & Michailidis, N. (2020). Comparison of additively manufactured vs. conventional maraging steel in corrosion-fatigue performance after various surface treatments. Procedia CIRP, 87, 469-473.

[157] :'Antunes, F., Santos, L., Capela, C., Ferreira, J., Costa, J., Jesus, J., & Prates, P. (2019). Fatigue crack growth in maraging steel obtained by selective laser melting. Applied Sciences, 9(20), 4412.

[158] : Branco, R., Costa, J. D., Berto, F., Razavi, S. M. J., Ferreira, J. A. M., Capela, C., ... & Antunes, F. (2018). Low-cycle fatigue behaviour of AISI 18Ni300 maraging steel produced by selective laser melting. Metals, 8(1), 32.

[159] : Croccolo, D., De Agostinis, M., Fini, S., Olmi, G., Robusto, F., Ćirić Kostić, S., ... & Bogojević, N. (2018). Fatigue response of as-built DMLS maraging steel and effects of aging, machining, and peening treatments. Metals, 8(7), 505.

[160] : Croccolo, D., De Agostinis, M., Fini, S., Olmi, G., Vranic, A., & Ciric-Kostic, S. (2016). Influence of the build orientation on the fatigue strength of EOS maraging steel produced by additive metal machine. Fatigue & Fracture of Engineering Materials & Structures, 39(5), 637-647.

[161] : Santos, L. M. S., Ferreira, J. A. M., Jesus, J. S., Costa, J. M., & Capela, C. (2016). Fatigue behaviour of selective laser melting steel components. Theoretical and Applied Fracture Mechanics, 85, 9-15.

[162] : Uematsu, Y., Kakiuchi, T., Nakajima, M., & Matsuo, K. (2021). Microstructures and Fatigue Behavior of Additively Manufactured Maraging Steel Deposited on Conventionally Manufactured Base Plate. Journal of Materials Engineering and Performance, 1-9.

[163] : Mary, R. N., Nazareth, R., Adimule, S. P., & Potla, K. (2021). Investigation of Corrosion Inhibition Property of Triazole-Based Schiff Bases on Maraging Steel in Acid Mixtures. Journal of Failure Analysis and Prevention, 21(2), 547-562.

[164] : Avelino, A. F., Araújo, W. S., Dias, D. F., dos Santos, L. P. M., Correia, A. N., & de Lima-Neto, P. (2018). Corrosion investigation of the 18Ni 300 grade maraging steel in aqueous chloride medium containing H2S and CO2. Electrochimica Acta, 286, 339-349.

[165] : Zhao, T., Wang, S., Liu, Z., Du, C., & Li, X. (2021). Effect of cathodic polarisation on stress corrosion cracking behaviour of a Ni (Fe, Al)-maraging steel in artificial seawater. Corrosion Science, 179, 109176.

[166] : Simson, T., Koch, J., Zetek, M., & Zetková, I. (2021, August). Corrosion Resistance of 18Ni-300 maraging steel manufactured by LPBF. In IOP Conference Series: Materials Science and Engineering (Vol. 1178, No. 1, p. 012051). IOP Publishing.

[167] : K. V. Durga Rajesh, Abdul Munaf Shaik & Tanya Buddi (2021): WEAR AND CORROSION ANALYSIS ON MARAGING STEEL MS1 AND STAINLESS STEEL 316L DEVELOPED BY DIRECT METAL LASER SINTERING PROCESS, Advances in Materials and Processing Technologies, DOI: $10.1080/2374068 \times .2021.1930797$

[168] : Wang, J. J., Zhang, M., Tan, X., Jing, W., Liu, E. J., Tor, S. B., & Li, H. (2018). Impact and fatigue characteristics of additively manufactured steel materials: A review. In Proc. Int. Conf. Prog. Addit. Manuf (Vol. 2018, pp. 487-492).

[169] : Nandwana, P., Kannan, R., & Leonard, D. N. (2020). Leveraging solute segregation in laser powder bed fusion to achieve superior strength and ductility via single-step heat treatment in ti-free grade 300 maraging steel. JOM, 72(12), 4221-4231.

[170] : Masoumi, M., de Barros, I. F., Herculano, L. F. G., Coelho, H. L. F., & de Abreu, H. F. G. (2016). Effect of microstructure and crystallographic texture on the Charpy impact test for maraging 300 steel. Materials Characterization, 120, 203-209.

CHAPITRE 3

INFLUENCE DU POST-TRAITEMENT SUR LA MICROSTRUCTURE ET LES PROPRIÉTÉS MÉCANIQUES DE L'ACIER C300 MARAGING FABRIQUE DE MANIÈRE ADDITIVE

(Article à soumettre)

Faiçal. Habassi[1, *], Manel. Houria[2], Noureddine. Barka[1], Mohammad. Jahazi[2],

[1] Mathematics, Computer Science and Engineering Department, Université du Québec à Rimouski (UQAR), 300 Allée des Ursulines, Rimouski, QC G5L 3A1, Québec, Canada

[2] Mechanical Engineering Department, École de Technologie supérieure (ÉTS), 1100 Rue Notre-Dame Ouest, Montréal, QC H3C 1K3, Québec, Canada

∗Corresponding author. E-mail : Faical.Habassi@uqar.ca

3.1 RESUME EN FRANÇAIS DU TROISIEME ARTICLE

Le procédé SLM a connu des évolutions majeures, notamment des développements liés à la fabrication de pièces en acier maraging. Alors que SLM vise à atteindre et à améliorer les propriétés mécaniques obtenues par les procédés traditionnels, il reste beaucoup à faire pour perfectionner et optimiser son utilisation pour les aciers maraging de manière rentable et efficace. L'objectif de ce travail est d'explorer divers paramètres de post-traitement liés à l'acier maraging SLM afin d'obtenir des comportements mécaniques de haut niveau dans le temps de traitement le plus court, en utilisant des solutions aqueuses de NaCl pour le refroidissement. Le premier objectif est d'obtenir un temps de traitement réduit par rapport aux valeurs les plus fréquentes rencontrées dans la littérature, qui est généralement d'environ 1 heure pour les traitements en solution et de 5-6 heures ou plus pour les traitements de vieillissement. Dans le cadre de la présente étude, les effets de divers paramètres de post-traitement (solution de refroidissement, température de vieillissement et temps de vieillissement) sur la microstructure et les comportements mécaniques, en particulier la

136

dureté et la résistance à la traction, de l'acier maraging SLM (C300) ont été étudiés. Une série d'éprouvettes de traction, fabriquées avec une densité d'énergie laser de 65 J/mm3, ont été soumises à un post-traitement puis à divers tests mécaniques afin d'étudier leurs performances. Une étape de traitement de solution d'homogénéisation (HT) commune a été effectuée à 1020 ° C pendant 15 min. Trois températures de vieillissement différentes (485 ℃, 585 ℃ et 685 ℃) et des durées de vieillissement (120 min, 150 min et 180 min) ont été utilisées sur les pièces. Pour les pièces telles que construites et traitées thermiquement, les changements de microstructure et de composition de phase sont les principaux facteurs qui affectent les variations des performances mécaniques de l'acier maraging SLM (C300). Plus précisément, ces variations sont déterminées par diverses caractéristiques microstructurales, telles que la taille des grains, la fraction de phase, ainsi que la distribution spatiale et la morphologie des phases dans la microstructure. Afin de caractériser les effets du traitement thermique sur la microstructure et sur le comportement mécanique, différentes techniques de microscopie, telles que la microscopie confocale à balayage laser (CLSM), la microscopie électronique à balayage (SEM) et la diffraction par rétrodiffusion d'électrons (EBSD), ont été utilisées. Pour quantifier le comportement mécanique de l'acier maraging SLM (C300), des mesures de dureté et des essais de traction ont été effectués après des traitements de vieillissement en solution d'homogénéisation (HAT). De plus, un modèle statistique a été développé en utilisant l'analyse de variance (ANOVA) pour prédire le comportement mécanique (dureté) et déterminer le paramètre significatif associé. Le modèle a lié le comportement mécanique aux propriétés de post-traitement dans la zone de travail. Par rapport aux pièces telles que construites, la microdureté et les résistances ultimes à la traction ont été considérablement améliorées après les traitements de vieillissement en solution d'homogénéisation (HAT). Les effets des paramètres de traitement thermique (solution de refroidissement, température de vieillissement et temps de vieillissement) sur les propriétés mécaniques dépendent principalement des changements de microstructure qui se produisent. Les résultats ont montré que les pièces traitées thermiquement avaient une microstructure plus fine et non continue, conduisant à une dureté plus élevée (~20-50 %) et à des propriétés de résistance ultime à la traction plus élevées (~25-55 %), par rapport à la

version telle que construite. Les pièces. La microdureté et la résistance ultime peuvent aller jusqu'à ~56 HRC et 2150 MPa, respectivement, au régime de traitement thermique optimal (traitement en solution à 1020 °C pendant 15 min + traitement de vieillissement à 480 °C pendant ~175 min).

Ce troisième article intitulé « *Influence of post-treatment on microstructure and mechanical properties of additively manufactured C300 Maraging steel* » a pu voir le jour grâce à la collaboration de l'équipe de recherche du Professeur Noureddine Barka et celle de Professeur Mohammed Jahazi. Le premier auteur, Faical Habassi, a mené la partie essentielle de la recherche concernant l'état de l'art, les essais de performance, l'analyse et l'interprétation des résultats ainsi que l'optimisation qui est le cœur du travail. L'essentiel des travaux de rédaction a été fait aussi par le premier auteur sous la supervision de Noureddine Barka et de Mohammed Jahazi. Manel Houria, le second auteur a apporté une partie essentielle, ce qui a aidé à améliorer la qualité du papier. Le professeur Noureddine Barka, qui est le troisième auteur a défini le projet ainsi la méthodologie à adopter. Quant au co-directeur, Mohammed Jahazi, il a apporté une partie essentielle grâce à sa connaissance approfondie de la métallurgie et des matériaux.

3.2 TITRE DU TROISIEME ARTICLE

Influence of post-treatment on microstructure and mechanical properties of additively manufactured C300 Maraging steel

3.3 ABSTRACT

The SLM process has undergone major evolutions, including developments related to the manufacture of maraging steel parts. While SLM aims to achieve and improve the mechanical properties obtained by traditional processes, much remains to be done to perfect and optimize its use for maraging steels in a cost-effective and efficient manner. The aim of this work is to explore various post-processing parameters related to SLM maraging steel in order to achieve high-level mechanical behaviors in the shortest processing time, using

138

aqueous NaCl solutions for cooling. The first goal is to obtain a reduced processing time versus the most frequent values encountered in the literature, which is generally approximately 1 hour for solution treatments and 5-6 hours or more for aging treatments. In the context of the present study, the effects of various post-treatment parameters (cooling solutions, aging temperature, and aging time) on the microstructure and mechanical behaviors, especially the hardness and tensile strength, of SLM maraging steel (C300) was investigated. A series of tensile specimens, manufactured with a laser energy density of 65 J/mm 3, were subjected to post-treatment and then to various mechanical tests in order to investigate their performance. A common homogenization solution treatment (HT) step was performed at 1020 °C for 15 min. Three different aging temperatures (485 °C, 585 °C, and 685 °C) and aging times (120 min, 150 min, and 180 min) were used on the parts. For as-built and heat-treated parts, microstructure and phase composition changes are the major factors that affect variations in the mechanical performance of SLM maraging steel (C300). Specifically, such variations are determined by various microstructural features, such as the grain size, the phase fraction, as well as the spatial distribution and morphology of the phases in the microstructure. In order to characterize the effects of heat treatment on the microstructure and on the mechanical behaviour, various microscopy techniques, such as confocal laser scanning microscopy (CLSM), scanning electron microscopy (SEM), and electrons backscatter diffraction (EBSD), were used. To quantify the mechanical behaviour of SLM maraging steel (C300), hardness measurements and tensile tests were performed after homogenization solution-aging treatments (HAT). Furthermore, a statistical model was developed using analysis of variance (ANOVA) to predict the mechanical behaviour (hardness) and determine the related significant parameter. The model related the mechanical behaviour to the post-treatment properties in the work region. Compared to the as-built parts, the microhardness and ultimate tensile strengths were significantly improved after homogenization solution-aging treatments (HAT). The effects of heat treatment parameters (cooling solutions, aging temperature and aging time) on mechanical properties depend primarily on the microstructure changes that occur. The results showed that the heat-treated parts had a finer and non-continuous microstructure, leading to higher hardness (~20-50%)

and higher ultimate tensile strength (~25–55%) properties, as compared to the as-built parts. The microhardness and ultimate strength can go up to ~56 HRC and 2150 MPa, respectively, at the optimal heat treatment regime (solution treatment at 1020 °C for 15 min + aging treatment at 480 °C for ~175 min).

3.4 INTRODUCTION

Additive manufacturing (AM) is an emerging manufacturing process in the tool and mold industry [1-2]. Specifically, AM has become a promising manufacturing technique for die-casting and tool making [1-2]. Gaedan et al. [1] and Durakovic et al. [2] have highlighted this in their paper regarding additive manufacturing and trends. The main advantages of AM in die casting include reduced material waste, improved functionality and customization of tools thanks to the freedom of design and flexibility accorded to mold designers. AM technology also allows to design dies with complex geometries, microstructures, and high-quality parts such as cooling channels [1-2], lattice structures [3], automotive-specific parts [4], and high-precision aerospace parts [5].

Selective Laser Melting (SLM) is one of the best known and most promising AM technologies [6-7]. The SLM process, its principles, advantages, and prospects have been extensively reviewed in the literature, including in works such as those of Gunasekaran et al. [6], and Chen et al. [7]. These previous works point to SLM technology as being in increasing development especially as it allows the production of complex and high-quality metallic parts [6-7]. That is the case even though the process must necessarily be completed by certain finishing operations, such as the removal of supports and long post-treatment [1-2, 6-7]. Compared to conventional manufacturing techniques, SLM offers many advantages, such as freedom of design, minimum material waste and high-quality finished parts [1-2, 6-7]. SLM is an AM powder bed fusion (PBF) technology that involves complex physical phenomena, such as heating, melting, and solidification of a metallic powder. When a heat source, generally in the form of a laser, is moved, the energy involved leads to the complete layer-by-layer melting of the powder [1-2, 6-7]; this melting is a function of the desired geometry.

Once a given layer is completed, the construction platform is lowered by the pre-melted layer thickness, and an additional powder layer is spread on the work platform. The process is repeated until the desired component construction is achieved. As SLM does not require long post-treatment, it can produce approximately fully dense metallic parts, with acceptable mechanical properties [6-7]. The SLM technology has proven to be suitable for the manufacture of hard tool steels [8-10], stainless steels [11-12], Ti-based alloys [13-14], aluminum alloys [15-17], Ni-based alloys [13, 18] and Mg-based alloys [19-20]. However, since SLM as a technology is still evolving [1-2, 6-7], certain elements call for further improvement in practice. The most limiting factors with the technology are manufacturing costs and the need for long-thermal post-processing. These two factors further breakdown mainly into the cost of machines, their low productivity and long thermal processing times. Furthermore, a lack of material standards specific to certain sectors hinders the use of these processes. AM is generally thus more suitable for small or medium series. Some processes will not allow specific surface orientations without the addition of supports, and this can generate subsequent costly post-processing [1-2, 6-7].

Maraging steels, which are nickel-rich alloys (Fe-Ni), are commonly used in the tool and mold industry [21-24] because of their high mechanical strength [21-22], wear resistance [21-22], toughness [21-22], machinability [23], and weldability [24]. Their final microstructure [25-27], density [25-27] and mechanical behaviors [25-27] can be modified through post-processing heat treatment [28-30] or process parameters [31], according to their applications. As-built SLM maraging steel reaches a comparable mechanical behaviour to the wrought state with fine cellular microstructure. Standford et al. [37] reported that an AM-fabricated maraging steel (C300) had a comparable mechanical performance to that of conventional forged C300 steel bars [37-39]. Similar results were reported by Kempen et al. [38] and Casalino et al. [39]. Recently, Mooney et al. [40] reported a cell solidification microstructure generally confined by residual austenite retained along the inter-boundaries. This result has been confirmed by Jagle et al. [41], in their comparative study between the micro-and nanostructure produced conventionally and by laser additive manufacturing. Tan et al [42] used a similar AM system to produce C300 alloy parts and observed a fully dense

dendritic cell microstructure. The post-processing heat treatment for steels, such as maraging steels, usually requires a combined post-treatment homogenization solution-aging treatment (HAT) (homogenization solution treatment (quenching operation) + aging treatment) consisting of a homogenization solution treatment (quenching operation using a cooling solution) (HT) followed by an aging treatment (AT) [31-36]. Therefore, it is considered as a critical step of SLM processes, which is mainly crucial for the density and microstructural characteristics of the manufactured object; these are the decomposition of the martensitic phase, precipitation of second phase particles, stress relief and porosity reduction. The cellular microstructure of the as-built parts is affected by post-treatments, which can affect the hardness and resistance of hardenable alloys, including maraging steel [37-42]. These microstructural changes are characterized in depth in this chapter.

In the context of post-processing heat treatment, recent years have seen research works on the effect of post-treatment parameters on SLM maraging steel. Although post-treatment represents a technique of choice for joining parts with high properties in SLM maraging steel due to the many advantages offered by the process, a lot remains to be done to improve and optimize it as the properties of the metal have led to its reputation as a difficult material to post-treat because long post-treatments are generally required [36-48]. In general, post treatments are able to reduce the stress of the SLM and generate a high hardenability in the microstructure, and therefore harder mechanical properties. Many researchers have investigated the effect of post-processing heat treatment on the final quality of SLM maraging steels. Recently, Ozer et al. [36] (2020) investigated the effects of different heat treatment parameters on the microstructure and mechanical behaviors of direct SLM maraging steel, especially hardness properties. They found that the maximum hardness exceeded 55 HRC after solution heat treatment and subsequent aging (SHT : 940 °C-2 hours-air cooling, 490 °C-6 hours-air cooling) and 56 HRC after direct aging (aging: 490 °C-6 hours-air cooling), as compared to 36 HRC in the as-built state. In the same study, they also pointed out that the corrosion behaviour is better in the as-built state. Similar results (hardness: 55 HRC, UTS: 2014 MPa) were reported by Tan et al. [42] (2017) and Mooney et al. [40] (2019) using a direct aging treatment at 490 °C for 6 hours, and 8hours, respectively. Koukolíková et al.

[43] (2021) reported that the mechanical behaviour of SLM maraging steel can largely increase after post-processing heat treatment. They found the maximum hardness and ultimate tensile strength exceeded ~620 HV and ~2157 MPa, respectively, after solution heat treatment and subsequent aging (SHT : 840 °C-1 hours-water cooling, 480 °C-6 hours-air cooling), as compared to 36 HRC and 1163 MPa in the as-built state. They also stated that the build direction of 45° leads to the best mechanical behaviors. Martínez et al. [44] (2021) reported that aging heat treatments between 460 and 490 °C (4-8 hours) resulted in the maximum hardness value (~55HCR). Earlier, Guo et al. [45] (2018) had studied the influence of various heat treatments on the microstructure and mechanical properties. Their results showed that the maximum mechanical behaviour was observed with a direct aging treatment at 460 °C for 12 hours. After this long treatment the hardness and ultimate tensile strength increase up to 628.9 HV and 2089.7 MPa, respectively. Similar results were reported by Bai et al. [46] (Hardness ~645 HV, UTS~2163 MPa, using heat treatment (SHT : 840 °C-1 hours-air cooling, 480 °C-6 hours-air cooling)), Yasa et al. [47] (Hardness ~58 HRC, UTS~2217 MPa, using heat treatment (direct aging 480 °C-5 hours-air cooling)), Kempen et al. [38] (Hardness ~58 HRC, UTS~2212 MPa, using a direct aging treatment (480 °C-5 hours-air cooling)) and Casati et al. [48] (Hardness ~630 HV, UTS~2017 MPa, using heat treatment (460 °C-8 hours-air cooling)). Considering an acceptable post-processing heat treatment time (~3 hours), a high temperature was generally used, and a lower maximum level was achieved. Guo et al. [45] (2018) observed a hardness of 605 HV and an ultimate tensile strength of 2032 MPa with direct aging at 530 °C for 3 hours. However, in this case, there was a fatal flaw in the sense that if the aging temperature exceeded a certain level, then the mechanical behaviors of SLM maraging steel parts would dramatically decrease; indeed, this is one critical limitation that has impeded its further application in the industry. This limitation can be seen in Casati et al. [48], in which it was reported that for an aging treatment at 540 °C, the maximum hardness (~560 HV) and tensile strength (~1957 MPa) can be reached in 1 hour before decreasing as the aging time is increased. In the same work, at an aging temperature of 600 °C, the mechanical behaviour began to decrease from its maximum (hardness: ~530 HV, UTS: 1660 MPa) in just 10 min. Furthermore, few previous works lend

specific importance to the effect of austenitizing temperature on laser sintered parts of different materials. Lian et al. [49] conducted work on the influence of austenitizing temperature on the microstructure of maraging steel. They noted that normal grain growth occurs at austenitizing temperatures ranging between 800 and 1000 °C. Using the same steel, Condé et al. [50] observed that direct aging of a part can gives it the hardest character, smallest strain to failure, and highest flexural strength due to the preferential secondary precipitates generated. The authors recommended relatively high homogenization temperatures (980 °C) to guarantee a more efficient micro-structural dissolution.

As illustrated in the literature, many researchers have reported their investigations on the effects of post-processing heat treatment on maraging steel parts. However, much remains to be done to perfect and further optimize the use of SLM and thermal post-processing for maraging steels to have a cost-effective and efficient process, especially in terms of reducing the long post-processing and optimizing their effects. This work aims to explore various post-processing parameters related to SLM maraging steel in a bid to achieve high-level mechanical behaviors in the shortest processing time. The first goal is to further optimize the most frequent processing times present in the literature, which is generally around 1 hours or more for the solution treatment and 5-6 hours or more for the aging treatment, using statistical tools such as ANOVA, preceded by a design of experiments using the Taguchi method. A Taguchi rotatable design with three factors and three levels was chosen to minimize the number of experimental conditions. An empirical relationship was established to predict the interrelation between hardness and the post-processing heat treatment parameters by incorporating independently controllable parameters. The optimization was accomplished using numerical tools, including response surface methodology (RSM), to find the optimal post-processing parameters needed to attain maximum hardness. A validation step was applied using the tensile test to validate the optimal post-processing parameters. The study employs confocal laser scanning microscopy (CLSM), scanning electron microscopy (SEM), and electrons backscatter diffraction (EBSD) to reveal the phase transformation and microstructure of as-built and heat-treated samples. Additionally, it offers some practical

recommendations in terms of solution treatment cooling, aging temperature, and aging time needed to successfully heat-treat SLM maraging steel (C300).

3.5 NOMENCLATURE

AM: Additive manufacturing,

SLM: Selective laser fusion,

HT: Homogenization solution treatment,

AT: Aging treatment,

HAT: Homogenization solution-aging treatments (HT+AT),

Ta: Aging temperature ($^{\circ}$ C),

S: Cooling Solution concentration (%),

timea: Aging time (min),

UTS: Ultimate tensile strength,

3.6 MATERIALS AND METHODS

Some tensile samples are manufactured by the SLM process using a specific maraging steel (C300) powder. Different post-treatments (in the context of a specific tempering and quenching process) were used in this investigation. The influence of post-treatment on the microstructure and the hardness were investigated for all the post-treatments. However, for the tensile test, one of the three aging treatments studied was selected, based on metallurgical and micro-hardness tests, and identified as the optimal aging treatment. Some of the tensile coupons homogenized by HT at 1020 ℃ for 15 min was aged according to this "optimal" treatment (ATop: 480℃ - 175 min). Tensile tests were performed on as-built and solution-aged parts (HATop) according to the "optimal" treatment. Details of the powder, the

tempering and quenching process, the metallography characterization, and the mechanical tests used are presented later in the present paper.

3.6.1   Materials

The maraging steel (C300) powder used in this study was manufactured by a gas atomization process, in an approximately spherical form and in the 15-45 µm particle size range. The micrograph of the maraging steel (C300) powder is shown in Figure 3.1 and the chemical composition are listed in Table 3.1.

Table 3. 1. Chemical composition (wt%) of MS1.

C	Ni	Co	Mo	Mn,Si	Ti	Al	Cr	P,S	Fe
0.03	17-19	8.5- 10	4.5-5.2	0.1	0.6-0.8	0.15	0.5	0.01	Bal.

Table 3. 2. Additive manufacturing process parameters.

Laser powder	Laser speed	Hatching space	Hatching direction	Resolution	
195 W	750 mm/s	0.1 mm	Stripe-like	40	µm
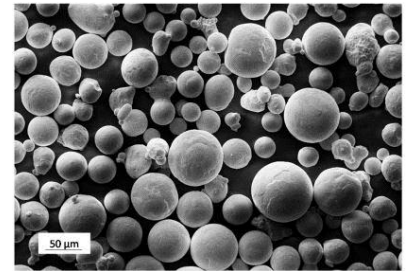
Figure 3. 1. MS1 Powder morphology [38].

3.6.2   Additive Manufacturing

A series of tensile coupon samples sized according to ASTM-E8 [51] (Figure 3.2 - dimension is in mm) were fabricated using an EOS-M290 device (SLM). The procedure parameters are shown in Table 3.2. The thickness of the powder layer was 40 µm. A nitrogen atmosphere was maintained throughout the fabrication process.
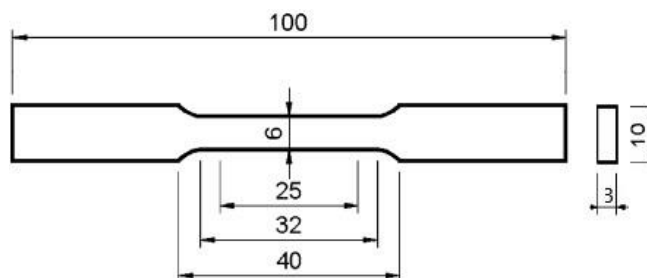
Figure 3. 2. Size of tensile test samples.

146

3.6.3 Quenching and Tempering

In order to investigate the influence of post-treatment on the microstructure and mechanical properties of SLM maraging steel parts, three types of thermal routes were employed (HAT1-HAT3). Each one of them included two steps.

The first step, which is a common one in the three post-treatments (HAT1, HAT3), consists of homogenization using homogenization solution treatments (HT; also known as austenitization and designated as HT1-HT3) at 1020 ℃ for 15 min in an aqueous salt solution quenching to produce a fully martensitic structure [52-53]. The concentration of the aqueous NaCl solution differs between the homogenization solution treatments (respectively 0% for HT1, 6% for HT2 and 12% for HT3). The second step consists of an aging treatment (designated as AT1-AT3). The aging cycles (Ta, timea) were performed at 485 ℃ (HAT1), 585 ℃ (HAT2), and 685 ℃ (HAT3), respectively. At each aging temperature, three aging times, respectively 120 min, 150 min, and 180 min were used. The effects of the aging temperature (Ta) and the aging times (timea) were evaluated.

To reduce the number of samples to be used and the number of experiments to be performed, a design of experiment approach using Taguchi's method was employed, choosing a combination of cooling solution "S" (used in homogenization solution treatment (HT)) - aging temperature (Ta) - aging time (timea), for selecting the priority of the experiments. Details and corresponding designations are given in Table 3.3 and Figure 3.3.

3.6.4 Metallography Characterization

All samples produced for metallography were analyzed using an OLYMPUS LEXT OLS4100 confocal laser scanning microscope (CLSM) to obtain large optical micrographs through an automated assembly operation. The scanning electron microscope (SEM), Hitachi TM3000 model, equipped with energy dispersive spectroscopy (EDS), was used for microstructure and chemical composition analysis (when possible) on some critical samples (high/low hardness, as-built or hardened). The microstructure, texture evolution, and

phase identification were studied on as-built samples by Electron BackScatter Diffraction (EBSD) analysis using a Hitachi SU8320 field emission gun (FEG-SEM), equipped with an e-flash plus detectors. The samples were tilted 70° to the backscattered electron detector. The step size and the accelerating voltages were 23 nm and 25 Kv, respectively. The Bruker-Esprit 2.2 software was used to analyze EBSD data.

Before microscopy observations, a preparation step was executed, during which the metallography and micro-hardness samples were cut from the sides of the manufactured AM coupons in a $10 \times 3 \times 4$ mm rectangular shape. They were polished using the standard polishing procedure to a 1 µm diamond paste size. After this step, the specimens selected for the EBSD analysis were mechanochemically polished with a colloidal silica solution (0.05 µm) using a BUEHLER VibroMet polisher for 10 hours. Then, the samples were prepared with the Hitachi IMP4000plus ion polisher to remove the subsurface deformed layer. The microstructure was revealed using Fry's reagent (1 g CuCl, 50 ml HCl, 50 ml HNO3, 150 ml H2O).

Table 3. 3. Post - treatment details for managing steel (C300) after SLM.

Samples		Solutionizing/Homogenizing heat treatment (HT)		Aging treatment (AT)		
		T(∘C)/time	solution S		Ta (∘C)	timea (min)
HT1		1020 ∘C-15min	S1		-	-
HT2		1020 ∘C-15min	S2		-	-
HT3		1020 ∘C-15min	S3		-	-
HAT1	HAT11	HT1		AT1	485	120
	HAT12	HT2			485	150
	HAT13	HT3			485	180
HAT2	HAT21	HT1		AT2	585	150
	HAT22	HT2			585	180
	HAT23	HT3			585	120
HAT3	HAT31	HT1		AT3	685	180
	HAT32	HT2			685	120
	HAT33	HT3			685	150
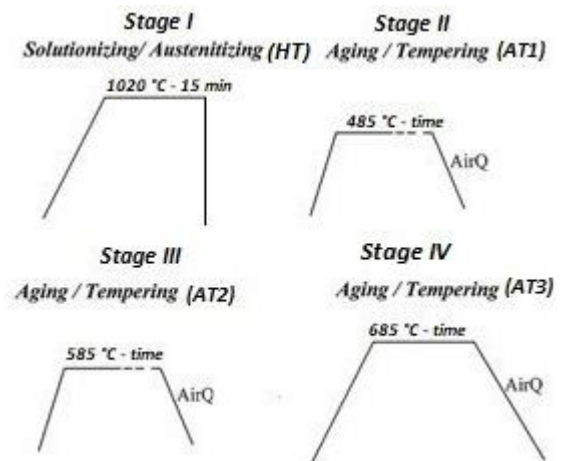
Figure 3. 3. Post - treatment cycles for MS (C300).

3.6.5   Mechanical Testing

Vickers (HV) and Rockwell C (HRC) hardness tests were performed on as-built samples, immediately after solution treatment, and after aging. A Clemex ST-2000 machine was used to perform the Vickers and Rockell C micro-hardness measurements, which were taken at an average of thirty points on the diagonal of the samples, with a 200 μm pitch. The applied load was 300 gf and the dwell time was 10 seconds. The tensile tests were carried out at room temperature using an "810 Material Test System" machine at a displacement speed of 0.01 mm/s. The loading direction was parallel to the build direction of the samples.

3.7   RESULTS ANALYSIS AND DISCUSSION

3.7.1   Metallographic examination - evolution of the microstructure of the matrix

It is known that the mechanical performance of maraging steels depends on the microstructure containing the hardening precipitate, and more specifically on the type and rate of creation (presence) of these hardening precipitates resulting from aging treatments, which has been proven by a few previous works [54-58]. Examinations of the maraging steel (C300) under confocal laser scanning microscopy (CLSM), SEM, and EBSD and for the three states (as-built (without any post-treatment), as-quenched (after HT1, HT2, and HT3), and as-aged (after HAT1, HAT2, and HAT3)) was carried out at 20 °C.

The effects of the conventional post-treatment methods applied, including homogenization solution treatments (HT1, HT2, and HT3) and aging steps from combined homogenization solution-aging treatments (HAT1, HAT2, and HAT3) were studied. Depending on the temperature range for the targeted phase transformations, Figure 3.4 displays the Fe-C diagram [59], the nickel (Ni) effect diagram [60], the phase diagram concerning the composition given in Table 3.1, showing all possible phases depending on temperature and Ni content for the steels. The vertical red line in Figure 3.4 (c) [61-62] indicates the nominal Ni content of 18 wt%. The gray rectangle was drawn to facilitate visualization of the phases of interest [61-62].
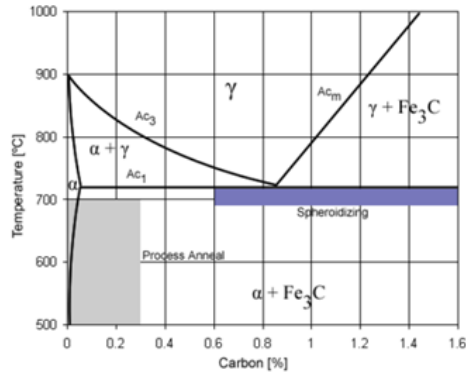
(a) Fe-C diagram for steels
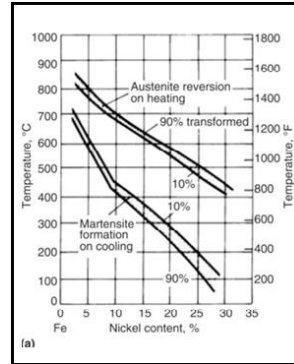
(b) Effect of additions (Ni)
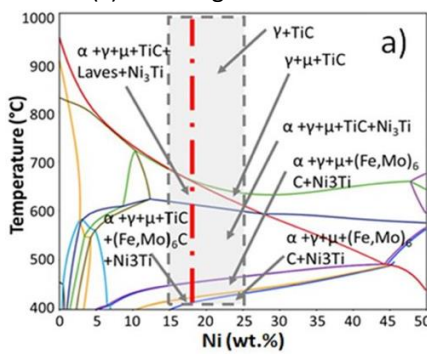
(c) Calculated equilibrium phase diagram
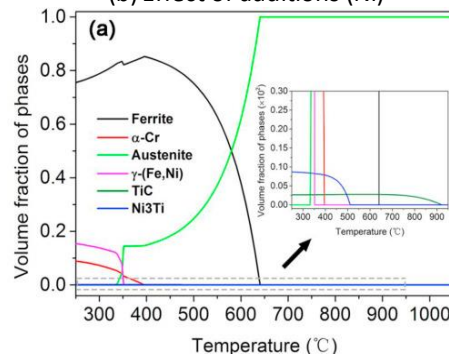
(d) Mole fraction of all equilibrium phases calculated by Thermo-Calc for the nominal Ni content as a function of temperature

Figure 3. 4. Phase diagram of nickel steels [59-62].

3.7.1.1 As-built Condition

Confocal laser scanning microscopy (CLSM) micrographs of as-built samples, shown in Figure 3.5 (a), consist of a ferritic matrix with very little austenitic traces generated by the cyclic reflow of the characteristic additive manufacturing (AM) layers. The structure of the grains is presented in a very fine cellular form. Some micro-defects (porosity) and cracks can be seen in Figure 3.5 (a). These defects are typically the result of incomplete melting of the powder and gas bubbles trapped in the melt [63-67]. Density measurement on 5 micrographs, using the image processing and analysis software, "ImageJ", on as-built maraging steel (C300) samples showed that the relative density was about 97%, which is quite similar to that of a conventional fully dense material.
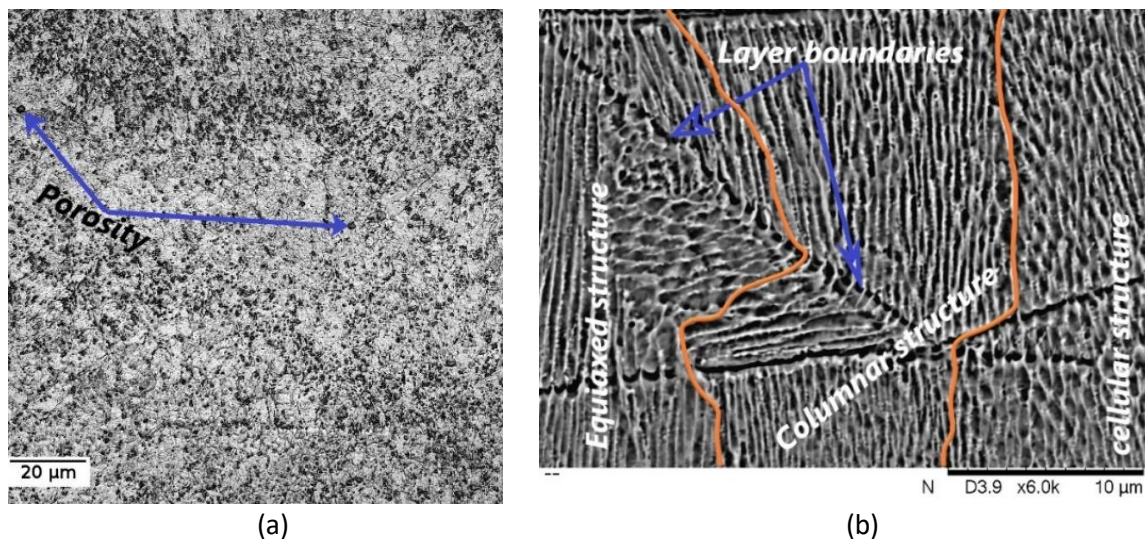
Figure 3. 5. As built specimens (a) confocal laser Micrographs (b) SEM Micrographs.

Scanning electron microscopy (SEM) micrographs of the as-built samples are shown in Figure 3.5 (b). The as-built microstructure (Figure 3.5 (b)) consists of the columnar and fine equiaxed grains. Columnar and equiaxed grains were observed at the bottom and top of the melt pool, respectively. Moreover, the cellular grains were formed between columnar grains. Similar results were reported by Allam et al. [68], Dehgahi et al. [69] and in a few other works [70-71], considering different steels. The fine equiaxed grains mainly appear as a result of the high-cooling rate during melt pool formation [68-71]. The orientation of the columnar grain almost coincides with the build direction. This phenomenon occurs because of the preferential cooling direction coincides with the build direction, as the powder surrounding the part acts as an isolation layer, and the only heat loss modes are conduction through substrate and convection/radiation from the top of the part. Moreover, it presents a relatively large amount of retained austenite and no noticeable secondary precipitation.

To understand the microstructure formation mechanism and its evolution, a microstructure analysis and a micro-texture analysis were performed using EBSD characterizations on the as-built sample.

In the SLM process, the growth of columnar grains is determined by the direction of heat flow influenced by the laser energy density [72], the direction [72] and the scanning

151

strategy [73-74]. During cell solidification, at relatively low rates, cells grow perpendicular to the liquid-solid interface regardless of the crystal orientation, but as the growth rate increases, the direction of cell growth deviates to the favorite direction of crystal growth [75-78]. So, it is important to determine the influence of laser energy density, direction, and scanning strategy on the crystallographic texture of samples fabricated by SLM to understand their anisotropic mechanical behaviour. This goal may be covered in future work.

Figure 3.6 (a-e) shows ferrite pole figures, ferrite inverse polar figures (IPF) maps relating to the Z (construction) and Y (scanning) laser directions, phase maps, grain boundaries, and a grain size distribution calculated from EBSD data of the as-built sample, which was selected for EBSD characterization (as a reference), to provide a detailed investigation and understand the SLM as-built microstructure of maraging steel (C300). Some results may be useful for predicting the possible evolution of the microstructure and micro-texture after the post-treatments done above. Phase maps (Figure 3.6 (a)) show that the microstructure contains two phases: ferrite with red color and austenite located in grain boundaries with green color, which represent the lowest percentages. Figure 3.6 (b, c) represents the grain boundaries, the grain size and the morphology. It shows fine and large grains homogeneously distributed. The colors of the grains are accepted for better contrast, and are not related to their orientation. The EBSD analysis of the as-built microstructure revealed that some fine austenite (γ) grains were distributed in a ferrite (α) matrix (Figure 3.6 (a, b)). The γ phases often appeared along the grain boundaries in the α-Fe matrix. This result strongly agrees with the results of previous studies [48, 52, 79]. A higher fraction of ferrite crystals was found in construction samples (approximately 89% ferrite crystals in the as-built samples). Notably, the fine γ grains were often located at the melt pool boundaries. This austenite phase was returned earlier than the residual (Figure 3.6 (a)). The microstructural morphologies observed in the α phase (Figure 3.6 (c)) will be easily transformed into the lath martensite structure after post-treatment. This is confirmed by EBSD characterizations in many research works [80-83], indicating that an α-Fe structure was developed in the as-built SLM maraging steels. Note that no particular crystallographic textures were observed in the α phase (Figure 3.6 c).

Figure 3.6 (b) shows phase maps with a superimposed boundary of as-built samples. The green lines represent low angle boundaries with misorientation (<5°); the red lines represent medium angle boundaries with misorientation (5°-15°) and the blue lines represent high angle grain boundaries (> 15°). For the small features, with misorientation of more than 15° inside the austenite grains, the software may detect them as grains. These maps show the random orientation of laths, indicating a complete reconstitution of the as-built microstructure during SLM. As can be seen, Figure 3.6 (b) shows that about 82% of the angles of disorientation between adjacent cells were greater than 15° (given by blue lines). They demonstrated large and fine grains in the powder particle. The percentage of angles between 5° and 10° was about 4%. Moreover, those less than 5° did not exceed 14%. This may indicate the presence of a sub-structure in the grain.

Figure 3.6 (d, e) represents the inverse pole figure IPFY and IPFZ maps of the as-built sample, respectively, according to the laser direction. IPFY results show a lack of dominance of any of the three colors (green, red, and blue) in the IPF orientation maps. This indicates that the basal (001), (101), and (111) planes of the grains are almost equivalently parallel to the directions of construction. The as-built microstructure exhibits randomly oriented crystals. The IPFZ map (in magnification of 5 µm) indicates that most grains have their basal (101) planes parallel to the laser scanning direction, but in a large view (a magnification of 100 µm) this is not immediately apparent. These crystals are realigned in a preferred orientation upon impact loading, under the effect of the temperature guard applied by the AM process. It can be confirmed by the pole figure results {100} {110} and {111} shown in Figure 3.6 (a) et 3.6 (f) that the as-built sample exhibits a crystalline structure [84-88] with two main components (Ferrite, Austenite).

We were able to investigate the microstructure of the as-built sample in greater detail using EBSD techniques. It was observed that the as-built microstructure consisted of fine grains with an average size of 3.2 ± 1.8 µm. Most of the grains were equiaxed, with a little rate of retained austenite. High resolution EBSD studies revealed the lath structure of the matrix, which was also confirmed by previous works [32, 42, 48-50, 52]. Here, EBSD was

performed to determine the crystallographic texture and the grain size distribution in the SLM samples. EBSD analysis of as-built samples can be very useful for approximately understanding and estimating the temperature effect on the maraging steel microstructure. This may be helpful in allowing us to answer a part of our problem of identifying, controlling, and predicting the influence of post-processing on the microstructure, and more particularly, on the mechanical performances. Based on those results, the present study and future work will further discuss the development of the microstructure in maraging steel during the SLM process.

In summary, with a moderately low laser power (<200 W) and a scanning strategy, the as-built SLM maraging steel (C300) sample has a cubic texture not aligned with the manufacturing direction. It is useful to study the influence of process parameters on the type and degree of the texture of SLM maraging steel (C300) samples. This is not the subject of this work but is highly recommended for future projects.

The microstructure of iron-carbon materials generally evolves with aging treatments. This development leads to changes in the microstructures of the metal matrix, such as tempering of the martensite formed as a result of the solution homogenization treatment (HT), the formation of residual austenite, the formation of strengthening precipitates, and grain widening. The type and extent of these microstructural changes vary alongside the aging treatment temperature. In this context, the as-quenched and as-aged microstructure of the samples is investigated in detail later in the present work.
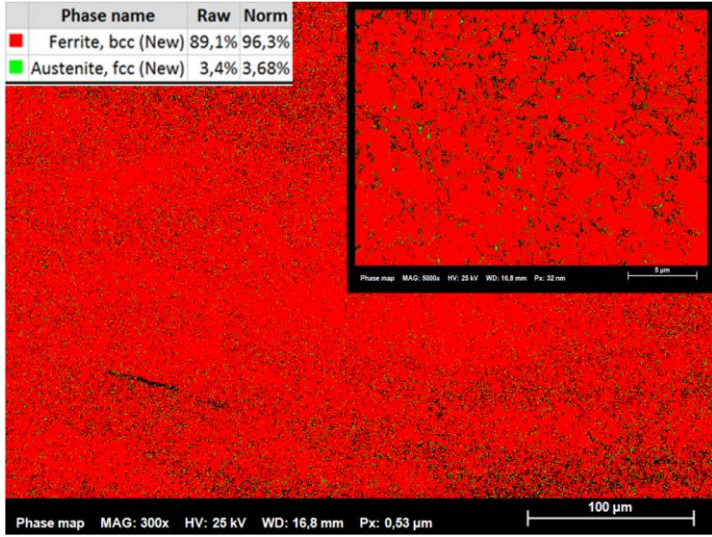
a)   Phase map
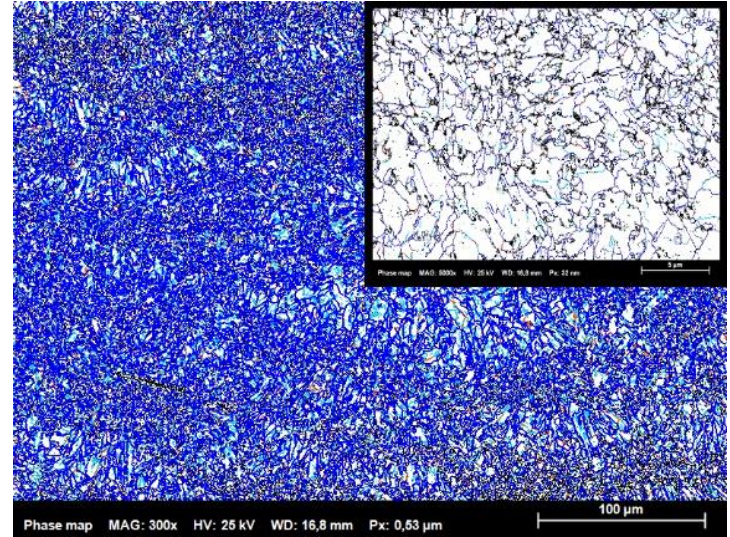
b)   Grain boundaries
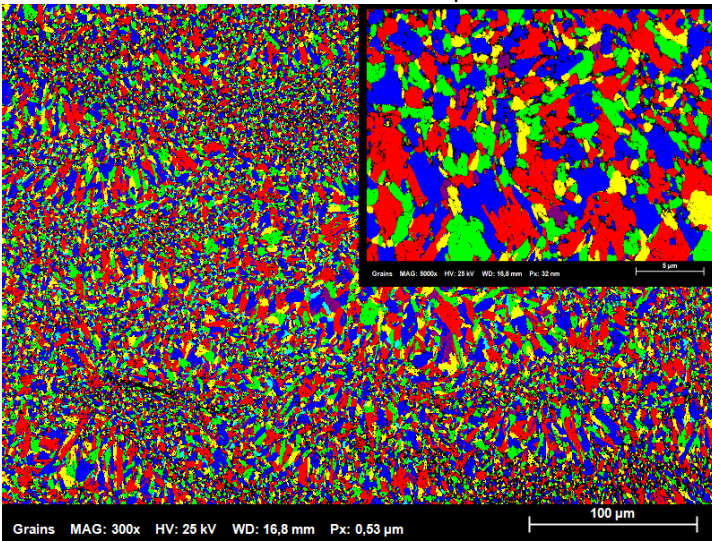
c)   Grain size distribution
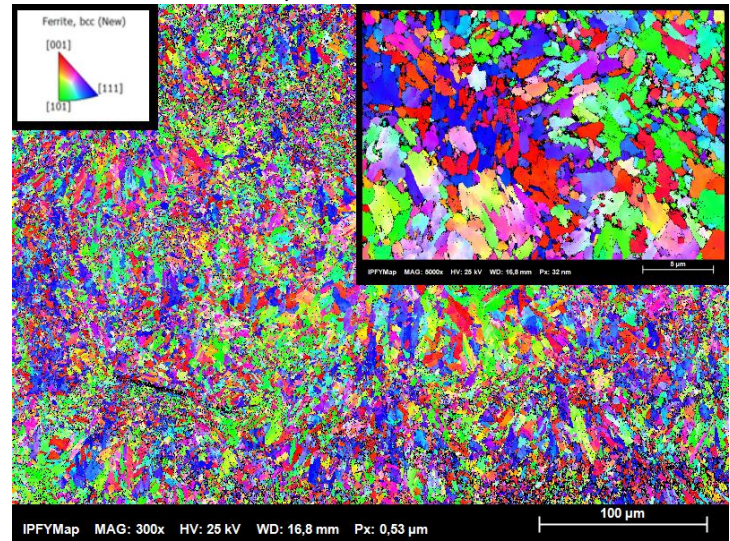
d)   Inverse pole Figure (IPF) map of Y direction which is parallel to extrusion direction
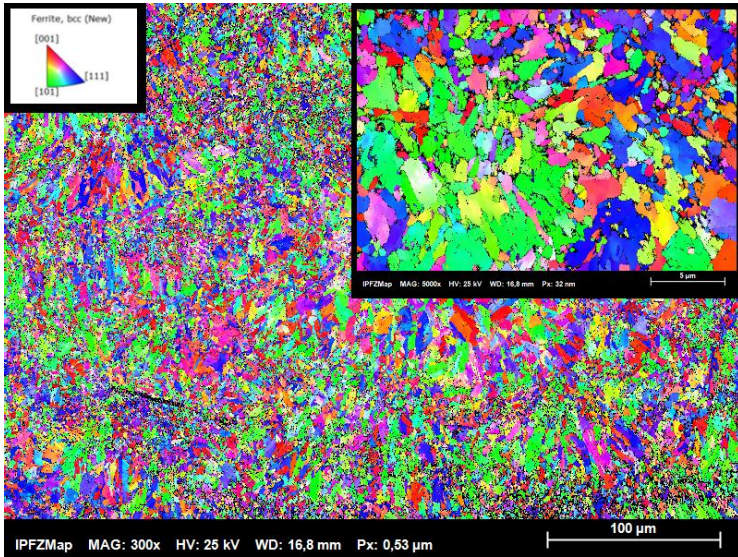
e) Inverse pole Figure (IPF) map of Z direction which is parallel to extrusion direction
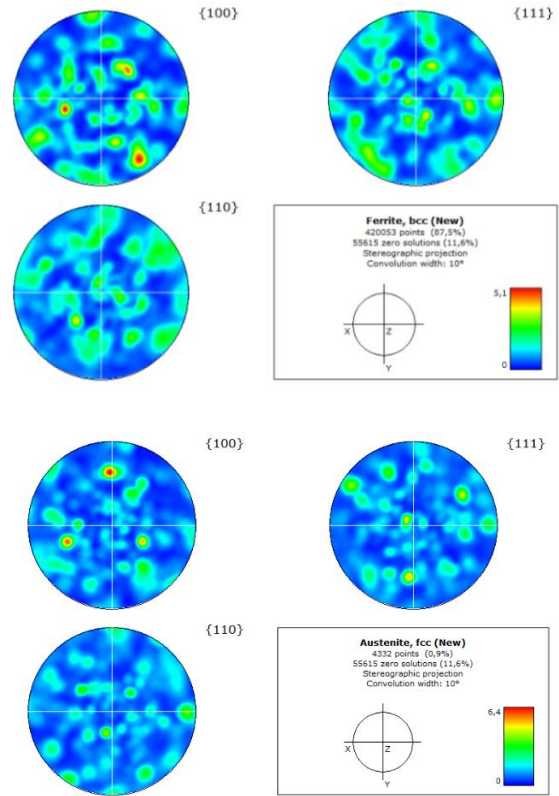
f) Pole Figure ferrite bcc and austenite fcc

Figure 3. 6. EBSD microstructure analysis.

3.7.1.2   As-quenched State - Influence of Homogenizing Treatment

The solution-treated (as-quenched parts) starting material was examined in terms of microstructure. Figures 3.7 (a, b, c) shows the microstructure after homogenization solution treatment conditions HT1, HT2, and HT3, respectively. Regardless of the cooling solution S, the microstructure observed at this zone consisted of a hardened martensite matrix. After HT, the cell structure was transformed into a large and uniformly distributed martensitic lath matrix. The high cooling rate and rapid solidification far from equilibrium conditions may lead to a homogeneous shear which can form laths in the martensitic structure. The scan

156

direction and melt morphology disappeared. Increasing the cooling solution concentration, which affects the cooling rate, made the martensitic structure clearer, bigger and easier to observe. Some bainite grains were observed at HT2 and HT3 (solution concentration respectively CNaCl = 6% = 0.06 = S2 and CNaCl = 12% = 0.12 = S3) (Figure 3.7 (b, c)). A complete transformation of the austenite occurred during heating, which led to the observation of a hardened martensitic matrix microstructure after cooling [89-91]. This transformation was likely to introduce induced macroscopic shear, which may explain the inconsistent orientation of the martensite in the cells and laths.

(a)   (b)   (c)
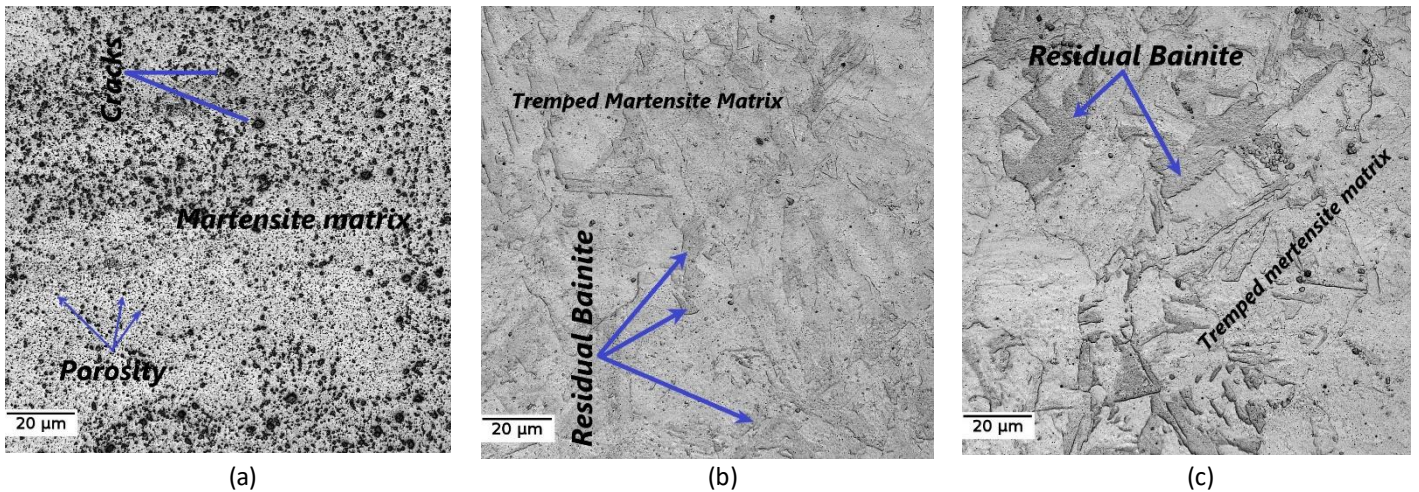
Figure 3. 7. Micrographs of (a) treated specimens (HT1) (b) treated specimens (HT2) (c) treated specimens (HT3).

The homogenized samples with HT2 and HT3 were selected for a further investigation of the microstructure. Scanning electron microscopy (SEM) micrographs of HT2 and HT3 post-treatment conditions are shown in Figure 3.8 (a-b). Figure 3.4 (a-d) will be useful for identifying the phase transformations and microstructure elements as a result of the applied post-treatment (for as-quenched state, but especially for the as-aged state). For a nominal nickel (Ni) content of $\simeq$ 18 wt%, complete austenitization takes place at about 680 °C, as shown in the phase diagram of nickel steels [62] depicted in Figure 3.4 (b-d). For maraging steels, even moderate quenching cycles can easily trigger a martensitic transformation [92], whereas a decrease in temperature requires an increase of holding time to ensure a complete

and stable martensitic transformation. From Figure 3.4 (c), homogenization solution treatment temperatures in the 800-1000 °C range should be sufficient to produce a fully austenitic matrix with the presence of some TIC precipitates. In the present work, all samples were homogenized using a homogenization solution treatment at 1020 °C for 15 min and cooled in different solutions (HT1, HT2, and HT3), which was higher than 680 °C. During cooling, the austenite obtained due to homogenization solution treatment transformed to a martensitic matrix structure. The extended quenching time of 15 min and solution concentration favors rapid cooling, and hence, martensitic transformation. Overall, the homogenization treatment (HT1, HT2, or HT3), promoted a reduction of the cellular and dendritic matrices.

After the different homogenization treatments (HT), the boundaries and cells gradually disappeared with the increase of temperature and holding time, as illustrated in Figure 3.8 (a-b). At high temperature (HT) (HT: 1020 °C - 15 min), the microstructure manifests largely intertwined laths, represented by orange (tempered martensite) and yellow arrows (bainite) in Figure 3.8 (a-b). This is because the high temperature during HT causes the austenite grain to grow, which leads to larger martensite laths after quenching. They are generally aligned parallel to each other with the same habit plane, and form groups called packets. Each packet is further subdivided into blocks (a group of laths with the same orientation) [93-97], and a packet contains a high density of tangled dislocations, which increases the material hardness [94]. The martensite morphologies change with the carbon content. Finer lath martensite forms where the carbon content is low (up to 0.8%); however, with a high carbon content, lenticular martensite also forms in addition to lath martensite [93, 95-97]. Furthermore, based on the results in Figure 3.8 (a-b), little or no residual austenite can be observed in the as-quenched samples (HT1, HT2, and HT3).

158
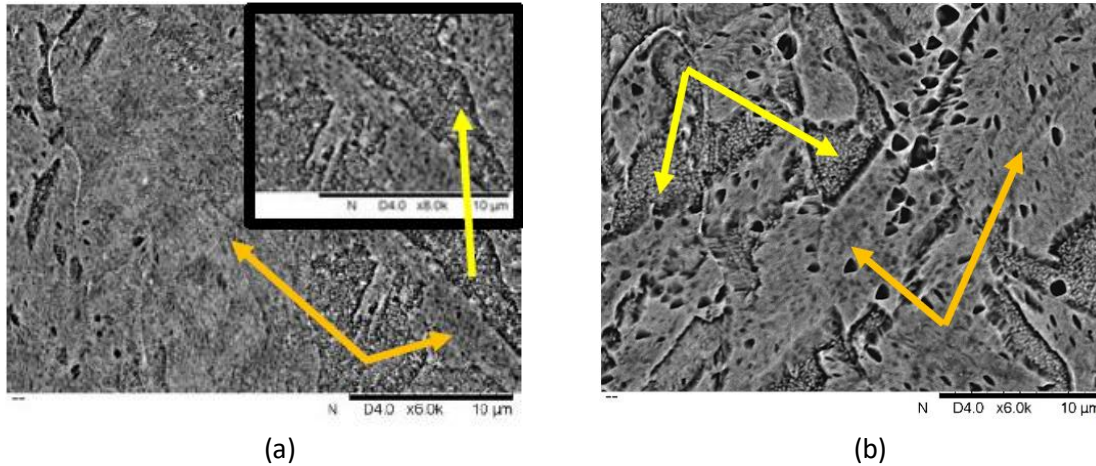
Figure 3. 8. Micrographs of (a) Specimens HT2 (b) Specimens HT3.

3.7.1.3   As-aged state - Influence of aging temperature and time

Aging at 485 °C

The 485 °C aging temperature is within the range of the main aging temperatures for several industrial applications, thanks to the good mechanical performance obtained when it is used for wrought materials [98-99]. Figure 3.9 (a, d, g) represents the microstructure of maraging steel C300 after aging at 485 °C during S1-120 (S1: cooling solutions for homogenization solution treatment (HT1), 120: aging time in min), S2-150, and S3-180 min, respectively. The microstructure has maintained the martensitic matrix. Densely distributed and extremely fine needle-like laths and precipitations appeared. With the increase in the cooling solution concentration due to HT and aging time, they grew unevenly in the martensite lath matrix. The formation of a large number of these precipitates led to an increase in hardness at an increased rate varying between 20% and 50%—according to the aging time—as compared to the as-built sample (See Tables 3.5 and 3.6). Considering the limitations of the resolution of the laser scanning confocal microscope, these precipitates are not easily identified. However, based on the literature [41, 52-53, 59-61] and the increase in hardness observed in our experimental work, at 485 °C, most of these precipitations can be attributed to the Ni3Ti precipitate. At this aging temperature, no residual austenite was observed, but bainite grains appeared at a cooling time of 180 min (Figure 3.9 (g)).

.

Aging at 585 °C

Figure 3.9 (b, e, h) shows the microstructure after aging at 585 °C at S1-150, S2-180, and S3-120 min, respectively. At this aging temperature, the strengthening of the samples' microstructure was faster. For the same aging time, the appearance rate of the laths was greater, and the laths and the precipitation had a coarser appearance than at 485 °C. Increasing the temperature from 485° C to 585° C caused a 12% decrease in the hardness, from an average of 51 HRC (485° C) to an average of 45 HRC (585° C). These results were confirmed by previous works [100-105]. Cabeza et al. [100] noted a loss in hardness at temperatures equivalent to 585° C in their study of maraging steel (C250). They reported that the hardness goes from 500 HV (at 500° C) to 420 HV (at 585° C). Similar results were reported by Li et al. [101] and Maloletnev et al. [102]. Increasing the aging time also has a negative effect on the hardness, and thus on the microstructure. As the aging time increased, inverted austenite began to form. This resulted in a gradual decrease in hardness, with a decrease rate that could go up to 28%, from ~52 HRC to ~37 HRC, between the HAT23 (HT3: S3+1020 °C+15 min, AT2: 585 °C) with an aging time of 120 min and HAT21 (HT1: S1+1020 °C+15 min, AT2: 585 °C) with an aging time of 150 min (Tables 3.3 and 3.6).

Aging at 685 °C

Figure 3.9 (c, f, i) depicts the microstructure after aging at 685 °C at S1-180, S2-120, and S3-150 min, respectively. At this elevated aging temperature, the microstructure of maraging steel (C300) showed a higher tendency to form austenite. Also, some perlite grain was observed (Figure 3.9 (c)). The influence of aging temperature on the microstructure and on hardness properties was investigated systematically. Increasing from 585 °C to 685 °C, the aging temperature had the opposite influence on strength and hardenability. A 19% decrease in hardness, from an average of ~45 HRC (585°C) to an average of ~38 HRC (685°C), was observed. With increasing aging time at a constant temperature of 585 °C, inverted austenite was formed in large amounts, not only inside the laths, but also along the

grain boundaries. This implies a 17% decrease in hardness to 35 HRC (HAT31 samples) from about 41 HRC (HAT33 samples).

For a better understanding of the microstructures of as-aged SLM samples after homogenization solution-aging treatment HAT, SEM analysis was carried out, and is discussed below.

(a) HAT11 (S1 - 485°C - 120min)

(b) HAT21 (S1 - 585°C - 150 min)

(c) HAT31 (S1 - 685°C - 180 min)
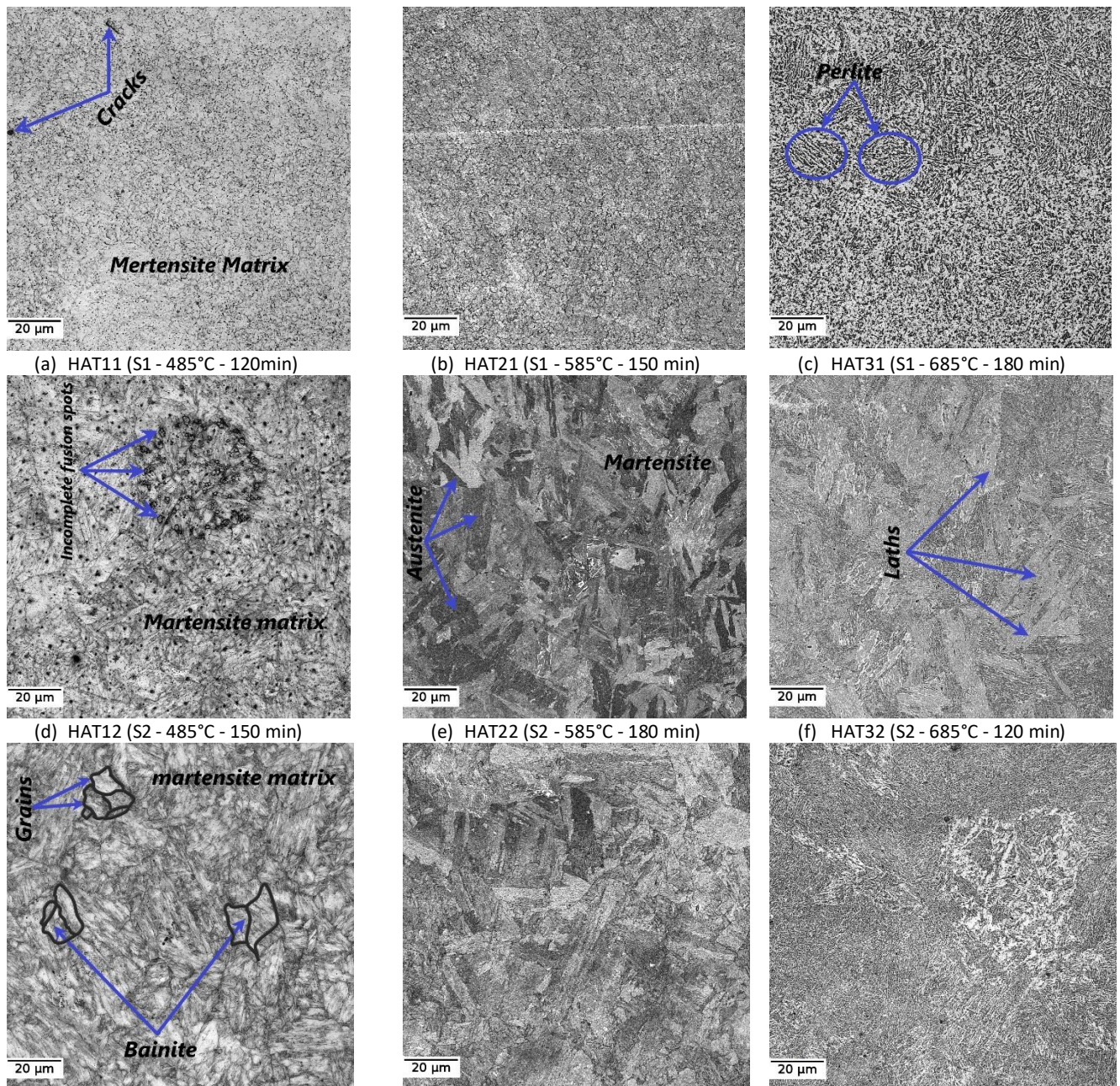
(d) HAT12 (S2 - 485°C - 150 min)

(e) HAT22 (S2 - 585°C - 180 min)

(f) HAT32 (S2 - 685°C - 120 min)

Figure 3. 9. Micrographs of as-aged specimens (a) HAT11 (b) HAT21 (c) HAT31 (d) HAT12 (e) HAT22 (f) HAT32 (g) HAT13 (h) HAT23 (i) HAT33.

Scanning electron microscopy (SEM) micrographs of the as-aged samples with different homogenization solution-aging treatment conditions (HAT1, HAT2, and HAT3) are shown in Figure 3.10 (a-c). Figure 3.4 (a-d) will be useful for identifying the phase transformations and microstructure elements resulting from the applied post-treatment. According to the calculated equilibrium phase diagram in Figure 3.4 (c), above 680 °C, only TiC precipitates remain, while the dissolution of other commonly reported secondary phases, such as µ, Ni_3Ti, and M_6C, is expected. This was already confirmed by Conde et al. [50] in SLM maraging steel C300. For maraging steels, even moderate quenching cycles can easily trigger a martensitic transformation [92], whereas a decrease in temperature requires an increase of holding time to ensure a complete and stable martensitic transformation. Overall, the thermal routes applied by homogenization solution-aging treatment HAT1 to HAT3, as shown in Figure 3.10 (a-c), promoted a reduction of the cellular and dendritic matrices.

Figure 3.10 (a-c) presents the microstructure of HAT samples, selected using well-defined criteria (samples representing all temperatures and aging times used, high and less hardness), at different homogenization solution treatment stages (HT) and aging temperatures. It was reported that the formation of a lath-like structure is favored when a small number of cycles are applied and when low aging temperatures are used [103-106], and conversely, that a large number of cycles or high-quenching temperature results in the formation of higher volume fractions of austenite with spherical and blocky morphologies, but with high thermal instability [106-107]. The microstructure observed in Figure 3.10 (a-c) followed this tendency, as the aging temperatures between 485 and 585 °C resulted in the appearance of mainly globular morphologies with few laths. The presence of spherical austenite traces can be observed (Figure 3.10 (b-c)). As mentioned before, after homogenization solution treatment (HT1, HT2, and HT3), little or no additional austenite was observed, as shown in Figure 3.8 (a-b). The homogenization solution-aging treatment (HAT) showed different austenite contents. Based on the results in Figure 3.7 (b-c), it can be

posited that the austenite present in the HAT1 to HAT3 conditions is most likely reverted instead of retained austenite. Given the similarity in post-treatment routes, this increment can be associated with the increase in aging time, from 120 to 180 min. Austenite reverted by aging was also observed in previous research [95, 108-111]. Reverted austenite is beneficial for maraging steels as it increases their ductility, and indeed allows the transformation-prompted plasticity effect (TRIP) [96].

When the temperature rises to 585 °C, for a holding time of 180 min, the martensitic laths become a bit blurred. Therefore, many irregular light bars are embedded in the dark matrix shown in Figure 3.10 (b). The aging cycling temperature at 685 °C resulted in microstructures composed mainly of typically quenched martensite interfaces in the form of quenched laths, as shown in Figure 3.10 (c). The high homogenization temperature (1020 °C) also presented a significant effect on HT1, HT2, and HT3, which may result in a zero or low austenite content. The latter may be related to the absence of an aging treatment. In addition to the structured and solubilized conditions, all homogenization solution-aging treatment routes, from HAT1 to HAT3, yielded secondary precipitates. The exact identification of these precipitates is beyond the scope of this work.

Nevertheless, according to the equilibrium calculations in Figure 3.4 (c), the strong precipitation of μ and Ni3Ti is expected for aging steps below 680 °C.

(a) HAT13 (S3 - 485 °C- 180 min)   (b) HAT22 (S2 - 585 °C- 180 min)   (c) HAT31 (S1 - 685 °C- 180 min)
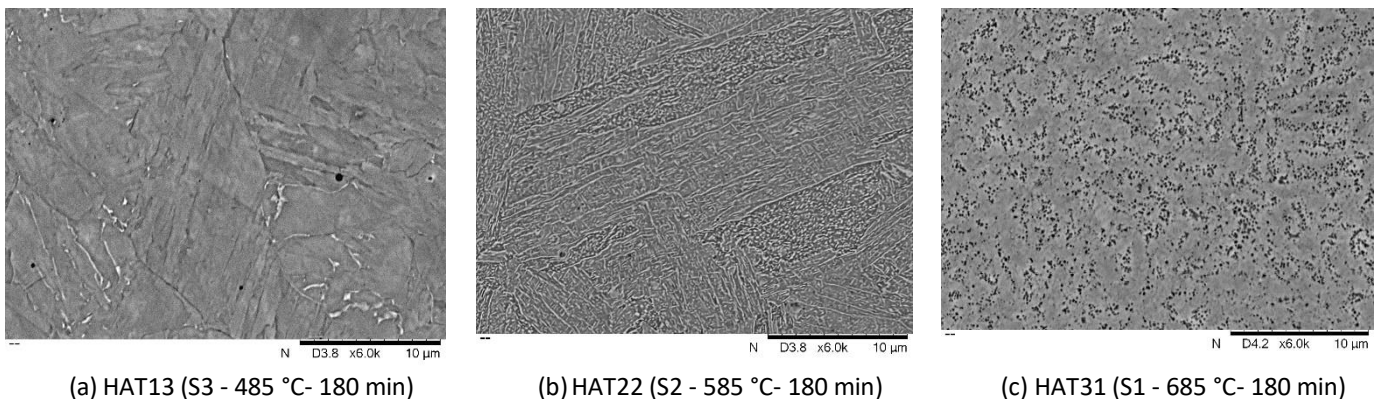
Figure 3. 10. Micrographs of (a) Specimens HAT13 (b) Specimens HAT22 (c) Specimens HAT31.

At the end of this microstructure characterization in as-built, as-quenched, and as-aged states, we can clearly observe that the microstructure changes are significantly affected by temperature and holding time. The as-built samples (Figures 3.5 and 3.6) show a cell and lath structure with a white edge. This is because, rapid quenching at high cooling rates gives the microstructure the ability to produce small grains. According to EDS analysis, the white boundary is composed of Fe, Ni, Co, Mo, Ti, and Al, and the Ni, Co, and Ti contents are much higher outside the dark zone, as shown in Figure 3.11 and Table 3. 4. This is mainly due to the lower solubility of Ni, Co, and Ti in the solid than in the liquid phase. During rapid cooling, they are forced to move to the liquid zone when grain formation is initiated. As neighboring grains meet, Ni-, Co-, and Ti-rich regions are formed in the boundary.

The high temperature (1020 °C) used during HT is able to gain enough energy for the addition's elements, including Ni, Co, Mo, and Ti to allow them to be diffused into the interior of the grains. As a result, the white boundaries and lines begin to break up and dissolve. This can be seen in samples homogenized by HT2 (Figure 3.8 (a)) and HT3 (Figure 3.8 (b)) before aging. According to EDS analysis, the light boundaries (Zone B) between cells (Zone S), presented in Figure 3.11 and proved by Table 3. 4, show higher Ni, Co, and Ti contents. In addition, for the samples aged by HAT1 to HAT3 presented in Figure 3.10 (a-c), it should be noted that the discontinuous boundaries are only the precipitated intermetallic phases, including Ni3Ti, Ni3Mo, and Ni3Al [112-114]. It is worth pointing out that it is difficult to identify Fe 2 Mo and Ni 3 (Ti, Mo) intermetallic compounds in the microstructure of as-built, as-quenched (different HT), and as-aged (different HAT) samples. The main reason is that the precipitate size is extremely small, the phase content is too low, and the distribution is highly dispersed [115-116]. Besides, the high magnification SEM micrographs reported in Figures 5 to 10 shows a significant difference between HAT1 and HAT3. The optical micrographs were also useful in providing clarifications about the microstructure and allowed to follow up the overall type and size of martensite according to the applied post-treatment.

However, more research is still needed to explore and understand the strengthening mechanism of HAT samples. Future work will focus on the texture, precipitation behaviour and reverse nucleation of austenite using transmission electron microscopy (TEM) and electron (backscatter) diffraction (EBSD).

Table 3. 4. EDS analyses: Chemical composition between Zone B and Zone S.

EDS	Fe	Ni	Co	Mo	TI	Cr	C
Zone B	65.38	18.09	9.65	4.98	0.73	0.25	0.93
Zone S	66.21	17.61	8.55	5.27	1.19	0.00	1.17

(a)   (b)
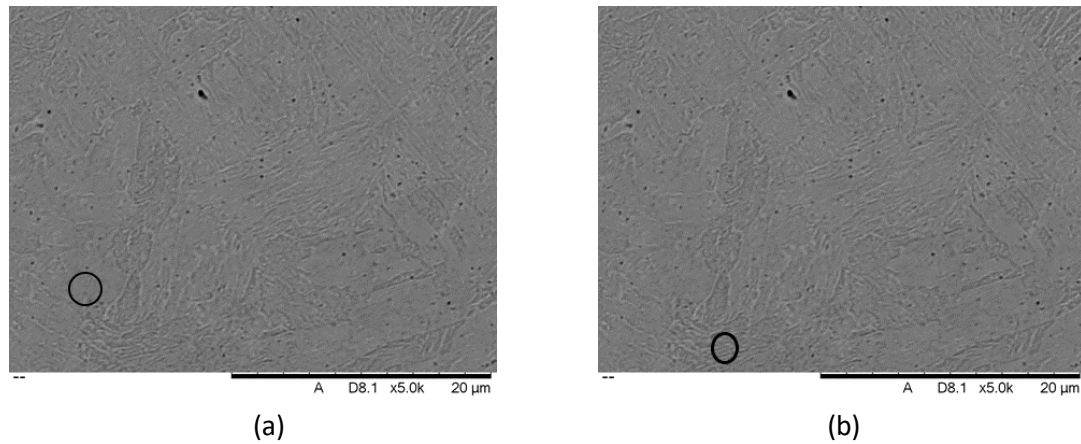
Figure 3. 11. Microstructure EDS analyze (a) Zone S (sombre) (b) Zone B (blanche).

3.8   HARDNESS BEHAVIOR – ANOVA ANALYSIS

Hardness profiles were measured along the diagonals of the samples' cross-sections. An investigation of the micro-hardness of the as-built, as-quenched (HT) and as-aged (HAT) samples were conducted. The average values of the results are shown in Tables (3.5) and (3.6).

165

3.8.1 As-built Samples - Solution Treated

Hardness measurements taken on as-built samples, and showed an average micro-hardness of about 37 HRC (365 VH). This correlates with the literature, on the one hand, and with the data sheet provided by EOS [117] for maraging steels, on the other hand.

Table 3. 5. Hardness of as-built and homogenized specimens.

Measured HRC Hardness HRC (HV)			
As built specimens	HT1 specimens	HT2 specimens	HT3 specimens
37 (365)	38 (367)	32 (320)	30.5 (307)

The hardness decreased after the homogenization solution treatments (HT1 to HT3) due to the cooling rate being increased by increasing the concentration of the cooling solution from HT1 to HT3. The hardness values listed in Table 3.5 show that the hardness of the samples cooled in solution S1 (water: C = 0%) was not significantly affected and remained practically at 37 HRC (365 HV) - 38 HRC (367 HV). The most significant decrease was found for the samples cooled in solution S2 (CNaCl = 6%). Hardness tests performed on these samples yielded an average of about 32 HRC (320 HV). The hardness measurements of the samples cooled in solution S3 (CNaCl = 12%) continued to decrease slightly towards 30.5 HRC (307 HV). This decrease in micro-hardness of the samples at different cooling rates, after the homogenization solution treatment, is explained by the fact that the maraging steel (C300) obtained its maraging state by aging treatment after quenching. This is because at this stage (just after quenching), the hardening precipitates are not yet formed. It can also be attributed to grain enlargement, as well as to the release of residual stresses after homogenization solution treatment. This is consistent with the literature regarding the poor hardenability of maraging steels. The above results indicate that homogenization solution treatment (HT) could reduce the micro-hardness of maraging steel fabricated by SLM by up to 17.6%, in the case of HT3 (cooling solution: S3).

3.8.2   Aged Samples

The hardness values taken from the as-aged samples (HAT) are listed in a Taguchi L9 orthogonal table consisting of 9 sets of post-treatment conditions. Experimental results, as well as predictive results given by an ANOVA study, are discussed afterward (Table 3.6).

Regardless of the cooling solution concentration (S1=0%=0, S2=6%=0.06 and S3=12%=0.12) during homogenization solution treatment (HT), the hardness increases in the as-built SLM maraging Steel (C300) samples aged at 485 °C in proportion to the aging time (timea). These results will be analyzed in detail in the next section, using the ANOVA method to develop a prediction model that describes the observed changes in hardness with the aging treatment parameters.

Table 3. 6. Taguchi L9-post-treatment conditions and the experimental results.

Taguchi's orthogonal array L9			Measured	Predictive
Solution S(%)/ concentration	Ta (°C)	timea (min)	HRC Hardness	HRC Hardness
S1	485	120	45.21	45.41
S1	585	150	37.32	37.15
S1	685	180	35.00	34.85
S2	485	150	54.46	54.32
S2	585	180	48.96	49.30
S2	685	120	41.04	40.72
S3	485	180	56.18	55.84
S3	585	120	52.68	52.70
S3	685	150	38.80	39.00

The results of the ANOVA analysis of hardness are reported in Figure 3.12. At a critical significance level of 0.05, the considered post-treatment parameters (cooling solution concentration (S1=0%=0, S2=6%=0.06, or S3=12%=0.12), aging temperature "Ta" (485 °C, 585 °C, or 685 °C), and aging time "timea" (120 min, 150 min, or 180 min)) and their interactions are statistically analyzed in terms of their significance for hardness. The results of the experiments performed on the parts - made according to a Taguchi L9 experiment table (Table 3.6) - were analyzed by Minitab 16 software. Figure 3.12 (a-b) shows the ANOVA results and the main effect factor graph, which shows that factors (post-treatment parameters) were statistically significant for hardness. The aging temperature (Ta) and the cooling

solution concentration (S) used during HT were the most significant factors influencing hardness (Figure 3.12 (a-b)), and aging time (timea) was the least significant factor for hardness. It is worth noting that the studied factors and their effects explain over 99% of the variations seen in responses, as evidenced by the correlation coefficients (R2 adj) from the ANOVA. The error of the ANOVA model is shown in the Error row of the table in Figure 3.12 (a). Based on Figure 3.12 (a) and the main effects plot shown in Figure 3.12 (b), it can be concluded that the order of the contribution of the processing parameters for hardness is mainly aging temperature (Ta) then cooling solutions (S) related to HT and then some interactions between them. The predictive hardness (HRC), presented in the last column of Table 3.6 was calculated by the prediction model derived from the ANOVA model and presented by the following regression equation:

$$HRC = 145.15 + 442.0 \text{ x } S - 0.08194 \text{ x } Ta - 0.898 \text{ x } timea - 1098.6 \text{ x } S \text{ x } S + 0.003317 \text{ x } timea \text{ x } timea - 1.510 \text{ x } S \text{ x } timea \tag{3.1}$$

This allowed us to plot the correlation curve between the predictive hardness and the experimentally measured hardness. The scatterplot always stays around an almost linear line as shown in Figure 3.13. This can be used as a validation of the model. In Figure 3.12 (a), the contribution of each post-treatment parameter to the hardness evolution is shown. The contour plot of the Response Surface Method (RSM), where many input variables—used by the Taguchi-ANOVA study—influence the hardness values of maraging steel (C300), is shown in Figure 3.12 (c, d, e). They present the Contour plot displaying the hardness using different combinations of post-treatment factors. This may allow some estimation of mechanical performance at similar or close conditions, which may make it easier for future investigations to predict the adequate treatment for the expected mechanical performance. The analysis of the obtained results indicated that the HRC hardness value of maraging steel (C300) was mainly influenced by the variation of aging temperature "Ta" (HAT) and cooling solution concentration/type "S" related to the homogenization solution treatment (HT). From

the hardness test results, proved by the ANOVA analysis, the highest hardness values were obtained at an aging temperature (Ta) of 485 ℃.

Source	DDL	Sum of Squares	Contribution	Adj SS	Adj MS	Value	P_Value
S	1	151.303	30.27%	57.814	57.814	245.96	0.004
Ta	1	280.303	56.08%	251.781	251.781	1071.17	0.001
timea	1	0.244	0.05%	14.342	14.342	61.02	0.016
S*S	1	31.284	6.26%	31.284	31.284	133.09	0.007
timea *timea	1	17.820	3.56%	17.820	17.820	75.81	0.013
S*timea	1	18.469	3.69%	18.469	18.469	78.57	0.012
Error	2	0.470	0.09%	0.470	0.235		
Total	8	499.894	100.00%				

Model summary	S	R^2	R^2 (adjust)	R^2 (prev)
	0.48	99.91 %	99.62 %	97.68 %

(a) Contribution of parameters for hardness

(b) The graph of the main effects for hardness

(c) Effects of S concentration and aging temperature Ta on hardness: contour plot

(d) Effects of aging temperature Ta and aging time timea on hardness: contour plot

(e) Effects of S concentration and aging time timea on hardness: contour plot
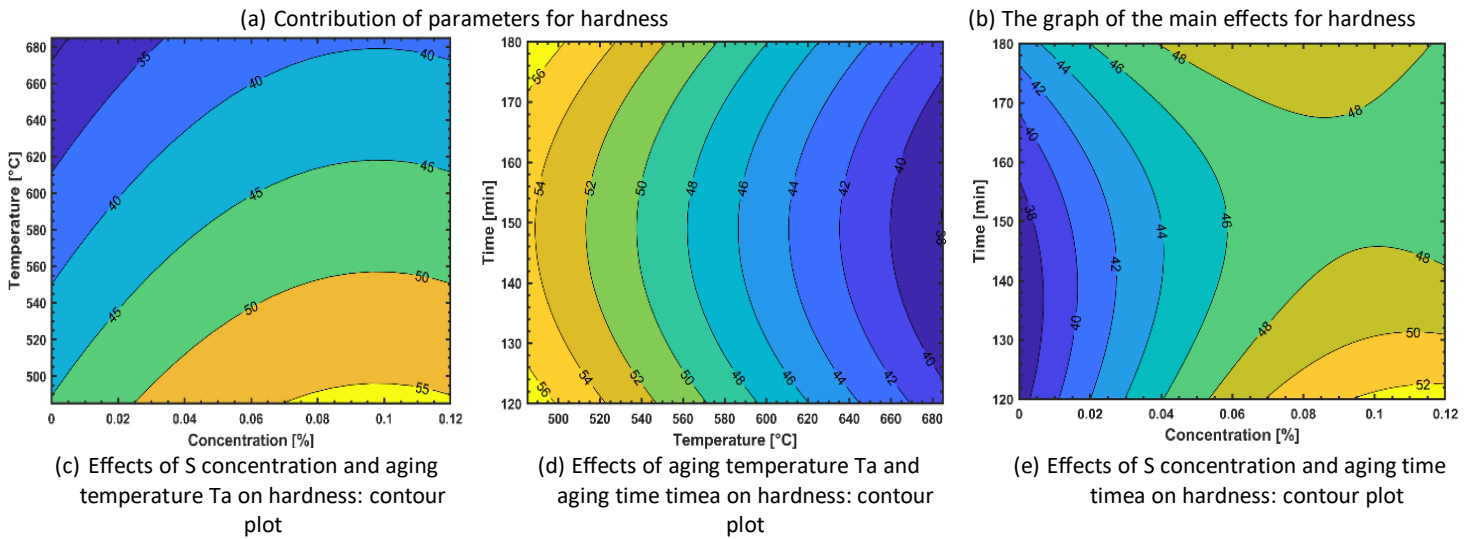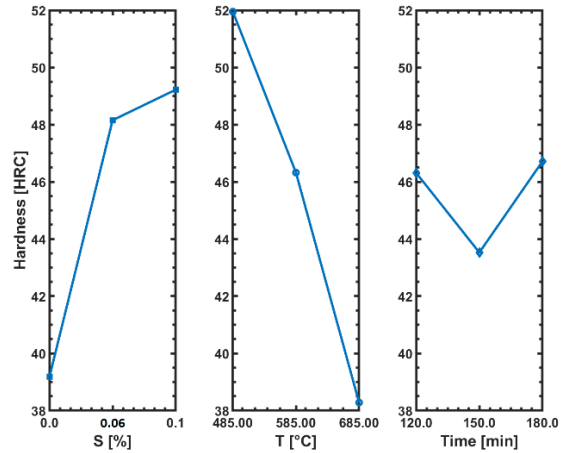
Figure 3. 12. Results of analysis of variance "ANOVA".

In addition, at 485 °C, the measured hardness, shown in Table 3. 6, is respectively around 45 HRC for an aging time of 120min, 54 HRC for an aging time of 150 min, and 56 HRC for an aging time of 180 min. Therefore, it is clear that a HAT treatment at 485 ℃ increases the hardness with a rate varying between 20% and 50%, according to the cooling solution concentration and the aging time, versus the as-built sample (37 HRC, Table 3. 5). This can be attributed to the formation of a large number of hardening precipitates, which is also the conclusion drawn in the literature [59-61].

Increasing the temperature of 485 ℃ (HAT1) to 585 ℃ (HAT2) caused a 12% decrease in the hardness, from an average of 51 HRC (485 ℃) to an average of 45 HRC (585 ℃), which was also confirmed by previous works [100-105]. in their study of maraging steel (C250), Cabeza et al. [100] noted a loss in hardness at temperatures equal to 585 ℃. They reported that the hardness goes from 500 HV (at 500 ℃) to 420 HV (at 585 ℃). Similar results were reported by Li et al. [101] and Maloletnev et al. [102]. Increasing the aging time also has a negative effect on the hardness, and thus on the microstructure. This results in a gradual decrease in hardness, with a decrease rate that can go up to 28% between the HAT23 (585 ℃ - 120 min), HAT22 (585 ℃-180), and HAT22 (585 ℃-180) treated samples.

Increasing the aging temperature (Ta) to or above 685 ℃ contributed significantly to the shrinkage of the maraging steel (C300). An opposite effect on the strength and hardness can be observed. A 19% decrease in the hardness values, from 45 HRC (585 ℃) to 38 HRC (685 ℃), was observed. This temperature has not previously been in the literature.
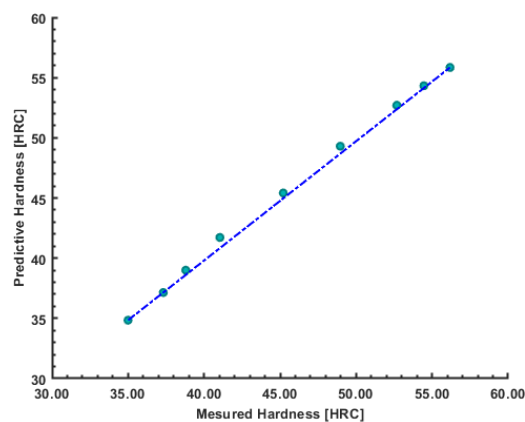
Figure 3. 13. Correlation curve - measured and predictive hardness.

The results obtained show that the use of the response surface methodology (RSM) as well as the experimental design allow to correctly and accurately determine and optimize the influence of the three chosen parameters (S, Ta, and timea) on post-processing effectiveness. The optimum values of these three parameters give a maximum efficiency of 99.91%. The reliability of the second-order model based on multiple regression was tested through an ANOVA analysis. The results showed that the explored models are highly significant and in

170

agreement with the experimental results. The efficiency and performance of a combined HAT-post-treatment are positively correlated with the cooling solution concentration related to HT (Figure 3.12 (b)), which is in agreement with the literature [118-119]. This influence has been widely studied in conventional post-treatment materials [120-121]. It has been observed that after the aging step, an increase in pollutant concentration leads to precipitation hardening of the microstructure, and consequently, to an increase in terms of hardness. Aging temperature has a negative relationship with the final hardness of the part, and this can be explained by the increase in residual or reverse austenite as the temperature rises [122]. The RSM contours clearly confirm the ANOVA results.

The homogenization solution-aging treatment conditions were chosen, using RSM Graphs, in the dark green range in Figure 3.12 (c-e). The optimal combination of the considered homogenization solution-aging treatment parameters for hardness consists of the cooling solution S3 (it is an aqueous NaCl solution with a concentration CNaCl=12%=0.12), an aging temperature (Ta) at level 1 (485 °C), and aging (timea) at level 3 (180 min).

Subsequently, only the optimal aging parameters were considered for validation with a tensile test. To achieve the expected performance, it is necessary to ensure that the aging treatment is optimal. That is why a little security merge was used, and the optimal aging parameters were considered at an aging temperature (Ta) of 480 °C, and aging time (timea) of 175 min.

3.9 MECHANICAL BEHAVIOR

Figure 3.14 shows the engineering stress/strain resulting from tensile testing of as-built maraging steel (C300) specimens homogenized at 1020 °C for 15 min, cooled in S = S1, S2 or S3 solutions, and aged at 480 °C for 175 min. The as-built conditions revealed relatively moderate mechanical strengths and high ductility as compared to the aged specimens. They had a tensile yield strength (Ys) of about 1020 MPa, a tensile yield strength at 0.2% of strain (Ys0.2%) of about 1285 MPa, and an ultimate tensile strength (UTS) of about 1385 MPa, as well as an elongation of about 12%. In the as-built state, a fracture occurred in the middle of

the tensile coupon gauge. This is in good agreement with the dictates of the maraging steel (C300) data sheet provided by EOS.

Post-treatments involving homogenization steps followed by aging steps thus increase the tensile strength by destroying the ductility of the steels [123]. The stress-strain curves in Figure 3.14 followed this tendency. It is remarkable that thermal aging at 480 °C improves the tensile strength and decreases the elongation of the additively manufactured maraging steel (C300) material. The rate of variation between these two mechanical performances depends on the cooling solution after solution treatment from S1 to S3.

The HT1 solution-treated coupons (S1, 1020 °C, 15 min) followed by ATop aging (480 °C, 175 min) exhibited a 23% gain in tensile strength as compared to the as-built coupons. This post-treatment (HT1+ATop) gave the material a tensile yield strength (Ys) of about 1110 MPa, a tensile yield strength at 0.2% of strain (Ys0.2%) of about 1350 MPa, and an ultimate tensile strength (UTS) of about 1705 MPa, and the elongation decreased to about 9%. Similar results were reported by Song et al. [124] using a solution treatment at 820 °C for 1 hour and an aging treatment at 500 °C for 6 hours. The HT2 solution-treated (S2, 1020 °C, 15 min) and ATop-aged (480 °C, 175 min) coupons exhibited a gain of about 50% in tensile strength as compared to the as-built coupons. This post-treatment (HT2+ATop) gave the material a tensile yield strength (Ys) of about 990 MPa, a tensile yield strength at 0.2% of strain (Ys0.2%) of about 1310 MPa, and an ultimate tensile strength (UTS) of about 2105 MPa, while the elongation decreased to about 5%. Similar results were reported by Kučerová et al. [125], using an annulling treatment at 840 °C for 2 hours and an aging treatment at 490 °C for 6 hours. The highest tensile strength and lowest ductility were obtained for HT3 solution-treated (S3, 1020 °C, 15 min) and ATop aged (480 °C, 175 min) samples. They showed a gain of about 55% in terms of mechanical tensile strength as compared to the as-built coupons. This post-treatment (HT3+ATop) gave the material a tensile yield strength (Ys) of about 1055 MPa, a tensile yield strength at 0.2% of strain (Ys0.2%) of about 1355 MPa, and an ultimate tensile strength (UTS) of about 2145 MPa, and the elongation decreased to approximately 4%. Similar results were reported by Shamsdini et al. [126],

using an aging treatment at 490 °C for 6 hours. It is inferred that the gain in UTS at this aging temperature is accompanied by a decrease in uniform elongation.
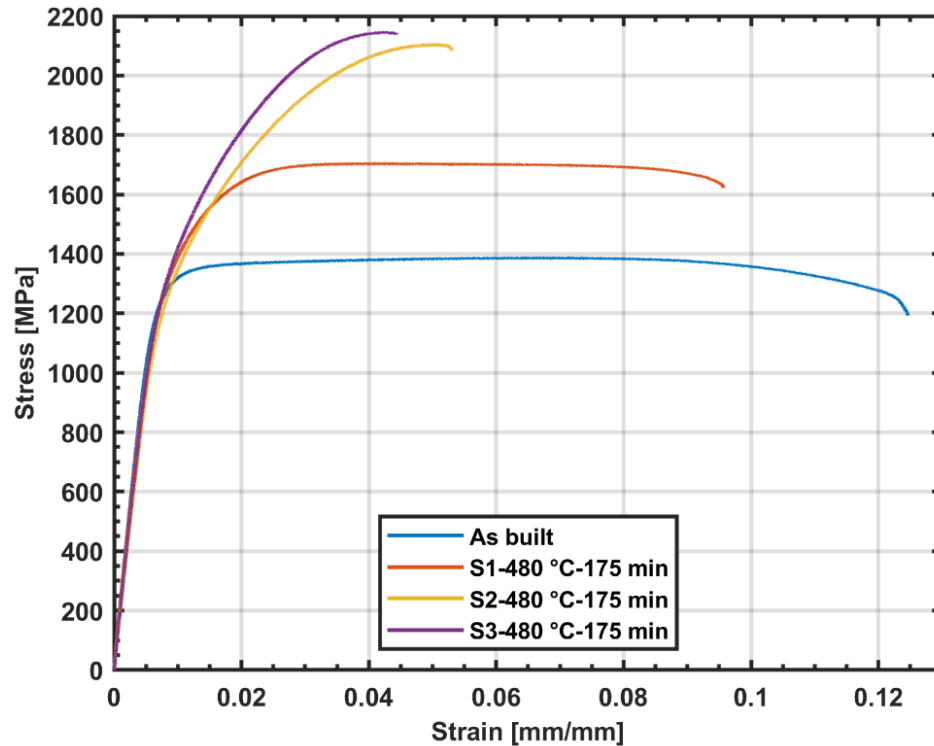
Figure 3. 14. Tensile performances - Stress-Strain curve.

In summary, from the results reported in Tables 3.5 and 3.6 and Figures 3.12 to 3.14, the HT and HAT samples show a nearly similar tendency of change in micro-hardness and tensile strength. For example, HT solution post-treatment reduces both the micro-hardness and tensile strength [123]. Indeed, rapid quenching at high-speed leads to rapid solidification of the molten bath. As a result, a microstructure composed of fine grains forms a martensite-like outcome with a high concentration of residual stresses. This can significantly inhibit dislocation movements to prevent crack formation and propagation. Martensite can improve tensile strength and micro-hardness, but following HT, the micro-hardness results show a reduction. The reason is that the martensitic transformation is lower than the deduction of fine gains and residual stress following HT. Therefore, the tensile strength and micro-

173

hardness eventually decrease. This indicates that the as-built and HT specimens exhibit mainly inhibitory ductile fractures [103].

As an overview, the microstructures and mechanical properties are very different between the as-built, HT, and HAT samples. However, due to microstructural distinctions, HAT samples show much higher micro-hardness and tensile strength, despite the loss in ductility seen in them. Since the same mechanical properties could be obtained with less post-processing than with HAT, it will be very important to reduce the cost of heat treatment of maraging steel by SLM.

3.10 CONCLUSION

The results presented in this study indicate that homogenization solution-aging treatments induce several changes to the microstructure of maraging steel, including the formation of highly fine precipitates and the reversion of austenite. As well, it contributes to higher hardness and moderate ductility, but at the expense of tensile strength. The precipitation reaction was captured indirectly via the increase in hardness observed during post-treatment, especially at low aging temperatures (Ta) (between 480-485 °C). Furthermore, depending on the post-treatment, a significant difference in fracture behaviour between the maraging steel (C300) specimens were observed. In the as-built specimens, fracture occurred in the middle of the tensile coupon gauge. Depending on the cooling solution concentration (from S1 to S3), the fracture starts to move closer to the head of the tensile specimens (stress concentration zone). This difference in behaviour is due to a combination of the differences in the microstructure and the distribution of hardening precipitates in the inner matrix of the material. This study undertook a preliminary metallurgical and mechanical characterization of selective laser melting on the powder bed of maraging steels (C300).

This article investigates the effects of various post-treatment processes, under the appellation homogenization solution-aging treatment, associated with selective laser melting (SLM) technology. A series of homogenization solution-aging treatment (HAT) experiments,

including homogenization solution treatment (HT) and aging treatment (AT) were conducted on SLM maraging steel (C300) samples. The mechanisms of microstructure, micro-hardness and tensile property evolution were investigated with different heat treatment conditions. The following conclusions can be drawn from the study:

- The considered post-treatment parameters (cooling solution concentration/type, aging temperature, and aging time) induce several changes to the microstructure of maraging steel (C300), including a more hardenable microstructure, by forming a very fine precipitate. These microstructural changes contribute to the hardening of the material.

- The microstructure of the as-built samples consists mainly of cells and dendrites. When the HT temperature is 1020 °C, the cells, the turns, and the grain boundaries of austenite and white melt track particles all disappear. For the HAT samples, the microstructure consists of lath martensite. However, when the temperature reaches 585 °C or the holding time reaches 3 hours, the lath martensite starts to disappear, and the martensite interfaces typically become quenched in the form of quenched laths until they are replaced by white and dark tissues.

- There is a remarkable interrelation between the mechanical properties (especially hardness) of maraging steel (C300) and the considered post-treatment parameters (cooling solution concentration/type, aging temperature, and aging time). A predictive model (Equation 3.1) of hardness evolution in relation with the considered post-treatment parameters was developed.

- Using ANOVA and RSM tools, the predictive models were analyzed. High determination coefficients, capable of ameliorating the accuracy of this predictive model, were observed.

- The results also highlight the fact that a cooling solution concentration and aging temperature have the strongest effects on hardness behaviour.

- Compared to as-built specimens, HTs reduce micro-hardness and tensile strength, and elongation at break does not increase due to the disappearance of fine grains obtained

175

in SLM. In contrast, all HATs used can significantly improve the micro-hardness and tensile strength, but they reduce the resulting elongations at the break.

- The optimal heat treatment process for high hardness and strength with acceptable ductility is therefore homogenization solution-aging treatment HAT13 composed of homogenization solution treatment (HT) at 1020 ℃ for 15 min in a NaCl solution concentration of 12% and an aging treatment at a temperature between 480-485 ℃ for ~3 hours with achievable micro-hardness up to 56 HRC and tensile strength up to 2145 MPa.

3.11 ACKNOWLEDGEMENT

3.12 REFERENCES

[1] : Gardan, J. (2016). Additive manufacturing technologies: state of the art and trends. International Journal of Production Research, 54(10), 3118-3132.

[2] : Durakovic, B. (2018). Design for additive manufacturing: Benefits, trends and challenges. Periodicals of Engineering and Natural Sciences (PEN), 6(2), 179-191.

[3] : Tao, W., & Leu, M. C. (2016, August). Design of lattice structure for additive manufacturing. In 2016 International Symposium on Flexible Automation (ISFA) (pp. 325-332). IEEE.

[4] : Sarvankar, S. G., & Yewale, S. N. (2019). Additive manufacturing in automobile industry. Int. J. Res. Aeronaut. Mech. Eng, 7(4), 1-10.

[5] : Liu, R., Wang, Z., Sparks, T., Liou, F., & Newkirk, J. (2017). Aerospace applications of laser additive manufacturing. In Laser additive manufacturing (pp. 351-371). Woodhead Publishing.

[6] : Gunasekaran, J., Sevvel, P., & Solomon, I. J. (2021). Metallic materials fabrication by selective laser melting: a review. Materials Today: Proceedings, 37, 252-256.

[7] : Chen, D., Wang, P., Pan, R., Zha, C., Fan, J., Liang, D., & Zhao, Y. (2020). Characteristics of Metal Specimens Formed by Selective Laser Melting: A State-of-the-Art Review. Journal of Materials Engineering and Performance, 1-28.

[8] : Strakosova, A., Roudnická, M., Ekrt, O., Vojtěch, D., & Michalcová, A. (2021). Hydrogen Embrittlement of the Additively Manufactured High-Strength X3NiCoMoTi 18-9-5 Maraging Steel. Materials, 14(17), 5073.

[9] : Katancik, M., Mirzababaei, S., Ghayoor, M., & Pasebani, S. (2020). Selective laser melting and tempering of H13 tool steel for rapid tooling applications. Journal of Alloys and Compounds, 849, 156319.

[10] : Lim, S. H., Ryou, K., Jang, K., Choi, W. S., Lee, H. M., & Choi, P. P. (2021). Hot cracking behavior of additively manufactured D2 steel. Materials Characterization, 111217.

[11] : Ettefagh, A. H., Guo, S., & Raush, J. (2020). Corrosion performance of additively manufactured stainless steel parts: A review. Additive Manufacturing, 101689.

[12] : Guzmán-Nogales, R., Estupiñán-López, F., Gaona-Tiburcio, C., Lopez-Botello, O. E., Ramírez-Rodríguez, J. G., & Zambrano-Robledo, P. C. (2021). Corrosion Resistance Measurement of 316L Stainless Steel Manufactured by Selective Laser Melting. Materials, 14(16), 4509.

[13] : Wen, S., Gan, J., Li, F., Zhou, Y., Yan, C., & Shi, Y. (2021). Research Status and Prospect of Additive Manufactured Nickel-Titanium Shape Memory Alloys. Materials, 14(16), 4496.

[14] : Hao, L., Liu, J., & Li, Y. (2021). Wetting and Spreading of AgCuTi on Selective Laser-Melted Ti-6Al-4V. Materials, 14(17), 4804.

[15] : Ghio, E., & Cerri, E. (2021). Work Hardening of Heat-Treated AlSi10Mg Alloy Manufactured by Single and Double Laser Selective Laser Melting: Effects of Layer Thickness and Hatch Spacing. Materials, 14(17), 4901.

[16] : Manca, D. R., Churyumov, A. Y., Pozdniakov, A. V., Ryabov, D. K., Korolev, V. A., & Daubarayte, D. K. (2019). Novel heat-resistant Al-Si-Ni-Fe alloy manufactured by selective laser melting. Materials Letters, 236, 676-679.

[17] : Subbiah, R., Bensingh, J., Kader, A., & Nayak, S. (2020). Influence of printing parameters on structures, mechanical properties and surface characterization of aluminium alloy manufactured using selective laser melting. The International Journal of Advanced Manufacturing Technology, 106(11), 5137-5147.

[18] : Xia, T., Wang, R., Bi, Z., Zhang, P., Sun, G., & Zhang, J. (2021). Microstructure and Mechanical Properties of Carbides Reinforced Nickel Matrix Alloy Prepared by Selective Laser Melting. Materials, 14(17), 4792.

[19] : Esmaily, M., Zeng, Z., Mortazavi, A. N., Gullino, A., Choudhary, S., Derra, T., ... & Birbilis, N. (2020). A detailed microstructural and corrosion analysis of magnesium alloy WE43 manufactured by selective laser melting. Additive Manufacturing, 35, 101321.

[20] : Zhang, W. N., Wang, L. Z., Feng, Z. X., & Chen, Y. M. (2020). Research progress on selective laser melting (SLM) of magnesium alloys: A review. Optik, 207, 163842.

[21] : Morrow, W. R., Qi, H., Kim, I., Mazumder, J., & Skerlos, S. J. (2007). Environmental aspects of laser-based and conventional tool and die manufacturing. Journal of Cleaner Production, 15(10), 932-943.

[22] :` Klocke, F., Arntz, K., Teli, M., Winands, K., Wegener, M., & Oliari, S. (2017). State-of-the-art laser additive manufacturing for hot-work tool steels. Procedia Cirp, 63, 58-63.

[23] : Fallböhmer, P., Rodríguez, C. A., Özel, T., & Altan, T. (2000). High-speed machining of cast iron and alloy steels for die and mold manufacturing. Journal of Materials Processing Technology, 98(1), 104-115.

[24] : Krajnik, P., & Kopač, J. (2004). Modern machining of die and mold tools. Journal of Materials Processing Technology, 157, 543-552.

[25] : Tian, J., Huang, Z., Qi, W., Li, Y., Liu, J., Hu, G. (2017, July). Dependence of microstructure, relative density and hardness of 18Ni-300 maraging steel fabricated by selective laser melting on the energy density. In Chinese Materials Conference (pp. 229-241). Springer, Singapore.

[26] : Fortunato, A., Lulaj, A., Melkote, S., Liverani, E., Ascari, A., Umbrello, D. (2018). Milling of maraging steel components produced by selective laser melting. The International Journal of Advanced Manufacturing Technology, 94(5-8), 1895-1902.

[27] : Peng, X., Kong, L., Fuh, J. Y. H., & Wang, H. (2021). A Review of Post-Processing Technologies in Additive Manufacturing. Journal of Manufacturing and Materials Processing, 5(2), 38.

[28] : Cheruvathur, S., Lass, E. A., & Campbell, C. E. (2016). Additive manufacturing of 17-4 PH stainless steel: post-processing heat treatment to achieve uniform reproducible microstructure. Jom, 68(3), 930-942.

[29] : Bahnini, I., Rivette, M., Rechia, A., Siadat, A., & Elmesbahi, A. (2018). Additive manufacturing technology: the status, applications, and prospects.

[30] : Khan, H. M., Karabulut, Y., Kitay, O., Kaynak, Y., & Jawahir, I. S. (2020). Influence of the post-processing operations on surface integrity of metal components produced by laser powder bed fusion additive manufacturing: a review. Machining Science and Technology, 25(1), 118-176.

[31] : Suzuki, A., Nishida, R., Takata, N., Kobashi, M., Kato, M. (2019). Design of laser parameters for selectively laser melted maraging steel based on deposited energy density. Additive Manufacturing, 28, 160-168.

[32] : Song, J., Tang, Q., Feng, Q., Ma, S., Setchi, R., Liu, Y., ... & Zhang, M. (2019). Effect of heat treatment on microstructure and mechanical behaviors of 18Ni-300 maraging steel manufactured by selective laser melting. Optics & Laser Technology, 120, 105725.

[33] : Broek, D. (2012). Elementary engineering fracture mechanics. Springer Science & Business Media.

[34] : RAJULU, C. G., & KRISHNA, A. G. AGING BEHAVIOUR AND TENSILE STRENGTH OF MARAGING STEEL PROCESSED BY LASER WELDING.

[35] : Marcisz, J., & Stępień, J. (2014). Short-time ageing of MS350 maraging steel with and without plastic deformation. Archives of Metallurgy and Materials, 59.

[36] : Özer, G., & Karaaslan, A. (2020). A Study on the Effects of Different Heat‑Treatment Parameters on Microstructure‑Mechanical Properties and Corrosion Behavior of Maraging Steel Produced by Direct Metal Laser Sintering. steel research international, 91(10), 2000195.

[37] : Stanford, M., Kibble, K., Lindop, M., Mynors, D., & Durnall, C. (2008). An investigation into fully melting a maraging steel using direct metal laser sintering (DMLS). Steel Res. Int, 2, 847-852.

[38] : K. Kempen, E. Yasa, L. Thijs, J.-P. Kruth, J. Van Humbeeck, Microstructure and mechanical properties of Selective Laser Melted 18Ni-300 steel, Phys. Procedia 12 (2011) 255263, https://doi.org/10.1016/j.phpro.2011.03.033.

[39] : G. Casalino, S.L. Campanelli, N. Contuzzi, A.D. Ludovico, Experimental investigation and statistical optimisation of the selective laser melting process of a maraging steel, Opt. Laser Technol. 65 (2015) 151158, https://doi.org/10.1016/j.optlastec. 2014.07.021.

[40] : Mooney, B., Kourousis, K. I., Raghavendra, R. (2019). Plastic anisotropy of additively manufactured maraging steel: Influence of the build orientation and heat treatments. Additive Manufacturing, 25, 19-31.

[41] : Jgle, E. A., Sheng, Z., Krnsteiner, P., Ocylok, S., Weisheit, A., Raabe, D. (2017). Comparison of maraging steel micro-and nanostructure produced conventionally and by laser additive manufacturing. Materials, 10(1), 8.

[42] : Tan, C., Zhou, K., Tong, X., Huang, Y., Li, J., Ma, W., ... & Kuang, T. (2016, July). Microstructure and mechanical properties of 18Ni-300 maraging steel fabricated by selective laser melting. In Proceedings of the 2016 6th International Conference on Advanced Design and Manufacturing Engineering (ICADME 2016) (pp. 404-410).

[43] : Koukolíková, M., Brunát, V., Wolf, G., Simson, T., & Koch, J. (2021, August). Advanced techniques applied to analyze the influence of the heat treatment on the mechanical properties, microstructure and texture of additively produced components from maraging steel. In IOP Conference Series: Materials Science and Engineering (Vol. 1178, No. 1, p. 012032). IOP Publishing.

[44] : Félix-Martínez, C., Ibarra-Medina, J., Fernández-Benavides, D. A., Cáceres-Díaz, L. A., & Alvarado-Orozco, J. M. (2021). Effect of the parametric optimization and heat treatment on the 18Ni-300 maraging steel microstructural properties manufactured by directed energy deposition. The International Journal of Advanced Manufacturing Technology, 1-22.

[45] : Guo, W. F., Guo, C., Zhu, Q. (2018). Heat treatment behavior of the 18Ni300 maraging steel additively manufactured by selective laser melting. In Materials Science Forum (Vol. 941, pp. 2160-2166). Trans Tech Publications Ltd.

[46] : Bai, Y., Yang, Y., Xiao, Z., & Wang, D. (2018). Selective laser melting of maraging steel: mechanical properties development and its application in mold. Rapid Prototyping Journal.

[47] : Yasa, E., Kempen, K., Kruth, J., Thijs, L., & Van Humbeeck, J. (2010, August). Microstructure and mechanical properties of maraging steel 300 after selective laser melting. In Solid freeform fabrication symposium proceedings (pp. 383-396).

[48] : Casati, R., Lemke, J. N., Tuissi, A., & Vedani, M. (2016). Aging behaviour and mechanical performance of 18-Ni 300 steel processed by selective laser melting. Metals, 6(9), 218.

[49] : Lian, Y., Ma, M., Zhang, J., Huang, J., Gao, W., Zhang, Z., & Zhao, C. (2019). Influence of Austenitizing Temperature on the Microstructure and Mechanical Properties of an Fe-Cr-Ni-Mo-Ti Maraging Stainless Steel. Journal of Materials Engineering and Performance, 28(9), 5466-5475.

[50] : Conde, F. F., Escobar, J. D., Oliveira, J. P., Bre ?, M., Jardini, A. L., Bose, W. W., Avila, J. A. (2019). Effect of thermal cycling and aging stages on the microstructure and bending strength of a selective laser melted 300-grade maraging steel. Materials Science and Engineering: A, 758, 192-201.

[51] : ASTM, A. E8/E8M-21, Standard Test Methods for Tension Testing of Metallic Materials. ASTM International, West Conshohocken, 2004.

[52] : E. A. Jgle, P.-P. Choi, J. V. Humbeeck, D. Raabe, Precipitation and austenite reversion behavior of a maraging steel produced by selective laser melting, J. Mater. Res. 29 (2014) 20722079.

[53] : Wang, M. M., Tasan, C. C., Ponge, D., Kostka, A., Raabe, D. (2014). Smaller is less stable: size effects on twinning vs. transformation of reverted austenite in TRIP-maraging steels. Acta Materialia, 79, 268-281.

[54] : Gribbin, S., Ghorbanpour, S., Ferreri, N. C., Bicknell, J., Tsukrov, I., & Knezevic, M. (2019). Role of grain structure, grain boundaries, crystallographic texture, precipitates, and porosity on fatigue behavior of Inconel 718 at room and elevated temperatures. Materials Characterization, 149, 184-197.

[55] : Sangid, M. D., Book, T. A., Naragani, D., Rotella, J., Ravi, P., Kenesei, P., ... & Xiao, X. (2018). Role of heat treatment and build orientation in the microstructure sensitive deformation characteristics of IN718 produced via SLM additive manufacturing. Additive Manufacturing, 22, 479-496.

[56] : Galy, C. (2019). Étude des interactions matériau/procédé en vue d'une optimisation des conditions opératoires du procédé de fabrication additive SLM sur des alliages d'aluminium pour des applications aéronautiques (Doctoral dissertation, Bordeaux).

[57] : Khorasani, A., Gibson, I., Goldberg, M., & Littlefair, G. (2017). On the role of different annealing heat treatments on mechanical properties and microstructure of selective laser melted and conventional wrought Ti-6Al-4V. Rapid Prototyping Journal.

[58] : Allam, T., Pradeep, K. G., Köhnen, P., Marshal, A., Schleifenbaum, J. H., & Haase, C. (2020). Tailoring the nanostructure of laser powder bed fusion additively manufactured maraging steel. Additive Manufacturing, 36, 101561.

181

[59] : Callister Jr, W. D., & Rethwisch, D. G. (2020). Fundamentals of materials science and engineering: an integrated approach. John Wiley & Sons.

[60] : Wegst, C., & Wegst, M. (2019). STAHLSCHLÜSSEL–Key to steel. *ISBN-13, 978*, 3-922599.

[61] : Conde, F. F., Escobar, J. D., Oliveira, J. P., Jardini, A. L., Bose Filho, W. W., & Avila, J. A. (2019). Austenite reversion kinetics and stability during tempering of an additively manufactured maraging 300 steel. Additive Manufacturing, 29, 100804.

[62] : Pardal, J. M., Tavares, S. S. M., Terra, V. F., Da Silva, M. R., Dos Santos, D. R. (2005). Modeling of precipitation hardening during the aging and overaging of 18NiCoMoTi maraging 300 steel. Journal of Alloys and Compounds, 393(1-2), 109-113.

[63] : Babamiri, B. B., Indeck, J., Demeneghi, G., Cuadra, J., & Hazeli, K. (2020). Quantification of porosity and microstructure and their effect on quasi-static and dynamic behavior of additively manufactured Inconel 718. Additive Manufacturing, 34, 101380.

[64] : Al-Maharma, A. Y., Patil, S. P., & Markert, B. (2020). Effects of porosity on the mechanical properties of additively manufactured components: a critical review. Materials Research Express.

[65] : Wang, P., Tan, X., He, C., Nai, M. L. S., Huang, R., Tor, S. B., & Wei, J. (2018). Scanning optical microscopy for porosity quantification of additively manufactured components. Additive Manufacturing, 21, 350-358.

[66] : Wang, P., Goh, M. H., Li, Q., Nai, M. L. S., & Wei, J. (2020). Effect of defects and specimen size with rectangular cross-section on the tensile properties of additively manufactured components. Virtual and Physical Prototyping, 15(3), 251-264.

[67] : Khosravani, M. R., Berto, F., Ayatollahi, M. R., & Reinicke, T. (2020). Fracture behavior of additively manufactured components: A review. Theoretical and Applied Fracture Mechanics, 109, 102763.

[68] : Allam, T., Pradeep, K. G., Köhnen, P., Marshal, A., Schleifenbaum, J. H., & Haase, C. (2020). Tailoring the nanostructure of laser powder bed fusion additively manufactured maraging steel. Additive Manufacturing, 36, 101561.

[69] : Dehgahi, S., Ghoncheh, M. H., Hadadzadeh, A., Sanjari, M., Amirkhiz, B. S., & Mohammadi, M. (2020). The role of titanium on the microstructure and mechanical properties of additively manufactured C300 maraging steels. Materials & Design, 194, 108965.

[70] : Tascioglu, E., Khan, H. M., Kaynak, Y., Coşkun, M., Tarakci, G., & Koç, E. (2021). Effect of aging and finish machining on the surface integrity of selective laser melted maraging steel. Rapid Prototyping Journal.

[71] : Amanov, A. (2021). Advancement of tribological properties of Ti –6Al –4V alloy fabricated by selective laser melting. Tribology International, 155, 106806.

[72] : AlMangour, B., Grzesiak, D., & Yang, J. M. (2017). Scanning strategies for texture and anisotropy tailoring during selective laser melting of TiC/316L stainless steel nanocomposites. Journal of Alloys and Compounds, 728, 424-435.

[73] : Bhardwaj, T., & Shukla, M. (2018). Effect of laser scanning strategies on texture, physical and mechanical properties of laser sintered maraging steel. Materials Science and Engineering: A, 734, 102-109.

[74] : AlMangour, B., Grzesiak, D., Borkar, T., & Yang, J. M. (2018). Densification behavior, microstructural evolution, and mechanical properties of TiC/316L stainless steel nanocomposites fabricated by selective laser melting. Materials & Design, 138, 119-128.

[75] : Xie, Y. J., & Wang, M. C. (2006). Microstructural morphology of electrospark deposition layer of a high gamma prime superalloy. Surface and Coatings Technology, 201(3-4), 691-698.

[76] : Kurzynowski, T., Gruber, K., Stopyra, W., Kuźnicka, B., & Chlebus, E. (2018). Correlation between process parameters, microstructure and properties of 316 L stainless steel processed by selective laser melting. Materials Science and Engineering: A, 718, 64-73.

[77] : McKeown, J. T., Kulovits, A. K., Liu, C., Zweiacker, K., Reed, B. W., LaGrange, T., ... & Campbell, G. H. (2014). In situ transmission electron microscopy of crystal growth-mode transitions during rapid solidification of a hypoeutectic Al–Cu alloy. Acta Materialia, 65, 56-68.

[78] : Liu, S., & Shin, Y. C. (2020). Integrated 2D cellular automata-phase field modeling of solidification and microstructure evolution during additive manufacturing of Ti6Al4V. Computational Materials Science, 183, 109889.

[79] : K. Kempen, E. Yasa, L. Thijs, J.-P. Kruth, J. Van Humbeeck, Microstructure and mechanical properties of Selective Laser Melted 18Ni-300 steel, Phys. Procedia 12 (2011) 255263, https://doi.org/10.1016/j.phpro.2011.03.033.

[80] : Sandvik, B. P. J., & Wayman, C. M. (1983). Characteristics of lath martensite: Part I. Crystallographic and substructural features. Metallurgical transactions A, 14(4), 809-822.

[81] : Kelly, P. M., Jostsons, A., & Blake, R. G. (1990). The orientation relationship between lath martensite and austenite in low carbon, low alloy steels. Acta metallurgica et materialia, 38 (6), 1075-1081.

[82] : Kitahara, H., Ueji, R., Tsuji, N., & Minamino, Y. (2006). Crystallographic features of lath martensite in low-carbon steel. Acta materialia, 54(5), 1279-1288.

[83] : Morito, S., Saito, H., Ogawa, T., Furuhara, T., & Maki, T. (2005). Effect of austenite grain size on the morphology and crystallography of lath martensite in low carbon steels. ISIJ international, 45(1), 91-94.

[84] : Shamsdini, S., Shakerin, S., Hadadzadeh, A., Amirkhiz, B. S., & Mohammadi, M. (2020). A trade-off between powder layer thickness and mechanical properties in additively manufactured maraging steels. Materials Science and Engineering: A, 776, 139041.

[85] : Pirgazi, H., Sanjari, M., Tamimi, S., Amirkhiz, B. S., Kestens, L. A., & Mohammadi, M. (2021). Texture evolution in selective laser melted maraging stainless steel CX with martensitic transformation. Journal of Materials Science, 56(1), 844-853.

[86] : Béreš, M., Wu, L., Santos, L. P. M., Masoumi, M., da Rocha Filho, F. A. M., Da Silva, C. C., ... & Da Silva, M. G. (2017). Role of lattice strain and texture in hydrogen embrittlement of 18Ni (300) maraging steel. International Journal of Hydrogen Energy, 42(21), 14786-14793.

[87] : Shamsdini, S., Pirgazi, H., Ghoncheh, M. H., Sanjari, M., Amirkhiz, B. S., Kestens, L., & Mohammadi, M. (2021). A relationship between the build and texture orientation in tensile loading of the additively manufactured maraging steels. Additive Manufacturing, 41, 101954.

[88] : Dehgahi, S., Pirgazi, H., Sanjari, M., Alaghmandfard, R., Tallon, J., Odeshi, A., ... & Mohammadi, M. (2021). Texture evolution during high strain-rate compressive loading of maraging steels produced by laser powder bed fusion. Materials Characterization, 111266.

[89] : Ebner, S., Suppan, C., Stark, A., Schnitzer, R., & Hofer, C. (2019). Austenite decomposition and carbon partitioning during quenching and partitioning heat treatments studied via in-situ X-ray diffraction. Materials & Design, 178, 107862.

[90] : Shirdel, M., Mirzadeh, H., & Parsa, M. H. (2015). Nano/ultrafine grained austenitic stainless steel through the formation and reversion of deformation-induced martensite: Mechanisms, microstructures, mechanical properties, and TRIP effect. Materials Characterization, 103, 150-161.

[91] : Somani, M. C., Jaskari, M., Sadeghpour, S., Hu, C., Misra, R. D. K., Nyo, T. T., ... & Karjalainen, L. P. (2020). Improving the yield strength of an antibacterial 304Cu austenitic stainless steel by the reversion treatment. Materials Science and Engineering: A, 793, 139885.

[92] : Sha, W., & Guo, Z. (2009). Maraging steels: modelling of microstructure. Properties and Applications, 63.

[93] : Maki, T. (2012). Morphology and substructure of martensite in steels. Phase transformations in steels, 34-58.

[94] : Ahmadkhaniha, D., Möller, H., & Zanella, C. (2021). Studying the Microstructural Effect of Selective Laser Melting and Electropolishing on the Performance of Maraging Steel. Journal of Materials Engineering and Performance, 1-18.

[95] : Shibata, A., Morito, S., Furuhara, T., & Maki, T. (2009). Substructures of lenticular martensites with different martensite start temperatures in ferrous alloys. Acta Materialia, 57(2), 483-492.

[96] : Williams, J. C., Taggart, R., & Polonis, D. H. (1970). The morphology and substructure of Ti-Cu martensite. Metallurgical Transactions, 1(8), 2265-2270.

[97] : Krauss, G. (1999). Martensite in steel: strength and structure. Materials science and engineering: A, 273, 40-57.

[98] : Becker, T. H., & Dimitrov, D. (2016). The achievable mechanical properties of SLM produced Maraging Steel 300 components. Rapid Prototyping Journal.

[99] : Tariq, F., Baloch, R. A., Ahmed, B., & Naz, N. (2010). Investigation into microstructures of maraging steel 250 weldments and effect of post-weld heat treatments. Journal of Materials Engineering and Performance, 19(2), 264-273.

[100] : Cabeza, M., Castro, G., Merino, P., Pena, G., Román, M., Semiao, J., & Vázquez, P. (2010). Optimization of Ageing Parameters of a Low Nickel Maraging Steel. In Materials Science Forum (Vol. 636, pp. 471-477). Trans Tech Publications Ltd.

[101] : Li, K., Yu, B., Misra, R. D. K., Wang, C., Tian, Z., & Shan, J. (2018). The significance and design of hybrid process in governing high strength-high toughness combination of fiber laser-welded T-250 maraging steel joint. Materials Science and Engineering: A, 718, 173-181.

[102] : Maloletnev, A. Y., L'vov, Y. B., Pestov, I. V., & Perkas, M. D. (1975). Resistance of maraging steel N18K9M5T to cyclic impact loads. Metal Science and Heat Treatment, 17(7), 584-588.

[103] : Conde, F. F., Escobar, J. D., Rodriguez, J., Afonso, C. R. M., Oliveira, M. F., & Avila, J. A. (2021). Effect of Combined Tempering and Aging in the Austenite Reversion, Precipitation, and Tensile Properties of an Additively Manufactured Maraging 300 Steel. Journal of Materials Engineering and Performance, 1-12.

[104] : Oliveira, A. R., Diaz, J. A. A., Nizes, A. D. C., Jardini, A. L., & Del Conte, E. G. (2021). Investigation of building orientation and aging on strength–stiffness performance of additively manufactured maraging steel. Journal of Materials Engineering and Performance, 30(2), 1479-1489.

[105] : He, B. B., Hu, B., Yen, H. W., Cheng, G. J., Wang, Z. K., Luo, H. W., & Huang, M. X. (2017). High dislocation density–induced large ductility in deformed and partitioned steels. Science, 357(6355), 1029-1032.

[106] : Escobar, J. D., Poplawsky, J. D., Faria, G. A., Rodriguez, J., Oliveira, J. P., Salvador, C. A. F., ... & Ramirez, A. J. (2018). Compositional analysis on the reverted austenite and tempered martensite in a Ti-stabilized supermartensitic stainless steel: Segregation, partitioning and carbide precipitation. Materials & Design, 140, 95-105.

[107] : Zhao, X., Lv, Y., Dong, S., Yan, S., He, P., Liu, X., ... & Xu, B. (2020). The effect of thermal cycling on direct laser-deposited gradient H13 tool steel: Microstructure evolution, nanoprecipitation behaviour, and mechanical properties. Materials Today Communications, 25, 101390.

[108] : Li, X., & Yin, Z. (1995). Reverted austenite during aging in 18Ni (350) maraging steel. Materials Letters, 24(4), 239-242.

[109] : LeBrun, T., Nakamoto, T., Horikawa, K., & Kobayashi, H. (2015). Effect of retained austenite on subsequent thermal processing and resultant mechanical properties of selective laser melted 17–4 PH stainless steel. Materials & Design, 81, 44-53.

[110] : Sha, W., Cerezo, A., & Smith, G. D. W. (1993). Phase chemistry and precipitation reactions in maraging steels: Part I. Introduction and study of Co-containing C-300 steel. Metallurgical and Materials Transactions A, 24(6), 1221-1232.

[111] : Tariq, F., Baloch, R. A., Ahmed, B., & Naz, N. (2010). Investigation into microstructures of maraging steel 250 weldments and effect of post-weld heat treatments. Journal of Materials Engineering and Performance, 19(2), 264-273.

[112] : Da Silva, A. K., Leyson, G., Kuzmina, M., Ponge, D., Herbig, M., Sandlöbes, S., ... & Raabe, D. (2017). Confined chemical and structural states at dislocations in Fe-9wt% Mn steels: A correlative TEM-atom probe study combined with multiscale modelling. Acta Materialia, 124, 305-315.

[113] : Galindo-Nava, E. I., Rainforth, W. M., & Rivera‑Díaz‑del‑Castillo, P. E. J. (2016). Predicting microstructure and strength of maraging steels: Elemental optimisation. Acta Materialia, 117, 270-285.

[114] : Lee, S., & De Cooman, B. C. (2016). Influence of carbide precipitation and dissolution on the microstructure of ultra-fine-grained intercritically annealed medium manganese steel. Metallurgical and Materials Transactions A, 47(7), 3263-3270.

[115] : Millan, J., Ponge, D., Raabe, D., Choi, P., & Dmitrieva, O. (2011). Characterization of Nano‑Sized Precipitates in a Mn‑Based Lean Maraging Steel by Atom Probe Tomography. steel research international, 82(2), 137-145.

[116] : Wang, M. M., Tasan, C. C., Ponge, D., Dippel, A. C., & Raabe, D. (2015). Nanolaminate transformation-induced plasticity–twinning-induced plasticity steel with dynamic strain partitioning and enhanced damage resistance. Acta Materialia, 85, 216-228.

[117] : https://www.eos.info/03_system-related-assets/material-related-contents/metal-materials-and-examples/metal-material-datasheet/werkzeugstahl_ms1_cx/ms1/ms-ms1-m280_m290_400w_material_data_sheet_05-14_en.pdf

[118] : Lin, Y. C., Wu, Q., He, D. G., Zhu, X. H., Liu, D. Y., & Li, X. H. (2020). Effects of solution time and cooling rate on microstructures and mechanical properties of 2219 Al alloy for a larger spun thin-wall ellipsoidal head. Journal of Materials Research and Technology, 9(3), 3566-3577.

[119] : Bendoumi, A., Makuch, N., Chegroune, R., Kulka, M., Keddam, M., Dziarski, P., & Przestacki, D. (2020). The effect of temperature distribution and cooling rate on microstructure and microhardness of laser remelted and laser-borided carbon steels with various carbon concentrations. Surface and Coatings Technology, 387, 125541.

[120] : Zai, L., Zhang, C., Wang, Y., Guo, W., Wellmann, D., Tong, X., & Tian, Y. (2020). Laser powder bed fusion of precipitation-hardened martensitic stainless steels: a review. Metals, 10(2), 255.

[121] : Nasiri, Z., Ghaemifar, S., Naghizadeh, M., & Mirzadeh, H. (2021). Thermal mechanisms of grain refinement in steels: a review. Metals and Materials International, 27(7), 2078-2094.

[122] : Zhu, H. M., Zhang, J. W., Hu, J. P., Ouyang, M. N., & Qiu, C. J. (2021). Effects of aging time on the microstructure and mechanical properties of laser-cladded 18Ni300 maraging steel. Journal of Materials Science, 56(14), 8835-8847.

[123] : Gong, P., Wynne, B. P., Knowles, A. J., Turk, A., Ma, L., Galindo-Nava, E. I., & Rainforth, W. M. (2020). Effect of ageing on the microstructural evolution in a new design of maraging steels with carbon. Acta Materialia, 196, 101-121.

[124] : Song, J., Tang, Q., Feng, Q., Ma, S., Setchi, R., Liu, Y., ... & Zhang, M. (2019). Effect of heat treatment on microstructure and mechanical behaviors of 18Ni-300 maraging steel manufactured by selective laser melting. Optics & Laser Technology, 120, 105725.

[125] : Kučerová, L., Burdová, K., Jeníček, Š., & Chena, I. (2021). Effect of solution annealing and precipitation hardening at 250° C –550 ℃ on microstructure and mechanical properties of additively manufactured 1.2709 maraging steel. Materials Science and Engineering: A, 814, 141195.

[126] : Shamsdini, S., Pirgazi, H., Ghoncheh, M. H., Sanjari, M., Amirkhiz, B. S., Kestens, L., & Mohammadi, M. (2021). A relationship between the build and texture orientation in tensile loading of the additively manufactured maraging steels. Additive Manufacturing, 41, 101954.

CHAPITRE 4

SENSIBILITÉ DES PERFORMANCES MÉCANIQUES ET DE LA MICROSTRUCTURE D'UN ACIER MARAGING AUX PARAMÈTRES DU PROCÉDÉ SLM

(Article à soumettre)

Faical. HABASSI[1, *], Noureddine. BARKA[1], Mohammed. JAHAZI[2],

[1] Mathematics, Computer Science and Engineering Department, Université du Québec à Rimouski (UQAR), 300 Allée des Ursulines, Rimouski, QC G5L 3A1, Québec, Canada

[2] Mechanical Engineering Department, École de Techonologie Superieure (ÉTS), 1100 Rue Notre-Dame Ouest, Montréal, QC H3C 1K3, Québec, Canada

*Corresponding author. E-mail : Faical.Habassi@uqar.ca

4.1 RESUME EN FRANÇAIS DU QUATRIEME ARTICLE

La fabrication additive (FA) est un procédé de fabrication révolutionnaire basé sur un ajout couche par couche d'un matériau, et qui passe par plusieurs techniques d'application, et utilisant différents matériaux. L'une de ces techniques est la fusion laser sélective (SLM), qui est une technologie AM émergente qui trouve des applications répandues dans de nombreux secteurs, grâce à ses nombreux avantages, telles que la grande liberté et la flexibilité qu'elle apporte à la table en termes de conception et de la réduction du gaspillage matériaux. La microstructure et les comportements mécaniques des pièces SLM finales sont interdépendants avec les paramètres de traitement SLM. Pour modéliser cette interrelation, un acier maraging (C300), utilisé dans plusieurs secteurs, dont l'Automobile et l'Aéronautique, est sélectionné pour une évaluation de la sensibilité de ses comportements (principalement densification/porosité, dureté et résistance à la traction) en fonction d'une petite variation des paramètres du processus SLM (principalement la puissance laser P (W), la vitesse de balayage V (mm/s) et l'espace d'éclosion H (µm)).

Une fois les résultats expérimentaux obtenus, des outils d'analyse statistique utilisant l'ANOVA sont appliqués pour déterminer les effets des paramètres du procédé sur la qualité et les performances mécaniques de l'acier maraging SLM (C300). Un modèle de prédiction est développé à partir de cette analyse pour prédéterminer la porosité, la dureté et la résistance à la traction ultime des pièces en acier maraging SLM (C300) obtenues à partir des paramètres de procédé considérés. Le modèle est également utilisé pour optimiser les paramètres de processus en utilisant une méthode de surface de réponse (RSM) pour déterminer les valeurs optimales. Les résultats prouvent que la variation de ces paramètres, en particulier l'espace d'éclosion et la puissance du laser, peut affecter de manière significative le comportement mécanique final des pièces en acier maraging (C300) détendu (490 °C, 4 h).

Les parties les plus denses (~99,4) et les plus dures (~58 HRC) sont obtenues en utilisant la combinaison de paramètres composés de P=320 W, V=1050 mm/s et H=80 μm, correspondant à une densité d'énergie laser de ~ 95,2 j/mm3, tandis que la partie de résistance ultime maximale à la traction (1828 MPa) est obtenue en utilisant la combinaison de paramètres composés de P=270 W, V=1050 mm/s et H=100 μm, correspondant à une densité d'énergie laser de ~64,2 j/mm3. Les résultats de l'analyse ANOVA ont révélé un coefficient de détermination prédit, R2 (pred.), de 97,72 % et 99,00 % et (R2 adj) 99,00 % pour la porosité, la dureté et les modèles de résistance à la traction ultime, respectivement, ce qui indique que les modèles développés les modèles de prédiction des propriétés des pièces en acier maraging SLM (C300) ont une grande précision.

Ce quatrième article intitulé « *Sensitivity of the mechanical performance and microstructure of a maraging steel to SLM process parameters* » est le fruit de collaboration entre plusieurs auteurs. En tant que premier auteur, ma contribution constitue la partie essentielle de la recherche concernant l'état de l'art, les essais de performance, l'analyse et l'interprétation des résultats ainsi que la sensibilité qui est le cœur du travail. L'essentiel des travaux de rédaction a été fait par le premier auteur sous la supervision de Noureddine Barka et de Mohammed Jahazi. Le professeur Noureddine Barka, qui est le second auteur a défini le

projet ainsi la méthodologie à adopter. Quant à mon co-directeur, Mohammed Jahazi, il a apporté une partie essentielle grâce à sa connaissance approfondie de la métallurgie et des matériaux.

4.2 TITRE DU QUATRIEME ARTICLE

Sensitivity of the mechanical performance and microstructure of a maraging steel to SLM process parameters

4.3 ABSTRACT

Additive manufacturing (AM) is a revolutionary manufacturing process based on a layer-by-layer addition of a material, and which proceeds through several application techniques, and using different materials. One such technique is selective laser melting (SLM), which is an emerging AM technology that is finding widespread applications in many sectors, thanks to its many advantages, such as the large freedom and flexibility it brings to the table in terms of design and material waste reduction. The microstructure and the mechanical behaviors of final SLM parts are interrelated with SLM processing parameters. To model this interrelation, a maraging steel (C300), which is used in several sectors, including Automotive and Aerospace, is selected for an evaluation of the sensitivity of his behaviors (mainly densification/porosity, hardness, and tensile strength) as a function of a small variation of SLM process parameters (mainly laser power P (W), scan speed V (mm/s), and hatching space H (μm)). Once the experimental results are obtained, statistical analysis tools using ANOVA are applied to determine the effects of process parameters on the quality and mechanical performance of SLM maraging steel (C300). A prediction model is developed from this analysis to predetermine the porosity, hardness, and ultimate tensile strength of SLM maraging steel parts (C300) obtained from the process parameters considered. The model is also employed to optimize process parameters using a response surface method (RSM) to determine optimal values. The results prove that varying these parameters, especially the hatching space and laser power, may significantly affect the final

mechanical behavior of stress-relieved (490 °C, 4 h) maraging steel (C300) parts. The densest (~99.4) and hardest (~58 HRC) parts are achieved using the combination of parameters composed of a P=320 W, V=1050 mm/s, and H=80 μm, corresponding to a laser energy density of ~95.2 j/mm 3, while the maximum ultimate tensile strength (1828 MPa) part is achieved using the combination of parameters composed of a P=270 W, V=1050 mm/s, and H=100 μm, corresponding to a laser energy density of ~64.2 j/mm 3. The outcomes of the ANOVA analysis revealed a predicted coefficient of determination, R2(pred.), of 97.72% and 99.00% and (R2 adj) 99.00% for porosity, hardness, and ultimate tensile strength models, respectively, which indicates that the developed prediction models of properties of SLM maraging steel (C300) parts have high accuracy.

4.4 INTRODUCTION

Additive manufacturing (AM) is a new manufacturing technique that allows the addition of melted metal, layer by layer [1-3]. In terms of design, no shape or geometry is impossible for AM. AM boasts certain characteristic advantages over traditional manufacturing techniques [1-3], including the rapid prototyping of complex products with high quality, large flexibility, reasonable costs, raw materials and energy optimization, and short production times [1-3]. That is what explains why this innovative technology is already well established in several areas using a large range of materials [4-6]. Many papers examining different materials that can be additively manufactured have been published. Azarniya et al. [7] (2019) studied the evolution of the microstructure and mechanical behaviors during laser metal deposition (LMD) of Ti-6Al-4V. Zhong et al. [8] (2017) studied the additive manufacturing of 316L stainless steel by electron beam melting for nuclear fusion applications. Keshavarzkermani et al. [9] (2018) investigated the impact of a direct laser melting process (DMSL) on grain formation and on the orientation of Inconel 718. Kempen et al. [10] (2015) optimized process parameters for selective laser fused aluminum alloy and characterized the material. Irrinki et al. [11] (2018) investigated the effects of powder characteristics and processing conditions on the corrosion performance of 17-4 PH

stainless steel fabricated by laser powder bed fusion. Herzog et al. [12] (2020) optimized the productivity of laser powder bed fusion (L-PBF) by hot isostatic pressing (HIP) of Ti alloy.

Among AM techniques, selective laser melting—a powder bed system—is one of the most promising processes [13-15] as it can deliver complex final parts with uniform layer geometry, uniform ultra-fine microstructures, and high mechanical performance [16-19]. Several physical phenomena, such as heating, fusion, and solidification [13-15], occur during the SLM process to fabricate complex metallic parts by melting successive powder layers, using a high heat source (laser). It is a repetitive process that goes on until the part is completely manufactured. The SLM technique has already been successfully applied to manufacture parts made of a wide range of materials such as steels [20-22], titanium [17, 19, 23], Inconel [24-25], and aluminum [26-27]. It must be emphasized that the process parameters are a decisive player that can highly affect the quality and mechanical behavior of final parts. Krishnan et al. [28] evaluated a DMLS AlSi10Mg. They found that the hatch distance is the most significant parameter influencing the porosity, the microstructure, and the mechanical properties. They also reported that the scanning speed was an important parameter affecting the hardness and density. Using other metal powder, Suzuki et al. [29] reported certain important changes in structural factors, including the relative density and depth of the weld pool, as a function of the process parameters used. Moreover, hardness cannot always be clarified by volumetric energy density, which is widely used in research fields related to the SLM process. For example, Nayak et al. [30] discussed the influence of different process parameters such as the layer thickness, construction orientation, laser power, and scanning speed, and observed that the energy density is the most significant parameter influencing the mechanical properties of the manufactured part.

Maraging steels, including maraging steel (C300), are therefore obvious candidates for use in selective laser melting, particularly considering their already superior strength in wrought materials [31-32]. This material derives its resistant character from a martensitic matrix which is reinforced by nano-inclusions (precipitates) following thermal aging treatments [33-34]. Precipitate strengthening mechanisms allow higher hardness, strength

and toughness in maraging steels [35-36], which is why it is commonly used in the aerospace [37-38], automotive [39-40], construction [41-42] and defense industries [41, 43]. The use of new technologies, including metal additive manufacturing, has the potential to introduce these steels into new avenues of research and manufacturing, via improvements of their microstructure and mechanical properties [41, 35-36].

AM maraging steel has been the subject of intense research in recent years. The papers published in the area cover process optimization, final quality, densification, and the metallurgic and mechanical behaviors. Wu et al. [44] (2020), Becker et al. [45] (2016), and Kempen et al. [46] (2011) investigated the effects of process parameters and heat treatment on selective laser fused maraging steel. They found that the maximum relative density of the selective laser melted part could reach over 99% and that the ultimate tensile strength exceeded 1200 MPa, in the as-built state, and 2000 MPa, after solution and aging treatment. The treatments used can be considered long as the total treatment time varies between 5 and 50 hours. Ullah et al. [47] (2020) and Mooney et al. [48] (2019) reported the plastic anisotropy of 18Ni (300) parts with three fabrication directions (0°, 45° and 90°), made using a laser additive manufacturing machine. However, heat treatment can significantly decrease this anisotropy. The authors investigated the effect of build direction on the hardness behavior of maraging steel (C300) and reported that a horizontal orientation (0°) leads to a higher hardness value than do vertical (90°) and inclined (45°) orientations. De Oliveira et al. [49] (2021) found that samples with a 90° vertical direction offer a better compression behavior and energy absorption capacity than horizontal parts at 0°. On the other hand, they reported that heat-treated samples can achieve a higher ultimate compressive strength than as-built parts, with a very lower total strain and energy absorption capacity. A similar compression peak stress (~ 200 MPa) has been reported by Contuzzi et al. [50] (2013), in the as-built condition. Meneghetti et al. [51] (2017) reported that additively fabricated 0° oriented maraging steel samples exhibited lower fatigue strength than 90° oriented samples. Yao et al. [52] (2020) illustrated that considering the heterogeneity of the temperature gradient, the distribution of heat input and the growth amount, the microstructure of SLM maraging steel (C300) presents two different morphologies, namely, an equiaxial and a

columnar substructure. They observed that the as-constructed samples have a random grain orientation with weak textures, which is attributable to the beam scan pattern (67° rotation). Condé et al. [53] (2019) studied the influence of heat treatment on the microstructure and mechanical properties. Their results showed that a direct aging treatment without solution treatment could lead to the highest hardness and flexural strengths with a non-homogenized composition retained. In addition, a higher temperature was required (980 °C) to achieve efficient dissolution of the as-built microstructure. All these works illustrate that with the adequate combination of process parameters, SLM maraging steel can achieve a comparable level of behavior as the wrought state.

Different process parameters can significantly affect the quality and the mechanical behavior of final parts. These behaviors include the laser power "P", the scan speed "V", the hatching space "H", the layer thickness "t", the energy density (which includes P, V, H, and t), the build direction and the scanning strategy. Several researchers have examined the correlation between process parameters and final part behaviors. An example is Bai et al. [54] (2017), who investigated how the process parameters influence the mechanism of evolution of mechanical properties of SLM maraging steel (C300). Only the correlation between process parameters and relative density has been explored, without a prediction model given. The authors reported that the relative density increases first and then decreases, as a function of the energy density level. Kempen et al. [46] (2011), using a constant power of 100 W, investigated the effect of varying the scanning speeds between 120-600 mm/s and the layer thickness between 30-60 µm on relative density and micro-hardness of SLM maraging steels. They found that increasing the scanning speed and layer thickness causes a decrease in both the relative density and micro-hardness. According to Huang et al. [55] (2020) in their research on the effects of process parameters on the relative density of SLM maraging steel (C300) parts, each parameter has a different level of importance in the SLM process. They indicated that the most influential parameters, from highest to lowest, can be ranked as follows: laser power> scanning distance> scanning speed> powder thickness. They also reported that the highest density (99.99%) can be reached for an energy density of 75-185 j/mm 3. Although commonly used, the energy density approach and/or the porosity

evolution mechanism may not be enough to explain the resulting microstructure and mechanical behavior, especially since the same energy density and/or porosity level may be achieved by using several parameter combinations. However, there is still a lot to learn in this regard since a small disturbance of one process parameter can significantly affect the final behaviors. In this respect, the effect of each process parameter (laser power, scan speed, and hatching space) must be studied to get a better understanding of the phenomena occurring during selective laser melting.

As stated above, many papers dealing with SLM maraging steel has been published. However, we could find very little by means of comprehensive and detailed research on its sensitivity behavior. Clearly, there is still a work to do in terms of perfecting and optimizing the use of SLM for maraging steels in the context of a cost-effective and efficient process. To fill this gap, this paper therefore sets out to conduct an in-depth study of the sensitivity of SLM maraging steel behaviors to small process parameter variations using stress-relieved maraging steel (C300) parts. The microstructure, densification rate, hardness and tensile strength of different samples are characterized. The ANOVA method was performed to find the optimum process parameters using statistical tools. A prediction model for each considered behavior (porosity, hardness, ultimate tensile strength) as a function of the process parameters considered (laser power P, scan speed V, hatching speed H) is proposed by processing the results of experiments of the ANOVA analysis.

4.5 EXPERIMENTAL PROCEDURES

4.5.1 Powder characteristics

In this study, a gas atomized maraging steel (C300) powder with a spherical morphology and a 15–53 μm size range (Figure 4.1), supplied by PLW Inc (Limestone Powder Wastes), was used. The chemical composition of the powder is shown in Table 4.1.

Table 4. 1. Chemical composition (wt%) of MS1.

C	Ni	Co	Mo	Mn,Si	Ti	Al	Cr	P,S	Fe
0.03	17-19	8.5- 10	4.5-5.2	0.1	0.6-0.8	0.15	0.5	0.01	Bal.
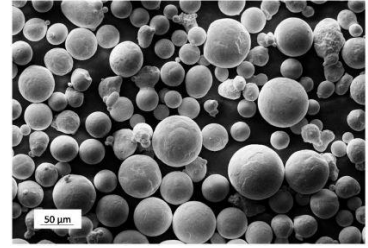
Figure 4. 1. MS1 Powder morphology [21].

4.5.2   SLM Process

The SLM EOS-M290 machine was used for the printing of the specimens. It mainly consisted of a Yb fiber laser with a maximum laser power of 400 W and a focused laser spot diameter approaching 100 μm, an automatic powder paving apparatus, an inert argon gas protection system and a computer system for process control. Sub-sized tensile specimens according to ASTM-E8 [56] were fabricated on the pure maraging steel substrate plate (Figure 4.2).
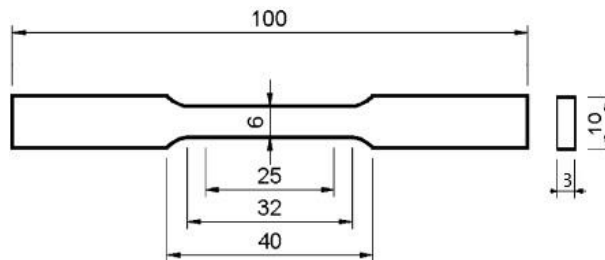
Figure 4. 2. Size of tensile test samples (mm).

The SLM process was conducted under argon atmosphere and with a constant powder layer thickness t = 40 μm. The following SLM parameters were used in the investigation: laser power P = 270 W, 295 W, and 320 W; scan speed V = 1000 mm/s, 1050 mm/s, and 1100 mm/s; hatch space H = 80 μm, 100 μm, and 120 μm according to a Taguchi experiment table (Table 4.2), in order to limit the number of experiments. All the specimens underwent a stress relief treatment at 490 °C for 4 hours in the air.

4.5.3 Microstructural and Porosity Evolution

For microstructural observation, the printed samples were first analyzed using an OLYMPUS LEXT OLS4100 confocal laser scanning microscope (CLSM) to obtain large optical micrographs through an automated assembly operation. A Field Emission Scanning Electron Microscope (FEG-SEM), model HITHACHI SU8230, equipped with energy dispersive spectroscopy (EDS), was used for microstructure and composition characterization. In the preparation phase, all the metallography and micro-hardness samples were cut from both edges of the manufactured AM coupons in a $10 \times 3 \times 4$ mm rectangular shape. They were polished using the standard polishing procedure to a size of 1 µm diamond paste. The microstructure was revealed using Fry's reagent (1 g CuCl, 50 mL HCl, 50 mL HNO3, 150 mL H2O). Porosity (pores and cracks) characterization was carried out based on 5 micrographs images recorded with the confocal laser scanning microscope, using ImageJ, a license-free software.

Table 4. 2. Taguchi experience Table.

Samples	Laser Power (w)	Laser Speed (mm/s)	Hatching space (µm)	Energy Density ($E=\frac{P}{V*H*t}$ j/mm^3)
#E1	270	1000	80	84.375
#E2	270	1050	100	64.285
#E3	270	1100	120	51.136
#E4	295	1000	100	73.750
#E5	295	1050	120	58.532
#E6	295	1100	80	83.807
#E7	320	1000	120	66.666
#E8	320	1050	80	95.238
#E9	320	1100	100	72.727

4.5.4 Tensile property tests

Rockwell C (HRC) hardness tests were performed on stress-relieved as-built samples using a Clemex ST-2000 machine. The hardness measurements were taken at an average of thirty points on the diagonal of the samples, with a 200 µm pitch. The applied load was 300 gf and the dwell time was 10 seconds. A mean hardness value of five indentations was

reported. The Ultimate Tensile Strength and Elongation (%) of SLM maraging steel (C300) samples were determined from the tensile tests conducted according to ASTM-E8 [56]. A tensile testing machine (810 Material Test System) with 0.01 mm/s test speed was used. The loading direction was parallel to the building direction of the samples. A mean tensile behavior value of five indentations was reported.

4.6   RESULTS AND DISCUSSION

4.6.1   Microstructural and Porosity evolution – ANOVA analysis

Studying the microstructure of SLM maraging steel (C300) parts helps to understand the melting process and investigate densification mechanisms in relation to process parameters. Representative high magnification CLSM and SEM micrographs are reported in Figure 4.3 and Figure 4.4, respectively.

Figure 4.3 (a-i) shows typical microstructures of the stress-relieved SLM maraging steel (C300), observed using confocal laser scanning microscopy (CLSM). In general, a high-cooling rate and a rapid solidification mode led to the formation of metastable microstructures with multi-substructures and bimodal grain sizes. This morphology is attributable to the high-cooling rate and the rapid solidification mode observed during the SLM process. High-temperature gradients, high and local cooling rates, as well as directional solidification in laser melting, result in cellular and columnar sub-grains appearing in the same molten pool. The cellular substructure, columnar substructure, equiaxed substructure, cell boundaries, melt pool boundaries, porosity, and hardening particles are typical microstructural features depicted in these figures. A bimodal grain size distribution, one with larger sizes and the other with smaller size areas, was observed, especially with increased energy density. Similar results have also been reported by [57-58]. Stress-relieved SLM maraging steel (C300) retains a martensitic matrix with varying levels of ferrite, bainite, and retained or returned austenite. The presence of ferrite is more visible in low and moderate laser energy density conditions (E<=65 j/mm 3). As reported by [59], the amount of

martensite laths varies as a function of the history of the thermal gradients applied, and therefore, the process energy density. At the same laser power, 270 W (Figure 4.3 (a-c)), 295 W (Figure 4.3 (d-f)), and 320 W (Figure 4.3 (g-i)), the retained austenite is more apparent with low-density energy.

Figure 4.3 (a-c) shows a representative microstructure of 3 different groups of samples (#E1, #E2, and #E3, respectively) with a constant laser power of 270 W and different process parameters (V = 1000, 1050, 1100 mm/s and H = 80, 100, 120 μm). The images illustrate how decreasing the energy density from #E1, #E2 to #E3, influences the microstructure. Furthermore, the microstructure of as-built SLM maraging steel (C300), without post-treatment steps, is austenitic [60-64]. Maraging steel (C300), stress relief-treated at 490 °C for 4 hours, with a low carbon content and a high solidification temperature, will tend to produce a martensite cellular-equiaxed matrix with small amounts of lath martensite [59]. However, its detailed characterization requires the use of a Transmission Electron Microscope (TEM), which is out of the scope of the present work. This is displayed more clearly in Figure 4.3 (c) and Figure 4.3 (h), where CLSM microstructure of two parts with low (#E3, ~50 j/mm 3) and high (#E8, ~95 j/mm 3) energy density is observed. This may be confirmed by SEM micrographs of these same two parts (low density: #E3, high density: #E8) shown in Figure 4.4 (a) and (b), respectively. The lower energy density (~50 j/mm 3) part #E3 (Figure 4.3(c) or Figure 4.4(a)) shows a microstructure with a large cellular substructure. Tan et al. [65-66] and Shamsdini et al. [67] observed a similar cellular structure in maraging steel fabricated by SLM. The proportion of cellular grains decreased by increasing the energy density until just a columnar microstructure could be observed (i.e., Figure 4.3 (h) et Figure 4.4(b)). The higher energy density (~95 j/mm 3) part #E8 (Figure 4.3(h) or Figure 4.4(b)) displays the horizontal band characteristic which determines the zones in between coarser and finer grain sizes. The resulting microstructure had a grain growth direction upwards in the building direction or perpendicular to the scanning direction.

In Figure 4.3 (d - i), only columnar-shaped austenite grains, in a martensitic matrix, with high angle boundaries and solute band boundaries are contrasted. This can give an idea

of the shape of the interfaces between layers without necessarily indicating their exact positions. During the solidification of maraging steel (C300) with a primary martensite matrix, the main addition elements (Ni, Co, Mo, and Ti), traces (P and S), and, to a lesser extent, Si, are distributed in the liquid [66-68]. This is because the solubility of substitutional elements, including Ni, Co, Mo, and Ti in the solid, is lower than that in the liquid [68]. The white boundary around the grain joints is composed of Fe, Ni, Co, Mo, Ti, and Al. However, the contents of Ni, Co, Mo, and Ti are much higher than those of the dark zone (zone D), as shown in Figure 4.5 and Table 4.3. These alloying elements are forced to move to the liquid zone when grain formation is initiated. As neighboring grains meet, regions rich in Ni, Co, Mo, and Ti form in the boundary (zone B). Depending on the laser power and the scanning speed, the solute bands in SLM maraging steel (C300) can be enriched or depleted [69-71] in the elements mentioned above.

A comparison of the microstructures of Figure 4.3 (a-c) with Figure 4.3 (d-f) and Figure 4.3 (g-i) allows to suggest a conclusion on the effect of variation of laser power. By increasing the laser power, the depth/width ratio of the layers decreases. This can disrupt the alignment of the heat transfer direction, and among other things, the evolution in the crystallographic texture. In Figure 4.3(d-i), a significant refinement of the spheroidal-shaped black inclusions as compared to Figure 4.3 (a-c) is also visible. A similar observation was reported by Yasa et al. [72]. This effect is linked to the amount of heat dissipation of the molten pool. During a single sweep, the powder dissipates heat more slowly than the solid material surrounding the weld pool during remelting, for example [72-73]. At low energy density values (<60 J/mm 3), the microstructure consists mainly of smaller grains with a random orientation. Increasing the energy density, a dominant orientation appears and the microstructure consists of several large and elongated grains [72-73]. This could be related to the strong influence of the melting-solidification conditions, which are controlled by the process parameters, on the size of the cellular substructure [72-73].

When comparing parts #E1 (Figure 4.3 (a)) and #E6 (Figure 4.3 (f)), which had an energy density (ED) of around ~84 J/mm 3, it was observed that #E6 (Figure 4.3 (f)) had a

slightly more bimodal size distribution, with some areas with coarser grains in between the horizontal bands. The main difference between #E1 and #E6 parts were the process parameter setting of P and V, where part #E1 had a P=270 W and V=1000 mm/s and part #E6 was set to P=295 W and V=1050 mm/s.
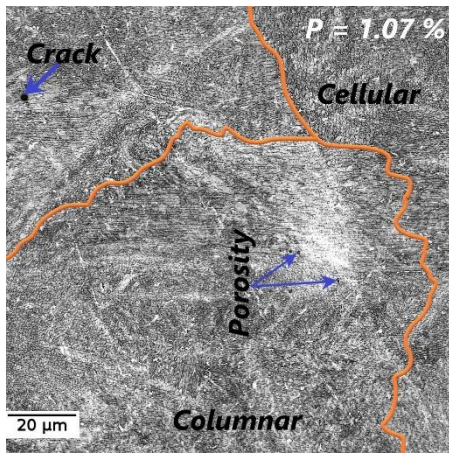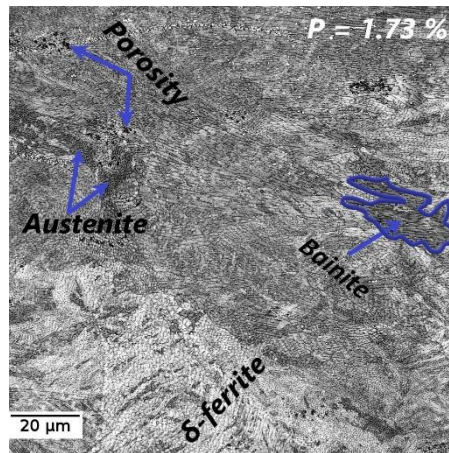
(j) Samples (#E1)   (k) Samples (#E2)   (l) Samples (#E3)
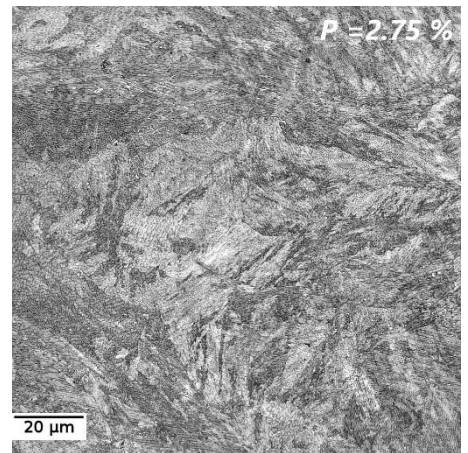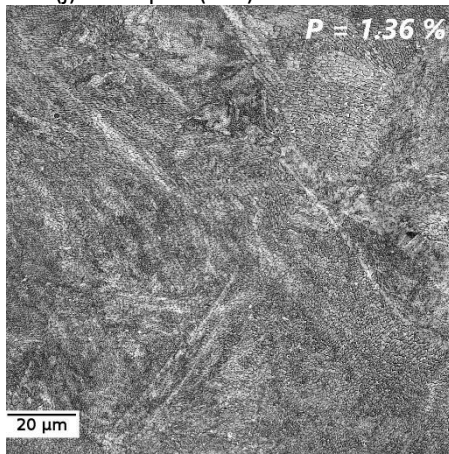
(m) Samples (#E4)   (n) Samples (#E5)   (o) Samples (#E6)

(p) Samples (#E7) (q) Samples (#E8) (r) Samples (#E9)
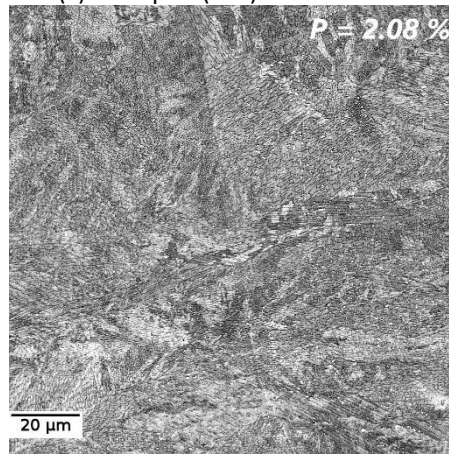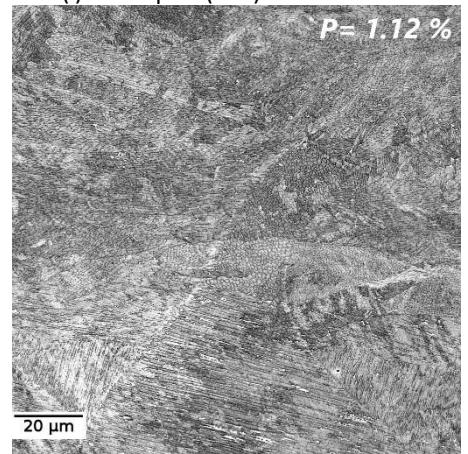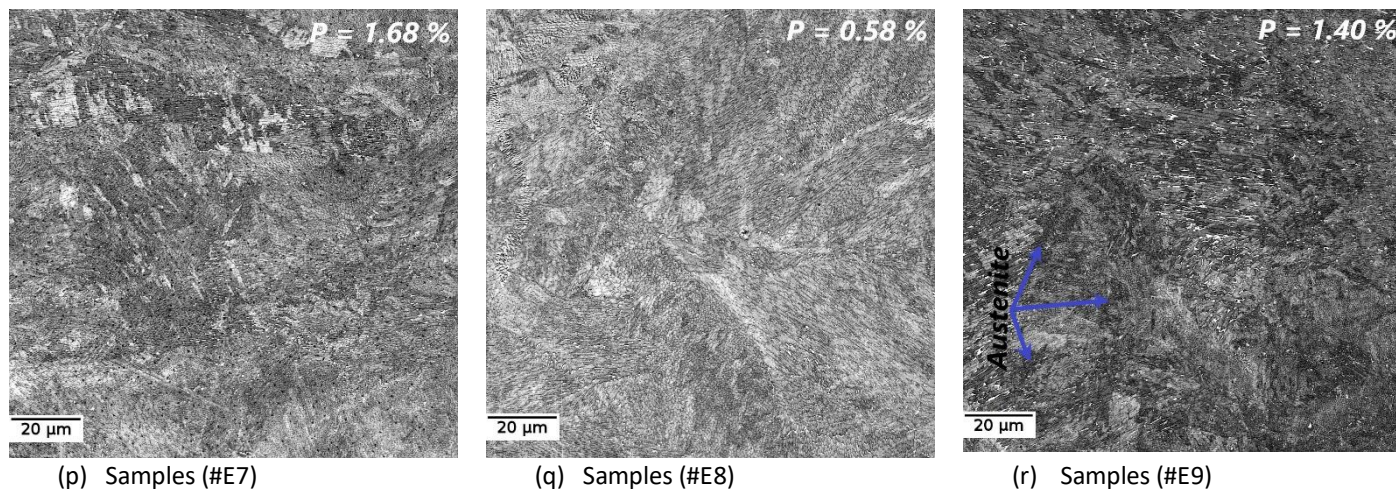
Figure 4. 3. Micrographs of stress-relieved as-built maraging steel (C300) Samples (a) #E1
(b) #E2 (c) #E3 (d) #E4 (e) #E5 (f) #E6 (g) #E7 (h) #E8 (i) #E9.

Figure 4.4 shows the microstructure of the samples selected for the SEM study, taken with a x6000 magnification. Samples selected for SEM had some critical mechanical performance, including part #E3, with the highest porosity and lowest hardness, part #E8, with the lowest porosity, the highest hardness, and the lowest ultimate tensile strength, and part #E2, with the highest ultimate tensile strength. Porosity, hardness, and tensile strength results will be shown and discussed later herein. The main micro-characteristics of the stress-relieved as-built samples consist of a cell and columnar structure with a white border (black arrows in Figure 4.4 (b-c)). As shown in Figure 4.4 (a-c), the internal structure of the columnar grains consists of cellular and dendritic columns with parallel growth directions, separated from each other by low angle boundaries. Figure 4.4 suggests that the morphology of the microstructure of the presented samples is columnar-dendritic in all cases, with a small number of cells, especially in high energy density, with the presence of δ-ferrite (blue arrows in Figure 4.4 (b-c)), martensite, retained austenite and hardening carbides. Figure 4.4 (b) clearly suggests that the main microstructure becomes refined with the application of the highest energy density considered for this study, which can be returned to the high-cooling rate. The columnar grains of this microstructure have a parallel growth direction, separated by a low angle boundary. Similar micrographs of cellular-columnar structures were presented

203

in previous works [65-66, 74]. In a TEM investigation, Tan et al. [65] reported the types and sizes of precipitates and the dislocation on cell boundaries, which are characterized by an enrichment in Mo, Ni and Ti. These elements constitute the banding lines around the cell grains. Moreover, the EDS analysis of the highest ED samples (#E8), which have the lowest porosity, highest hardness, and lowest ultimate tensile strengths of all the samples, and which are shown in Figure 4.5. The EDS analysis reports the chemical composition of the white border containing Fe, Ni, Co, Mo, Ti, and Al. As the solubility of the substitutional elements, including Ni, Co, Mo, and Ti in the solid is less than that in liquid, the Mo and Ti contents are much higher than those of the dark zone, as shown in Figure 4.5 and Table 4.3.
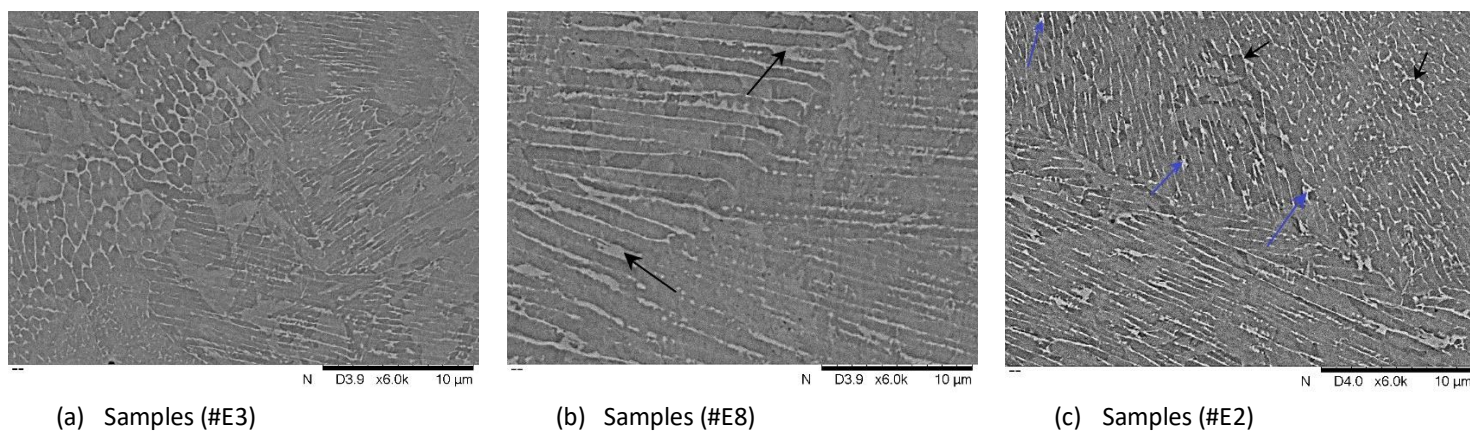
(a) Samples (#E3)　　　　(b) Samples (#E8)　　　　(c) Samples (#E2)

Figure 4. 4. SEM Micrographs of (a) #E3 specimens – lower ED and hardness (b) #E8 specimens–higher ED and hardness (c) #E2 specimens–higher UTS.

The EDS results shown in Figure 4.5 and Table 4.3 agrees with the typical characteristics of intercellular distribution due to rapid solidification [57-58]. According to EDS analysis, grain boundary regions (indicated by black arrows in Figure 4.4 (a-c)) are rich in Ni, Co, Mo, and Ti. The authors of in [75-78] observed the cellular limits by TEM examinations. They observed an extensive network of dislocations, as well as an enrichment in Ni, Co, Ti, and Mo. Intercellular solidification is characterized by a primary martensite matrix. This also confirms the presence, as expected, of ferrite as separate primary particles (indicated by blue arrows in Figure 4.4 (a-c)) only at the columnar grain boundaries. As

predicted, in the case of variants (#E2) and (#E3), the ferrite particles occurred locally in the intercellular regions and around the columnar grain boundaries (Figure 4.5 (a, b)) in amounts greater than for (#E8). This is because the process energy density for the variants (#E3) is lower than those for (#E2), which is lower than those for (#E8). The fraction and size of nano-inclusions depend on the degree of superheating of the liquid and the temperature gradient. The nanometric size spherical inclusions are indicated in Figure 4.5 by black circles. This intercellular investigation, performed via EDS, indicates the solidification mode with primary martensite, which may confirm the presence of δ-ferrite in banding lines, intercellular, and grain boundaries. Tan et al. [65] reported similar observations, using TEM micrographs.

(c)   (d)
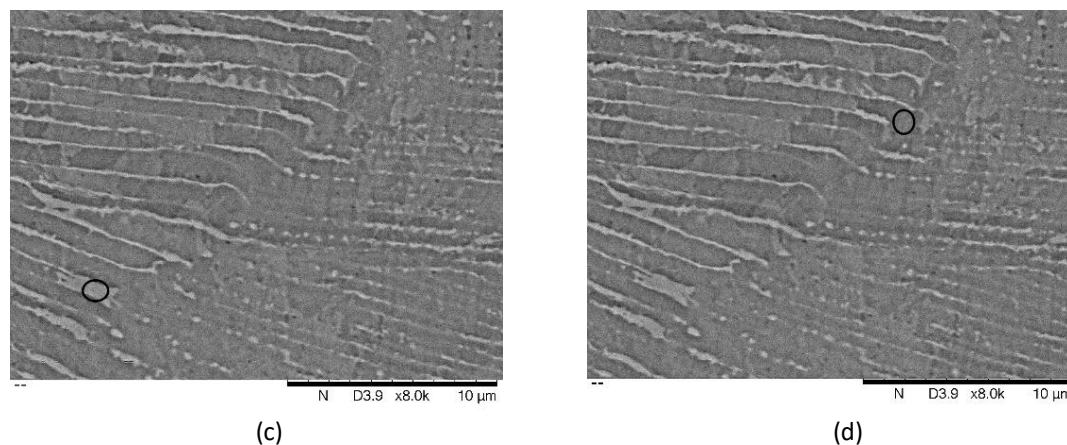
Figure 4. 5. Microstructure EDS analyze (a) Zone B (b) Zone D.

Table 4. 3. EDS analyze: Chemical composition between Zone B and Zone S.

EDS	Fe	Ni	Co	Mo	TI	Cr	C
Zone B	63.02	17.69	10.15	6.75	1.27	0.20	0.82
Zone D	70.33	13.92	8.38	5.42	0.90	0.27	0.78

At this stage, our different microstructure observations confirm that the process parameters play an important role in controlling the internal composition of the microstructure, which agrees with the literature [79-80]. Also, they can affect the mechanical behaviors, such as the densification, hardness, and tensile strength. In summary, a significant

microstructural heterogeneity was developed in the SLM maraging steel (C300). The microstructure showed a multi-substructure and bimodal grain size distribution, which was more observed at higher ED. At lower ED, a more homogeneous grain size distribution can be observed (Figure 4.3 (c), Figure 4.4 (a), which present CLSM and SEM micrographs of lowest ED - part #E3). This can be attributed to the effect of the automatic remelting of an already solidified layer upon melting of the next layer, which can allow the prior austenite grains to grow, and the solidification then results in more martensite laths, as was seen. The already solidified layers may be partially or fully remelted, generating a grain size growth inside the remelted region according to the build direction. Therefore, more martensitic laths can be observed in this remelted region. These martensitic laths tend to form in an upward-sloping direction following the direction of construction. Far from the remelted region of each layer—i.e., between the lathes—a finer martensite structure was generated due to the high thermal gradients. In fact, given that the thermal gradient is highest at the bottom of the molten pool, solidification and phase transformation are fastest near the solid mass or the substrate. Often, the microstructure is strongly influenced by the thermal gradient. Therefore, it can be assumed that the process parameter that influences the heat or energy input in a short period of time would therefore have a significant effect on the thermal gradient. The process parameters, which may contribute to the thermal gradient, are mainly laser power (P) and the exposure time (which depend on the scan speed). The hatching space (H) and the layer thickness (t) can also affect the initial microstructure since they will affect the laser energy density ED penetration and the automatic remelted region thickness, but their effects can be limited because both parameters (H, t) are already controlled by the other process parameters, to provide a good selective laser melting operation with adequate coverage and penetration.

Furthermore, based on the CLSM micrographs observations, a porosity and density analysis were done, using the "ImageJ" software. The porosity measurement results for the nine groups of specimens are listed in Table 4.4 and shown on the top right corner of the microstructure micrographs, presented in Figure 4.3. Figure 4.6 shows the detected porosity variations as a function of laser input energy density for the nine specimen groups. Overall,

the porosity decreases with the increase in laser input energy density. It should be emphasized that when the ED is between ~65 and ~85 J/mm 3 (i.e., samples #E2, #E7, #E9, #E7, #E6, and #E1), the porosity tends to decrease with a steady soft slope, which is an important and useful indication to produce AM parts. As shown in Table 4.4 and Figure 4.6, the lowest and highest porosities measured were for samples #E8, which were produced with the highest energy density (~95 J/mm 3), and samples #E3, which were produced with the lowest energy density (~50 J/mm 3). The porosity levels measured in samples #E3 produced at 50 J/mm 3 are greater by about 2.7% and are less than 0.6% for samples #E8 produced at 95 J/mm 3. Determining the porosity level is very important in order to assess the densification of parts. Based on the above results, samples #E8 have the highest material density of 99.42%, whereas samples #E3 have the least density of 97.25%. Under similar conditions, Tan et al. [66] and Król et al. [74] reported similar porosity results in the case of SLM maraging steel (C300). Such low porosity levels thus prove that the SLM process can produce fully dense final parts made of maraging steel (C300). Also, it is noticeable that the porosity decreases as the energy density increases.

Table 4. 4. Porosity - Relative density rate.

Sample	#E1	#E2	#E3	#E4	#E5	#E6	#E7	#E8	#E9
Energy Density (J/mm 3)	84.375	64.285	51.136	73.750	58.532	83.807	66.666	95.238	72.727
Porosity (%)	1.07	1.73	2.75	1.36	2.08	1.12	1.68	0.58	1.40
Relative density (%)	98.93	98.27	97.25	98.64	97.92	98.88	98.32	99.42	98.6
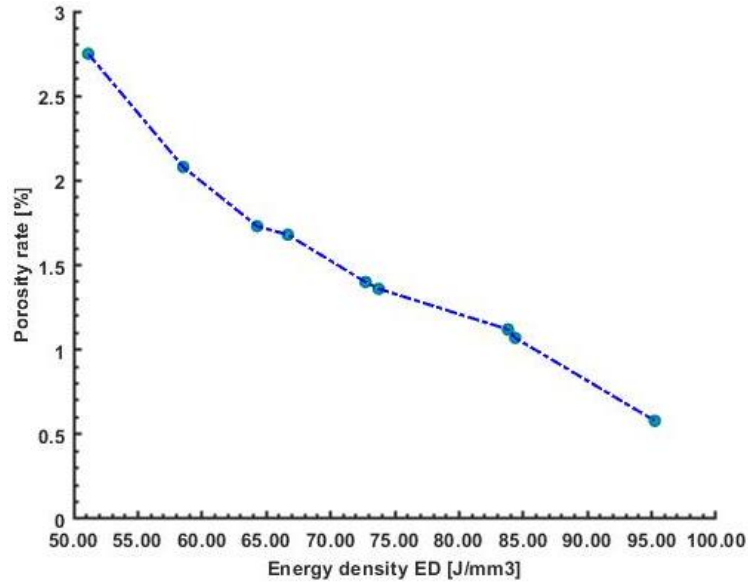
Figure 4. 6. Porosity percentage as a function of volumetric energy density ED.

Figure 4.7 illustrates variations in porosity among the nine sample groups (#E1 - #E9) with changes in the process parameters considered, namely, laser power, scan speed, and hatching space. According to the extremum difference analysis method [75], the value of the extremum difference can be used to quantify the influence of each SLM process parameter on the porosity level. This means that the greater the extremum difference, the greater the influence of a factor will be. As shown in Figure 4.7 (a), the following extremum difference values were obtained for each factor: 0.63% for laser power, 0.39% for scan speed, and 1.24% for hatching space. Globally, the extremum difference values for energy density are about 1.5%. Therefore, the influence of the three factors on porosity in the sequence is hatch spacing> laser power> scan speed. The hatching space is the most significant factor influencing the porosity rate, whereas the scan speed has little effect. Figure 4.7 (a) shows that the porosity decreases with an increase in laser power. In fact, the porosity decreases by 0.33%—going from 1.85% to 1.52%—as the laser power increases from 270 W to 295 W. Then, it decreases to 1.22% with an increase in the laser power to 320 W. Normally, a higher laser power value will bring about stronger energy, which may reduce the porosity [76]. However, when the energy density exceeds a certain value [77], the increased input heat may gasify some powders, which may result in a higher porosity. Figure 4.7 (a) shows that the

porosity value follows a very low increasing trend as the increase in scan speed from 1000 to 1100 mm/s, with a total increment of 0.38%. It is interesting to note that the increase in the scan speed from 1000 to 1100 mm/s has a small effect on the variation of porosity level, as shown in Figure 4.7 (a). When the scan speed drops to a certain value, excessive energy input will be generated, which will cause a higher porosity [78].

Figure 4.7 (a) also shows that the porosity increases sharply with an increase in hatching space, from 80 µm to 120 µm, with a total increment of 1.25%. The small hatch spacing condition increases the overlap area of adjacent scanning lines, which may generate higher laser beam energy. Thus, the uniform distribution of energy will cause the powder between the scanning lines to melt completely, and the depth of the melting lines will tend to be evenly arranged. As a result, the subsequent melting liquid grows on the solidified scanning lines and substrate (i.e., solidified layer). As such, each scanning line proceeds stably from liquid to solid. It can be anticipated from the results of Figure 4.7 (a) and from the RSM graph presented in Figure 4.7 (b-d) that the optimal combination, in terms of porosity, of the three processing parameters is a laser power of 320 W, a scan speed of 1000 mm/s, and a hatch spacing of 80 µm, with a constant layer thickness of 40 µm. For this combination, the volumetric energy density E is easily calculated by the following equation: E=P/(V*H*t) j/mm 3 = 100 j/mm 3.

Figure 4.7 (b) illustrates the corresponding contour plots of the effects of laser power and scanning speed on the porosity rate, while the hatching space was set at the middle level (H=100 µm). It can be observed that the porosity increases with a decrease in power and an increase in scanning speed. When the scanning speed is 1100 mm/s and the power is 270 W, the maximum porosity is more than 2%. However, when the scanning speed is 1000 mm/s and the power is 320 W, the minimum porosity is less than 1.2%. This indicates that a smaller scanning speed and larger laser power should be considered during SLM to reduce the porosity rate.

Figure 4.7 (c) displays the corresponding contours, highlighting the effect of laser power and hatching space on the porosity rate, while the scanning speed is set at middle level

(V=1000 mm/s). The results need to show that the porosity decreases with an increase in laser power. In addition, with an increase in hatching space from 80 µm to 120 µm, the porosity increases from 1.2% to 2.4% at a power of 270 W, and increases significantly from 0.8% to 1.8% at a power of 320 W. The analysis shows that the interaction effect is significant. It also shows that a lower hatching space with a larger power in the test range is more conducive to a lower porosity rate. Figure 4.7 (d) displays the effects of scanning speed and hatching space on the porosity rate, while the power was set at the middle level. The porosity increases significantly from 0.8% to 1.2% with an increase in scanning speed from 1000 mm/s to 1100 mm/s, at a hatching space of 0.08 mm, and at hatching space of 0.12 mm, the porosity increases from 2% to 2.4%, which indicates that a low hatching space and a low scanning speed are beneficial for reducing the porosity rate.
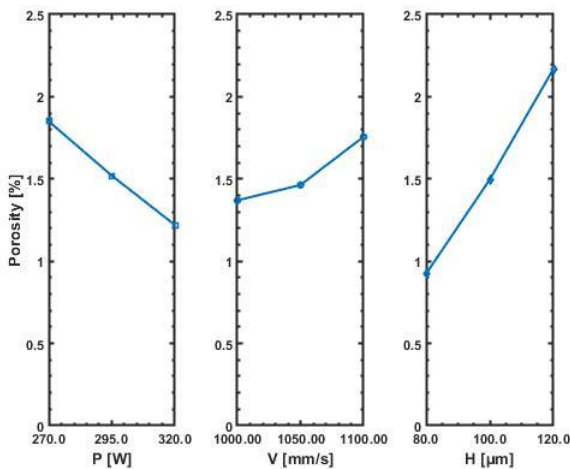
(a) Process parameters main effects for porosity
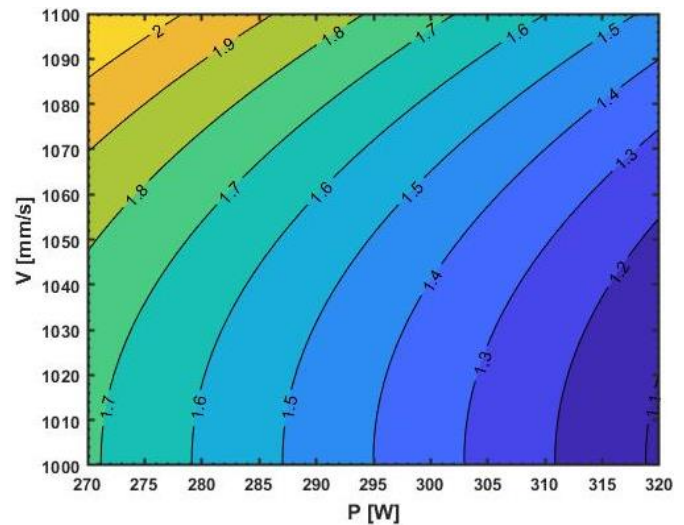
(b) Effects of P and V on porosity amount: contour plot (with H= 100 µm)
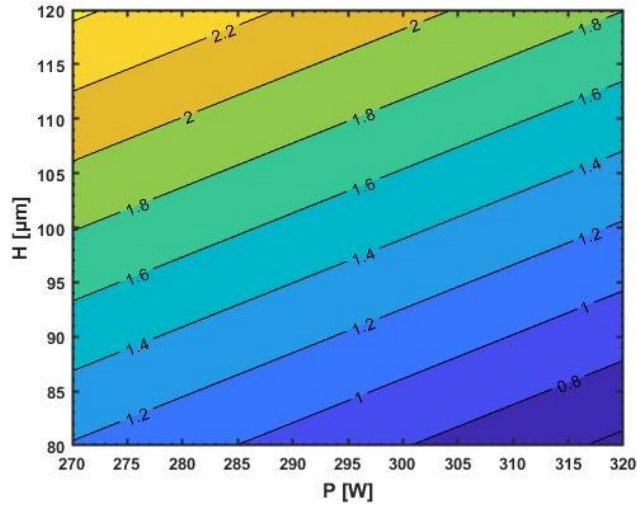
(c) Effects of P and H on porosity amount : contour plot
(with V= 1050 mm/s)
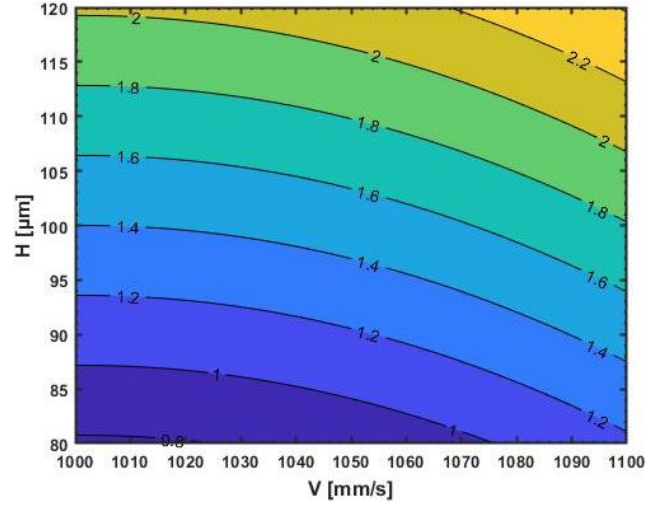
(d) Effects of V and H on porosity amount : contour plot
(with P= 295 W)

Figure 4. 7. Variation of resulted porosity (%) with processing parameters of laser power
(P), scan speed (V) and hatch spacing (H).

Table 4.5 presents the results of the ANOVA analysis, including the contribution of each factor. In this analysis, F is used to evaluate the significance of each factor on the porosity, which was computed and compared with a critical value [79]. DF is the degree of freedom, which is the number of the assigned levels minus 1 for a given factor. SS is the sum of squares relating to a factor. MS is the mean square of a factor, which is the sum of squares divided by the related degree of freedom. The sum of squares of the errors correlated to all factors was evaluated at 0.01, as shown in Table 4.5. In ANOVA, P-SIG indicates the significance level of the related factor. If P-SIG is less than 0.05, the related factor is statistically significant, and if P-SIG is less than 0.01, the related factor is highly significant [80]. Otherwise, the related factor is insignificant. From the P-SIG values shown in Table 4.5, it is evident that the laser power and hatching space factors are highly significant on the porosity amount of the SLM parts, whereas the scan speed with a P-SIG value of 0.06 shows an insignificant effect on the resulting porosity. From Table 4.5, it is obvious that the hatching space and laser power are the main factors influencing the porosity rate. To quantify the effect of each input parameter, its percentage contribution is calculated. The second column of Table 4.5 shows the percentage contribution of each factor to the porosity rate. Depending on the ANOVA results, the contribution rates of the laser power, scanning speed

211

and hatching space to porosity were 18.71%, 7.05%, and 73.28%, respectively. It can be concluded that the effect of the hatching space and laser power on the porosity is significant, and that the most important factor affecting the porosity is the hatching space (~73%).

Table 4. 5. Results of analysis of variance (ANOVA) due to obtained porosity.

Factor	Contribution (%)	DF	SS	MS	F	P-SIG
P	18,71	1,00	0,60	0,60	226,44	0,00
V	7,05	1,00	0,22	0,02	6,92	0,06
H	73,28	1,00	2,33	2,33	886,69	0,00
V*V	0,63	1,00	0,02	0,02	7,61	0,05
Error	0,33	4,00	0,01	0,01		
Total	100,00	8,00	3,18			

Model summary	S	R2	R2(adj)	R2(planned)		
	0.0512754	99.67	99.34	97.72		

The statistical regression model of Equation (4.1) can be used to predict porosity by collecting the analyzed variables. The following equation represents the ultimate empirical porosity rate model:

$$\text{Porosity} = 42.1 - 0.012600.*P - 0.0801.*V + 0.03117.*H + 0.000040.*V.*V \qquad (4.1)$$

The porosity predictive model presented in Equation (4.1), resulting from ANOVA analysis, allows to plot the correlation curve between the predictive and the experimentally measured porosity rates (Table 4.4, Figure 4.6). The scatterplot always stays around an almost linear line, as shown in Figure 4.8.
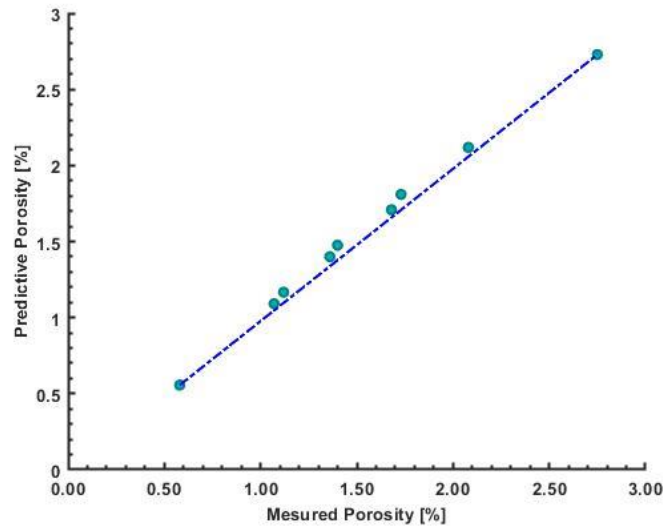
Figure 4. 8. Correlation between measured and predictive Porosity amount (%).

Because it is necessary to test the significance of porosity model (equation 4.1), ANOVA is used to evaluate the porosity experimental measurements. Table 4.5 lists ANOVA statistics for porosity models. The coefficient R^2 refers to the ratio of regression variation to total variation. It evaluates the goodness of fit. When R^2 is close to 1, the difference between predicted and measured values is very small. For the porosity rate, the R^2 of the regression model is 99.67% in Table 4.5, which shows that the model can explain 99.67% of the total output value changes. Besides, if the adjusted R^2 and predicted R^2 are high and close, the regression model can fully explain the process. In Table 4.5 of this study, the adjusted R^2 value is 99.34%, which indicates that only 0.66% of the changes cannot be explained by the regression model, showing that the fitting degree of the model is good. To illustrate the influence of process parameters on the interaction of the porosity rate. RSM corresponding contour graphs were generated based on the regression model, presented in Equation 4.1. The interaction between different combinations of factors can easily be understood from the curve section. The curvature of each contour plot indicates whether the interaction between two independent factors is significant. When the contour is ellipsoid, it shows that the two factors have larger interactions, and when it is spherical, then the interaction between the two factors is smaller.

213

4.6.2   Mechanical Behavior – ANOVA Analysis

Energy density is an important factor in determining the final mechanical behavior of parts produced by the SLM process [81-83]. It can influence the relative density, microstructure, and mechanical performance of such parts. In this study, three factors (process parameters) affecting the energy density in SLM maraging steel (C300) powder, namely, the laser power (P), scanning speed (V), and hatching space (H), as well as their interactions were investigated using the Taguchi-ANOVA method to determine the sensitivity of mechanical properties to them. This range of the factors was chosen to disrupt the process parameters a bit, with the laser power (P) ranging from 270 to 320 W, with a disturbance of 25 W, the scanning speed (V) ranging from 1000 to 1100 mm/s, with a disturbance of 50 mm/s, and the hatching space (H) ranging from 80 to 120 µm, with a disturbance of 20 µm, as shown in Table 4.2. The influence of these factors on the mechanical performance of parts was investigated by conducting hardness and tensile experimental tests and using an ANOVA analysis of the experiments results.

The results of the hardness tests are listed in Table 4.6. Sample (# E3), which was produced with a laser power of 270 W, scan speed of 1100 mm/s, and a hatch distance of 0.12 mm, has the weakest hardness and scan density. In contrast, sample (# E8) which was manufactured with corresponding values of 320 W, 1050 mm/s and 0.08 mm has the highest hardness of all the samples. This may be attributable to the porosity level measured in the previous section. In fact, samples the #E3 group has the highest porosity (2.75%), and consequently, its hardness values will be the lowest. The #E8 sample group has the lowest porosity (0.58%), and so its value will naturally be highest. As the porosity increases, the hardness and the relative density of the part decrease. This result agrees with the literature [84-89], which observed that the density is correlated with the hardness of sintered parts. The energy density was also calculated from the nominal values of the process parameters and the hardness values are measured and reported in Table 4.6.

Table 4. 6. Results of hardness tests.

samples	#E1	#E2	#E3	#E4	#E5	#E6	#E7	#E8	#E9
Energy Density (J/mm 3)	84.375	64.285	51.136	73.750	58.532	83.807	66.666	95.238	72.727
Measured Hardness (HRC)	56.16	50.55	47.17	53.22	49.21	55.920	51.25	58.26	53.03

The ultimate strength (UTS) was measured and is shown in Table 4.7 and tensile strain graphs are plotted in Figure 4.9. The results were classified into 3 categories according to laser power. The tensile properties for stress-relieved as-built maraging steel (C300) were measured between 1450-1650 MPa for the yield strength and between 1707-1828 MPa for the ultimate tensile strength. Sample (#E2), which was fabricated using 270 W of laser power, 1050 mm/s of scanning speed and 0.1 mm of hatching distance, has the highest UTS of all the specimens, while sample (#E8), which was processed with corresponding values of 320 W, 1050 mm/s and 0.08 mm, has the lowest UTS of all the specimens.

Table 4. 7. Results of UTS tests.

sample	#E1	#E2	#E3	#E4	#E5	#E6	#E7	#E8	#E9
Energy Density (J/mm 3)	84.375	64.285	51.136	73.750	58.532	83.807	66.666	95.238	72.727
Measured UTS (MPa)	1735	1828	1800	1775	1785	1730	1765	1707	1763
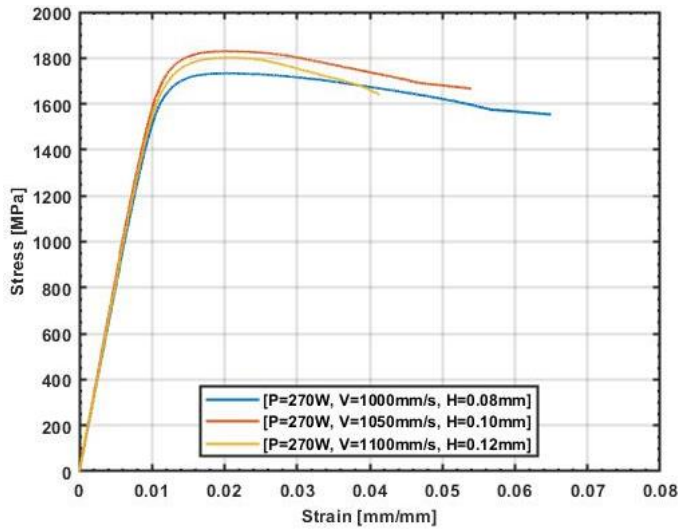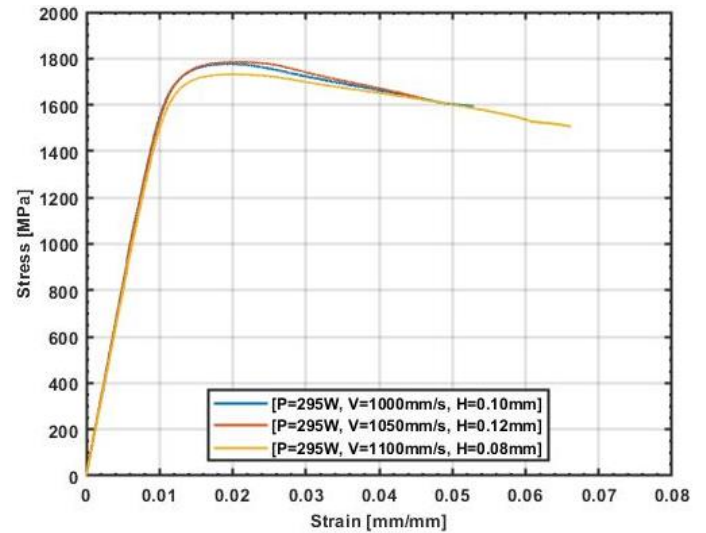
(a)   (b)
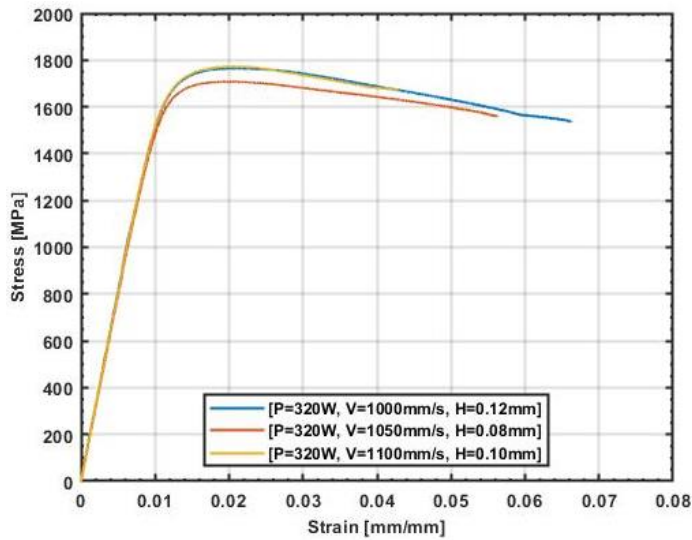
(c)

Figure 4. 9. Tensile performances - Stress-Strain curve (a) P=270 W, (b) P=295 W (c) P=320 W.

For this study, an Analysis of Variance (ANOVA) with a general linear model and based on the L9 Taguchi table (3 factors at 3 levels (Table 4.2)), was adopted. For each combination of factor levels, the same number of observations was considered. The factors considered herein are discrete variables. The Analysis of Variance (ANOVA) aims to evaluate the significance of the effects of the factors under consideration. A critical significance level of 0.05 was chosen. The "P-SIG" indicator output from ANOVA indicates whether or not the effect of a given factor is significant. Generally, the values of this indicator are very low, especially for the main effects of the factors considered and the first-order interactions between them. If the "P-SIG" indicator exceeds the critical significance level, the effect of the factor studied will automatically be overlooked, i.e., ANOVA considers this factor to be insignificant in statistical terms. Figure 4.10, Table 4.8, and Equation 4.1, as well as Figure 4.12, Table 4.9, and Equation 4.2 contain the results of the ANOVA analysis for hardness and tensile strength, respectively.

At the critical significance level of 0.05, the parameters of the SLM process and their interactions are statistically significant for hardness and for tensile strength. The details of

216

the experimental results are presented in the Table (4.6, 4.7) and Figure 4.9—made according to a Taguchi L9 experiment table—were analyzed by Minitab 16 software. The ANOVA results for the main factors and interactions are shown in Figures 4.10 and 4.12 and equations (4.1) and (4.2). Figure 4.10 (a) and Figure 4.12 (a) show the ANOVA results, which indicate that the factors (process parameters) were statistically significant for both the hardness and ultimate tensile strength. Laser power was the most significant factor influencing the hardness (Figure 4.10 (a)), and, in the case of ultimate tensile strength (Figure 4.12 (a)), the hatching space was the most significant factor. It is worth noting that the studied factors and their effects explain over 99% of the variations seen in responses, as evidenced by the correlation coefficients (R2 adj) from the ANOVA. The statistical regression models of equations (4.2) and (4.3) correspond to a mathematical prediction of responses:

$$\text{Hardness} = 88.14 + 0.05777*P - 0.01505*V - 0.5530*H + 0.001819*H*H \qquad (4.2)$$

$$\text{UTS} = -4317 - 10.327*P + 11.490*V + 33.158*H + 0.015600*P*P - 0.004800*V*V - 0.087500*H*H - 0.013500\ V*H \qquad (4.3)$$

Where P is laser power, V is scanning speed, and H is the Hatching space.

Further statistical analyses were used to study the process behaviors and optimize the process parameters. Figure 4.10 (c-e), and Figure 4.12 (c-e) show the process behavior trends. Each stripe in the contour plots indicates a range of values describing the process behavior under specific combinations of factors within the experimental region. These contour plots describe trends to optimize hardness and tensile strength are shown in Figure 4.10 (c-e), and Figure 4.12 (c-e), respectively, using black arrows. Considering the laser power, the maximum of hardness (> 57 HRC) was reached at the higher laser power level and the lower hatching space, while the maximum of tensile strength was reached at the lower laser power level and the higher hatching space.

The behavior observed in the contour plots can be understood by analyzing the influence of the individual and combined process parameters on the output, particularly the

hardness and tensile strength. As discussed earlier, increasing the laser power led to increased hardness and decreased tensile strength.

For instance, considering the hardness, Figure 4.10 (c, d, e) shows the contour plot of the response surface method (RSM) with the tendencies of the parameters with respect to the response of the hardness values of maraging steel (C300) as a function of the levels of factors used by the Taguchi-ANOVA study. It presents the contour plot displaying the hardness using different combinations of post-processing factors. As noted previously, it can be seen that the hatching space is the most influential parameter for hardness, followed by laser power and scanning speed. The interactions of the hatching space with the laser power and scanning speed also affect the hardness of samples manufactured by SLM. The main effect graph for hardness is shown in Figure 4.10 (a). The magnitude of the main effect further confirms that the process parameter having the most influence on the hardness is the hatching space. Increasing the hatching space from 0.08 mm to 0.12 mm has an adverse effect and leads to a 15% reduction in hardness. Unlike the hatch distance, the laser power has a positive influence on hardness. When the laser power increased from 270 W to 320 W, the hardness also increased. However, an 18.5% increase in the laser power increased the hardness by 5.6%. This allowed us to conclude that the effect of a laser power variation is less important than hatching space. Finally, increasing the scanning speed from 1000 mm/s to 1100 mm/s decreases the hardness of the specimens by 2.9%. A convergence towards good hardness values is observed with a hatching space of 0.08 mm. Figure 4.10 (a, b) shows the influence of energy density on hardness. Considering a hatching space of 0.12 mm, a higher sensitivity of the final macroscopic properties is observed on the variation of the energy density. Indeed, the hardness increased from 5% to 9.3% as the energy density went from 0.9 to 1.8 J/mm 2. When the hatching space was reduced from 0.12 mm to 0.1 mm and then to 0.08 mm, the hardness became less sensitive to changes in energy density. Considering a hatching space of 0.08 mm, a higher sensitivity of the final macroscopic properties is observed on the variation of the energy density. As indicated above, the hardness increased from 0.1% to 3.9%, respectively, with a change in energy density of up to 0.9 J/mm 2. Regarding the laser power, it is shown that an increase in its value of about 10% has a smaller effect than that of

the hatching space on the properties of the part. The increase in power by a value of 25 W involves increasing the hardness by a value of 2.8%.

(a) Process parameters main effects for Hardness

(b) Effects of P and V on hardness: contour plot (with H= 100 µm)

(c) Effects of P and H on hardness : contour plot (with V= 1050 mm/s)

(d) Effects of V and H on hardness : contour plot (with P= 295 W)
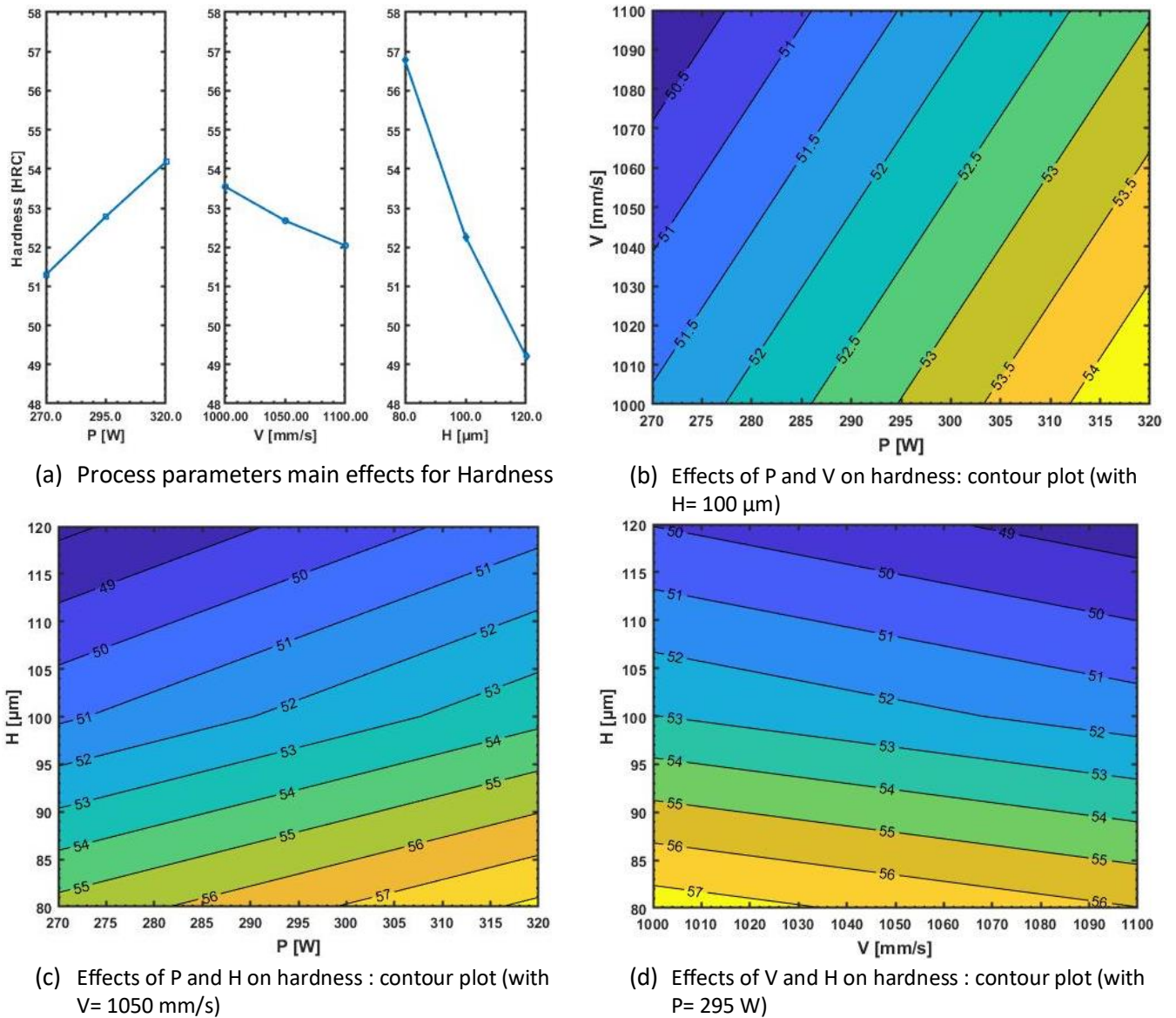
Figure 4. 10. Variation of resulted Hardness with processing parameters of laser power (P), scan speed (V) and hatch spacing (H).

Table 4.8 presents the results of the ANOVA analysis, where it can be seen that the laser power and hatching space factors have a significant effect on the hardness of the SLM parts, whereas the scan speed shows an insignificant effect on the resulting hardness behavior. It can also be seen that the hatching space and laser power are the main factors

influencing the hardness values. To quantify the effect of each input parameter, its percentage contribution was calculated. The second column of Table 4.8 shows the percentage contribution of each factor to the hardness behavior. Depending on the ANOVA results, the contribution rates of laser power, scanning speed and hatching space to porosity were 12.13%, 3.29%, and 83.37%, respectively. It can therefore be said that the effect of the hatching space and laser power on the hardness is significant, and that the most important factor affecting the hardness value is the hatching space (~83%).

Table 4. 8. Results of analysis of variance (ANOVA) due to obtained Hardness.

Factor	Contribution (%)	DF	SS	MS	F	P-SIG
P	12.13	1,00	12.514	12.5137	270.21	0,000
V	3.29	1,00	3.398	3.3975	73.36	0,001
H	83.37	1,00	2.439	2.4387	52.66	0,002
H*H	1.03	1,00	1.059	1.0585	22.86	0,009
Error	0.18	4,00	0.185	0.0463		
Total	100,00	8,00	103.150			

Model summary	S	R2	R2(adj)	R2(planned)		
	0.215199	99.82%	99.64%	99.00%		

Exploring the prediction model presented in Equation 4.2, a correlation graph was plotted in Figure 4.11, which confirms a high correlation interrelation between the predictive and the experimentally measured hardness values. Figure 4.11 shows that the scatterplot (correlation graph) always stays around an almost linear line.

An ANOVA analysis of hardness results was carried out to evaluate the significance of the regression models illustrated in Equation 4.2. Table 4.8 lists ANOVA statistics for the hardness models. The coefficient R^2 refers to the ratio of regression variation to total variation. It evaluates the goodness of fit. When R^2 is close to 1, the difference between predicted and measured values is very small. For hardness, the R^2 of the regression model is 99.82% in Table 4.8, which shows that the model can explain 99.82% of the total output value changes. Besides, if the adjusted R^2 and predicted R^2 are high and close, the regression

model can fully explain the process. In Table 4.8, the adjusted R2 value is 99.64%, which indicates that only 0.36% of the changes cannot be explained by the regression model, which shows that the fitting degree of the model is good.
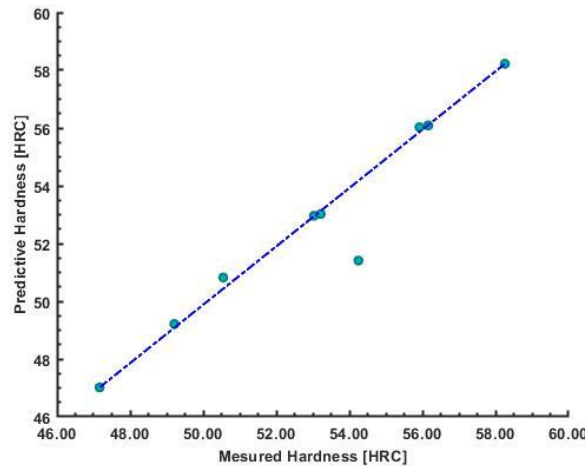
Figure 4. 11. Correlation between measured and predictive Hardness (HRC).

To illustrate the influence of process parameters on the hardness, RSM corresponding contour graphs were generated based on the regression model, presented in Equation 4.2. The interaction between different combinations of factors can be determined from the curve section. The curvature of each contour plot indicates whether or not the interaction between two independent factors is significant. Figure 4.10 (b) illustrates the corresponding contour plots of the effect of laser power and scanning speed on the hardness value, while the hatching space was set at the middle level (H=100 µm). It can be observed that the hardness increases with a decrease in scanning speed and an increase in laser power. When the scanning speed is 1100 mm/s and the power is 270 W, the minimum hardness is less than 50 HRC. However, when the scanning speed is 1000 mm/s and the power is 320 W, the maximum hardness is more than 54 HRC. This indicates that a smaller scanning speed and a larger laser power should be avoided during SLM to increase the hardness behavior. Figure 4.10 (c) displays the corresponding contours, highlighting the effects of laser power and hatching space on hardness, while the scanning speed is set at the middle level (V=1000 mm/s). The results show that the hardness value increases with an increase in laser power. Furthermore, with an

221

increase in hatching space from 80 µm to 120 µm, the hardness decreases from 54 HRC to 48 HRC at a power of 270 W, and decreases significantly from 58 HRC to 51 HRC at a power of 320 W. The analysis shows that a lower hatching space with a larger power in the test range is more conducive to higher hardness. Figure 4.10 (d) illustrates the effect of the scanning speed and hatching space on the hardness, while the power was set at the middle level (P=295 W). It is clear that at the same hatching space level, the scanning speed has no significant effect on the hardness behavior.

For the tensile behavior, Figure 4.12 illustrates the ANOVA results for the ultimate tensile strength (UTS). Figure 4.12 (a) shows the effect of the main factor on the ultimate tensile strength. The hatching space and laser power have the most important effect on UTS. The contour plot of the Response Surface Method (RSM) with the parameters tendencies in relation to the response of the UTS values of Maraging Steel (C300) as a function of the factor levels used by the Taguchi-ANOVA study is shown in Figure 4.12 (b, c, d). It presents the contour plot displaying the hardness using different combinations of post-processing factors. In Figure 4.12 (b, c, d), the contour lines show the UTS values. As noted previously, it can be observed that the laser power is the most influential parameter for the tensile characteristic, followed by the hatching space. From Figure 4.12 (a, b), it could be concluded that the laser speed has no significant effect on the mechanical propriety of manufactured parts. The interactions between these processing parameters also affect the UTS of the SLM maraging steel (C300). Increasing the laser power from 270 W to 320 W has a detrimental effect and causes a 2.4% reduction of the ultimate strength (UTS). Each increase of the laser power by 25 W causes a 1 to 1.5% reduction of the UTS. For the hatching distance, the laser power has the opposite influence on the tensile proprieties. When the hatching distance was increased from 0.08 mm to 0.1 mm, the UTS also increased. However, a 25% increment of the hatching distance increased the UTS by 3.5%. Consequently, the effect of hatching space small changes is less significant than laser power perturbation. Increasing the hatching distance more to than 0.1 mm causes some overlap issues and has a negative effect on the tensile proprieties.
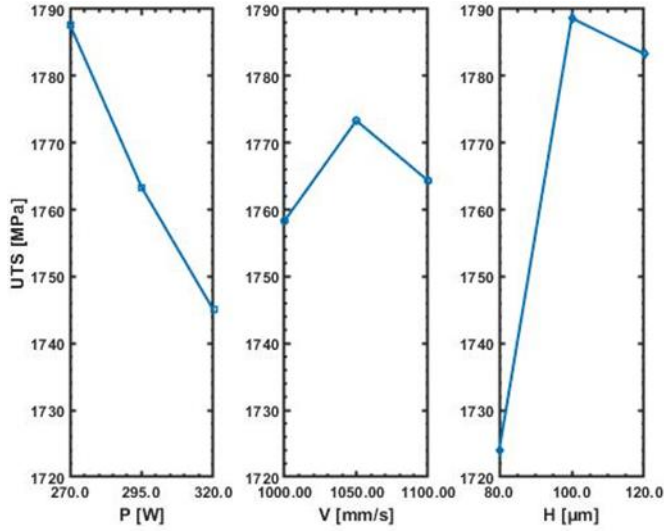
(a) Process parameters main effects for UTS
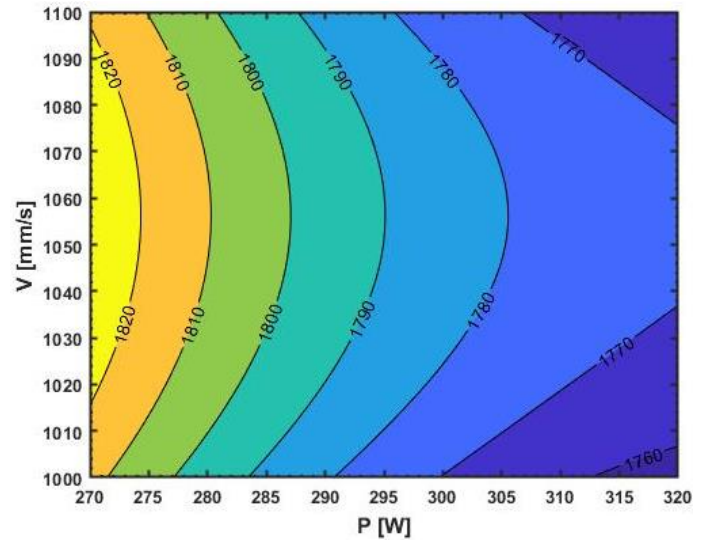
(b) Effects of P and V on UTS : contour plot (with H= 100 µm)
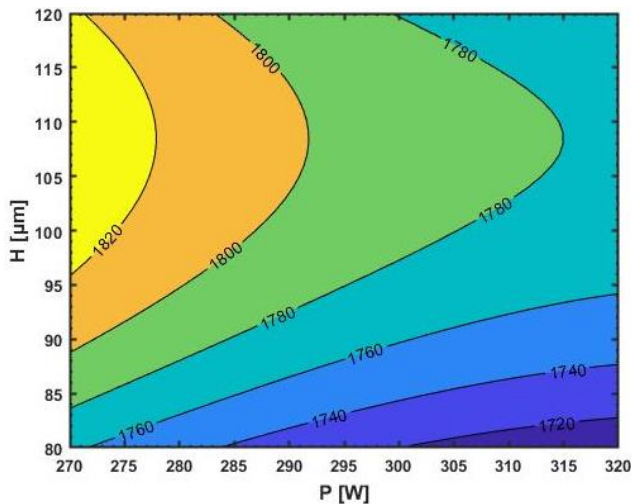
(c) Effects of P and H on UTS : contour plot (with V= 1050 mm/s)
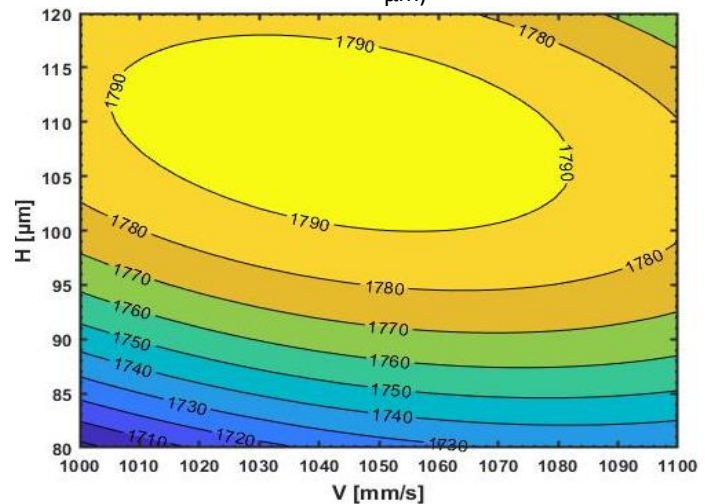
(d) Effects of V and H on UTS : contour plot (with P= 295 W)

Figure 4. 12. Variation of resulted UTS with processing parameters of laser power (P), scan speed (V) and hatch spacing (H).

Table 4.9 gives the results of the ANOVA analysis, where it is evident that the laser power and hatching space factors, as well as the square of the hatching space have a significant effect on the porosity of the SLM parts, whereas the scan speed with a P-SIG value of 0.014 has an insignificant effect on the resulting UTS. From Table 4.9, it is obvious that the hatching space and laser power are the main factors influencing the UTS. To quantify the effect of each input parameter, its percentage contribution is calculated. The second

223

column of Table 4.9 shows the percentage contribution of each factor to the porosity rate. Depending on the ANOVA results, the contribution rates of laser power, scanning speed and hatching space to porosity were 24.41%, 0.48%, and 47.21%, respectively.

Table 4. 9. Results of analysis of variance (ANOVA) due to obtained UTS.

Factor	Contribution (%)	DF	SS	MS	F	P-SIG
P	24.41	1	188.1	188.15	1128.88	0.019
V	0.48	1	368.9	368.91	2213.45	0.014
H	47.21	1	1624.8	1624.84	9749.04	0.006
P*P	0.16	1	152.1	152.10	912.60	0.021
V*V	2.57	1	288.0	288.00	1728.00	0.015
H*H	21.90	1	2450.0	2450.00	14700.00	0.005
V*H	3.26	1	364.5	364.50	2187.00	0.014
Error	0.00	1	0.2	0.17		
Total	100.00	8	11186.0			

Model summary	S	R2	R2(adj)	R2(planned)
	0.408248	100.00%	99.99%	*

Figure 4. 13 explores the prediction model illustrated in Equation 3 to compare the predictive UTS to the measured results. A high correlation was observed, and the scatterplot always stayed around an almost linear line.
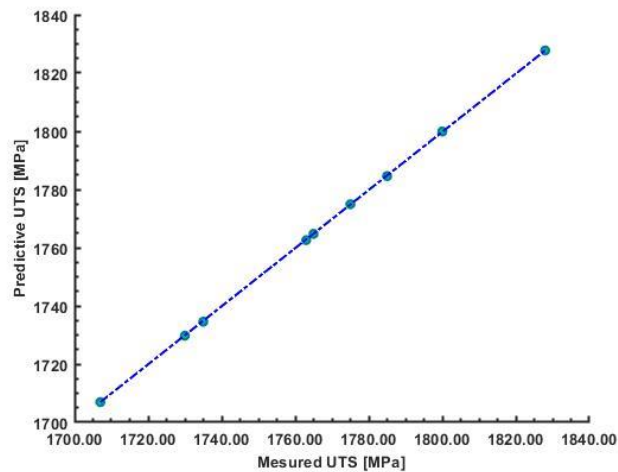
Figure 4. 13. Correlation between measured and predictive UTS (%).

The significance of the regression model resulting from the ANOVA study needs to be evaluated. Table 4.9 lists ANOVA statistics for the present work UTS model. For UTS, the R2 of the regression model is 100% in Table 4.9, which shows that the model can explain 100% of the total output value changes. Besides, if the adjusted R2 and predicted R2 are high and close, the regression model can fully explain the process. In Table 4.9 of this study, the adjusted R2 value is 99.99%, which indicates that only 0.01% of the changes cannot be explained by the regression model, which shows that the fitting degree of the model is good. To illustrate the influence of process parameters on the UTS, RSM corresponding contour graphs were generated based on the regression model, presented in Equation 4.3. Figure 4.12 (b) illustrates the corresponding contour plots of the effect of laser power and scanning speed on UTS, while the hatching space was set at the middle level (H=100 µm). It can be observed that the UTS increases with a decrease of laser power and that there is no significant effect on scanning speed. Figure 4.12 (c) displays the corresponding contours, highlighting the effect of laser power and hatching space on UTS, while the scanning speed is set at the middle level (V=1000 mm/s). The results need to show that the UTS increase with a decrease in laser power. In addition, with an increase in hatching space from 80 µm to 120 µm, UTS increases from 1780 MPa to 1820 MPa at a power of 270 W, and increases significantly from 1720 MPa to 1780 MPa at a power of 320 W. The analysis shows that a higher hatching space with a lower laser power in the test range is more conducive to a higher UTS. Figure 4.12 (d) displays the effects of scanning speed and hatching space on UTS, while the power was set at the middle level (P=295 W). The scanning speed has no significant effect on the tensile behavior.

4.7 CONCLUSIONS

Maraging steel (C300) specimens were successfully fabricated by SLM using laser power values of 270 W, 295 W and 320 W, scan speeds of 0.1 m/s, 0.105 m/s and 0.11 m/s, hatching spaces of 0.08 mm, 0.1 mm and 0.12 mm, and a constant layer thickness of 40 µm. Experiments were carried out with the aim of investigating the correlation between laser power, laser speed ad hatch spacing on the resulting microstructure and mechanical

properties. This paper aimed to carry out a sensitivity study permitting to determine the global effects of several relevant SLM parameters, mainly laser power P, scan speed V and hatch distance H, on the densification, hardness, and tensile behavior of SLM maraging steel (C300), using statistical tools (ANOVA). This ANOVA statistical tool allows to modulate the interrelation between the considered process parameters (P, V, H) and the considered final behavior (porosity, hardness, ultimate tensile strength (UTS)).

The research can be summarized as follows:

- There is a remarkable sensitivity relationship between the mechanical properties of SLM maraging steel (C300) and the SLM process parameters.
- The results also highlight the fact that the laser power and hatch spacing have the strongest influence on porosity, hardness, and ultimate strength, while the laser speed does not induce significant effects over the tested range.
- Hardness has a greater sensitivity to small changes in process parameters than does the ultimate tensile strength, UTS.
- A typical microstructure with a multi-substructure and bimodal grain size, in general, was observed.
- The microstructure was largely affected by the thermal gradient, the cooling and solidification mode. These are themselves affected by the energy density, and thus by the process parameters involved in the energy density such as the laser power.
- The highest relative density (99.42%) was achieved using P=320 W, V=1050 mm/s, and H=0.08 mm=80 μm, corresponding to a laser energy density of ~95.2 j/mm 3, while the maximum ultimate tensile strength (1828 MPa) part was achieved using a combination of parameters composed of P=270 W, V=1050 mm/s, and H=0.1 mm=100 μm, corresponding to a laser energy density of ~64.2 j/mm 3.
- Using ANOVA and RSM tools, the predictive models were analyzed. High determination coefficients were observed, which can improve the accuracy of these predictive models.

4.8 ACKNOWLEDGEMENT

4.9 REFERENCES

[1] : Cooke, S., Ahmadi, K., Willerth, S., & Herring, R. (2020). Metal additive manufacturing: Technology, metallurgy and modelling. Journal of Manufacturing Processes, 57, 978-1003.

[2] : Singh, S., Ramakrishna, S., & Singh, R. (2017). Material issues in additive manufacturing: A review. Journal of Manufacturing Processes, 25, 185-200.

[3] : Gibson, I., Rosen, D. W., Stucker, B., & Khorasani, M. (2021). Additive manufacturing technologies (Vol. 17). Cham, Switzerland: Springer.

[4] : Frazier, W. E. (2014). Metal additive manufacturing: a review. Journal of Materials Engineering and performance, 23(6), 1917-1928.

[5] : Singamneni, S., Yifan, L. V., Hewitt, A., Chalk, R., Thomas, W., & Jordison, D. (2019). Additive manufacturing for the aircraft industry: a review. J. Aeronaut. Aerosp. Eng, 8(214), 2.

[6] : Negi, S., Dhiman, S., & Sharma, R. K. (2013). Basics, applications and future of additive manufacturing technologies: A review. Journal of Manufacturing Technology Research, 5(1/2), 75.

[7] : Azarniya, A., Colera, X. G., Mirzaali, M. J., Sovizi, S., Bartolomeu, F., Wits, W. W., ... & Zadpoor, A. A. (2019). Additive manufacturing of Ti –6Al –4V parts through laser metal deposition (LMD): Process, microstructure, and mechanical properties. Journal of Alloys and Compounds, 804, 163-191.

[8] : Zhong, Y., Rännar, L. E., Liu, L., Koptyug, A., Wikman, S., Olsen, J., ... & Shen, Z. (2017). Additive manufacturing of 316L stainless steel by electron beam melting for nuclear fusion applications. Journal of nuclear materials, 486, 234-245.

[9] : Keshavarzkermani, A., Sadowski, M., & Ladani, L. (2018). Direct metal laser melting of Inconel 718: Process impact on grain formation and orientation. Journal of Alloys and Compounds, 736, 297-305.

[10] : Kempen, K., Thijs, L., Van Humbeeck, J., & Kruth, J. P. (2015). Processing AlSi10Mg by selective laser melting: parameter optimisation and material characterisation. Materials Science and Technology, 31(8), 917-923.

[11] : Irrinki, H., Harper, T., Badwe, S., Stitzel, J., Gulsoy, O., Gupta, G., & Atre, S. V. (2018). Effects of powder characteristics and processing conditions on the corrosion performance of 17-4 PH stainless steel fabricated by laser-powder bed fusion. Progress in Additive Manufacturing, 3(1), 39-49.

[12] : Herzog, D., Bartsch, K., & Bossen, B. (2020). Productivity optimization of laser powder bed fusion by hot isostatic pressing. Additive Manufacturing, 36, 101494.

[13] : Guo, N., & Leu, M. C. (2013). Additive manufacturing: technology, applications and research needs. Frontiers of Mechanical Engineering, 8(3), 215-243.

[14] : Patterson, A. E., Messimer, S. L., & Farrington, P. A. (2017). Overhanging features and the SLM/DMLS residual stresses problem: Review and future research need. Technologies, 5(2), 15.

[15] : Huang, Y., Leu, M. C., Mazumder, J., & Donmez, A. (2015). Additive manufacturing: current state, future potential, gaps and needs, and recommendations. Journal of Manufacturing Science and Engineering, 137(1).

[16] : Zhang, Y., Majeed, A., Muzamil, M., Lv, J., Peng, T., & Patel, V. (2021). Investigation for macro mechanical behavior explicitly for thin-walled parts of AlSi10Mg alloy using selective laser melting technique. Journal of Manufacturing Processes, 66, 269-280.

[17] : Singla, A. K., Banerjee, M., Sharma, A., Singh, J., Bansal, A., Gupta, M. K., ... & Goyal, D. K. (2021). Selective laser melting of Ti6Al4V alloy: Process parameters, defects and post-treatments. Journal of Manufacturing Processes, 64, 161-187.

[18] : Maconachie, T., Leary, M., Lozanovski, B., Zhang, X., Qian, M., Faruque, O., & Brandt, M. (2019). SLM lattice structures: Properties, performance, applications and challenges. Materials & Design, 183, 108137.

[19] : Li, Z., Kucukkoc, I., Zhang, D. Z., & Liu, F. (2018). Optimising the process parameters of selective laser melting for the fabrication of Ti6Al4V alloy. Rapid Prototyping Journal.

[20] : Salman, O. O., Brenne, F., Niendorf, T., Eckert, J., Prashanth, K. G., He, T., & Scudino, S. (2019). Impact of the scanning strategy on the mechanical behavior of 316L steel synthesized by selective laser melting. Journal of Manufacturing Processes, 45, 255-261.

[21] : Casati, R., Lemke, J. N., Tuissi, A., & Vedani, M. (2016). Aging behaviour and mechanical performance of 18-Ni 300 steel processed by selective laser melting. Metals, 6(9), 218.

[22] : Sarkar, S., Mukherjee, S., Kumar, C. S., & Nath, A. K. (2020). Effects of heat treatment on microstructure, mechanical and corrosion properties of 15-5 PH stainless steel parts built by selective laser melting process. Journal of Manufacturing Processes, 50, 279-294.

[23] : Nguyen, D. S., Park, H. S., & Lee, C. M. (2020). Optimization of selective laser melting process parameters for Ti-6Al-4V alloy manufacturing using deep learning. Journal of Manufacturing Processes, 55, 230-235.

[24] : Liu, P., Hu, J., Sun, S., Feng, K., Zhang, Y., & Cao, M. (2019). Microstructural evolution and phase transformation of Inconel 718 alloys fabricated by selective laser melting under different heat treatment. Journal of Manufacturing Processes, 39, 226-232.

[25] : dos Santos Paes, L. E., Pereira, M., Xavier, F. A., Weingaertner, W. L., D'Oliveira, A. S. C. M., Costa, E. C., ... & Scotti, A. (2021). Understanding the behavior of laser surface remelting after directed energy deposition additive manufacturing through comparing the use of iron and Inconel powders. Journal of Manufacturing Processes, 70, 494-507.

[26] : Fielden-Stewart, Z., Coope, T., Bacheva, D., & Kim, B. C. (2021). Effect of the surface morphology of SLM printed aluminium on the interfacial fracture toughness of metal-composite hybrid joints. International Journal of Adhesion and Adhesives, 105, 102779.

[27] : Ding, X., & Wang, L. (2017). Heat transfer and fluid flow of molten pool during selective laser melting of AlSi10Mg powder: Simulation and experiment. Journal of Manufacturing Processes, 26, 280-289.

[28] Krishnan, M., Atzeni, E., Canali, R., Calignano, F., Manfredi, D., Ambrosio, E. P., & Iuliano, L. (2014). On the effect of process parameters on properties of AlSi10Mg parts produced by DMLS. Rapid Prototyping Journal.

[29] Suzuki, A., Nishida, R., Takata, N., Kobashi, M., & Kato, M. (2019). Design of laser parameters for selectively laser melted maraging steel based on deposited energy density. Additive Manufacturing, 28, 160-168.

[30] Nayak, P. K., Sahu, A. K., & Mahapatra, S. S. (2020). Effect of Process Parameters on the Mechanical Behavior of FDM and DMLS Build Parts. Materials Today: Proceedings, 22, 1443-1451.

[31] : TAN, C., ZHOU, K., MA, W., & ZENG, D. (2019). Research progress of laser additive manufacturing of maraging steels. Acta Metall Sin, 56(1), 36-52.

[32] : Bouzakis, E., Arvanitidis, A., Kazelis, F., Maliaris, G., & Michailidis, N. (2020). Comparison of additively manufactured vs. conventional maraging steel in corrosion-fatigue performance after various surface treatments. Procedia CIRP, 87, 469-473.

[33] : Kim, D., Kim, T., Ha, K., Oak, J. J., Jeon, J. B., Park, Y., & Lee, W. (2020). Effect of heat treatment condition on microstructural and mechanical anisotropies of selective laser melted maraging 18Ni-300 steel. Metals, 10(3), 410.

[34] : Bodziak, S., Al-Rubaie, K. S., Dalla Valentina, L., Lafratta, F. H., Santos, E. C., Zanatta, A. M., & Chen, Y. (2019). Precipitation in 300 grade maraging steel built by selective laser melting: Aging at 510 C for 2 h. Materials Characterization, 151, 73-83.

[35] : Bajaj, P., Hariharan, A., Kini, A., Kürnsteiner, P., Raabe, D., & Jägle, E. A. (2020). Steels in additive manufacturing: A review of their microstructure and properties. Materials Science and Engineering: A, 772, 138633.

[36] : Suryawanshi, J., Prashanth, K. G., & Ramamurty, U. (2017). Tensile, fracture, and fatigue crack growth properties of a 3D printed maraging steel through selective laser melting. Journal of alloys and compounds, 725, 355-364.

[37] : Kasana, S. S., & Pandey, O. P. (2021). Effect of multipass cold plastic deformation and heat treatment on the mechanical properties of C250 marageing steel for aerospace applications. Proceedings of the Institution of Mechanical Engineers, Part L: Journal of Materials: Design and Applications, 1464420721989373.

[38] : Wuriti, G. S., Chattopadhyaya, S., & Tessy, T. (2020, December). Acoustic emission examination of high-strength steel M250 pressure vessels for aerospace applications. In IOP Conference Series: Materials Science and Engineering (Vol. 998, No. 1, p. 012037). IOP Publishing.

[39] : Ding, H., Zhu, G., Xiang, C., Pei, F., Chen, J., Wang, Y., & Chen, Q. (2020). Excellent combination of plasticity and ultra-high strength in a low-alloy automotive steel treated by conventional continuous annealing. Materials Science and Engineering: A, 791, 139694.

[40] : Tonizzo, Q., Mazière, M., Perlade, A., & Gourgues-Lorenzon, A. F. (2020). Effect of austenite stability on the fracture micromechanisms and ductile-to-brittle transition in a medium-Mn, ultra-fine-grained steel for automotive applications. Journal of Materials Science, 55(22), 9245-9257.

[41] : Fonseca, D. P. M. D., Feitosa, A. L. M., Carvalho, L. G. D., Plaut, R. L., & Padilha, A. F. (2021). A Short Review on Ultra-High-Strength Maraging Steels and Future Perspectives. Materials Research, 24.

[42] : Bai, Y., Yang, Y., Xiao, Z., & Wang, D. (2018). Selective laser melting of maraging steel: mechanical properties development and its application in mold. Rapid Prototyping Journal.

[43] : Anderson, R. E., & Crimmins, P. P. (1964). EVALUATION OF HIGH NICKEL STEEL FOR APPLICATION IN LARGE BOOSTER MOTOR FABRICATION. AEROJET-GENERAL CORP SACRAMENTO CALIF.

[44] : Wu, W., Wang, X., Wang, Q., Liu, J., Zhang, Y., Hua, T., & Jiang, P. (2020). Microstructure and mechanical properties of maraging 18Ni-300 steel obtained by powder bed based selective laser melting process. Rapid Prototyping Journal.

[45] : Becker, T. H., & Dimitrov, D. (2016). The achievable mechanical properties of SLM produced Maraging Steel 300 components. Rapid Prototyping Journal.

[46] : Kempen, K., Yasa, E., Thijs, L., Kruth, J. P., & Van Humbeeck, J. (2011). Microstructure and mechanical properties of Selective Laser Melted 18Ni-300 steel. Physics Procedia, 12, 255-263.

[47] : Ullah, R., Akmal, J. S., Laakso, S., & Niemi, E. (2020). Anisotropy of additively manufactured 18Ni-300 maraging steel: Threads and surface characteristics. Procedia CIRP, 93, 68-78.

[48] : Mooney, B., Kourousis, K. I., & Raghavendra, R. (2019). Plastic anisotropy of additively manufactured maraging steel: Influence of the build orientation and heat treatments. Additive Manufacturing, 25, 19-31.

[49] : de Oliveira, A. R., de Andrade Mendes Filho, A., Masoumi, M., & Del Conte, E. G. (2021). Compression and energy absorption of maraging steel primitive scaffolds produced by powder bed fusion. The International Journal of Advanced Manufacturing Technology, 116(3), 1271-1283.

[50] : Contuzzi, N., Campanelli, S. L., Casavola, C., & Lamberti, L. (2013). Manufacturing and characterization of 18Ni marage 300 lattice components by selective laser melting. Materials, 6(8), 3451-3468.

[51] : Meneghetti, G., Rigon, D., Cozzi, D., Waldhauser, W., & Dabalà, M. (2017). Influence of build orientation on static and axial fatigue properties of maraging steel specimens produced by additive manufacturing. Procedia Structural Integrity, 7, 149-157.

[52] : Yao, Y., Wang, K., Wang, X., Li, L., Cai, W., Kelly, S., ... & Yan, F. (2020). Microstructural heterogeneity and mechanical anisotropy of 18Ni-330 maraging steel fabricated by selective laser melting: The effect of build orientation and height. Journal of Materials Research, 35(15), 2065-2076. [] :

[53] : Conde, F. F., Escobar, J. D., Oliveira, J. P., Béreš, M., Jardini, A. L., Bose, W. W., & Avila, J. A. (2019). Effect of thermal cycling and aging stages on the microstructure and bending strength of a selective laser melted 300-grade maraging steel. Materials Science and Engineering: A, 758, 192-201.

[54] : Bai, Y., Yang, Y., Wang, D., & Zhang, M. (2017). Influence mechanism of parameters process and mechanical properties evolution mechanism of maraging steel 300 by selective laser melting. Materials Science and Engineering: A, 703, 116-123.

[55] : Huang, W., Zhang, W., & Chen, X. (2020, March). Effect of SLM Process Parameters on Relative Density of Maraging Steel (18Ni-300) Formed Parts. In IOP Conference Series: Materials Science and Engineering (Vol. 774, No. 1, p. 012027). IOP Publishing.

[56] : ASTM, E. 9. (2001). Standard test methods for tension testing of metallic materials. Annual book of ASTM standards. ASTM.

[57] : Pirgazi, H., Sanjari, M., Tamimi, S., Amirkhiz, B. S., Kestens, L. A., & Mohammadi, M. (2021). Texture evolution in selective laser melted maraging stainless steel CX with martensitic transformation. Journal of Materials Science, 56(1), 844-853.

[58] : Xu, X., Ganguly, S., Ding, J., Guo, S., Williams, S., & Martina, F. (2018). Microstructural evolution and mechanical properties of maraging steel produced by wire+ arc additive manufacture process. Materials Characterization, 143, 152-162.

[59] : Kurz, W., Rappaz, M., & Trivedi, R. (2021). Progress in modelling solidification microstructures in metals and alloys. Part II: dendrites from 2001 to 2018. International Materials Reviews, 66(1), 30-76.

[60] : Gong, P., Wynne, B. P., Knowles, A. J., Turk, A., Ma, L., Galindo-Nava, E. I., & Rainforth, W. M. (2020). Effect of ageing on the microstructural evolution in a new design of maraging steels with carbon. Acta Materialia, 196, 101-121.

[61] : Gope, D. K., Kumar, P., Chattopadhyaya, S., Wuriti, G., & Thomas, T. (2021, March). An investigation into microstructure and mechanical properties of maraging steel weldment. In IOP Conference Series: Materials Science and Engineering (Vol. 1104, No. 1, p. 012014). IOP Publishing.

[62] : Conde, F. F., Avila, J. A., Oliveira, J. P., Schell, N., Oliveira, M. F., & Escobar, J. D. (2021). Effect of the as-built microstructure on the martensite to austenite transformation in a 18Ni maraging steel after laser-based powder bed fusion. Additive Manufacturing, 46, 102122.

[63] : Yao, Y., Wang, K., Wang, X., Li, L., Cai, W., Kelly, S., ... & Yan, F. (2020). Microstructural heterogeneity and mechanical anisotropy of 18Ni-330 maraging steel fabricated by selective laser melting: The effect of build orientation and height. Journal of Materials Research, 35(15), 2065-2076.

[64] : Ahmadkhaniha, D., Möller, H., & Zanella, C. (2021). Studying the Microstructural Effect of Selective Laser Melting and Electropolishing on the Performance of Maraging Steel. Journal of Materials Engineering and Performance, 1-18.

[65] : Tan, C., Zhou, K., Ma, W., Zhang, P., Liu, M., & Kuang, T. (2017). Microstructural evolution, nanoprecipitation behavior and mechanical properties of selective laser melted high-performance grade 300 maraging steel. Materials & Design, 134, 23-34.

[66] : Tan, C., Zhou, K., Kuang, M., Ma, W., & Kuang, T. (2018). Microstructural characterization and properties of selective laser melted maraging steel with different build directions. Science and technology of advanced materials, 19(1), 746-758.

[67] : Shamsdini, S., Shakerin, S., Hadadzadeh, A., Amirkhiz, B. S., & Mohammadi, M. (2020). A trade-off between powder layer thickness and mechanical properties in additively manufactured maraging steels. Materials Science and Engineering: A, 776, 139041.

[68] : Liu, K., YU, P., & KOU, S. (2020). Solidification Cracking Susceptibility of Stainless Steels: New Test and Explanation. Welding Journal, 99(10).

[69] : Suryawanshi, J., Prashanth, K. G., & Ramamurty, U. (2017). Mechanical behavior of selective laser melted 316L stainless steel. Materials Science and Engineering: A, 696, 113-121.

[70] : Galindo-Nava, E. I., Rainforth, W. M., & Rivera-Díaz-del-Castillo, P. E. J. (2016). Predicting microstructure and strength of maraging steels: Elemental optimisation. Acta Materialia, 117, 270-285.

[71] : Wang, B., Duan, Q. Q., Zhang, P., Zhang, Z. J., Li, X. W., & Zhang, Z. F. (2020). Investigation on the cracking resistances of different ageing treated 18Ni maraging steels. Materials Science and Engineering: A, 771, 138553.

[72] : E. Yasa, J. Deckers, J.-P. Kruth, The investigation of the influence of laser remelting on density, surface quality and microstructure of selective laser melting parts, Rapid Prototype J. 17 (2011) 312–327.

[73] : Demir, A. G., & Previtali, B. (2017). Investigation of remelting and preheating in SLM of 18Ni300 maraging steel as corrective and preventive measures for porosity reduction. The International Journal of Advanced Manufacturing Technology, 93(5), 2697-2709.

[74] : Król, M., Snopiński, P., Hajnyš, J., Pagáč, M., & Łukowiec, D. (2020). Selective laser melting of 18NI-300 maraging steel. Materials, 13(19), 4268.

[75] : Islam, M., Hossain, M., & Hussain, M. (2016). MODIFIED EXTREMUM DIFFERENCE METHOD (MEDM) FOR SOLVING COST MINIMIZING TRANSPORTATION PROBLEMS.

[76] : Wang, D., Song, C., Yang, Y., & Bai, Y. (2016). Investigation of crystal growth mechanism during selective laser melting and mechanical property characterization of 316L stainless steel parts. Materials & Design, 100, 291-299.

[77] : Kučerová, L., Zetková, I., Jeníček, Š., & Burdová, K. (2020). Hybrid parts produced by deposition of 18Ni300 maraging steel via selective laser melting on forged and heat treated advanced high-strength steel. Additive Manufacturing, 32, 101108.

[78] : Mooney, B., & Kourousis, K. I. (2020). A review of factors affecting the mechanical properties of maraging steel 300 fabricated via laser powder bed fusion. Metals, 10(9), 1273.

[79] : Cui, L., Jiang, S., Xu, J., Peng, R. L., Mousavian, R. T., & Moverare, J. (2021). Revealing relationships between microstructure and hardening nature of additively manufactured 316L stainless steel. Materials & Design, 198, 109385.

[80] : Zhang, B., Li, Y., & Bai, Q. (2017). Defect formation mechanisms in selective laser melting: a review. Chinese Journal of Mechanical Engineering, 30(3), 515-527.

[81] : Shipley, H., McDonnell, D., Culleton, M., Coull, R., Lupoi, R., O'Donnell, G., & Trimble, D. (2018). Optimisation of process parameters to address fundamental challenges during selective laser melting of Ti-6Al-4V: A review. International Journal of Machine Tools and Manufacture, 128, 1-20.

[82] : Galy, C., Le Guen, E., Lacoste, E., & Arvieu, C. (2018). Main defects observed in aluminum alloy parts produced by SLM: from causes to consequences. Additive manufacturing, 22, 165-175.

[83] : Choi, J. P., Shin, G. H., Brochu, M., Kim, Y. J., Yang, S. S., Kim, K. T., ... & Yu, J. H. (2016). Densification behavior of 316L stainless steel parts fabricated by selective laser melting by variation in laser energy density. Materials Transactions, M2016284.

[84] : Larimian, T., Kannan, M., Grzesiak, D., AlMangour, B., & Borkar, T. (2020). Effect of energy density and scanning strategy on densification, microstructure and mechanical properties of 316L stainless steel processed via selective laser melting. Materials Science and Engineering: A, 770, 138455.

[85] : Tucho, W. M., Lysne, V. H., Austbø, H., Sjolyst-Kverneland, A., & Hansen, V. (2018). Investigation of effects of process parameters on microstructure and hardness of SLM manufactured SS316L. Journal of Alloys and Compounds, 740, 910-925.

[86] : Phutela, C., Aboulkhair, N. T., Tuck, C. J., & Ashcroft, I. (2020). The effects of feature sizes in selectively laser melted Ti-6Al-4V parts on the validity of optimised process parameters. Materials, 13(1), 117.

[87] : Fonseca, E. B., Gabriel, A. H., Araújo, L. C., Santos, P. L., Campo, K. N., & Lopes, E. S. (2020). Assessment of laser power and scan speed influence on microstructural features and consolidation of AISI H13 tool steel processed by additive manufacturing. Additive Manufacturing, 34, 101250.

[88] : Kaschel, F. R., Celikin, M., & Dowling, D. P. (2020). Effects of laser power on geometry, microstructure and mechanical properties of printed Ti-6Al-4V parts. Journal of Materials Processing Technology, 278, 116539.

[89] : Suzuki, A., Nishida, R., Takata, N., Kobashi, M., & Kato, M. (2019). Design of laser parameters for selectively laser melted maraging steel based on deposited energy density. Additive Manufacturing, 28, 160-168.
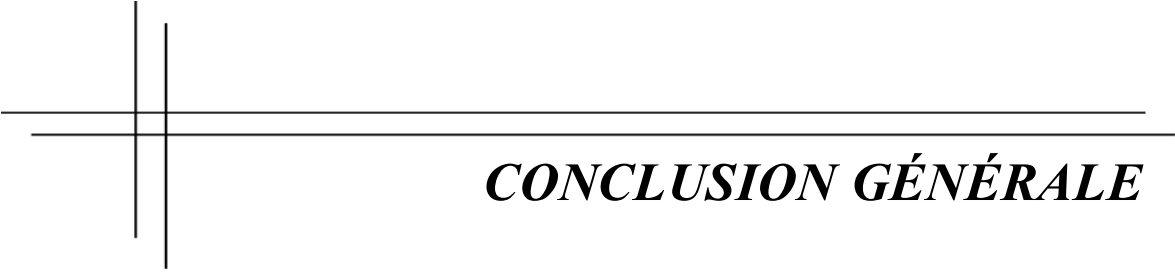
CONCLUSION GÉNÉRALE

Le procédé SLM est envisagé pour l'élaboration de pièces en acier maraging destinées à des applications avancées dans divers domaines comme l'industrie automobile et aérospatiale. Mais, il n'existe pas des protocoles ou bien des normes spécifiques pour les propriétés mécaniques finales des aciers maraging élaborés par SLM. Les travaux de recherche présentés dans ce document s'attachent à décrire le procédé de fusion sélective par laser (selective laser melting, SLM) appliqué à des aciers maraging. Cette description passe par l'étude des éléments nécessaires au fonctionnement du procédé, en particulier les interrelations entre les performances mécaniques produites avec, à la fois, les paramètres de processus SLM d'une part, et les paramètres de post-traitement thermique d'autre part. L'intérêt s'est ensuite porté sur le produit fini, sa microstructure, sa densité, ses défauts et ses performances mécaniques. Pour y arriver, le premier objectif était principalement focalisé sur l'étude de l'influence d'une série de traitements thermiques sur les performances mécaniques finales. Ce premier objectif avait pour but de chercher l'interrelation entre les performances mécaniques et les paramètres des post-traitements thermiques appliqués. Une optimisation des paramètres de post-traitement thermique a été réalisée pour maximiser les bénéfices apportés par les post-traitements thermiques sur la qualité et les performances mécaniques des pièces. Puis, le second objectif était destiné à étudier l'influence des paramètres du procédé sur la solidification et la microstructure générées à partir de lit de poudre ainsi que la sensibilité des performances mécaniques finales à ces paramètres, qui complètent les travaux réalisés pour appréhender le comportement du matériau. Pour cela, il était important de trouver des modèles de prédiction pour pouvoir améliorer le processus SLM. Les travaux d'optimisation ont permis de trouver les valeurs de paramètres qui permettent d'avoir la meilleure combinaison des paramètres de processus SLM dans la région de travail avec les meilleures propriétés mécaniques. Afin de répondre à ces objectifs, deux axes de recherche ont été menés dont chacun avait pour dessein de faire avancer la recherche pour accéder aux buts fixés liés aux problématiques.

La première phase de cette étude avait pour but d'investiguer l'effet de post-traitement sur la microstructure et les performances mécaniques et d'optimiser les paramètres de ces post-traitements. En effet, suite à la fabrication additive, un recours à des post-traitements est souvent indispensable dans le but d'homogénéiser la microstructure et d'améliorer les performances mécaniques finales. Un post-traitement composé d'une étape d'homogénéisation en solution et d'une étape de vieillissement. Une série des traitements thermiques a été effectuée sur l'acier maraging (C300) dont l'étape d'homogénéisation à 1020 °C pour 15 min est commune. Les facteurs considérés parmi les paramètres possibles de traitement thermique sont la solution de refroidissement (la concentration), la température de vieillissement et le temps de vieillissement. Trois solutions aqueuses de NaCl (S1 : concentration égale à 0 %, S2 : concentration égale à 6 %, S3 : concentration égale à 12 %), trois températures de vieillissement (485 °C, 585 °C, et 685 °C) et trois temps de vieillissement (120 min, 150 min, et 180 min) ont été considérés. La microstructure et les propriétés mécaniques de l'acier maraging (C300) traitées ont été évaluées et comparées. Le traitement thermique d'homogénéisation en solution à 1020 °C pendant 15 min a un effet significatif sur la microstructure. La forme et la taille des grains, ainsi que la taille des cellules, raffinent plus après ce traitement thermique. La microdureté est l'une des grandeurs impactées par le traitement thermique. Indépendamment de la solution de refroidissement, la dureté diminue légèrement après ce traitement thermique. Cette baisse est attribuée à la transformation austénite-martensite. Le traitement de vieillissement a un effet significatif sur la microstructure et les propriétés mécaniques des aciers maraging élaborés par SLM. Cependant, la nature de cet effet varie en fonction de la température et temps de vieillissement. Le traitement de vieillissement provoque un durcissement de l'acier maraging (C300) jusqu'à un maximum et par la suite nous avons un adoucissement. Plus la température de vieillissement, la dureté achève son maximum plus rapidement. Mais au-dessus d'une certaine température, ce maximum est plus faible. L'analyse ANOVA, effectuée sur les résultats expérimentaux, génère un modèle prédictif pour la dureté. Les travaux d'optimisations réalisés dans cette partie montrent que le traitement de vieillissement optimal est réalisé à une température de 480-485 °C dans un intervalle de 120-180 min.

Le deuxième axe a permis d'étudier l'influence de trois paramètres du procédé SLM (la puissance P, la vitesse V et l'espace d'hachurage h) sur la microstructure et les performances mécaniques de pièces en acier maraging. Cette partie vise en premier lieu à analyser la sensibilité des performances mécaniques aux paramètres de processus SLM. De nombreux résultats ont pu être tirés de cette étude. Ils sont propres à l'imprimante EOS290 et à l'acier maraging (C300). Les paramètres de référence préconisés par le constructeur de la machine EOS pour l'élaboration de pièces en acier maraging sont : P = 295 W, V = 1000 mm/s, h = 100 µm. À travers cette partie, il a été possible d'analyser l'effet d'une petite variation des valeurs de ces paramètres sur la densité, la microstructure et les propriétés en traction. Premièrement, on a pu évaluer l'effet de la puissance (P = 270 W, 295 W et 320 W), de la vitesse de balayage (V = 1000 mm/s, 1050 mm/s et 1100 mm/s) et de l'espace d'hachurage (h = 80 µm, 100 µm et 120 µm) sur la microstructure et la densité de l'acier maraging. L'étude expérimentale montre que l'espace d'hachurage, à travers son intérêt pour un bon chevauchement entre les couches, puis la puissance laser sont les facteurs les plus significatifs. Pour l'obtention d'une pièce dense à plus de 98 %, la puissance laser doit être supérieure à 270 W, la vitesse de balayage doit être ciblée autour de 1000 mm/s et l'espace d'hachurage doit être ciblé autour de 80 µm. Pour la suite, un plan d'expérience basé sur la méthode Taguchi L9 a été établi. Les résultats des analyses expérimentales montrent une grande influence du gap sur les propriétés mécaniques des pièces en plus des effets de paramètres de processus SLM. En utilisant ANOVA, un modèle de prédiction de la dureté et de la résistance ultime des pièces en acier maraging (C300) qui a été développé pour approximer la valeur de ces sorties à partir des paramètres admis à l'aide de la méthode de régression, une forte corrélation a été trouvée. La méthode de la surface de réponse a montré un effet paradoxal des paramètres sur la dureté et les paramètres en traction (résistance mécanique, la ductilité). La dureté est favorisée par une puissance se situant autour ou plus de 320 W, une vitesse se situant autour ou moins de 1000 W et un espace d'hachurage se situant autour ou moins de 80 µm tandis que la résistance mécanique est favorisée par une puissance se situant autour ou moins de 270 W, une vitesse se situant entre 1020 mm/s et 1080 mm/s et une espace d'hachurage plus que 95 µm.

Certaines études complémentaires n'ont pas pu être effectuées durant ce mémoire. Elles pourraient s'avérer bénéfiques et complémentaires à ce travail. Cette partie représente les horizons qui peuvent être explorés à partir des résultats de la recherche réalisée ainsi que les suggestions pour approfondir le sujet dans l'avenir :

- Explorer les effets de paramètres de processus SLM et de post-traitement sur d'autres propriétés mécaniques des matériaux, telles que la résistance à la fatigue, la résistance à la corrosion ou encore la résistance à l'impact ;

- Simuler par éléments finis les différents comportements (thermique, mécanique, et métallurgique) ;

- Étudier le durcissement surfacique par faisceau laser de l'acier maraging (C300) comme une solution rapide à même effet que les traitements thermiques ;

- Élargir ses études sur d'autres alliages et viser un domaine plus large pour l'utilisation de la technique SLM ;

- Élargir ses études vers des composites métalliques.

RÉFÉRENCES BIBLIOGRAPHIQUES

Righettini, P., & Strada, R. (2021). Driving Technologies for the Design of Additive Manufacturing Systems. HighTech and Innovation Journal, 2(1), 20-28.

Gibson, I., Rosen, D. W., Stucker, B., & Khorasani, M. (2021). Additive manufacturing technologies (Vol. 17). Cham, Switzerland: Springer.

Law, W. K., Wong, K. C., Wang, H., Sun, Z., & Lim, C. S. (2021). Microstructure Evolution in Additively Manufactured Steel Molds: A Review. Journal of Materials Engineering and Performance, 1-17.

Cao, Q., Zhang, J., Chang, S., Fuh, J. Y. H., & Wang, H. (2020). The effect of support structures on maraging steel MS1 parts fabricated by selective laser melting at different building angles. Rapid Prototyping Journal.

Gibson, I., Rosen, D., Stucker, B., & Khorasani, M. (2021). Development of additive manufacturing technology. In Additive manufacturing technologies (pp. 23-51). Springer, Cham.

Wang, Y., Luo, L., Liu, T., Wang, B., Luo, L., Zhao, J., ... & Fu, H. (2021). Tuning process parameters to optimize microstructure and mechanical properties of novel maraging steel fabricated by selective laser melting. Materials Science and Engineering: A, 823, 141740.

AFNOR, « NF ISO/ASTM 52915 Spécifications normalisées pour le format de fichier pour la fabrication additive (AMF) », 2016.

Durakovic, B. (2018). Design for additive manufacturing: Benefits, trends and challenges. Periodicals of Engineering and Natural Sciences (PEN), 6(2), 179-191.

Wang, Y., Chen, X., Jayalakshmi, S., Singh, R. A., Sergey, K., & Gupta, M. (2020). Process Parameters, Product Quality Monitoring, and Control of Powder Bed Fusion. Transactions on Intelligent Welding Manufacturing, 89-108.

Tan, C., Weng, F., Sui, S., Chew, Y., & Bi, G. (2021). Progress and perspectives in laser additive manufacturing of key aeroengine materials. International Journal of Machine Tools and Manufacture, 103804.

Zhang, X., Yocom, C. J., Mao, B., & Liao, Y. (2019). Microstructure evolution during selective laser melting of metallic materials: A review. Journal of Laser Applications, 31(3), 031201.

De Souza, A. F., Al-Rubaie, K. S., Marques, S., Zluhan, B., & Santos, E. C. (2019). Effect of laser speed, layer thickness, and part position on the mechanical properties of maraging 300 parts manufactured by selective laser melting. Materials Science and Engineering: A, 767, 138425.

Yang, Y., Gong, Y., Li, C., Wen, X., & Sun, J. (2021). Mechanical performance of 316 L stainless steel by hybrid directed energy deposition and thermal milling process. Journal of Materials Processing Technology, 291, 117023.

Bai, Y., Zhao, C., Yang, J., Hong, R., Weng, C., & Wang, H. (2021). Microstructure and machinability of selective laser melted high-strength maraging steel with heat treatment. Journal of Materials Processing Technology, 288, 116906.

Zhang, B., Li, Y., & Bai, Q. (2017). Defect formation mechanisms in selective laser melting: a review. Chinese Journal of Mechanical Engineering, 30(3), 515-527.

Mutua, J., Nakata, S., Onda, T., & Chen, Z. C. (2018). Optimization of selective laser melting parameters and influence of post heat treatment on microstructure and mechanical properties of maraging steel. Materials & Design, 139, 486-497.

Mugwagwa, L., Yadroitsev, I., & Matope, S. (2019). Effect of Process Parameters on Residual Stresses, Distortions, and Porosity in Selective Laser Melting of Maraging Steel 300. Metals, 9(10), 1042.

Bai, Y., Yang, Y., Wang, D., & Zhang, M. (2017). Influence mechanism of parameters process and mechanical properties evolution mechanism of maraging steel 300 by selective laser melting. Materials Science and Engineering: A, 703, 116-123.

Yao, Y., Huang, Y., Chen, B., Tan, C., Su, Y., & Feng, J. (2018). Influence of processing parameters and heat treatment on the mechanical properties of 18Ni300 manufactured by laser based directed energy deposition. Optics & Laser Technology, 105, 171-179.

Guo, W. F., Guo, C., & Zhu, Q. (2018). Heat treatment behavior of the 18Ni300 maraging steel additively manufactured by selective laser melting. In Materials Science Forum (Vol. 941, pp. 2160-2166). Trans Tech Publications Ltd.

Conde, F. F., Escobar, J. D., Oliveira, J. P., Béreš, M., Jardini, A. L., Bose, W. W., & Avila, J. A. (2019). Effect of thermal cycling and aging stages on the microstructure and bending strength of a selective laser melted 300-grade maraging steel. Materials Science and Engineering: A, 758, 192-201.

241

Kempen, K., Vrancken, B., Buls, S., Thijs, L., Van Humbeeck, J., & Kruth, J. P. (2014). Selective laser melting of crack-free high density M2 high speed steel parts by baseplate preheating. Journal of Manufacturing Science and Engineering, 136(6).

Yuan, L., Ding, S., & Wen, C. (2019). Additive manufacturing technology for porous metal implant applications and triple minimal surface structures: A review. Bioactive Materials, 4, 56-70.

Gu, H., Wei, C., Li, L., Han, Q., Setchi, R., Ryan, M., & Li, Q. (2020). Multi-physics modelling of molten pool development and track formation in multi-track, multi-layer and multi-material selective laser melting. International Journal of Heat and Mass Transfer, 151, 119458.

Bai, Y., Zhao, C., Wang, D., & Wang, H. (2022). Evolution mechanism of surface morphology and internal hole defect of 18Ni300 maraging steel fabricated by selective laser melting. Journal of Materials Processing Technology, 299, 117328.

Bodziak, S., Al-Rubaie, K. S., Dalla Valentina, L., Lafratta, F. H., Santos, E. C., Zanatta, A. M., & Chen, Y. (2019). Precipitation in 300 grade maraging steel built by selective laser melting: Aging at 510 C for 2 h. Materials Characterization, 151, 73-83.

Kim, D., Kim, T., Ha, K., Oak, J. J., Jeon, J. B., Park, Y., & Lee, W. (2020). Effect of heat treatment condition on microstructural and mechanical anisotropies of selective laser melted maraging 18Ni-300 steel. Metals, 10(3), 410.

Mugwagwa, L., Yadroitsev, I., & Matope, S. (2019). Effect of process parameters on residual stresses, distortions, and porosity in selective laser melting of maraging steel 300. Metals, 9(10), 1042.

Kim, D., Kim, T., Ha, K., Oak, J. J., Jeon, J. B., Park, Y., & Lee, W. (2020). Effect of heat treatment condition on microstructural and mechanical anisotropies of selective laser melted maraging 18Ni-300 steel. Metals, 10(3), 410.

Yin, S., Chen, C., Yan, X., Feng, X., Jenkins, R., O'Reilly, P., ... & Lupoi, R. (2018). The influence of aging temperature and aging time on the mechanical and tribological properties of selective laser melted maraging 18Ni-300 steel. Additive Manufacturing, 22, 592-600.

Huang, W., Zhang, W., & Chen, X. (2020, March). Effect of SLM Process Parameters on Relative Density of Maraging Steel (18Ni-300) Formed Parts. In IOP Conference Series: Materials Science and Engineering (Vol. 774, No. 1, p. 012027). IOP Publishing.

Jägle, E. A., Sheng, Z., Kürnsteiner, P., Ocylok, S., Weisheit, A., & Raabe, D. (2017). Comparison of maraging steel micro-and nanostructure produced conventionally and by laser additive manufacturing. Materials, 10(1), 8.

Casati, R., Lemke, J. N., & Vedani, M. (2017). Microstructural and Mechanical Properties of As Built, Solution treated and Aged 18Ni (300 grade) Maraging Steel Produced by Selective Laser Melting.

Becker, T. H., & Dimitrov, D. (2016). The achievable mechanical properties of SLM produced Maraging Steel 300 components. Rapid Prototyping Journal.

Bai, Y., Yang, Y., Wang, D., & Zhang, M. (2017). Influence mechanism of parameters process and mechanical properties evolution mechanism of maraging steel 300 by selective laser melting. Materials Science and Engineering: A, 703, 116-123.

Dehgahi, S., Alaghmandfard, R., Tallon, J., Odeshi, A., & Mohammadi, M. (2021). Microstructural evolution and high strain rate compressive behavior of as-built and heat-treated additively manufactured maraging steels. Materials Science and Engineering: A, 815, 141183.

Mooney, B., Kourousis, K. I., & Raghavendra, R. (2019). Plastic anisotropy of additively manufactured maraging steel: Influence of the build orientation and heat treatments. Additive Manufacturing, 25, 19-31.

Croccolo, D., De Agostinis, M., Fini, S., Olmi, G., Vranic, A., & Ciric-Kostic, S. (2016). Influence of the build orientation on the fatigue strength of EOS maraging steel produced by additive metal machine. Fatigue & Fracture of Engineering Materials & Structures, 39(5), 637-647.